

Quantification of Cation Sorption to Engineered Barrier Materials Under Extreme Conditions

Fuel Cycle Research and Development

Brian Powell
Clemson University

In collaboration with:
University of California, Berkeley

JC de la Garza, Federal POC
Carlos Jove-Colon, Technical POC

**FINAL REPORT: QUANTIFICATION OF CATION SORPTION TO ENGINEERED
BARRIER MATERIALS UNDER EXTREME CONDITIONS**

DOE NEUP Project: 11-3180

Lead University: Clemson University

Lead Principal Investigator:

Brian A. Powell, Clemson University
Associate Professor, Fjeld Professor in Nuclear Environmental Engineering and Science
Department of Environmental Engineering and Earth Sciences
Clemson University
342 Computer Court
Anderson, SC 29625
Office: (864) 656-1004
Email: bpowell@clemson.edu

Co-Investigators: Mark Schlautman, Clemson University

Linfeng Rao, Lawrence Berkeley National Laboratory

Heino Nitsche, University of California Berkeley

Note after Dr. Nitsche passed away in 2014, Dr. Ken Gregorich has taken on the lead Co-PI role at University of California Berkeley.

Project Period: 10/1/2012-9/30/2015, Project Final Report

Report Submission Date: 2/2/2016

TABLE OF CONTENTS

PROJECT OBJECTIVES	3
PROJECT MILESTONES, ACHIEVEMENTS, and FUTURE WORK	3
TASK DESCRIPTIONS and PROGRESS FOR EACH MILESTONE.....	5
STUDENTS AND POSTDOCS	7
ENCOUNTERED or EXPECTED PROBLEMS and CONCERNS	7
APPENDIX A: Reports for Milestone: M3NU-11-SC-CU__-0204-025: Calorimetric titrations of actinide sorption to iron oxide minerals	9
APPENDIX B: Reports for Milestone: M2NU-11-SC-CU_-0204-029: Examination of actinide sorption to hematite under variable temperatures	55
APPENDIX C: Report for Milestone: M3NU-11-SC-CU__-0204-026: X-ray absorption spectroscopic characterization of actinide speciation at hematite:water and montmorillonite:water interfaces.....	106
APPENDIX D: Milestone: M2NU-11-SC-CU__-0204-028: Examination of actinide sorption to montmorillonite at variable temperatures and variable ionic strengths.	122
APPENDIX E: REPORT FOR Milestone: M3NU-11-SC-CU__-0204-0210: Calorimetric titrations of actinide sorption to montmorillonite	160
APPENDIX F: Report for Milestone: M3NU-11-SC-CU__-0204-0211: Evaluation of bentonite performance under repository conditions.....	168

PROJECT OBJECTIVES

The objective of this research is to examine mechanisms and thermodynamics of actinide sorption to engineered barrier materials (iron (oxyhydr)oxides and bentonite clay) for nuclear waste repositories under high temperature and high ionic strength conditions using a suite of macroscopic and microscopic techniques which will be coupled with interfacial reaction models. This work directly addresses the expressed need in Technical Work Scope Identifier FC-6 for understanding “aqueous speciation and surface sorption at high temperature and high ionic strengths anticipated in near field conditions.” Gaining a mechanistic understanding of interfacial processes governing the sorption/sequestration of actinides at mineral-water interfaces is fundamental for the accurate prediction of actinide behavior in waste repositories. Although macroscale sorption data and various spectroscopic techniques have provided valuable information regarding speciation of actinides at solid-water interfaces, significant knowledge gaps still exist with respect to sorption mechanisms and our ability to quantify sorption, particularly at high temperatures and ionic strengths.

This objective will be met through three major tasks:

- Task 1: Influence of oxidation state on actinide sorption to iron oxides and clay minerals at elevated temperatures and ionic strengths
- Task 2: Calorimetric titrations of actinide-mineral suspensions
- Task 3: Evaluation of bentonite performance under repository conditions

The deliverables will consist of a qualitative conceptual model and a quantitative thermodynamic speciation model describing actinide partitioning to minerals and sediments, which is based upon a mechanistic understanding of specific sorption processes as determined from both micro-scale and macro-scale experimental techniques. The speciation model will be a thermodynamic aqueous and surface complexation model of actinide interactions with mineral surfaces that is self-consistent with macroscopic batch sorption data, calorimetric and potentiometric titrations, X-ray absorption Spectroscopy (XAS, mainly Extended X-ray Absorption Fine Structure (EXAFS)), and electron microscopy analyses. The novelty of the proposed work lies largely in the unique system conditions which will be examined (i.e. elevated temperature and ionic strength) and the manner in which the surface complexation model will be developed in terms of specific surface species identified using XAS. These experiments will thus provide a fundamental understanding of the chemical and physical processes occurring at the solid-solution interface under expected repository conditions. Additionally, the focus on thermodynamic treatment of actinide ion interactions with minerals as proposed here will provide information on the driving forces involved and contribute to the overall understanding of the high affinity many actinide ions have for oxide surfaces. The utility of this model will be demonstrated in this work through a series of advective and diffusive flow experiments (Task 3 below).

PROJECT MILESTONES, ACHIEVEMENTS, AND FUTURE WORK

All milestones outlined for this project were met. The project started in FY11 and received a one year no-cost extension to allow for a fourth year of work. The no cost extension was needed due to 1) the initial delay in setting up this project with DOE-NE and 2) the unfortunate passing of our collaborator, Professor Heino Nitsche at University of California- Berkeley. The major achievements of each milestone are listed in Table 1. While each of the milestones set forth in the project were met, additional data and studies for many of the milestones are still required to improve our understanding of the systems. Therefore, the data in these reports is considered preliminary and additional quantitative models will be developed to describe the data which will be included in peer reviewed manuscripts to be written in the coming months. Critical future work from this project includes:

1. Additional studies examining surface protonation/deprotonation of mineral surfaces and actinide sorption to mineral surfaces using isothermal titration calorimetry (ITC) will be performed and accurate models to analyze the available data will be developed. Our current efforts using simple double layer and triple layer models are not able to fully describe the data.

2. While we have collected x-ray absorption spectroscopy (XAS) data for several new systems at variable ionic strengths, we are still unable to collect data at elevated temperatures in real time. Development of sampling protocols or new XAS sample cells to facilitate these measurements will be very useful.
3. Additional analysis and experiments are needed to examine ion leaching from clay minerals (i.e. native uranium and europium leaching at low pH) and the influence of high ionic strength background solutions on actinide sorption to clay minerals.

Table 1: List of project mile stones, completion date, and major achievement.

Milestone Title	Completion Date	Major Achievement(s)
M3NU-11-SC-CU__-0204-025: Calorimetric titrations of actinide sorption to iron oxide minerals	9/30/2015	Endothermic sorption of uranium and europium to hematite was verified using isothermal titration calorimetry.
M2NU-11-SC-CU_-0204-029: Examination of actinide sorption to hematite under variable temperatures	9/30/2015	Sorption of Eu(III), Th(IV), Np(V), U(VI), and Pu(IV) to hematite was monitored from 15 °C to 80 °C. Sorption increased with increasing temperature indicating an endothermic process.
M3NU-11-SC-CU__-0204-026: X-ray absorption spectroscopic characterization of actinide speciation at hematite:water and montmorillonite:water interfaces	9/30/2015	Np(V) and Pu(IV) sorption to hematite and montmorillonite were monitored as a function of ionic strength and temperature. The majority of data was for Np(V). The results indicated that the surface speciation of Np(V) is independent of ionic strength but does appear to change at higher temperatures.
M2NU-11-SC-CU__-0204-028: Examination of actinide sorption to montmorillonite at variable temperatures and variable ionic strengths.	9/30/2015	Eu(III), Th(IV), Np(V), and U(VI) sorption to montmorillonite was examined as a function of ionic strength (0.01 M, 0.10 M, and 1.0 M NaCl) and temperature (25 °C, 50 °C, and 80 °C) across the pH range 4 to 9. Sorption increased with increasing pH in all cases consistent with the hypothesis of sorption being an endothermic process driven by a favorable entropy. In many cases, sorption decreased with increasing ionic strength due to competition with Na ⁺ .
M3NU-11-SC-CU__-0204-0210: Calorimetric titrations of actinide sorption to montmorillonite	9/30/2015	This milestone was met but only a small amount of data was collected. Sorption of Eu(III) to montmorillonite was examined and the results indicated that reaction heats were primarily associated with dilution of the high ionic strength salt solutions. However, the data clearly show that Eu(III) sorption is an endothermic process, similar to observations with hematite.
M3NU-11-SC-CU__-0204-0211: Evaluation of bentonite performance under repository conditions	9/30/2015	Diffusion of Np(V) through montmorillonite was examined at 25 °C and 50 °C. Breakthrough was consistent with stronger sorption of Np(V) to montmorillonite at elevated temperatures.

TASK DESCRIPTIONS AND PROGRESS FOR EACH MILESTONE

Milestone: M3NU-11-SC-CU__ -0204-025: Calorimetric titrations of actinide sorption to iron oxide minerals

Objective:

In this work the enthalpy of actinide sorption to hematite was measured using isothermal titration microcalorimetry. Experiments focused on Eu(III) and U(VI) sorption to hematite at 25°C. The data indicated that sorption of both Eu(III) and U(VI) are endothermic. This is consistent with our overarching hypothesis that sorption of actinide cations is driven by an entropically favored dehydration of the ion upon sorption.

Reporting Status:

Two reports were uploaded onto the PICSNE site describing calorimetric titrations of Eu(III) and U(VI) to hematite. Two reports are provided in Appendix A of this summary. The reports are titled:

- Estes, S. and Powell, B. A., “Calorimetric determination of the enthalpy of Eu(III) sorption to hematite”
- Estes, S. and Powell, B. A., “The thermodynamics of U(VI) sorption to hematite”

Milestone: M2NU-11-SC-CU_ -0204-029: Examination of actinide sorption to hematite under variable temperatures

Objective:

In this task Eu(III), Th(IV), Pu(IV), Np(V), and U(VI) sorption to potential steel corrosion product hematite will be examined at temperatures ranging from 25°C to 80°C.

Reporting status:

We have completed several reports describing data collected in this area. A copy of each report is provided in Appendix B of this summary. We plan for each of these to be submitted to peer reviewed journals and submitted as our reports for each milestone. These include the following:

- Mangold, J. and Powell, B. A., “Examination of Uranium and Neptunium sorption to hematite versus ionic strength and temperature”
- Estes, S. and Powell, B. A., “The thermodynamics of U(VI) sorption to hematite”. (Note this overlaps with milestone M3NU-11-SC-CU__ -0204-025 above).
- Estes, S. and Powell, B. A., “Examination of Np(V), Th(IV), and Pu(V/IV) sorption to hematite as a function of temperature

Milestone: M3NU-11-SC-CU__ -0204-026: X-ray absorption spectroscopic characterization of actinide speciation at hematite:water and montmorillonite:water interfaces

Objective:

X-ray absorption spectroscopy was used to characterize the speciation of actinides at hematite:water and montmorillonite:water interfaces. Experiments focused on Np(V) and Pu. Data are currently available in the peer reviewed literature for Eu(III) and U(VI). We have completed studies of Np(V)-hematite and Np(V)-montmorillonite systems. Data for the Pu systems have become available from a separately funded

project so they were not examined as part of this project. To utilize our additional beamtime, we continued our studies of Np(V)-mineral reactions in greater detail

Reporting status:

A report describing the data for this milestone has been submitted and a copy of the report is provided in Appendix C of this summary. A separate report will be submitted for this milestone but the data was also described with other milestones for eventual publication in peer reviewed literature.

- Olive, D., Wang D., Powell B. A., “XAS studies of actinide sorption to hematite and montmorillonite”

Milestone: M2NU-11-SC-CU__-0204-028: Examination of actinide sorption to montmorillonite at variable temperatures and variable ionic strengths.

Objective:

In this task Eu(III), Th(IV), Np(V), and U(VI) sorption to montmorillonite was examined at temperatures ranging from 25 °C to 80 °C and ionic strengths ranging from 1mM to 1M. Data collection for this milestone is complete and we are currently working on quantitative models of the data for publication of peer reviewed papers. Due to the experimental difficulty in working with Pu(IV) and monitoring oxidation states in the systems, the decision was made to focus only on Eu(III), Np(V), Th(IV), and U(VI) and examine larger datasets and experimental variables.

Reporting status:

The following reports were submitted describing these data and is provided in Appendix D of this summary. The Np(V) dataset has been combined with x-ray absorption spectroscopy data in a draft peer reviewed manuscript.

- Powell, B. A., Baldwin, J., Black, E. M., DeMille, R., Waterhouse, T., “Examination of actinide sorption to montmorillonite as a function of temperature and ionic strength.
- Olive, D. T., Wang, D. L., Baldwin, J., Black, E. M., DeMille, R., Waterhouse, T., Powell, B. A. “Examination of neptunium sorption to montmorillonite as a function of temperature and ionic strength”

Milestone: M3NU-11-SC-CU__-0204-0210: Calorimetric titrations of actinide sorption to montmorillonite

Objective:

The following report was uploaded to PICSNE which describes work done up to the end of this project on September 30, 2015. Because of the difficulties encountered modeling the hematite ITC data, we did not have sufficient time to perform detailed experiments with montmorillonite. So this is an abbreviated study examining surface reactivity of montmorillonite and Eu(III) sorption at 25 °C and ionic strengths of 0.01 M, 0.10M and 1.0 M using NaCl. The results are considered a preliminary study and are not suitable for publication. A great lesson in subtraction of dilution heats was learned. When performing the titrations, the 0.01 M NaOH titrant solution must be adjusted to the appropriate ionic strength. Otherwise, dilution heats from the changing ionic strength cause a swamping signal and masks the true data.

Reporting status:

The following report was submitted in fulfillment of this milestone and is provided in Appendix E of this summary.

- Xie, Y., and Powell, B. A., “Examination of Eu(III) sorption to montmorillonite using isothermal titration calorimetry

Milestone: M3NU-11-SC-CU__ -0204-0211: Evaluation of bentonite performance under repository conditions

Objective:

The intent of the experiments in this task will be to evaluate bentonite performance under repository conditions. Diffusion cell experiments were performed under variable temperature conditions to examine the influence of temperature on actinide diffusion through montmorillonite clay. The initial goal was to monitor multiple actinides. The data from batch sorption experiments describing the influence of temperature and ionic strength on actinide sorption were to be used to evaluate the diffusion data. However, due to the available time on the project and requirements to complete the batch sorption work, we were only able to start experiments examining Np(V) diffusion through montmorillonite clay at 25 oC and 50 oC in 0.01 M NaCl at pH 6. The influence of bulk density was examined by performing experiments with bulk densities of 1.15, 1.30, 1.45, and 1.60 g cm⁻³.

Reporting Status:

The following report was uploaded to PICSNE showing the data collected up to the end of this project on September 30, 2015. The studies are continuing and additional data will be included in an eventual peer reviewed publication based on this study. In particular, we will complete the experiments at 50 °C and attempt experiments at 80 °C. Additionally, we will segment the clay plugs from all experiments and measure the Np concentration as a function of distance from the inlet of the cell. A more rigorous quantitative model than what is presented below will be applied to the data which will also include evaluation of the solid phase Np concentration measurements.

STUDENTS AND POSTDOCS

Name	Citizenship	Major
Shanna Estes	USA	Earth and Environmental Sciences
<i>Tyler Waterhouse</i>	USA	Earth and Environmental Sciences
<i>Jonathan Baldwin</i>	USA	Earth and Environmental Sciences
Deborah Wang	USA	Chemistry
<i>Chunli Yang</i>	China	Chemistry
Daniel Olive (postdoc)	USA	Physics
Ran Chen (postdoc)	USA	Physics
Jerry Mangold (postdoc)	USA	Earth and Environmental Sciences
<i>Chao Xu (postdoc)</i>	China	Chemistry
<i>Erin Black</i>	USA	Earth and Environmental Sciences
<i>Richard DeMille</i>	USA	Earth and Environmental Sciences
Yu Xie	China	Earth and Environmental Sciences

ENCOUNTERED OR EXPECTED PROBLEMS AND CONCERNS

One major issue that has arisen is the need for more mechanistically based surface complexation models for analysis of the experimental data. We have discovered in analyzing our calorimetry data that more advanced triple layer models may provide additional mechanistic information regarding the mineral surfaces and associated reactions. However, these more advanced models also come with additional fitting parameters which much be constrained. Therefore, we can easily have systems which may have a non-unique solution and thus the final constants provided by the model may be unreliable. We have spent the majority of our time modeling these data trying to find a balance between a physically realistic model

and a model with an appropriate number of fitting parameters to be technically reliable. Much of the data provided in this report has not been set for review in peer reviewed literature. Additional models will be developed prior to publishing these data.

APPENDIX A: REPORTS FOR MILESTONE: M3NU-11-SC-CU__-0204-025: CALORIMETRIC TITRATIONS OF ACTINIDE SORPTION TO IRON OXIDE MINERALS

Appendix contains the following reports:

- Estes, S. and Powell, B. A., “Calorimetric determination of the enthalpy of Eu(III) sorption to hematite”
- Estes, S. and Powell, B. A., “The thermodynamics of U(VI) sorption to hematite”

Calorimetric Determination of the Enthalpy of Eu(III) Sorption onto Hematite

*Shanna L. Estes and Brian A. Powell**

Environmental Engineering and Earth Sciences, Clemson University, 342 Computer Court,
Anderson, SC 29625, United States

DOE NEUP Project: Quantification of cation sorption to engineered barrier materials under extreme conditions (Project #11-3180)

Report in fulfillment of Milestone: M3NU-11-SC-CU__-0204-025: Calorimetric titrations of actinide sorption to iron oxide minerals

ABSTRACT

Modeling or predicting actinide sorption processes in the environment requires both a fundamental understanding of actinide sorption mechanisms, and the availability of thermodynamic constants which are valid over a wide range of conditions. Reaction enthalpies are particularly important for modeling actinide sorption at temperatures other than 25 °C. However, few researchers have quantified this thermodynamic parameter. In this work, we demonstrate the combined use of isothermal titration calorimetry and surface complexation modeling to quantify the enthalpy of Eu(III) (a trivalent actinide analog) sorption onto hematite. The cumulative measured heat from four titrations, in which 0.01 M NaOH was injected into a hematite suspension containing Eu(III), was combined to quantify the sorption enthalpy. The calculated enthalpy for Eu(III) sorption onto hematite ($I = 0.01$ M NaCl) was 127.81 ± 2.84 kJ mol⁻¹, which agreed well with a previously reported van't Hoff enthalpy.

INTRODUCTION

Sorption onto natural reactive surfaces can greatly affect the migration of actinides within the environment. For this reason, a fundamental understanding of actinide sorption mechanisms over a wide range of environmentally relevant conditions must be developed. Although many researchers have made significant progress toward this goal (reviewed by Geckeis et al.¹), most have studied actinide sorption at only ambient laboratory temperatures (~20 – 25 °C).

Consequently, the thermodynamic parameters needed to model actinide sorption processes at the various temperatures expected in natural systems, or the elevated temperatures (~80 °C) expected in future geologic nuclear waste repositories,² are not available in the literature.

Recently, we demonstrated that sorption of Eu(III) (a trivalent actinide analog) onto hematite (α -Fe₂O₃) increases with increasing temperature (i.e., the reaction was endothermic).³ Such endothermic sorption behavior has also been observed for several transition metals,^{4,5} actinides,^{6,7} and for other lanthanide/mineral systems,^{8–11} and suggests that in the near-field of geologic nuclear waste repositories, sorption processes may be more favorable than previously expected. In many of these studies,^{4–6,10} including our study of the Eu(III)/hematite system, sorption enthalpies were approximated from the slopes of van't Hoff plots ($\log K$ vs T^{-1}). Although these van't Hoff enthalpies provide the means to predict actinide sorption at temperatures not previously studied, van't Hoff enthalpies are inherently indirect and can have large uncertainties.¹²

Isothermal titration calorimetry (ITC) measures the evolution of heat during a chemical reaction, allowing one to directly quantify reaction enthalpies ($\Delta_r H$).^{13,14} Although ITC is more commonly used to study biological processes (e.g., ligand-binding reactions¹⁴), ITC has also

been used to study uranium¹⁵ and neptunium¹⁶ hydrolysis, and several researchers have demonstrated that, when combined with batch sorption studies, ITC can be effectively used to study metal sorption thermodynamics.^{17–20} Therefore, the objective of this study was to quantify the enthalpy of Eu(III) sorption onto hematite using ITC and a surface complexation model (SCM)³ developed previously.

MATERIALS AND METHODS

Reagents. Hematite (α -Fe₂O₃) was synthesized and characterized by Estes et al.³ Standardized HCl (0.01, 0.1 N, Metrohm), HNO₃ (67 – 70%, BDH Aristar Plus), and NaCl (99%, BDH) were used as received. Standardized NaOH (0.01, Metrohm) was opened and stored in an anoxic glove box (~1% H₂, 99% N₂, Coy) during use to limit CO₂ dissolution. Eu(III) working solutions (~1 mM in 0.01 M NaCl) were prepared from EuCl₃·xH₂O (98%, Alfa Aesar) – actual concentrations were determined using inductively-coupled plasma mass spectrometry (Thermo X Series 2, using ²⁴²Pu as an internal standard). All solutions and suspensions were prepared in distilled, de-ionized, and de-gassed (boiled and cooled under N₂ purge) ultrapure H₂O (>18 MΩ·cm, ELGA Purelab).

Isothermal Titration Calorimetry. Calorimetric titrations were performed at 25 °C with an isothermal microcalorimeter (TAM III, TA Instruments). This calorimeter measures the difference in heat flow (i.e., power) between sample and reference ampoules (1 mL stainless steel) as a function of time. For all titrations, the reference ampoule contained a hematite suspension identical to that in the sample ampoule, and the titrant was delivered to the sample ampoule through a stainless steel needle from a 250 µL glass syringe. The calorimeter setup did not permit active purging of the ampoule headspace with an inert gas, so some CO₂ dissolution

during the titrations cannot be excluded. Additionally, pH measurement during the titrations was not possible. Therefore, only initial and final suspension pH were measured (Ross semi-micro, Thermo) and are reported as the average $\pm 1\sigma$.

To minimize the number of adjustable parameters during the non-linear regression analysis (see below), the enthalpies for protonation ($\Delta_r H_2$) and de-protonation ($\Delta_r H_3$) of the hematite surface were determined separately from the enthalpy of Eu(III) sorption onto hematite. $\Delta_r H_2$ and $\Delta_r H_3$ were determined by titrating 800 μL of a 7.77 or 7.91 g L^{-1} hematite suspension in 0.01 M NaCl (pH 6.65 ± 0.18) with 200 μL (9.98 μL increments) of either 0.01 N HCl (acid titration) or 0.01 N NaOH (base titration). Measured pH values at the end of the acid and base titrations were 2.79 ± 0.05 and 10.83 ± 0.15 , respectively. To determine the enthalpy of Eu(III) sorption onto hematite ($\Delta_r H_4$), 810 μL of a 6.71 g L^{-1} hematite suspension in 0.01 M NaCl and containing 1.56×10^{-4} M EuCl_3 at pH 3.09 ± 0.09 (adjusted with 0.1 N HCl) was titrated with 150 μL (4.97 μL increments) of 0.01 N NaOH. Titrant injection intervals ranged from 25 – 45 min., and throughout all titrations, ionic strength (0.01 M NaCl) and mixing (150 rpm with gold impeller) were constant. Thermogram peaks were automatically integrated using TAM Assistant software (TA Instruments) to give the measured heat (Q) for each titrant injection. The heat due to dilution and mixing ($Q_{dil.}$) was determined from separate experiments in which a hematite suspension was titrated with 0.01 M NaCl. The net heat (Q_{net}) for each injection was calculated as the difference between Q and $Q_{dil.}$. In most cases, $Q_{dil.}$ was negligible.

Enthalpy Quantification. The enthalpies for hematite protonation and de-protonation and for Eu(III) sorption onto hematite were calculated using the equation

$$Q_{T,calc.} = \sum_{i=1}^j \Delta n_i \cdot \Delta_r H_i \quad (1)$$

where Q_T is the cumulative heat evolved after each injection from all chemical reactions i to j , Δn_i is the cumulative moles of product formed from reaction i , and $\Delta_r H_i$ is the enthalpy of reaction i . The moles of each reaction product formed were calculated by modeling the titration conditions using a modified version of FITEQL²¹ and our previously developed SCM.³ Details of the SCM are given in Table 1. Enthalpy values for each reaction were either obtained from the literature or calculated by fitting the measured cumulative heat ($Q_{T,meas.}$) with a multiple independent-variable non-linear regression (user defined from Eq. 1) using the graphical analysis software package Origin (OriginLab, Northhampton, MA). All enthalpies are reported $\pm 1\sigma$.

RESULTS AND DISCUSSION

Quantification of Hematite Protonation and De-protonation Enthalpies. Five acid and four base titrations were used to quantify the enthalpies of hematite protonation ($\Delta_r H_2$) and de-protonation ($\Delta_r H_3$). Changes in surface speciation during the titrations were simulated with FITEQL using the parameters and reactions given in Table 1. Because it is not possible to separate hematite protonation and de-protonation reactions by experiment, we simultaneously determined $\Delta_r H_2$ and $\Delta_r H_3$ for each titration by fitting $Q_{T,meas.}$ as a function of moles of $\equiv \text{FeOH}_2^+$, $\equiv \text{FeO}^-$, and OH^- formed. The resulting fits and enthalpies for individual titrations are shown in the Supporting Information (Figs. S1, S2; Table S1).

Table 1. Hematite characteristics, surface complexation model reactions and constants, and reaction enthalpies from the literature or calculated in this work.

		parameter /	value /	calculated	referenced
<i>i</i>		reaction	log <i>K</i>	$\Delta_r H_i^a$	$\Delta_r H_i^a$
		pzc	7.36 ^b		
		BET surface area (m ² g ⁻¹)	30.7 ^b		
		site density (sites nm ⁻²)	4.28 ^b		
1	K_w°	H ₂ O ↔ H ⁺ + OH ⁻	-13.99 ^c		55.8 ^d
2	K_+	≡ FeOH + H ⁺ ↔ ≡ FeOH ₂ ⁺	6.19 ^e	3.06 ± 0.93	-32.2 ^b , -41.4 ^f
3	K_-	≡ FeOH ↔ ≡ FeO ⁻ + H ⁺	-8.11 ^e	38.59 ± 0.46	32.2 ^b , 48.5 ^f
4	K_{SC}	2 ≡ FeOH + Eu ³⁺ ↔ (≡ FeO) ₂ Eu ⁺ + 2H ⁺	-1.08 ^g	127.81 ± 2.84	131 ± 8 ^b

^a kJ mol⁻¹

^b Estes et al.³

^c *I* = 0 M, *T* = 25 °C; calculated according to Bandura and Lvov²⁵ using the standard density of water.²⁶

^d From Martell et al.²⁷.

^e Calculated by Estes et al.³ using a single-site diffuse layer model (DLM); *I* = 0.01 M NaCl, *T* = 25 °C, referenced to the 1.0 M standard state.

^f Sverjensky and Sahai²²

^g Calculated from values given by Estes et al.³ for a single-site DLM and the equation from Wang and Giammar²⁸: $\log K_{SC} = \log K_3 - \log(N^+AC_s)$, where $\log K_3$ is -3.91, N^+ is the molar site density (7.11×10^{-6} mol m⁻²), *A* is the specific surface area (30.7 m² g⁻¹), and *C_s* is the solid phase concentration used in this work (6.71 g L⁻¹); *I* = 0.01 M NaCl, *T* = 25 °C, referenced to the 1.0 M standard state.

Calculated average enthalpies for protonation ($\Delta_r H_2$) and de-protonation ($\Delta_r H_3$) of the hematite surface are given in Table 1. $\Delta_r H_3$ agrees well with the theoretical value (48.5 kJ mol⁻¹)

proposed by Sverjensky and Sahai²² and with our previously estimated value (32.2 kJ mol⁻¹).³

However, $\Delta_r H_2$ is significantly different from values reported in the literature (Table 1).

Additionally, $\Delta_r H_2$ calculated here is slightly endothermic, whereas in all other reports, the protonation enthalpy, for hematite and other metal oxides, is exothermic.^{3,19,22–24} Several

explanations for this disagreement were considered: (1) CO₂ dissolution during the titrations; (2)

inability of the SCM to accurately predict the hematite chemistry during the titrations; or (3) formation of unidentified chemical species during the titrations. Incorporating CO₂ dissolution and the subsequent formation of aqueous carbonate species in the SCM significantly worsened our fit results, suggesting that CO₂ dissolution during the titrations did not significantly affect $Q_{T,meas.}$. Furthermore, predicted final hematite suspension pH values agreed within $\pm 3\%$ of all measured values, suggesting that the SCM adequately simulated the hematite chemistry during the acid and base titrations, and further suggesting that CO₂ dissolution was insignificant. The formation of unidentified chemical species, perhaps due to impurities present on the hematite surface, is also a possible explanation for the disagreement between calculated and reported protonation enthalpies. However, this too seems unlikely because the SCM was developed from accurately predicted potentiometric titrations of this hematite at 25 °C.³ For the purposes of the current work, the calculated values of $\Delta_r H_2$ and $\Delta_r H_3$ adequately described the calorimetric acid and base titrations and will therefore be used for quantification of the Eu(III) sorption enthalpy. However, it is clear that additional investigation is needed to verify the hematite protonation and de-protonation enthalpies.

Quantification of Eu(III) Sorption Enthalpy. Four calorimetric base titrations were completed to quantify the enthalpy of Eu(III) sorption onto hematite. To achieve measurable sorption heat during the titrations, high concentrations of Eu(III) were necessary. Despite these elevated Eu(III) concentrations, equilibrium modeling with Visual MINTEQ indicated that Eu(OH)₃ remained undersaturated over the course of each titration. Including CO₂ dissolution and the formation of aqueous carbonate species (including EuCO₃⁺) worsened our fit results, again suggesting that CO₂ dissolution during the titrations was negligible. Furthermore, formation of

EuOH^{2+} during the titrations was also negligible and was therefore excluded. The final SCM included only the four reactions shown in Table 1.

A typical titration thermogram and the corresponding simulated changes in surface speciation are shown in Fig. 1. Results from the SCM indicated that both pH and concentration of adsorbed Eu(III) increased as the titrations progressed, with the greatest amount of Eu(III) sorption occurring during the second half of each titration (Fig. 1). The final average measured pH at the end of each titration (8.2 ± 1.1) differed from the final predicted pH (9.4) and was more variable than for the hematite acid and base titrations. However, this discrepancy was likely due to small variations in the initial pH of each suspension.

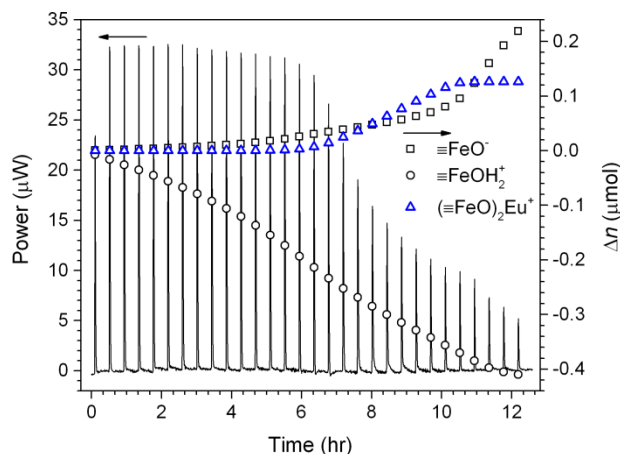


Figure 1. Typical titration thermogram for Eu(III) sorption onto hematite (left y-axis), and change in hematite surface species as a function of titration progress (right y-axis). Titration parameters: $[\text{Eu(III)}]_0 = 1.56 \times 10^{-4} \text{ M}$, $[\alpha\text{-Fe}_2\text{O}_3] = 6.71 \text{ g L}^{-1}$, $I = 0.01 \text{ M NaCl}$, $T = 25 \text{ }^\circ\text{C}$, titrant = 0.01 M NaOH , injection volume = $4.97 \text{ } \mu\text{L}$.

The enthalpy of Eu(III) sorption onto hematite ($\Delta_r H_4$) was calculated by simultaneously fitting $Q_{T,meas.}$ for each titration as a function of moles of $(\equiv \text{FeO})_2\text{Eu}^+$, $\equiv \text{FeOH}_2^+$, $\equiv \text{FeO}^-$, and OH^-

formed. The resulting fit and the measured cumulative heat for each titration are shown in Fig. 2 as a function of $(\equiv \text{FeO})_2\text{Eu}^+$, and the calculated $\Delta_r H_4$ is given in Table 1. Although the cumulative heat evolved during the Eu(III) titrations was reproducible (Fig. 2), the cumulative heat evolved during titration 3 appeared artificially low. Therefore, we also calculated the Eu(III) sorption enthalpy for each titration individually. However, the sorption enthalpy calculated from titration 3 was not statistically different (95% confidence level via Q -test^{29,30}) than the sorption enthalpies calculated from the other three titrations (see Fig. S3, Table S2), and, therefore, could not be excluded from our calculations. There was no statistical difference in $\Delta_r H_4$ calculated from the two fitting methods.

Previously, we used a van't Hoff analysis to approximate the enthalpy of Eu(III) sorption onto hematite.³ Although the enthalpy value from that work was derived from batch sorption experiments at much lower Eu(III) and hematite concentrations, the $\Delta_r H_4$ calculated here is in excellent agreement with the value we previously reported (Table 1), suggesting that the SCM adequately describes Eu(III) sorption onto hematite even at these much higher concentrations. Additionally, the Eu(III) coordination environment at the hematite surface (inner-sphere bidentate mononuclear) determined from extended x-ray absorption fine structure (EXAFS) spectroscopy agreed with surface complexation modeling results,³ further supporting that this SCM can be used for a wide range of Eu(III) and hematite concentrations.

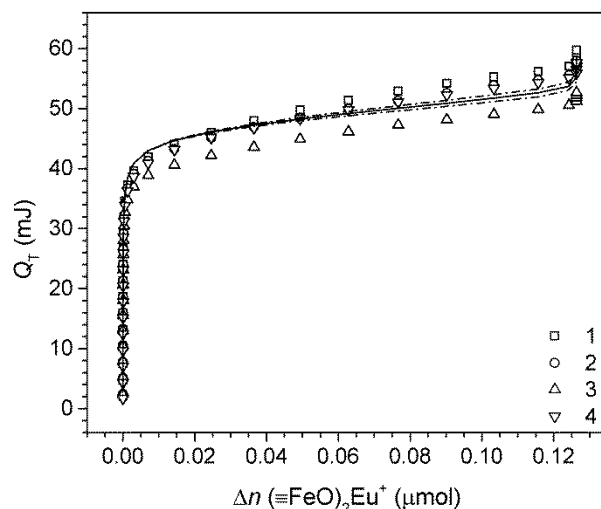


Figure 2. Cumulative enthalpy plot as a function of $(\equiv\text{FeO})_2\text{Eu}^+$ formation. Titration parameters: $[\text{Eu(III)}]_0 = 1.56 \times 10^{-4} \text{ M}$, $[\alpha\text{-Fe}_2\text{O}_3] = 6.71 \text{ g L}^{-1}$, $I = 0.01 \text{ M NaCl}$, $T = 25 \text{ }^\circ\text{C}$, titrant = 0.01 M NaOH , injection volume = $4.97 \text{ }\mu\text{L}$. Open symbols are the measured cumulative heat for each titration 1 – 4; the solid line is the cumulative heat simultaneously calculated from all titration data (adjusted $R^2 = 0.987$); the dashed lines are the 95% upper and lower confidence limits.

Although we ultimately used a calorimetric base titration to quantify the enthalpy of Eu(III) sorption onto hematite, we initially attempted to directly measure the Eu(III) sorption heat by titrating hematite (at $\text{pH} \sim 6$) with a Eu(III) solution (see Fig. S4). However, very little heat evolved during these titrations, making the signal to noise ratio in the thermograms too poor for confident peak integration and enthalpy quantification. We hypothesized that this minimal heat evolution was due to enthalpic competition between the Eu(III) sorption reaction and changes in suspension pH as Eu(III) sorption increased. Similar to the work by Morel et al.²⁰ for Eu(III) sorption onto alumina ($\gamma\text{-Al}_2\text{O}_3$), increasing the Eu(III) concentration in the titrant may have improved the signal to noise ratio, but it would have also eliminated our ability to maintain an ionic strength of 0.01 M NaCl throughout the titration. Therefore, we used the alternative base

titration method described above. However, because these Eu(III) titrations were quite interesting, displaying both exothermic and endothermic peaks in the thermograms (see Fig. S4), we further analyzed the data from one of the titrations. Complete analysis details are given in the Supporting Information. Although we have less confidence in this value, the Eu(III) sorption enthalpy calculated from this titration was $127.5 \pm 1.5 \text{ kJ mol}^{-1}$ (see Fig. S5), which is in excellent agreement with both the enthalpy calculated above and the van't Hoff enthalpy³ we reported previously.

We have used isothermal titration calorimetry to quantify the enthalpy of Eu(III) sorption onto hematite. Our results clearly indicate that the reaction is endothermic, which agrees well with several other studies,^{9,20} and which indicates an inner-sphere sorption mechanism in which some dehydration of the Eu(III) ion occurs.³¹ Without readily available thermodynamic parameters and an understanding of the pertinent sorption mechanisms, efforts to accurately predict actinide sorption processes in the environment are mostly futile. Therefore, we encourage future researchers to employ the calorimetric techniques presented in this work to study other metal/mineral systems.

ASSOCIATED CONTENT

Supporting Information. Cumulative enthalpy plots and fits for all hematite acid and base titrations (Figs. S1 and S2); calculated enthalpy values for individual hematite acid and base titrations (Table S1); cumulative enthalpy plot for the Eu(III) base titrations with individual fits (Fig. S3); calculated enthalpy values for individual Eu(III) base titrations (Table S2); titration thermograms for Eu(III) titrations at pH 6 (Fig. S4); cumulative enthalpy plot and fit for the

Eu(III) titration at pH 6; and brief instructions for extrapolating endothermic heat from Eu(III) titrations at pH 6. This material is available free of charge via the Internet at <http://pubs.acs.org>.

AUTHOR INFORMATION

Corresponding Author

* Tel.: +1 864 656 1004; E-mail Address: bpowell@clemson.edu

Funding Sources

This research was funded by the U.S. Department of Energy, Office of Biological and Environmental Research Nuclear Energy University Partnership Program under project number 11-3180.

ACKNOWLEDGMENT

The authors thank R. Chen for his preliminary work investigating the operational features of the TAM III.

REFERENCES

- (1) Geckeis, H.; Lützenkirchen, J.; Polly, R.; Rabung, T.; Schmidt, M. Mineral–Water Interface Reactions of Actinides. *Chem. Rev.* **2013**, *113*, 1016–1062.
- (2) *Yucca Mountain Science and Engineering Report, Rev. 1*; DOE/RW-0539-1; U.S. Department of Energy, Office of Civilian Radioactive Waste Management: North Las Vegas, NV, 2002.
- (3) Estes, S. L.; Arai, Y.; Becker, U.; Fernando, S.; Yuan, K.; Ewing, R. C.; Zhang, J.; Shibata, T.; Powell, B. A. A Self-Consistent Model Describing the Thermodynamics of Eu(III) Adsorption onto Hematite. *Geochim. Cosmochim. Acta* **2013**, *122*, 430–447.

- (4) Angove, M. J.; Johnson, B. B.; Wells, J. D. The Influence of Temperature on the Adsorption of Cadmium(II) and Cobalt(II) on Kaolinite. *J. Colloid Interface Sci.* **1998**, *204*, 93–103.
- (5) Rodda, D. P.; Johnson, B. B.; Wells, J. D. Modeling the Effect of Temperature on Adsorption of Lead(II) and Zinc(II) onto Goethite at Constant pH. *J. Colloid Interface Sci.* **1996**, *184*, 365–377.
- (6) Almazan-Torres, M. G.; Drot, R.; Mercier-Bion, F.; Catalette, H.; Den Auwer, C.; Simoni, E. Surface Complexation Modeling of uranium(VI) Sorbed onto Zirconium Oxophosphate versus Temperature: Thermodynamic and Structural Approaches. *J. Colloid Interface Sci.* **2008**, *323*, 42–51.
- (7) Lu, N.; Reimus, P. W.; Parker, G. R.; Conca, J. L.; Triay, I. R. Sorption Kinetics and Impact of Temperature, Ionic Strength and Colloid Concentration on the Adsorption of Plutonium-239 by Inorganic Colloids. *Radiochim. Acta* **2003**, *91*, 713–720.
- (8) Bauer, A.; Rabung, T.; Claret, F.; Schäfer, T.; Buckau, G.; Fanghänel, T. Influence of Temperature on Sorption of Europium onto Smectite: The Role of Organic Contaminants. *Appl. Clay Sci.* **2005**, *30*, 1–10.
- (9) Tertre, E.; Berger, G.; Simoni, E.; Castet, S.; Giffaut, E.; Loubet, M.; Catalette, H. Europium Retention onto Clay Minerals from 25 to 150 °C: Experimental Measurements, Spectroscopic Features and Sorption Modelling. *Geochim. Cosmochim. Acta* **2006**, *70*, 4563–4578.

- (10) Ridley, M. K.; Machesky, M. L.; Wesolowski, D. J.; Palmer, D. A. Surface Complexation of Neodymium at the Rutile-Water Interface: A Potentiometric and Modeling Study in NaCl Media to 250°C. *Geochim. Cosmochim. Acta* **2005**, *69*, 63–81.
- (11) Ridley, M. K.; Hiemstra, T.; Machesky, M. L.; Wesolowski, D. J.; van Riemsdijk, W. H. Surface Speciation of Yttrium and Neodymium Sorbed on Rutile: Interpretations Using the Charge Distribution Model. *Geochim. Cosmochim. Acta* **2012**, *95*, 227–240.
- (12) Gans, P.; Sabatini, A.; Vacca, A. Simultaneous Calculation of Equilibrium Constants and Standard Formation Enthalpies from Calorimetric Data for Systems with Multiple Equilibria in Solution. *J. Solut. Chem.* **2008**, *37*, 467–476.
- (13) Christensen, J. J.; Ruckman, J.; Eatough, D. J.; Izatt, R. M. Determination of Equilibrium Constants by Titration Calorimetry: Part I. Introduction to Titration Calorimetry. *Thermochim. Acta* **1972**, *3*, 203–218.
- (14) Freire, E.; Mayorga, O. L.; Straume, M. Isothermal Titration Calorimetry. *Anal. Chem.* **1990**, *62*, 950A – 959A.
- (15) Zanonato, P.; Bernardo, P. D.; Bismondo, A.; Liu, G.; Chen, X.; Rao, L. Hydrolysis of Uranium(VI) at Variable Temperatures (10--85 C). *J. Am. Chem. Soc.* **2004**, *126*, 5515–5522.
- (16) Rao, L.; Srinivasan, T. G.; Garnov, A. Y.; Zanonato, P.; Bernardo, P. D.; Bismondo, A. Hydrolysis of Neptunium(V) at Variable Temperatures (10--85 C). *Geochim. Cosmochim. Acta* **2004**, *68*, 4821–4830.
- (17) Fang, L.; Cai, P.; Li, P.; Wu, H.; Liang, W.; Rong, X.; Chen, W.; Huang, Q. Microcalorimetric and Potentiometric Titration Studies on the Adsorption of Copper by P. Putida

and B. Thuringiensis and Their Composites with Minerals. *J. Hazard. Mater.* **2010**, *181*, 1031–1038.

(18) Fang, L.; Huang, Q.; Wei, X.; Liang, W.; Rong, X.; Chen, W.; Cai, P. Microcalorimetric and Potentiometric Titration Studies on the Adsorption of Copper by Extracellular Polymeric Substances (EPS), Minerals and Their Composites. *Bioresour. Technol.* **2010**, *101*, 5774–5779.

(19) Morel, J.-P.; Marmier, N.; Hurel, C.; Morel-Desrosiers, N. Effect of Temperature on the Acid–base Properties of the Alumina Surface: Microcalorimetry and Acid–base Titration Experiments. *J. Colloid Interface Sci.* **2006**, *298*, 773–779.

(20) Morel, J.-P.; Marmier, N.; Hurel, C.; Morel-Desrosiers, N. Effect of Temperature on the Sorption of Europium on Alumina: Microcalorimetry and Batch Experiments. *J. Colloid Interface Sci.* **2012**, *376*, 196–201.

(21) Herbelin, A.; Westall, J. C. *FITEQL. A Computer Program for the Determination of Chemical Equilibrium Constants from Experimental Data*; Department of Chemistry, Oregon State University: Corvallis, OR, USA, 1999.

(22) Sverjensky, D. A.; Sahai, N. Theoretical Prediction of Single-Site Enthalpies of Surface Protonation for Oxides and Silicates in Water. *Geochim. Cosmochim. Acta* **1998**, *62*, 3703–3716.

(23) Fokkink, L. G. J.; de Keizer, A.; Lyklema, J. Temperature Dependence of the Electrical Double Layer on Oxides: Rutile and Hematite. *J. Colloid Interface Sci.* **1989**, *127*, 116–131.

(24) Kosmulski, M.; Matysiak, J.; Szczypa, J. Standard Enthalpies of Proton Adsorption on Hematite in Various Solvent Systems. *Bull. Pol. Acad. Sci. Chem.* **1993**, *41*, 333–337.

- (25) Bandura, A. V.; Lvov, S. N. The Ionization Constant of Water over Wide Ranges of Temperature and Density. *J. Phys. Chemitry Ref. Data* **2006**, *35*, 15–30.
- (26) Standard Density of Water. In *CRC Handbook of Chemistry and Physics*; Haynes, W. M., Ed.; CRC Press/Taylor and Francis: Boca Raton, FL, 2013; pp. 6–7 – 6–8.
- (27) Martell, A. E.; Smith, R. M.; Motekaitis, R. J. *NIST Critically Selected Stability Constants of Metal Complexes*; NIST Standard Reference Database 46, version 8; NIST: Gaithersburg, MD, USA, 2004.
- (28) Wang, Z.; Giammar, D. E. Mass Action Expressions for Bidentate Adsorption in Surface Complexation Modeling: Theory and Practice. *Environ. Sci. Technol.* **2013**, *47*, 3982–3996.
- (29) Dean, R. B.; Dixon, W. J. Simplified Statistics for Small Numbers of Observations. *Anal. Chem.* **1951**, *23*, 636–638.
- (30) Rorabacher, D. B. Statistical Treatment for Rejection of Deviant Values: Critical Values of Dixon’s “Q” Parameter and Related Subrange Ratios at the 95% Confidence Level. *Anal. Chem.* **1991**, *63*, 139–146.
- (31) Brown, G. E.; Henrich, V. E.; Casey, W. H.; Clark, D. L.; Eggleston, C.; Felmy, A.; Goodman, D. W.; Grätzel, M.; Maciel, G.; McCarthy, M. I.; et al. Metal Oxide Surfaces and Their Interactions with Aqueous Solutions and Microbial Organisms. *Chem. Rev.* **1999**, *99*, 77–174.

Supporting Information

Figure S 1. Cumulative enthalpy plot for the hematite acid titrations.	27
Figure S 2. Cumulative enthalpy plot for the hematite base titrations.....	28
Figure S 3. Cumulative enthalpy plot as a function of $\equiv\text{FeO}_2\text{Eu}^+$ formation	30
Figure S 4. Two titration thermograms for Eu(III) sorption onto hematite at pH ~ 6.	32
Figure S 5. Cumulative enthalpy plot as a function of $\equiv\text{FeO}_2\text{Eu}^+$ formation for a Eu(III) titration at pH ~ 6.	33
Table S 1. Enthalpy values calculated from each acid or base titration, and the adjusted R^2 for each fit.....	29
Table S 2. Enthalpy values calculated from each Eu(III) base titration, and the adjusted R^2 for each fit.....	31

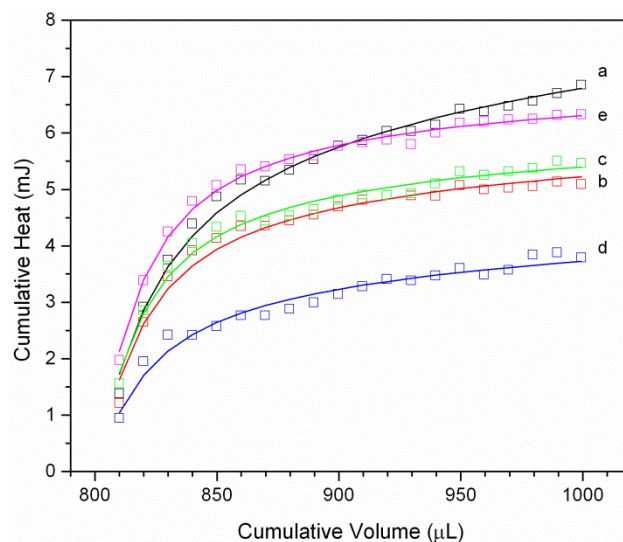


Figure S 1. Cumulative enthalpy plot for the hematite acid titrations. Titration parameters: $[\alpha\text{-Fe}_2\text{O}_3] = 7.77 \text{ g L}^{-1}$ (c – e) or 7.91 g L^{-1} (a – b), $I = 0.01 \text{ M NaCl}$, $T = 25 \text{ }^\circ\text{C}$, titrant = 0.01 M HCl , injection volume = $9.98 \text{ }\mu\text{L}$. Open symbols are the measured cumulative heat for each titration a – e, and the solid line is the calculated heat for each titration (adjusted R^2 values are given in Table S 1).

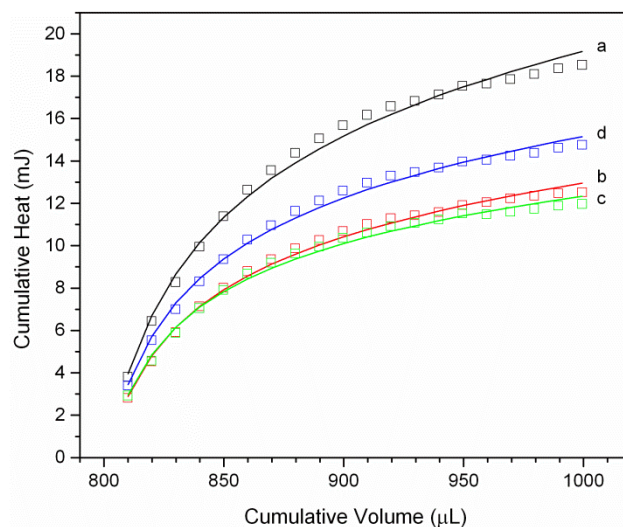


Figure S 2. Cumulative enthalpy plot for the hematite base titrations. Titration parameters: $[\alpha\text{-Fe}_2\text{O}_3] = 7.91 \text{ g L}^{-1}$, $I = 0.01 \text{ M NaCl}$, $T = 25 \text{ }^\circ\text{C}$, titrant = 0.01 M HCl , injection volume = $9.98 \text{ } \mu\text{L}$. Open symbols are the measured cumulative heat for each titration a – d, and the solid line is the calculated heat for each titration (adjusted R^2 values are given in Table S 1).

Table S 1. Enthalpy values calculated from each acid or base titration, and the adjusted R² for each fit.

	$\Delta_r H_3$ (kJ mol ⁻¹) $\equiv \text{FeOH} \leftrightarrow \equiv \text{FeO}^- + \text{H}^+$		$\Delta_r H_2$ (kJ mol ⁻¹) $\equiv \text{FeOH} + \text{H}^+ \leftrightarrow \equiv \text{FeOH}_2^+$		adjusted R ²
	value	1 σ	value	1 σ	
acid a	38.74	1.58	-4.75	0.43	0.990
acid b	41.81	1.59	-0.94	0.43	0.980
acid c	42.77	1.46	-0.98	0.40	0.982
acid d	22.70	1.56	-2.24	0.42	0.963
acid e	52.94	0.98	-0.49	0.27	0.994
base a	28.53	1.71	16.18	5.40	0.991
base b	39.72	1.06	1.10	3.36	0.992
base c	42.76	1.14	6.97	3.62	0.989
base d	37.37	1.24	12.72	3.93	0.992
average	38.59	0.46	3.06	0.93	

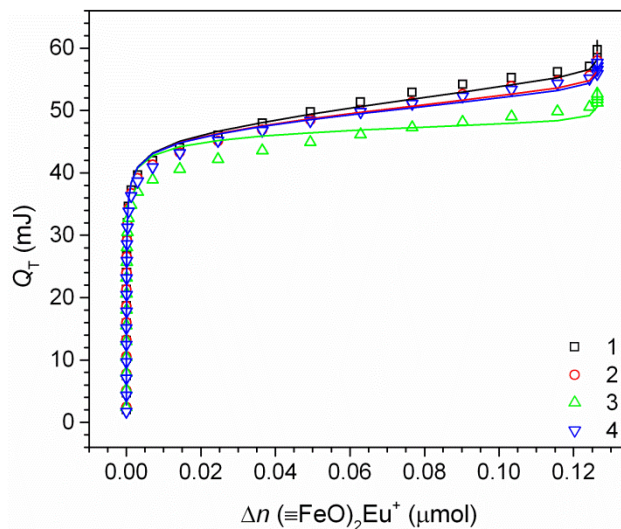


Figure S 3. Cumulative enthalpy plot as a function of $(\equiv\text{FeO})_2\text{Eu}^+$ formation. Titration parameters: $[\text{Eu(III)}]_0 = 1.56 \times 10^{-4} \text{ M}$, $[\alpha\text{-Fe}_2\text{O}_3] = 6.71 \text{ g L}^{-1}$, $I = 0.01 \text{ M NaCl}$, $T = 25^\circ\text{C}$, titrant = 0.01 M NaOH , injection volume = $4.97 \mu\text{L}$. Open symbols are the measured cumulative heat for each titration 1 – 4, and solid lines are the corresponding calculated cumulative heat for each titration (adjusted R^2 values are given in Table S 2).

Table S 2. Enthalpy values calculated from each Eu(III) base titration, and the adjusted R² for each fit.

$\Delta_r H_4$ (kJ mol ⁻¹) $2 \equiv \text{FeOH} + \text{Eu}^{3+}$ $\leftrightarrow (\equiv \text{FeO})_2\text{Eu}^+ + 2\text{H}^+$			
	value	1 σ	adjusted R ²
1	104.76	2.72	0.997
2	119.29	3.00	0.996
3	164.50	5.60	0.985
4	122.71	4.01	0.994
average	127.81	2.00	

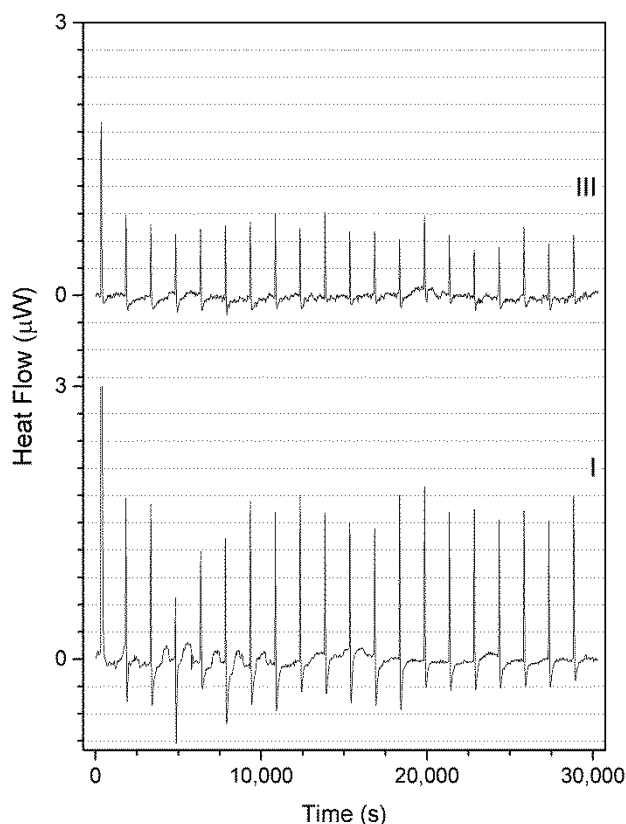


Figure S 4. Two titration thermograms for Eu(III) sorption onto hematite at pH ~ 6. Titration parameters: $[\text{Eu(III)}]_0 = 0 \text{ M}$, $[\alpha\text{-Fe}_2\text{O}_3] = 7.77 \text{ g L}^{-1}$, $I = 0.01 \text{ M NaCl}$, $T = 25 \text{ }^\circ\text{C}$, titrant = 0.1 mM EuCl_3 in 0.01 M NaCl at pH ~ 6, injection volume = $9.98 \text{ }\mu\text{L}$.

*We used the Gaussian peak fitting tool in Origin to extrapolate the heat associated with only the endothermic peaks shown for titration I in Figure S 4. We assumed that the heat associated with the endothermic peaks were representative of the Eu(III) sorption heat. This heat data was fit in the same manner as the Eu(III) base titrations, except only considering the reactions on the hematite surface (i.e., OH^- formation was excluded).

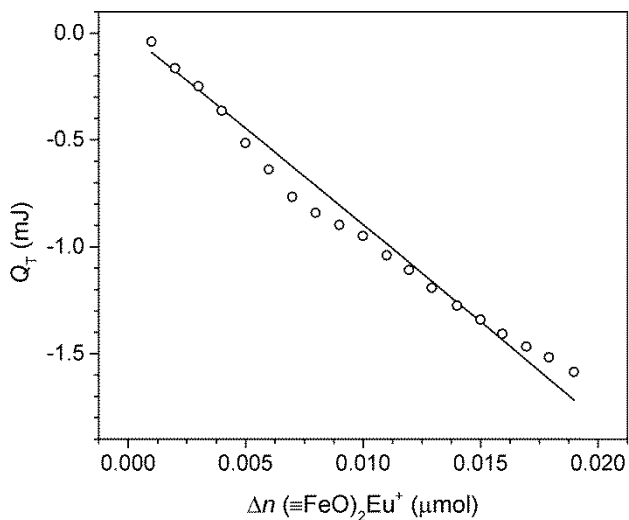


Figure S 5. Cumulative enthalpy plot as a function of $(\equiv\text{FeO})_2\text{Eu}^+$ formation for a Eu(III) titration at pH ~ 6. Titration parameters: $[\text{Eu(III)}]_0 = 0 \text{ M}$, $[\alpha\text{-Fe}_2\text{O}_3] = 7.77 \text{ g L}^{-1}$, $I = 0.01 \text{ M NaCl}$, $T = 25 \text{ }^\circ\text{C}$, titrant = 0.1 mM EuCl_3 in 0.01 M NaCl at pH ~ 6, injection volume = $9.98 \text{ } \mu\text{L}$. Open symbols are the cumulative heat extrapolated from endothermic peaks in titration I in Figure S 4; and the solid line is the calculated cumulative heat (adjusted $R^2 = 0.975$); the calculated $\Delta_r H_4 = 127.5 \pm 1.5 \text{ kJ mol}^{-1}$.

The Thermodynamics of U(VI) Sorption onto Hematite

*Shanna L. Estes and Brian A. Powell**

Environmental Engineering and Earth Sciences, Clemson University, 342 Computer Court, Anderson, SC
29625, United States

*Corresponding author. Tel.: +1 864 656 1004; E-mail address: bpowell@clemson.edu

DOE NEUP Project: Quantification of cation sorption to engineered barrier materials under extreme conditions (Project #11-3180)

Report in fulfillment of Milestone: M2NU-11-SC-CU_-0204-029: Examination of actinide sorption to hematite under variable temperatures

1. INTRODUCTION

Understanding the role of temperature on uranium and other actinide sorption to engineered barrier materials and natural sediments is vital for development of a scientifically defensible nuclear waste repository. In this work sorption of uranium to hematite is examined using variable temperature batch sorption experiments and isothermal titration calorimetry (ITC). The data are modeled using a double layer surface complexation model. Sorption enthalpies are calculated from the batch sorption data by making a van't Hoff plot of the surface complexation constants versus temperatures. These values are compared with the direct measurements of sorption enthalpy using ITC. While both approaches for determining sorption enthalpies indicated the reactions are endothermic, the ITC derived values were significantly higher. This is possible due to different speciation in the systems given the significantly higher concentration of U(VI) used in ITC experiments or to other reactions not considered. However, despite the differences in values, the overall increase in sorption with increasing temperature is consistent with the hypothesis that displacement of hydrating waters upon sorption provides an entropic driving force for these sorption reactions.

2. MATERIALS AND METHODS

2.1 Reagents

Hematite (α -Fe₂O₃) was synthesized and characterized by Estes et al. (2013). HNO₃ (67 – 70%, BDH Aristar Plus), NaCl (99%, BDH), and standardized HCl (0.01, 0.1 N, Metrohm) and NaOH (0.01, 0.1 N, Metrohm) were used as received. Calibration standards (in 2% HNO₃) and working solution #1 (WS1, 6.30×10^{-5} M U(VI) in 0.01 N HCl) were prepared by diluting a U plasma standard (1,000 $\mu\text{g L}^{-1}$ in 2% HNO₃, High Purity Standards). Working solution #2 (WS2, ~1 mM U(VI) in 0.01 M NaCl) was prepared from UO₂(NO₃)₂·6H₂O (99.9 – 100%, EMS). Solutions and suspensions for the batch sorption work were prepared in ultrapure H₂O (>18 M Ω ·cm, Millipore SuperQ or ELGA Purelab). For the calorimetry experiments, all suspensions and solutions were prepared in de-gassed (boiled and cooled under N₂ purge) ultrapure H₂O. Additionally, the standardized NaOH (0.01 N, Metrohm) used for the calorimetry experiments was opened and stored in an anoxic glove box (~1% H₂, 99% N₂, Coy) to limit CO₂ dissolution.

2.2 Multi-Temperature Batch Sorption

Batch sorption experiments were conducted in 125 mL screw top polycarbonate (PC) Erlenmeyer flasks. Before use, each flask was washed once with 2% HNO₃, rinsed three times with ultrapure H₂O, and dried in an oven at 105 °C. Hematite was added to each flask as the dry solid, and then suspended in 0.01 M NaCl. These initial suspensions were mixed at room temperature for approximately 48 hours to adequately hydrate the hematite. After this step, an aliquot of WS1 was added to each flask, and the pH of each suspension was immediately adjusted using HCl or NaOH. The final suspensions contained 0.51 g L⁻¹ hematite, $(2.16 \pm 0.06) \times 10^{-8}$ M U(VI) (system A) or $(4.35 \pm 0.06) \times 10^{-8}$ M U(VI) (system B), and 0.01 M NaCl in a total volume of ~60 mL. The suspension pH ranged from 3 to 6.5, and all reaction systems were prepared in duplicate.

Immediately following the above preparation, all flasks were placed in a temperature controlled orbital shaker (VWR) at 15 °C. After 3 days of mixing, the pH of each suspension was measured using a combination pH electrode with automatic temperature compensation (Thermo 9157BNMD), and the

suspensions were sampled by removing a 1.5 mL homogenous aliquot from each. Sample aliquots were centrifuged at 20,000g for 30 min to sediment particles larger than ~60 nm. After centrifugation, 1 mL of supernatant was diluted with 9 mL of 2% HNO₃ and analyzed for total U by inductively-coupled plasma mass spectrometry (ICP-MS, Thermo X Series 2) with ²⁴²Pu as an internal standard. After 2 – 4 additional days of mixing, the suspensions were sampled a second time, and equilibrium was assumed if there were no significant differences between measured U concentrations for the two sampling events. If equilibrium was not achieved, the suspensions were mixed for an additional 2 – 4 days, and then sampled again. Once equilibrium was achieved (within three sampling events for all temperatures), the reaction temperature was increased, and this procedure was repeated to give U(VI) sorption data at 15, 25, 35, 50, and 80 °C. The flasks were moved into a reciprocal shaking water bath (VWR) to measure U(VI) sorption at 80 °C.

2.3 Isothermal Titration Calorimetry

All calorimetric titrations were performed in 1 mL stainless steel ampoules at 25 °C with an isothermal microcalorimeter (TA Instruments TAM III), which measures the heat flow (i.e., power) difference between reference and sample ampoules. The contents of the reference ampoule were always identical to the contents initially present in the sample ampoule. Although solutions and suspensions used for the calorimetric titrations were CO₂ free, some CO₂ dissolution during the titrations cannot be excluded because the ampoule headspace could not be actively purged with an inert gas. Additionally, it was not possible to monitor changes in suspension pH during the titrations. As such, the suspension pH was only measured before and after the titrations, and pH values are reported as the average for all titrations $\pm 1\sigma$.

For each titration, the titrant was delivered into the sample ampoule from a 250 μ L glass syringe via a stainless steel needle. A total of three titrations were completed in which a hematite suspension (810 μ L, 5.14 g L⁻¹) at pH 3 (adjusted with 0.1 N HCl) in 0.01 M NaCl and containing 2.59×10^{-4} M UO₂(NO₃)₂ (from WS2) was titrated with 150 μ L (4.97 μ L increments) of 0.01 N NaOH. The titrant was injected every 25 min., and both ionic strength (0.01 M NaCl) and mixing (150 rpm with gold impeller)

remained constant throughout each titration. Peaks in each thermogram were automatically integrated by the TAM Assistant software (TA Instruments) to give the measured heat (Q) for each injection. The dilution and mixing heat for each injection ($Q_{dil.}$) was determined from a separate experiment by titrating a hematite suspension with 0.01 M NaCl. For each injection, the net heat (Q_{net}) was calculated from the difference:

$$Q_{net} = Q - Q_{dil.} \quad (1)$$

, and the cumulative measured heat ($Q_{T, meas.}$) was calculated from:

$$Q_{T, meas.} = Q_{net, x} + Q_{net, x-1} + Q_{net, x-2} + \cdots Q_{net, x-\infty} \quad (2)$$

where x is the titrant injection number.

2.4 Surface Complexation Modeling

The surface complexation model (SCM) was developed from batch sorption data collected at each temperature using a modified version of FITEQL 4.0 (Herbelin and Westall, 1999). A description of the FITEQL modifications are given by Estes et al. (2013). The SCM was developed using the single-site diffuse layer model (DLM) (Dzombak and Morel, 1990), which was chosen both for comparison with previous work, and because it has few adjustable parameters. U(VI) sorption data from both batch systems A and B were combined and fit simultaneously to develop a SCM which described sorption at multiple U(VI) concentrations. All experimental data was assigned a 5% relative error, and the ratio of the weighted sum of squares to the degrees of freedom (WSOS/DF) was used to indicate fit quality. The Davies model was used for all activity corrections, and the Davies A parameter was adjusted for temperature according to Langmuir (1997). The equilibrium constants developed using FITEQL are referenced to the 1.0 M standard state and are reported $\pm 1\sigma$. However, we also report calculated equilibrium constants referenced to both the mole fraction (Wang and Giammar, 2013) and site-occupancy (Sverjensky, 2003) standard states. We note that all bidentate reactions are represented with the notation $(\equiv\text{FeOH})_2$ or $(\equiv\text{FeO})_2$. However, this does not indicate bidentate binuclear surface

coordination – such surface site specificity is not possible with the DLM. Instead this notation simply indicates that two surface sites are needed to describe the surface reaction mass balance.

2.5 Thermodynamic Parameter Quantification

U(VI) sorption enthalpies were quantified from the van't Hoff relationship and from the calorimetric titrations. The calorimetric enthalpy was calculated using the equation

$$Q_{T,calc.} = \sum_{i=1}^j \Delta n_i \cdot \Delta_r H_i \quad (3)$$

where Q_T is the cumulative heat evolved after each injection from all chemical reactions i to j , Δn_i is the cumulative moles of product formed from reaction i , and $\Delta_r H_i$ is the enthalpy of reaction i . FITEQL and the SCM developed in this work were used to model the titration conditions and calculate the moles of each reaction product formed after each titrant injection. Enthalpy values were then calculated by fitting the measured cumulative heat ($Q_{T,meas.}$) with a multiple-independent variable non-linear regression (user defined from Eq. 1) using the graphical analysis software package Origin (OriginLab, Northhampton, MA). The van't Hoff and calorimetric enthalpies are reported $\pm 1\sigma$.

3. RESULTS

3.1 Multi-Temperature Batch Sorption

3.1.2 Effect of Temperature

Typical for the sorption of cationic metals onto mineral surfaces (Brown et al., 1999), U(VI) sorption increased from 0 to 100% over a narrow pH range (~ 1.5 pH units), regardless of initial U(VI) concentration (Fig. 1). As temperature increased from 15 to 80 °C, a noticeable shift in the U(VI) sorption edge to lower pH occurred (Fig. 1). Re-plotting the batch sorption data as a function of “pH – $\frac{1}{2}pK_w$,” which effectively eliminated temperature dependence in the x-axis, also demonstrated a clear, albeit smaller, shift in the U(VI) sorption edge (Fig. A1). This result indicates that U(VI) sorption onto hematite increased with increasing temperature (i.e., the reaction is endothermic), which is consistent with

previous reports of endothermic sorption behavior for several transition metals (Rodda et al., 1996; Angove et al., 1998), lanthanides (Ridley et al., 2005; Bauer et al., 2005; Tertre et al., 2006; Ridley et al., 2012; Estes et al., 2013), and actinides (Lu et al., 2003; Almazan-Torres et al., 2008).

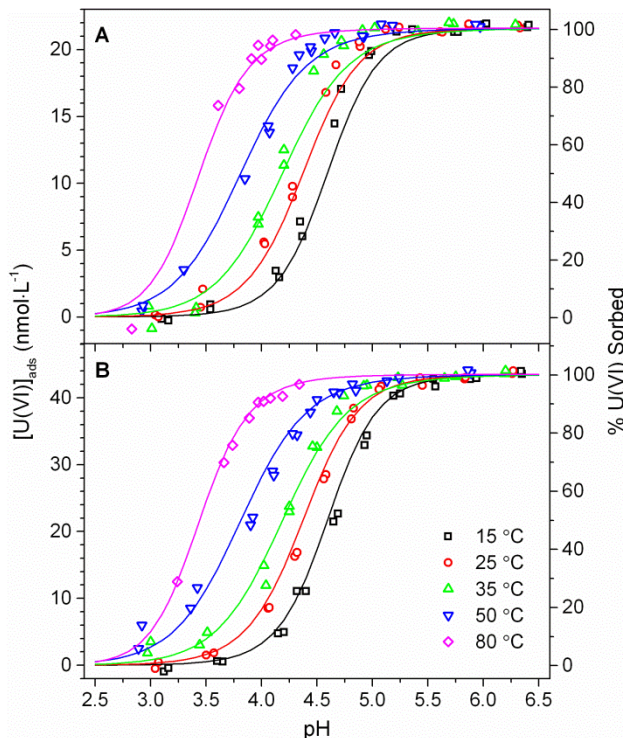


Figure 3. U(VI) sorption onto hematite as a function of pH and temperature for total U(VI) concentrations $(2.16 \pm 0.06) \times 10^{-8}$ M (A) and $(4.35 \pm 0.06) \times 10^{-8}$ M (B). Solid lines are the corresponding best fit surface complexation models (single-site DLM), which represent the following U(VI) surface complexes: $(\equiv\text{FeOH})_2\text{UO}_2^{2+}$ and $(\equiv\text{FeO})_2\text{UO}_2\text{OH}^-$ at 15 and 25 °C; $(\equiv\text{FeOH})_2\text{UO}_2^{2+}$ at 35 and 50 °C; and $(\equiv\text{FeO})_2\text{UO}_2$ at 80 °C. The WSOS/DF values, in order of increasing temperature, were 2.98, 0.91, 15.94, 5.02, and 0.04.

3.1.2 Surface Complexation Model Development

Based on the expected aqueous U(VI) speciation in the batch experiments (Fig. 2), we included formation of both the first and second U(VI) hydrolysis products in the SCM. The formation of UO_2Cl^+ was also included in the SCM, but was generally negligible over the experimental pH range. Although the batch systems were open to the atmosphere and aqueous uranyl-carbonate complexes are expected

above pH ~5.5 (speciation model not shown), including aqueous or surface uranyl-carbonate species in the SCM did not improve our fit results, likely because our experimental conditions resulted in 100% U(VI) sorption below pH 5.5 at all studied temperatures (Fig. 1). Furthermore, previous studies have demonstrated that, in the presence of atmospheric CO₂, uranyl-carbonate surface complexes are not dominant until above pH ~6 (Waite et al., 1994; Wazne et al., 2003). Therefore, we chose to exclude carbonate speciation in the final SCMs. Formation constants for the included aqueous U(VI) species were adjusted to each studied temperature using reported reaction enthalpies (Table 1) and the van't Hoff equation. All hematite characteristics and surface acidity constants were previously defined by Estes et al. (2013), with the exception of the acidity constants at 80 °C, which we calculated using the van't Hoff equation. All reactions and equilibrium constants included in the final SCM are listed in Table 1.

For each temperature, several possible U(VI) surface reactions were considered (listed in Table A1) during SCM optimization. The reactions which yielded the best fits (i.e., lowest WSOS/DF) are listed in Table 1 with the corresponding calculated equilibrium constants. For all temperatures, the best fits to our batch sorption data were given by one or more bidentate uranyl surface complexes (Fig. 1). At 15 and 25 °C, the U(VI) sorption data were accurately modeled with two surface complexes, $(\equiv\text{FeOH})_2\text{UO}_2^{2+}$ and $(\equiv\text{FeO})_2\text{UO}_2\text{OH}^-$ (Fig. 1). As temperature increased from 15 to 25 °C, the contribution of $(\equiv\text{FeO})_2\text{UO}_2\text{OH}^-$ to the overall uranyl surface speciation decreased (Fig. 3), and at 35 and 50 °C, the sorption data were best fit using only $(\equiv\text{FeOH})_2\text{UO}_2^{2+}$. At the highest studied temperature, 80 °C, the data were best fit using a fully de-protonated bidentate surface complex, $(\equiv\text{FeO})_2\text{UO}_2^0$.

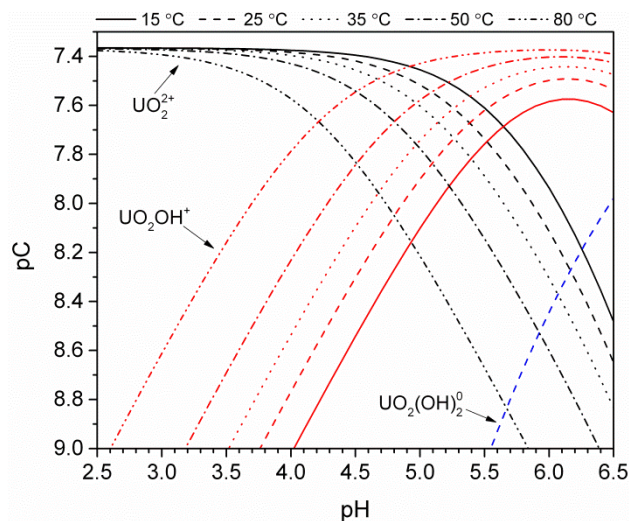


Figure 4. Aqueous speciation of U(VI) as a function of pH and temperature in the absence of CO₂. Modeled using Visual MINTEQ, with equilibrium constants given by Guillaumont et al. (2003). The modeling conditions ($[U(VI)]_T = 4.35 \times 10^{-8}$ M, $I = 0.01$ M NaCl) were equivalent to the batch sorption study with a higher total U(VI) concentration (system B). The enthalpy value for the second hydrolysis product is not defined; therefore, only the 25 °C model is shown.

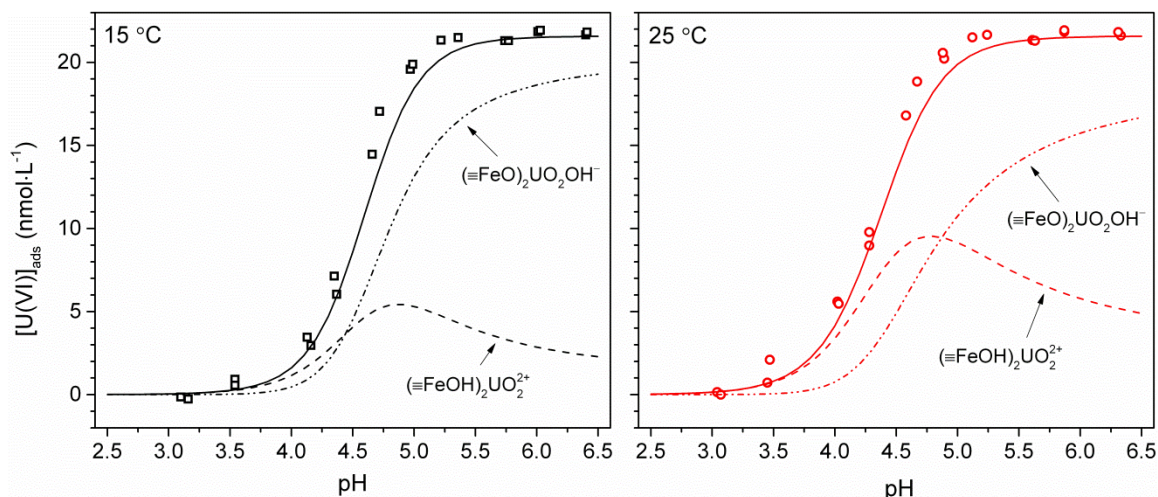


Figure 5. Distribution of U(VI) surface complexes at 15 and 25 °C for batch sorption system A ($[U(VI)]_T = (2.16 \pm 0.06) \times 10^{-8}$ M). Solid lines are the total SCM (i.e., sum of $(\equiv FeOH)_2UO_2^{2+}$ and $(\equiv FeO)_2UO_2OH^-$). A similar surface complex distribution was observed at 15 and 25 °C in system B ($[U(VI)]_T = (4.35 \pm 0.06) \times 10^{-8}$ M).

Table 2. Hematite characteristics, surface complexation model parameters, reactions, and constants, and reaction enthalpies.

<i>i</i>	parameter / reaction	<i>T</i> °C	value / log <i>K</i>	log <i>K</i> _χ	log <i>K</i> [‡]
	pzc		7.36 ^a		
	<i>A</i> _s , BET surface area (m ² g ⁻¹)		30.7 ^a		
	<i>N</i> _s , site density (10 ¹⁸ sites m ⁻²)		4.28 ^a		
	<i>N</i> [‡] , molar site density (10 ⁻⁶ mol m ⁻²)		7.11		
	<i>C</i> _s , solid phase concentration (g L ⁻¹) [batch sorption experiments only]		0.51		
1	<i>K</i> _w [°] H ₂ O ↔ H ⁺ + OH ⁻ Δ _r <i>H</i> ₁ = 55.8 kJ mol ⁻¹ ^c	15 25 35 50 80	-14.34 ^b -13.99 ^b -13.68 ^b -13.26 ^b -12.60 ^b		
2	<i>K</i> ₊ ≡FeOH + H ⁺ ↔ ≡FeOH ₂ ⁺ Δ _r <i>H</i> ₂ = -32.2 kJ mol ⁻¹ ^a	15 25 35 50 80	6.39 ^d 6.19 ^d 6.01 ^d 5.75 ^d 5.31 ^f		6.51 ^{a,e} 6.31 ^{a,e} 6.13 ^{a,e} 5.87 ^{a,e} 5.43 ^e
3	<i>K</i> ₋ ≡FeOH ↔ ≡FeO ⁻ + H ⁺ Δ _r <i>H</i> ₃ = 32.2 kJ mol ⁻¹ ^a	15 25 35 50 80	-8.30 ^d -8.11 ^d -7.92 ^d -7.67 ^d -7.23 ^f		-8.18 ^{a,e} -7.99 ^{a,e} -7.80 ^{a,e} -7.55 ^{a,e} -7.11 ^e
4	* <i>β</i> _{1,1} UO ₂ ²⁺ + H ₂ O ↔ UO ₂ OH ⁺ + H ⁺ Δ _r <i>H</i> ₄ = 43.46 kJ mol ⁻¹ ⁱ	15 25 35 50 80	-5.51 ^g -5.25 ^h -5.00 ^g -4.66 ^g -4.06 ^g		
5	* <i>β</i> _{2,1} UO ₂ ²⁺ + H ₂ O ↔ UO ₂ (OH) ₂ + 2H ⁺	15 25 35 50 80	-12.15 ^j -12.15 ^h -12.15 ^j -12.15 ^j -12.15 ^j		
6	<i>K</i> _{UO₂Cl⁺} UO ₂ ²⁺ + Cl ⁻ ↔ UO ₂ Cl ⁺ Δ _r <i>H</i> ₆ = 8 kJ mol ⁻¹ ^h	15 25 35	0.12 ^g 0.17 ^h 0.22 ^g		

		50	0.28 ^g		
		80	0.39 ^g		
7	K_{SC1}	15	12.77 ± 0.03^k	8.82 ^l	32.71 ^m
	$2\equiv\text{FeOH} + \text{UO}_2^{2+} \leftrightarrow (\equiv\text{FeOH})_2\text{UO}_2^{2+}$	25	$13.01 \pm 0.02^{k,n}$	9.06 ^l	32.95 ^m
		35	13.19 ± 0.01^k	9.24 ^l	33.13 ^m
		50	13.37 ± 0.02^k	9.42 ^l	33.31 ^m
		80	—	—	—
8	K_{SC2}	15	-8.22 ± 0.06^k	-12.17 ^l	11.72 ^m
	$2\equiv\text{FeOH} + \text{UO}_2^{2+} \leftrightarrow$ $(\equiv\text{FeO})_2\text{UO}_2\text{OH}^- + 3\text{H}^+$	25	$-7.82 \pm 0.09^{k,n}$	-11.77 ^l	12.12 ^m
		35	—	—	—
		50	—	—	—
		80	—	—	—
9	K_{SC3}	15	—	—	—
	$2\equiv\text{FeOH} + \text{UO}_2^{2+} \leftrightarrow$ $(\equiv\text{FeO})_2\text{UO}_2 + 2\text{H}^+$	25	—	—	—
		35	—	—	—
		50	—	—	—
		80	1.43 ± 0.04^k	-2.52 ^l	21.37 ^m

^a Estes et al. (2013)

^b $I = 0$ M; calculated from the standard density of water (Haynes, 2013) according to Bandura and Lvov (2006).

^c Martell et al. (2004)

^d Calculated by Estes et al. (2013) using a single-site diffuse layer model (DLM); $I = 0.01$ M NaCl; referenced to the 1.0 M standard state.

^e Referenced to the site occupancy standard state (Sverjensky, 2003), and calculated with the equation: $\log K^\ddagger = \log K + \log \frac{N_s A_s}{N^\ddagger A^\ddagger}$, where N^\ddagger and A^\ddagger are the theoretical site density (10×10^{18} sites m^{-2}) and surface area ($10 \text{ m}^2 \text{ g}^{-1}$) suggested by Sverjensky (2003).

^f $\log K_+$ and $\log K_-$ at 80 °C were calculated using the van't Hoff equation, the $\log K_+$ and $\log K_-$ values at 25 °C, and the protonation ($\Delta_r H_2$) and de-protonation ($\Delta_r H_3$) enthalpies listed in this table.

^g $I = 0$ M; $\log K$ values for aqueous uranyl reactions at 15, 35, 50, and 80 °C were calculated using the van't Hoff equation, the $\log K$ values at 25 °C, and the reaction enthalpies listed in this table.

^h $I = 0$ M; Guillaumont et al. (2003).

ⁱ $\Delta_r H_4$ was calculated from the formation enthalpies ($\Delta_f H_m^\circ$) given by Guillaumont et al. (2003) for the species UO_2^{2+} , UO_2OH^+ , and H_2O (l). H^+ is the reference state, therefore $\Delta_f H_m^\circ(\text{H}^+) = 0 \text{ kJ mol}^{-1}$. The calculated $\Delta_r H_4$ agrees well with the value determined by Zanonato et al. (2004) (46.5 kJ mol^{-1}).

^j The reaction enthalpy for $^*\beta_{2,1}$ is unknown. Therefore, the same $\log ^*\beta_{2,1}$ was used for each experimental temperature.

^k Calculated using a single-site DLM and referenced to the 1.0 M standard state; $I = 0.01$ M NaCl. The exponent for $\equiv\text{FeOH}$ was defined as 2 in both the FITEQL mass balance and mass action expressions. As such, the $\log K$ values determined here for the U(VI) surface complexation reactions are dependent on solid phase concentration. To apply our SCM, researchers should use the $\log K_\chi$ values as described in note l below.

^l Referenced to the mole fraction standard state as suggested by Wang and Giammar (2013), and calculated with the equation: $\log K_\chi = \log K + \log(N^\ddagger A_s C_s)$. Researchers that wish to use our SCM can

directly input the $\log K_\chi$ values into modeling software which implements the mole fraction standard state. When using modeling software which implements the 1.0 M standard state (e.g., FITEQL), researchers should convert the $\log K_\chi$ into $\log K$ values using the above equation and the molar site density, specific surface area, and solid phase concentration specific to their reaction conditions.

^m Referenced to the site occupancy standard state (Sverjensky, 2003), and calculated with the equation: $\log K^\ddagger = \log K + \log \left(\frac{(N_s A_s)^2 \cdot C_s}{N^\ddagger A^\ddagger} \right)$. N^\ddagger , and A^\ddagger are given in note *e* above.

ⁿ The $\log K$ values were corrected for the hematite concentrations used in the calorimetric titrations ($C_s = 5.14 \text{ g L}^{-1}$) as described in note *l* above. The corrected $\log K$ values for formation of $(\equiv\text{FeOH})_2\text{UO}_2^{2+}$ and $(\equiv\text{FeO})_2\text{UO}_2\text{OH}^-$ were 11.998 and -8.832 , respectively.

3.1.3 Thermodynamic Parameter Quantification: van't Hoff Enthalpy

Quantifying reaction enthalpies using the van't Hoff approach requires the availability of formation constants defined for three or more temperatures. Because the SCM predicted a change in U(VI) surface speciation as temperature increased, we were only able to use the van't Hoff approach to quantify the formation enthalpy of $(\equiv\text{FeOH})_2\text{UO}_2^{2+}$. A plot of the $(\equiv\text{FeOH})_2\text{UO}_2^{2+}$ formation constants as a function of inverse temperature (i.e., a van't Hoff plot) is given in Appendix A (Fig. A2). A least-squares linear regression indicated that this data set deviated from linearity, which suggests that the formation enthalpy of $(\equiv\text{FeOH})_2\text{UO}_2^{2+}$ is not constant over the studied temperature range (i.e., $\Delta C_p \neq 0$). Therefore, we calculated the $(\equiv\text{FeOH})_2\text{UO}_2^{2+}$ formation enthalpy and heat capacity using the extended van't Hoff equation:

$$\log K - \log K^\circ = \frac{\Delta_r H_7 - T^\circ \Delta C_{p,7}}{\ln 10 \cdot R} \cdot \left(\frac{1}{T^\circ} - \frac{1}{T} \right) + \frac{\Delta C_{p,7}}{R} \cdot \log \frac{T}{T^\circ} \quad (4)$$

where $\log K$ is the $(\equiv\text{FeOH})_2\text{UO}_2^{2+}$ formation constant at each temperature, $\log K^\circ$ is the $(\equiv\text{FeOH})_2\text{UO}_2^{2+}$ formation constant at 25 °C, $\Delta_r H_7$ is the formation enthalpy at 25 °C, $\Delta C_{p,7}$ is the change in heat capacity at 25 °C, T is the absolute temperature, T° is the absolute reference temperature (298.15 K), and R is the universal gas constant. Using a non-linear least-squares regression with simultaneous optimization of both thermodynamic parameters (Fig. 5), the calculated $\Delta_r H_7$ and $\Delta C_{p,7}$ are $35.5 \pm 0.2 \text{ kJ mol}^{-1}$ and $-741 \pm 14 \text{ J K}^{-1} \text{ mol}^{-1}$. Additional thermodynamic parameters ($\Delta_r S_7$, $\Delta_r G_7$) derived from $\Delta_r H_7$ are listed in Table 2.

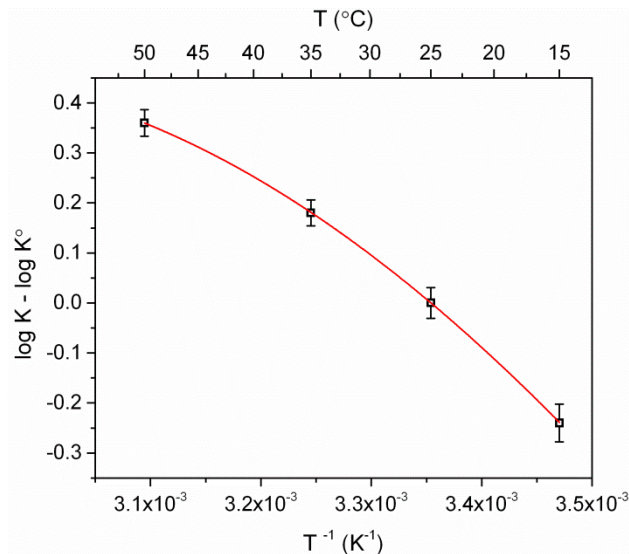


Figure 6. Extended van't Hoff plot using $\log K$ values for the surface complex $(\equiv\text{FeOH})_2\text{UO}_2^{2+}$. $\log K^\circ$ is the $(\equiv\text{FeOH})_2\text{UO}_2^{2+}$ formation constant at 25 °C. The solid line is the non-linear fit with an adjusted R^2 equal to 0.999.

Table 3. Calculated thermodynamic parameters for U(VI) sorption onto hematite.^a

	$\Delta_r G_i^b$ (kJ mol ⁻¹)	$\Delta_r H_i$ (kJ mol ⁻¹)	$\Delta_r S_i^c$ (J mol ⁻¹ K ⁻¹)	$\Delta_r C_{p,i}$ (J mol ⁻¹ K ⁻¹)
$(i = 7) \quad 2\equiv\text{FeOH} + \text{UO}_2^{2+} \leftrightarrow (\equiv\text{FeOH})_2\text{UO}_2^{2+}$				
νH	-74.3 ± 0.1	$+35.5 \pm 0.2$	$+368 \pm 1$	-741 ± 14
<i>cal.</i>	-74.3 ± 0.1	$+81.5 \pm 3.9$	$+522 \pm 13$	—
$(i = 8) \quad 2\equiv\text{FeOH} + \text{UO}_2^{2+} + \text{H}_2\text{O} \leftrightarrow (\equiv\text{FeO})_2\text{UO}_2\text{OH}^- + 3\text{H}^+$				
<i>cal.</i>	$+44.6 \pm 0.5$	$+102 \pm 3$	$+193 \pm 9$	—

^a All values are for 25 °C and $I = 0.01$ M NaCl; “ νH ” indicates values derived from the van't Hoff analysis, “*cal.*” indicates values derived from ITC.

^b Calculated from: $\Delta_r G_i = -RT \cdot \ln K$, where T is 298.15 K.

^c Calculated from: $\Delta_r G_i = \Delta_r H_i - T\Delta_r S_i$, where T is 298.15 K.

3.2 Isothermal Titration Calorimetry

3.2.1 Evolution of Heat and Surface Speciation

High concentrations of U(VI) (2.59×10^{-4} M) were necessary to produce measureable heat during the calorimetric titrations; however, equilibrium modeling with Visual MINTEQ indicated that all relevant U(VI) solid phases were undersaturated throughout the titrations. A total of three calorimetric

titrations were performed, with each yielding a thermogram (typical example in Fig. 4) with well resolved exothermic peaks. Aqueous and surface speciation during the titrations were simulated using the SCM developed in Section 3.1.2.

As the calorimetric titrations progressed, the SCM (Table 1) indicated that pH and U(VI) sorption increased (Fig. 4), and that formation of U(VI) surface complexes was greatest during the second half of the titration. The increased heat observed in the thermogram at ~10 hr (Fig. 4) corresponds well with the predicted transition in U(VI) surface speciation from primarily $(\equiv\text{FeOH})_2\text{UO}_2^{2+}$ to primarily $(\equiv\text{FeO})_2\text{UO}_2\text{OH}^-$. Because the formation of $(\equiv\text{FeO})_2\text{UO}_2\text{OH}^-$ results in the release of three protons (Table 1), this increased heat may be due to additional proton neutralization (i.e., formation of H_2O). The final measured suspension pH (7.6 ± 0.3) was in fairly good agreement with the pH predicted by the SCM (8.9).

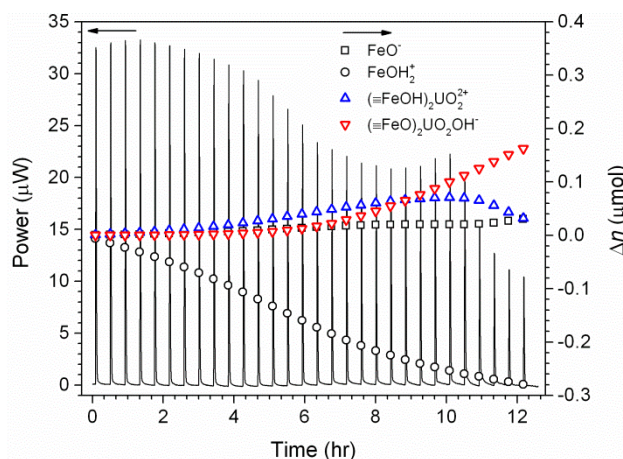


Figure 7. Typical titration thermogram for U(VI) sorption onto hematite (left y-axis), and change in hematite surface speciation as a function of titration progress (right y-axis). Titration parameters: $[\text{U(VI)}]_0 = 2.59 \times 10^{-4} \text{ M}$, $[\alpha\text{-Fe}_2\text{O}_3] = 5.14 \text{ g L}^{-1}$, $I = 0.01 \text{ M NaCl}$, $T = 25 \text{ }^\circ\text{C}$, titrant = 0.01 M NaOH , injection volume = $4.97 \text{ } \mu\text{L}$.

3.2.2 Thermodynamic Parameter Quantification: Calorimetric Enthalpy

From the calorimetric titration data, the formation enthalpy of both $(\equiv\text{FeOH})_2\text{UO}_2^{2+}$ ($\Delta_r H_7$) and $(\equiv\text{FeO})_2\text{UO}_2\text{OH}^-$ ($\Delta_r H_8$) were calculated by fitting $Q_{T, \text{meas.}}$ (for all titrations simultaneously) as a

function of moles of product formed from each reaction listed in Table 1 (25 °C only).

Formation enthalpies for both surface complexes were optimized simultaneously. The cumulative enthalpy plot and resulting fit are shown in Fig. 6 as a function of the formation of U(VI) surface species expected at 25 °C. The calculated formation enthalpies of $(\equiv\text{FeOH})_2\text{UO}_2^{2+}$ and $(\equiv\text{FeO})_2\text{UO}_2\text{OH}^-$ are $81.5 \pm 3.9 \text{ kJ mol}^{-1}$ and $102 \pm 3 \text{ kJ mol}^{-1}$, respectively. Additional thermodynamic parameters derived from these enthalpies are listed in Table 2.

Although the resulting fit to the cumulative enthalpy plot is quite satisfactory (Fig. 6), the calculated $\Delta_r H_7$ is significantly higher than the same value calculated from the van't Hoff analysis (Table 2). There are two possible reasons for this disagreement. First, previous studies have demonstrated that U(VI) sorption onto iron oxy(hydr)oxides is non-linear over a wide range of U(VI) concentrations (Missana et al., 2003; Jang et al., 2007). This non-linear isotherm behavior could indicate surface saturation or changes in uranyl surface speciation as equilibrium U(VI) concentrations increase. For this reason, our SCM, which was developed from batch experiments at much lower U(VI) concentrations, may not adequately describe U(VI) sorption onto hematite at the concentrations used in the calorimetric titrations.

Second, it is possible that there are chemical reactions which contribute to the measured cumulative heat, but which are not included in the SCM. Because we were unable to purge the ampoule headspace during the calorimetric titrations, CO_2 dissolution and the subsequent formation of carbonate complexes may have contributed to the cumulative heat. However, the cumulative heat expected from these reactions after each injection is less than 1% of the heat expected from the other aqueous or surface reactions. Therefore, CO_2 dissolution does not explain the disagreement in calculated enthalpies. Another reaction which may contribute to the measured cumulative heat is the sorption of electrolyte onto the hematite surface. However, we

cannot account for this reaction with the DLM. Regardless of the reason for the discrepancy in calculated enthalpies, it is clear that the formation of both $(\equiv\text{FeOH})_2\text{UO}_2^{2+}$ and $(\equiv\text{FeO})_2\text{UO}_2\text{OH}^-$ is endothermic.

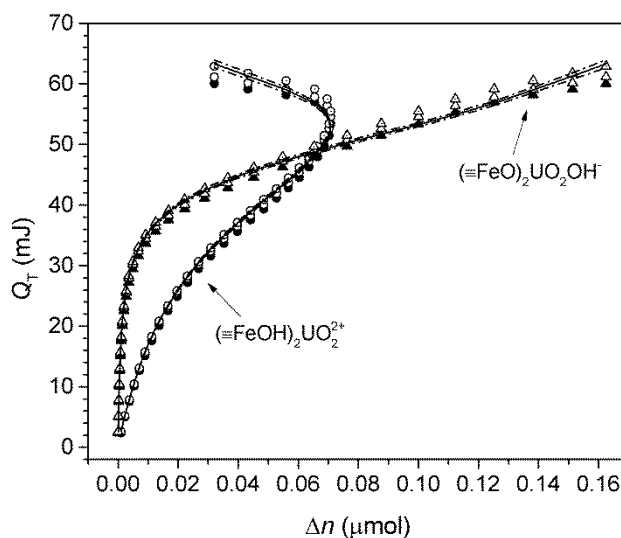


Figure 8. Cumulative enthalpy plot as a function of $(\equiv\text{FeOH})_2\text{UO}_2^{2+}$ and $(\equiv\text{FeO})_2\text{UO}_2\text{OH}^-$ formation. Titration parameters: $[\text{U(VI)}]_0 = 2.59 \times 10^{-4} \text{ M}$, $[\alpha\text{-Fe}_2\text{O}_3] = 5.14 \text{ g L}^{-1}$, $I = 0.01 \text{ M NaCl}$, $T = 25 \text{ }^\circ\text{C}$, titrant = 0.01 M NaOH , injection volume = $4.97 \text{ } \mu\text{L}$. Symbols are the measured cumulative heat for three titrations, and solid lines are the cumulative heat simultaneously calculated from all titration data (adjusted $R^2 = 0.997$); the dashed lines are the 95% upper and lower confidence limits.

4. DISCUSSION

4.1 Comparison with Previous Sorption Studies

4.1.1 U(VI) Surface Complexation

Although many researchers have developed SCMs to describe U(VI) sorption onto various iron oxy(hydr)oxides, direct comparisons with our results are difficult because of differences between modeling approaches or experimental conditions. For example, Waite et al. (1994) studied U(VI) sorption onto ferrihydrite in open systems and proposed a two-site, two-species model which included a

bidentate uranyl complex, $(\equiv\text{Fe}_{\text{s,w}}\text{O}_2)\text{UO}_2$, at $\text{pH} < 6$, and a bidentate uranyl-carbonate complex, $(\equiv\text{Fe}_{\text{s,w}}\text{O}_2)\text{UO}_2\text{CO}_3^{2-}$, at $\text{pH} > 6.5$. Although their SCM adequately modeled U(VI) sorption data for a variety of experimental conditions, it doesn't appear that they explored the full range of possible surface reaction stoichiometries. Zeng et al. (2009) and Missana et al. (2003) found that U(VI) sorption onto hematite nanoparticles and goethite, respectively, was best described with a bidentate uranyl surface complex. However, they also did not consider many alternative reactions in the development of their SCMs. Jang et al. (2007) developed a SCM using isotherm data for U(VI) sorption onto hydrous ferric oxide (HFO) at several circum-neutral pH values. Because their model was developed from these neutral pH isotherm data where U(VI) concentrations were $\sim 1 \mu\text{M}$, their model required monodentate and bidentate uranyl surface complexes, as well as aqueous and surface polynuclear uranyl complexes. Wazne et al. (2003) also used monodentate uranyl surface complexes to describe U(VI) sorption onto ferrihydrite in experiments where total U(VI) concentrations were $\sim 4 \times 10^{-6} \text{ M}$. Neither polynuclear uranyl complexes nor monodentate uranyl surface complexes (a less favorable surface binding configuration) are expected in our batch sorption experiments where U(VI) concentrations are less than $5 \times 10^{-8} \text{ M}$.

Perhaps the most thoroughly developed SCM comes from Hiemstra et al. (2009), who used the CD-MUSIC model to fit 168 experimental data points collected from the literature for U(VI) sorption onto ferrihydrite. Allowing only inner-sphere uranyl surface complexation at the singly coordinated terminal oxygen sites on the edges of Fe octahedra, they considered five possible uranyl surface complexes for CO_2 free systems. The surface reactions which best described the cumulative sorption data were given by $\equiv(\text{FeOH})_2\text{UO}_2$, $\equiv(\text{FeOH})_2\text{UO}_2\text{OH}$, and $\equiv(\text{FeOH})_2\text{UO}_2(\text{OH})_2$, where the net charge imparted to the electric double layer (EDL) for each species was +2, +1, and 0, respectively. Furthermore, Hiemstra et al. (2009) stated that $\equiv(\text{FeOH})_2\text{UO}_2\text{OH}$ was the most important surface species, based on the standard deviation of the calculated equilibrium constant. In a similar manner, we also considered many possible surface reaction stoichiometries in our SCM and determined that $(\equiv\text{FeOH})_2\text{UO}_2^{2+}$ and $(\equiv\text{FeO})_2\text{UO}_2\text{OH}^-$ gave the

best fit to our U(VI) sorption data (Section 3.1.2). Because we used a single-site DLM to describe our data, we were not able to distinguish the location of charge within the EDL, or to specify uranyl coordination to specific surface sites (e.g., $\equiv\text{FeOH}^{-1/2}$, $\equiv\text{Fe}_3\text{O}^{-1/2}$, etc.). However, we can make some comparisons with the SCM developed by Hiemstra et al. (2009). First, the uranyl surface complexes in our 25 °C model compare well with the complexes suggested by Hiemstra et al. (2009), although we find that the hydrolyzed surface species ($(\equiv\text{FeO})_2\text{UO}_2\text{OH}^-$) is somewhat less important based on both the standard deviation of the log K value (Table 1) and percent speciation (Fig. 3). Second, our SCM suggests that the average net charge imparted to the EDL over the studied pH range, based on the relative concentrations of each complex at each data point, is +0.7, which is close to the +1 charge of the dominant surface complex in the Hiemstra et al. (2009) model, $\equiv(\text{FeOH})_2\text{UO}_2\text{OH}$. While the main focus of this paper is not SCM development, the agreement we find between our model and the Hiemstra et al. (2009) model gives us confidence that our SCM is reasonable, and therefore we can use it to better understand the thermodynamics of U(VI) sorption onto hematite.

4.1.2 Temperature-Dependent Surface Speciation

Ridley et al. (2005) previously reported that Nd(III) hydrolysis at the rutile surface increased with increasing temperature. From their results, and based on aqueous uranyl speciation models, which indicate that uranyl hydrolysis increases with increasing temperature (Fig. 2), one might expect the percentage of hydrolyzed uranyl-hematite surface complexes to also increase with increasing temperature. However, this was not the trend observed in our modeling results (Section 3.1.2). Instead, we observed a change in speciation from a combination of $(\equiv\text{FeOH})_2\text{UO}_2^{2+}$ and $(\equiv\text{FeO})_2\text{UO}_2\text{OH}^-$ at low temperatures, to only $(\equiv\text{FeOH})_2\text{UO}_2^{2+}$ at 35 and 50 °C, to $(\equiv\text{FeO})_2\text{UO}_2$ at the highest temperature studied. Upon further analysis, we find that the evolution of uranyl surface complexes reported here is consistent with the expected increase in negative surface charge (i.e., increased concentration of $\equiv\text{FeO}^-$) as temperature increases and the hematite pzc decreases (Estes et al., 2013). In other words, as temperature and the distribution of negatively charged surface sites increase, electrostatic attraction favors sorption of the divalent UO_2^{2+} over the monovalent UO_2OH^+ . Furthermore, because the dielectric constant of water

decreases as temperature increases, we expect greater aqueous destabilization of the more highly charged uranyl ion compared with UO_2OH^+ , and, therefore, greater sorption of UO_2^{2+} than UO_2OH^+ .

4.1.3 Sorption Enthalpy

Sorption enthalpies are expected to fluctuate based on the sorbent and analyte binding configuration. Despite this, the van't Hoff and calorimetric formation enthalpies calculated for $(\equiv\text{FeOH})_2\text{UO}_2^{2+}$ (Table 2) are within or similar to the range reported ($\sim 4 - 70 \text{ kJ mol}^{-1}$) for sorption of other divalent metals (e.g., Zn(II), Pb(II), Cu(II), Cd(II)) onto various minerals (Rodda et al., 1996; Angove et al., 1998). Additionally, Almazan-Torres et al. (2008) reported an enthalpy of 58 kJ mol^{-1} for U(VI) sorption onto the phosphate sites in zirconium oxophosphate, which is similar to the van't Hoff enthalpy we calculated for the formation of $(\equiv\text{FeOH})_2\text{UO}_2^{2+}$. However, the formation enthalpies for both $(\equiv\text{FeOH})_2\text{UO}_2^{2+}$ and $(\equiv\text{FeO})_2\text{UO}_2\text{OH}^-$ are less than the enthalpy we previously calculated for Eu(III) sorption onto hematite ($(\equiv\text{FeO})_2\text{Eu}^+$, $\Delta_r H = +131 \text{ kJ mol}^{-1}$) (Estes et al., 2013). As will be discussed further in the next section, this larger sorption enthalpy may be due to a stronger interaction between Eu^{3+} and the hematite surface.

4.2 Thermodynamic Interpretation

To form an inner-sphere surface complex, some dehydration of the uranyl ion must occur upon sorption (Brown et al., 1999). Because dehydration will increase the total system disorder, yet also requires energy for bond breakage, dehydration is an endothermic, entropically favorable reaction (Choppin, 1983). On the other hand, the formation of an outer-sphere surface complex will not require uranyl dehydration, and therefore sorption will be dominated by electrostatic attraction and will likely be exothermic (Choppin, 1983). For this reason, we infer from the calculated thermodynamic parameters (Table 2) that U(VI) sorption onto hematite results in the formation of inner-sphere surface complexes. In support of this finding, extended X-ray absorption fine structure (EXAFS) data indicate that U(VI) forms bidentate mononuclear or bidentate binuclear inner-sphere complexes on the surfaces of hematite (Bargar et al., 2000; Zeng et al., 2009), ferrihydrite (Waite et al., 1994; Reich et al., 1998; Rossberg et al., 2009), goethite (Moyes et al., 2000; Sherman et al., 2008), and lepidocrocite (Moyes et al., 2000). Furthermore, EXAFS data suggest that the equatorial U – O coordination number (CN) is approximately 5 for U(VI)

surface complexes, indicating that at least two H₂O molecules are removed from the primary hydration sphere of the aqueous uranyl ion upon sorption to iron oxy(hydr)oxide surfaces.

Similar to this work, we previously demonstrated that Eu(III) sorption onto hematite is also an endothermic, entropically favorable reaction (Estes et al., 2013). However, the formation enthalpy (+131 kJ mol⁻¹) and entropy (+439 J mol⁻¹ K⁻¹) of the Eu(III) surface complex were significantly larger than the entropy or enthalpy determined in this work for either U(VI) surface complex. From EXAFS data and quantum computational modeling, we suggested that the large Eu(III) sorption entropy was due to the loss of approximately five H₂O molecules from the Eu(III) primary hydration sphere (Estes et al., 2013). We therefore propose that the smaller sorption entropies of the U(VI) surface complexes result from the loss of fewer H₂O molecules from the uranyl hydration sphere. Additionally, Trivedi and Axe (2001) suggested that larger sorption enthalpies are indicative of greater bonding strength between sorbate and sorbent. Therefore, the smaller sorption enthalpies of the uranyl surface complexes may indicate a weaker interaction between U(VI) and hematite compared with Eu(III) and hematite. Possibly due to steric hindrance induced from the uranyl di-oxo moiety, greater distances have been observed in EXAFS data between U and Fe (~3.4 Å) (Waite et al., 1994; Bargar et al., 2000) compared with Eu and Fe (~3.1 Å) (Estes et al., 2013) for bidentate mononuclear surface complexes, which further suggests a weaker interaction between U(VI) and the hematite surface.

5. CONCLUSIONS

The results presented in this paper clearly indicate that U(VI) sorption onto hematite is endothermic and entropically favorable, likely due to dehydration of the uranyl ion upon sorption. The role that dehydration will play on the environmental transport of uranium is not yet clear. However, the loss of fewer hydrating waters and the weaker interaction with the hematite surface compared with Eu(III), may result in greater desorption of U(VI) from environmental surfaces and therefore greater environmental transport of U(VI).

ACKNOWLEDGEMENTS

The authors thank J. Mangold for many helpful discussions. This research was funded by the U.S. Department of Energy Office of Biological and Environmental Research through the Nuclear Energy University Partnership Program (project number 11-3180).

REFERENCES

- Almazan-Torres M. G., Drot R., Mercier-Bion F., Catalette H., Den Auwer C. and Simoni E. (2008) Surface complexation modeling of uranium(VI) sorbed onto zirconium oxophosphate versus temperature: Thermodynamic and structural approaches. *J. Colloid Interface Sci.* **323**, 42–51.
- Angove M. J., Johnson B. B. and Wells J. D. (1998) The Influence of Temperature on the Adsorption of Cadmium(II) and Cobalt(II) on Kaolinite. *J. Colloid Interface Sci.* **204**, 93–103.
- Bandura A. V. and Lvov S. N. (2006) The ionization constant of water over wide ranges of temperature and density. *J. Phys. Chemistry Ref. Data* **35**, 15–30.
- Bargar J. R., Reitmeyer R., Lenhart J. J. and Davis J. A. (2000) Characterization of U(VI)-carbonate ternary complexes on hematite: EXAFS and electrophoretic mobility measurements. *Geochim. Cosmochim. Acta* **64**, 2737–2749.
- Bauer A., Rabung T., Claret F., Schäfer T., Buckau G. and Fanghänel T. (2005) Influence of temperature on sorption of europium onto smectite: The role of organic contaminants. *Appl. Clay Sci.* **30**, 1–10.
- Brown G. E., Henrich V. E., Casey W. H., Clark D. L., Eggleston C., Felmy A., Goodman D. W., Grätzel M., Maciel G., McCarthy M. I., Nealson K. H., Sverjensky D. A., Toney M. F. and Zachara J. M. (1999) Metal Oxide Surfaces and Their Interactions with Aqueous Solutions and Microbial Organisms. *Chem. Rev.* **99**, 77–174.
- Choppin G. R. (1983) Solution Chemistry of the Actinides. *Radiochim. Acta* **32**, 42–53.
- Dzombak D. and Morel F. M. M. (1990) *Surface complexation modeling: Hydrous ferric oxide.*, Wiley, New York, NY.
- Estes S. L., Arai Y., Becker U., Fernando S., Yuan K., Ewing R. C., Zhang J., Shibata T. and Powell B. A. (2013) A self-consistent model describing the thermodynamics of Eu(III) adsorption onto hematite. *Geochim. Cosmochim. Acta* **122**, 430–447.
- Guillaumont R., Fanghanel T., Neck V., Fuger J., Palmer D. A., Grenthe I. and Rand M. H. (2003) *Update on the chemical thermodynamics of uranium, neptunium, plutonium, americium and technetium.* eds. F. J. Mompean, M. Illemassene, C. Domenech-Orti, and K. BEN SAID, Elsevier, New York, NY.
- Haynes W. M. ed. (2013) Standard Density of Water. In *CRC Handbook of Chemistry and Physics* CRC Press/Taylor and Francis, Boca Raton, FL. pp. 6–7 – 6–8.
- Herbelin A. and Westall J. C. (1999) *FITEQL. A computer program for the determination of chemical equilibrium constants from experimental data.*, Department of Chemistry, Oregon State University, Corvallis, OR, USA.
- Hiemstra T., Riemsdijk W. H. V., Rossberg A. and Ulrich K.-U. (2009) A surface structural model for ferrihydrite II: Adsorption of uranyl and carbonate. *Geochim. Cosmochim. Acta* **73**, 4437–4451.
- Jang J.-H., Dempsey B. A. and Burgos W. D. (2007) A Model-Based Evaluation of Sorptive Reactivities of Hydrous Ferric Oxide and Hematite for U(VI). *Environ. Sci. Technol.* **41**, 4305–4310.
- Langmuir D. (1997) *Aqueous Environmental Geochemistry.*, Prentice Hall, Upper Saddle River, NJ.
- Lu N., Reimus P. W., Parker G. R., Conca J. L. and Triay I. R. (2003) Sorption kinetics and impact of temperature, ionic strength and colloid concentration on the adsorption of plutonium-239 by inorganic colloids. *Radiochim. Acta* **91**, 713–720.
- Martell A. E., Smith R. M. and Motekaitis R. J. (2004) *NIST Critically Selected Stability Constants of Metal Complexes.*, NIST, Gaithersburg, MD, USA.

- Missana T., García-Gutiérrez M. and Maffiotte C. (2003) Experimental and modeling study of the uranium (VI) sorption on goethite. *J. Colloid Interface Sci.* **260**, 291–301.
- Moyes L. N., Parkman R. H., Charnock J. M., Vaughan D. J., Livens F. R., Hughes C. R. and Braithwaite A. (2000) Uranium Uptake from Aqueous Solution by Interaction with Goethite, Lepidocrocite, Muscovite, and Mackinawite: An X-ray Absorption Spectroscopy Study. *Environ. Sci. Technol.* **34**, 1062–1068.
- Reich T., Moll H., Arnold T., Denecke M. A., Hennig C., Geipel G., Bernhard G., Nitsche H., Allen P. G., Bucher J. J., Edelstein N. M. and Shuh D. K. (1998) An EXAFS study of uranium(VI) sorption onto silica gel and ferrihydrite. *J. Electron Spectrosc. Relat. Phenom.* **96**, 237–243.
- Ridley M. K., Hiemstra T., Machesky M. L., Wesolowski D. J. and van Riemsdijk W. H. (2012) Surface speciation of yttrium and neodymium sorbed on rutile: Interpretations using the charge distribution model. *Geochim. Cosmochim. Acta* **95**, 227–240.
- Ridley M. K., Machesky M. L., Wesolowski D. J. and Palmer D. A. (2005) Surface complexation of neodymium at the rutile-water interface: A potentiometric and modeling study in NaCl media to 250°C. *Geochim. Cosmochim. Acta* **69**, 63–81.
- Rodda D. P., Johnson B. B. and Wells J. D. (1996) Modeling the Effect of Temperature on Adsorption of Lead(II) and Zinc(II) onto Goethite at Constant pH. *J. Colloid Interface Sci.* **184**, 365–377.
- Rossberg A., Ulrich K.-U., Weiss S., Tsushima S., Hiemstra T. and Scheinost A. C. (2009) Identification of Uranyl Surface Complexes on Ferrihydrite: Advanced EXAFS Data Analysis and CD-MUSIC Modeling. *Environ. Sci. Technol.* **43**, 1400–1406.
- Sherman D. M., Peacock C. L. and Hubbard C. G. (2008) Surface complexation of U(VI) on goethite (α -FeOOH). *Geochim. Cosmochim. Acta* **72**, 298–310.
- Sverjensky D. A. (2003) Standard states for the activities of mineral surface sites and species. *Geochim. Cosmochim. Acta* **67**, 17–28.
- Tertre E., Berger G., Simoni E., Castet S., Giffaut E., Loubet M. and Catalette H. (2006) Europium retention onto clay minerals from 25 to 150 °C: Experimental measurements, spectroscopic features and sorption modelling. *Geochim. Cosmochim. Acta* **70**, 4563–4578.
- Trivedi P. and Axe L. (2001) Predicting Divalent Metal Sorption to Hydrous Al, Fe, and Mn Oxides. *Environ. Sci. Technol.* **35**, 1779–1784.
- Waite T. D., Davis J. A., Payne T. E., Waychunas G. A. and Xu N. (1994) Uranium(VI) adsorption to ferrihydrite: Application of a surface complexation model. *Geochim. Cosmochim. Acta* **58**, 5465–5478.
- Wang Z. and Giammar D. E. (2013) Mass Action Expressions for Bidentate Adsorption in Surface Complexation Modeling: Theory and Practice. *Environ. Sci. Technol.* **47**, 3982–3996.
- Wazne M., Korfiatis G. P. and Meng X. (2003) Carbonate Effects on Hexavalent Uranium Adsorption by Iron Oxyhydroxide. *Environ. Sci. Technol.* **37**, 3619–3624.
- Zanonato P., Di Bernardo P., Bismondo A., Liu G., Chen X. and Rao L. (2004) Hydrolysis of Uranium(VI) at Variable Temperatures (10–85 °C). *J. Am. Chem. Soc.* **126**, 5515–5522.
- Zeng H., Singh A., Basak S., Ulrich K.-U., Sahu M., Biswas P., Catalano J. G. and Giammar D. E. (2009) Nanoscale Size Effects on Uranium(VI) Adsorption to Hematite. *Environ. Sci. Technol.* **43**, 1373–1378.

APPENDIX B: REPORTS FOR MILESTONE: M2NU-11-SC-CU_-0204-029: EXAMINATION OF ACTINIDE SORPTION TO HEMATITE UNDER VARIABLE TEMPERATURES

This appendix contains the following two reports submitted in fulfillment of this milestone.

- Mangold, J. and Powell, B. A., “Examination of Uranium and Neptunium sorption to hematite versus ionic strength and temperature”
- Estes, S. and Powell, B. A., “Examination of Np(V), Th(IV), and Pu(V/IV) sorption to hematite as a function of temperature

Examination of Uranium and Neptunium sorption to hematite versus ionic strength and temperature

Jeremiah Mangold and Brian A. Powell

Environmental Engineering and Earth Sciences, Clemson University

DOE NEUP Project: Quantification of cation sorption to engineered barrier materials under extreme conditions (Project #11-3180)

Report in fulfillment of Milestone: M2NU-11-SC-CU_-0204-029: Examination of actinide sorption to hematite under variable temperatures

Introduction

The objective of this research is to examine mechanisms and thermodynamics of actinide sorption to engineered barrier materials (iron (oxyhydr)oxides and bentonite clay) for nuclear waste repositories under high temperature and high ionic strength conditions using a suite of macroscopic and microscopic techniques which will be coupled with interfacial reaction models. In this work the sorption of uranium and neptunium to hematite was examined as a function of actinide concentration, temperature, and ionic strength. In addition to the sorption experiments, potentiometric titrations of hematite have been performed as a function of temperature and ionic strength. In this report the data are presented and discussed and a separate report will follow with a quantitative model of the data.

Materials and Methods

Hematite (α -Fe₂O₃) was synthesized by transformation of ferrihydrite using a method adapted from Schwertmann and Cornell (1991). Powder x-ray diffraction (XRD, Rigaku MiniFlex) was used to confirm the identity of the synthesized mineral as hematite. The specific surface area (SSA) of the mineral was determined to be 43.87 m²/g via N₂ BET analysis (courtesy of Onur Guven Apul).

Ultrapure water (Elga-PURELAB flex) with a resistivity of 18.2 M Ω was utilized in preparing all solutions used for this study.

All hematite that was reused from the potentiometric and micro-calorimetric acid-base titrations was dialyzed using dialysis tubing with a 6,000 – 8,000 molecular weight cut off (MWCO) (Spectrapor) and ultrapure water that was replaced almost daily with fresh ultrapure water. The dialysis process was deemed complete when the ultrapure water, in contact with the dialysis tubing for at least one day's time, had a conductivity of less than 5 μ S/cm (Oakton®, ECTestr 11+ Multi-Range).

Actinide Variable Temperature Batch Sorption Studies

Variable temperature batch sorption studies investigating the uptake of uranium and neptunium to hematite in single solute systems with the analyte concentration ranging between 1 μ g/L to 1 mg/L were conducted over the temperature range of 25 to 80 °C in solutions of 0.01 M and 1 M NaCl. Uranium –

hematite isotherm experiments were conducted at pH 5 while neptunium – hematite isotherm experiments were conducted at pH 7. Carbon dioxide was not excluded from these experiments.

Batch reactors were prepared using polycarbonate Erlenmeyer flasks with screw tops (VWR®, Catalog # 89095-260) that were previously cleaned with 2% HNO₃ (prepared from BDH Aristar® Plus Nitric Acid, VWR® Catalog # 87003-261) and rinsed with ultrapure water repeatedly to remove any residual plastic present in the containers. Stock solutions of 0.01 M and 1M NaCl were prepared by dissolving 0.58 g and 58 g of NaCl salt (BDH, ACS grade), respectively, into 1 L of ultrapure water. A hematite stock solution with a solid's concentration of 10 g/L was prepared by measuring out 2 g of hematite in a 250 mL polycarbonate centrifuge bottle, adding 200 mL of ultrapure water, and subsequently mixing the suspension vigorously for approximately 24 hours using a magnetic stir bar and stir plate.

Uranium working solution of 100 mg/L and 1 mg/L were each prepared by pipetting an aliquot of a 1,000 mg/L uranium stock solution stored in 2% HNO₃ (High-Purity™ Standards; Charleston, South Carolina, USA) into a 15 mL polypropylene centrifuge tube and diluted with ultrapure water. Similarly, ²³⁷Np working solutions of 100 mg/L and 1 mg/L were individually prepared by pipetting an aliquot of a 1.5 mmol/L ²³⁷Np(V) stock solution (Eckert and Zeigler, Atlanta, GA) into a 15 mL polypropylene centrifuge tube (VWR®, Catalog # 89039-670) and diluted with ultrapure water.

There were a total of four systems studied in this work: (1) U and hematite in 0.01 M NaCl, (2) U and hematite in 1 M NaCl, (3) Np and hematite in 0.01 M NaCl, and (4) Np and hematite in 1 M NaCl. A total of ten batch reactors were prepared for each system to be studied, eight reactors with varying concentrations of the analyte of interest (1, 5, 10, 50, 100, 200, 500, and 1,000 µg/L), one duplicate reactor (100 µg/L), and one control reactor with no analyte present. All additions to the reactors were measured gravimetrically. The reactors were prepared by first pipetting in 0.6 mL of the 10 g/L hematite stock suspension, followed by 60 mL of 0.01 M or 1 M NaCl. Then either U or Np was spiked into the reactor using the appropriate working solution. Upon adding in the radionuclide to the reactor, the Erlenmeyer flask was then capped and mixed vigorously (VWR® Pulsing Vortex Mixer) for several minutes to ensure a well-mixed suspension. The pH of each reactor was then adjusted to the desired value for the analyte being studied (pH 5 for U, pH 7 for ²³⁷Np) using 0.1 M or 0.01 M NaOH and HCl (Metrohm certified titrants). During the initial pH adjustment, the pH was measured using a Thermo Scientific Orion Star A214 pH meter and Orion 8103RN Ross Semi-Micro Combination pH probe at room temperature.

Once the reactors had been prepared and pH adjusted, they were placed in an incubated shaker (Thermo Scientific MaxQ 4450) set at 25°C and allowed to equilibrate for a minimum of 5 days. All reactors were sampled twice with at least 48 hours in between sampling events to confirm equilibrium had been reached. Reactor pH was checked and adjusted as needed, typically every two days. At elevated temperatures, pH was measured using a Thermo Scientific Triode, refillable, epoxy body pH with automatic temperature compensation. The pH probe was calibrated prior to use using pH buffer solutions of 4.01, 7, and 10.01 (Orion 910104, 910107, and 910110). Once equilibrium had been reached for a set of reactors at 25 °C, the reactors were either placed back in the incubated shaker at a temperature setting of 50 °C or in a shaking water bath (VWR® 18L Shaking Water Bath) at 50 °C. Subsequently, once the reactors had reached equilibrium at 50 °C, they were then placed in a shaking water bath at 80 °C and allowed to equilibrate.

Sampling events were conducted by first mixing vigorously the contents of a reactor for approximately 20 seconds using a pulsing vortex mixer, immediately followed by pipetting out 1.3 mL of the reactor suspension and ejecting the volume into a micro-centrifuge tube (VWR® MicroTubes with silicone O-Rings). Upon completing this procedure for all reactors to be sampled during a given sampling event, the samples in the micro-centrifuge tubes were then centrifuged at least 20 minutes at 7,200 g. If a clear supernatant was not observed, additional centrifugation time was added. After the samples were centrifuged, an aliquot of the supernatant was taken out of each micro-centrifuge tube and placed in a separate 15 mL polypropylene centrifuge tube. The aliquot placed in the 15 mL centrifuge tube was then diluted with 2% HNO₃ and analyzed using inductively coupled plasma mass spectrometry (ICP-MS, Thermo X Series II). The ICP-MS was calibrated using NIST traceable ²³⁷Np and ²³⁸U standards. A ²⁴²Pu internal standard was used for all analyses.

Potentiometric titrations of hematite

Potentiometric titrations of hematite were conducted at 25 and 50 °C using an automated titrator set up (Metrohm 836 Titrando with Tiamo Version 1.2 software). The hematite suspension titrated in these experiments was prepared by measuring out 0.4 g of hematite, a pre-determined amount of NaCl, dependent on the ionic strength being studied, and 50 mL of degassed ultrapure water. These contents were then placed into a water jacketed titration vessel (Metrohm, Catalog #6.1418.150) under a N₂ atmosphere, acidified down to pH 3.5, and allowed to mix overnight. In some cases where larger hematite particles persisted, the titration vessel and its contents were sonicated (Branson 1510 Sonicator) to help break up particle aggregates.

The water jacketed titration vessel was temperature controlled by means of a refrigerated/heated circulating bath (VWR® Shaker Bath). The pH of the system was measured using a Metrohm Aquatrode Plus pH probe that was calibrated daily with pH buffer solutions of 4.01, 7.00, and 10.01. The temperature of the suspension in the reactor vessel was monitored using a Metrohm Pt temperature probe which allowed for the reported pH of the system be automatically temperature compensated by the titration software. Hematite suspensions were initially titrated up with 0.10 N NaOH and then immediately titrated back down using 0.10 N HCl, all while under a N₂(g) atmosphere with a N₂(g) flow rate of approximately 4 L/min. All titrants used in this work were Metrohm NIST-Traceable Certified Titrants. Titrant was injected into the hematite suspension in 25 µL aliquots after the pH had stabilized from the previous injection (signal drift <0.1 mV/min) or every five minutes, whichever came first. The temperature and pH of the system was recorded by the Tiamo™ software.

At all temperatures studied, the N₂ gas blown into the titration vessel was first bubbled through a NaOH/KOH CO₂ trap followed by an ultrapure water bath before reaching the titration vessel. The ultrapure water bath served to humidify the N₂(g) prior to its introduction into the titration vessel, thereby minimizing/eliminating any evaporation in the titration vessel caused by the N₂(g). At 50 °C the ultrapure water bath which the N₂(g) was bubbled through was heated using a temperature probe controlled hot plate with the probe placed inside the water bath thereby ensuring that the water bath was kept at a constant temperature during the experiment.

Hematite Calorimetry

Isothermal calorimetric acid and base titrations of hematite suspensions were performed using a TA Instruments TAM III microcalorimeter with stainless steel ampoules. All calorimetric titrations were run

using the TAM III microcalorimeter's dynamic correction measurement principle. Prior to each experiment, the microcalorimeter underwent a full dynamic calibration.

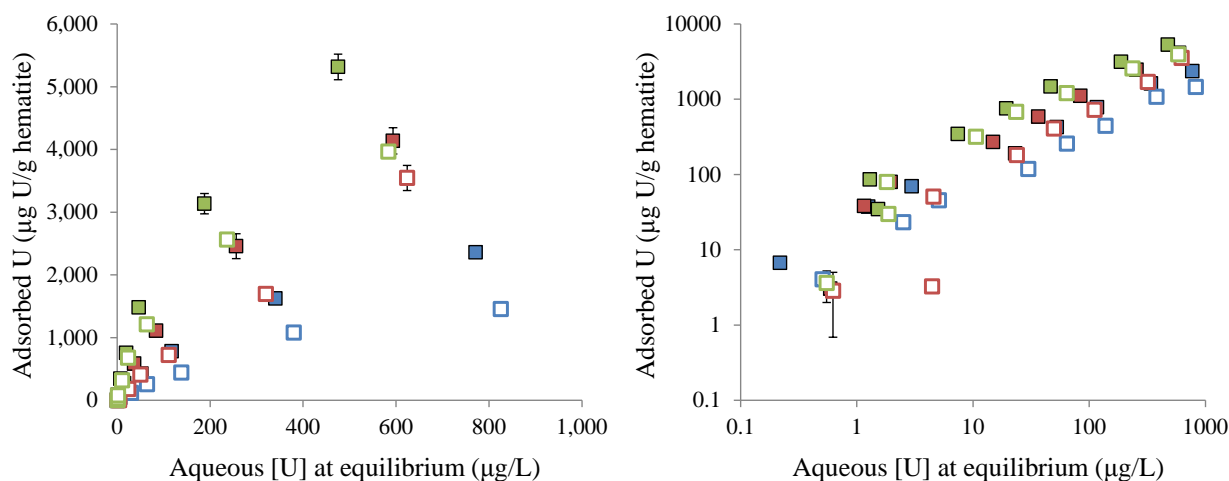
Four hematite suspensions with ionic strengths of 0.01M, 0.1 M, 0.4 M, and 1 M NaCl were prepared using degassed ultrapure water and stored in a glove box under a N₂ atmosphere. The sample and reference ampoules used for the calorimetric titrations were prepared by adding 0.8 mL of a given hematite suspension to each ampoule inside the glove box. Once the ampoules were taken out of the glove box, their pH was measured prior to them being lowered into the calorimeter. In all cases, pH was measured using an Orion 8175BNWP Ross Sure-Flow Semi-Micro pH probe that was always calibrated prior to use with pH buffer solutions of 4.01, 7, and 10.01. It should be noted that while exposure to atmospheric carbon dioxide could not be avoided once the ampoules were removed from the glove box, all reasonable efforts were made to minimize the amount of time that the hematite suspension in the ampoules was in contact with the atmosphere.

Acid and base titrations were performed by injecting 5 μ L of 0.01 N HCl or 0.01 N NaOH (Metrohm Titrants, NIST-Traceable) respectively, into the sample ampoule by means of an automated syringe pump (TA Instruments 3810 syringe pump). The titrant was injected over a 10 second period of time with a 35 minute interval between titrant injections. The number of titrant injections was typically set at 30; however there were a couple instances where 20 or 25 injections were used instead for an experiment. The contents of the sample ampoule were stirred using an 18 karat gold impellor at a rate of 150 revolutions per minute. Once the titration experiment had ended, the pH of the sample and reference ampoules was re-measured and the hematite suspension was then dialyzed and freeze dried for future use.

1. Results and Discussion

Actinide Variable Temperature Batch Sorption Studies

Uranium and neptunium sorption to hematite at pH 5 and 7, respectively, was investigated at 25, 50, and 80 $^{\circ}$ C in solutions of 0.01 M and 1 M NaCl (Figure 1).



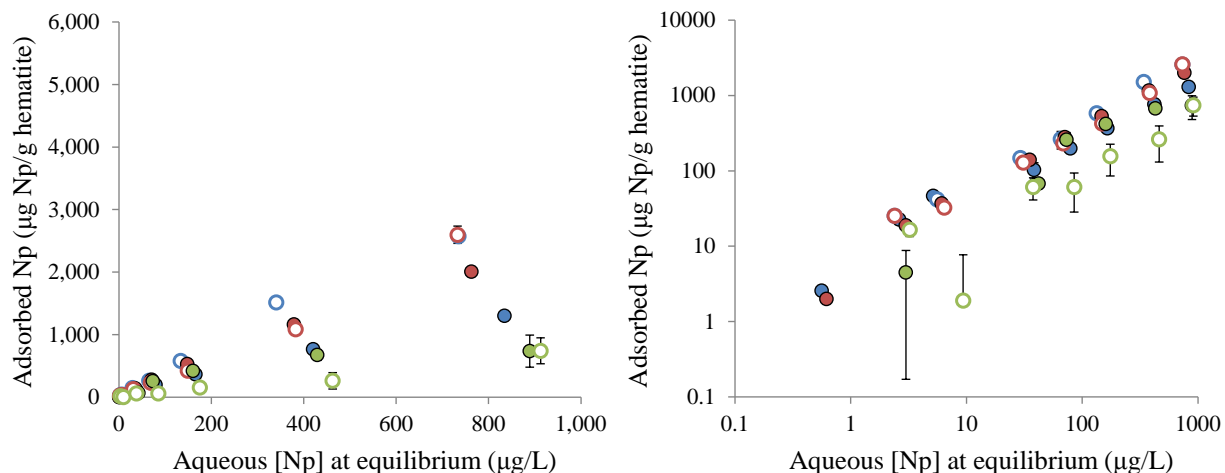


Figure 1 Uranium (plots a and b) and Neptunium (plots c and d) sorption to hematite on linear (plots a and c) and log (plots b and d) scales. Sorption data at 25, 50, and 80 °C is colored blue, red, and green, respectively. Sorption data in 0.01 M and 1 M NaCl solutions is differentiated using closed and open symbols, respectively. U and Np sorption data collected at pH 5 and 7, respectively.

Uranium

Over the temperature range studied, uranium sorption to hematite was found to increase with increasing temperature and decrease with increasing ionic strength (Figure 1a and Figure 1b). Examining the uranium sorption data in conjunction with its aqueous speciation at pH 5 (Figure 2) provides insight as to potential mechanisms for uranium uptake on hematite. For both the 0.01 M and 1.0 M NaCl systems, uranyl hydrolysis products become increasingly important as temperature rises to 50 and 80 °C. This fact, coupled with the observed rise in uranium sorption with temperature, suggests that uranyl hydrolysis products are some of the primary sorbing species responsible for uranium uptake under the conditions tested. In particular, the UO_2OH^+ species appears to be the most probable hydrolysis product to complex with the hematite surface given its prevalence under all experimental conditions investigated. Further inspection of Figure 2 reveals that the uranyl chloride aqueous complexes only impact uranium speciation in the 1.0 M NaCl system. Given this information, along with the observed decrease in uranium sorption with increasing ionic strength, implies that uranyl chloride aqueous complexes may not sorb strongly or perhaps at all to the hematite surface for the conditions tested in this work.

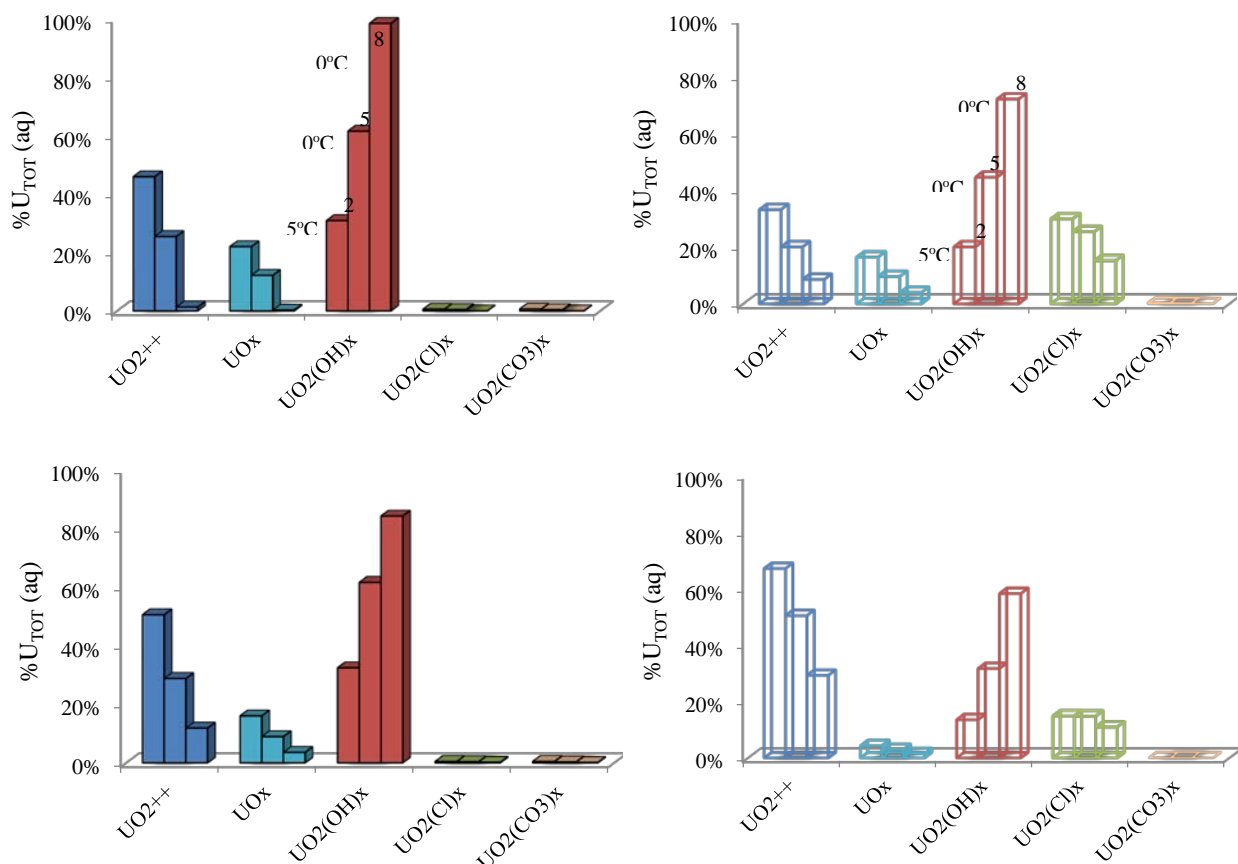


Figure 2 Uranium aqueous speciation at pH 5, presented as a percent distribution of the total uranium present in solution for 0.01 M NaCl (plots a and c) and 1.0 M NaCl (plots b and d). In each plot, the percent distribution of a given species at 25, 50, and 80 °C is presented in ascending order from left to right. The aqueous species distribution is depicted in terms of activities (plots a and b) and concentrations (plots c and d). Model simulations were conducted in the modeling program FIT4FD and the v8r6 database from Lawrence Livermore National Lab. The results presented here are for a total uranium concentration of 10^{-5} M. It should be noted that there was no noticeable changes in speciation when the model was run at lower total concentrations of uranium.

The rise in uranium sorption with temperature is indicative of an endothermic sorption reaction as illustrated by the Van't Hoff equation

$$\ln K = \frac{-\Delta H_{rxn}^{\theta}}{RT} + \frac{\Delta S_{rxn}^{\theta}}{R} \quad \text{Equation 1}$$

where K is the equilibrium constant of a reaction, ΔH_{rxn}^{θ} and ΔS_{rxn}^{θ} are the standard reaction enthalpy and standard reaction entropy, respectively, at temperature T, R is the universal gas constant, and T is the temperature of the system.

Since Gibbs free energy of reaction is defined as

$$\Delta G_{rxn}^{\ominus} = \Delta H_{rxn}^{\ominus} - T\Delta S_{rxn}^{\ominus}$$

Equation 2

where ΔG_{rxn}^{\ominus} is the Gibbs free energy of reaction at standard state conditions, it is evident that in order for an endothermic reaction to be thermodynamically favorable, it must possess a positive entropy term. Hence, uranium sorption to hematite is thought to be an entropically driven process. The reason for this positive entropy of reaction is believed to stem from the displacement of water molecules present in the primary solvation shell of aqueous uranium species as they complex with the mineral surface.

Neptunium

Neptunium's sorption behavior to hematite over the range of conditions studied proved to not be as straightforward as in the case of uranium. The influence of ionic strength on Np sorption was variable depending on the temperature of the system (cf. Figure 1). At 25, 50, and 80 °C Np sorption appears to be enhanced, unaffected, and reduced, respectively, as ionic strength increases from 0.01 M to 1.0 M NaCl. Over the temperature range studied, Np sorption to hematite was found to decrease with increasing temperature in the 1 M NaCl system; whereas in the 0.01 M NaCl system, Np sorption increased from 25 to 50 °C and subsequently dropped as the temperature rose from 50 to 80 °C.

In the absence of spectroscopic data, consideration of neptunium's sorption data alongside its predicted aqueous speciation at pH 7 (Figure 3) is instructive in helping identify potential sorption species/processes. Inspection of Figure 3 shows that the free neptunyl ion, NpO_2^+ , is the dominant Np aqueous species under all experimental conditions tested in this work. In particular, for the 0.01 M NaCl system, the NpO_2^+ aqueous species makes up nearly 100% of Np in the aqueous phase over the temperature range studied, suggesting that the free neptunyl ion, NpO_2^+ , is one of the primary aqueous species sorbing to hematite under these conditions. Furthermore, Figure 3 illustrates the increasing importance of the neptunyl chloride aqueous species, NpO_2Cl^0 , in the 1.0 M NaCl system as temperature rises. In light of this fact, and given Np's enhanced uptake in the 1.0 M NaCl system versus the 0.01M NaCl system at 25°C, the NpO_2Cl^0 aqueous species sorbing to hematite appears to be a strong possibility.

It should be noted that while the aqueous speciation of certain cations has been extensively studied and the corresponding equilibrium constants for these species are well established, this is not necessarily the case for actinides such as neptunium. Hence, the v8r6 database used in generating the aqueous speciation charts presented in Figures 2 and 3 is not considered to be an exhaustive list of all possible aqueous species, but rather a record of the aqueous species that have been experimentally observed and possess reliable equilibrium constants. In fact, for some of the aqueous species present in the v8r6 database, equilibrium constants are only available at 25°C so utilization of these constants at higher temperatures is tenuous at best. In short, the aqueous speciation data presented in Figures 2 and 3, while useful for helping postulate potential sorption species/mechanisms, may not be entirely accurate.

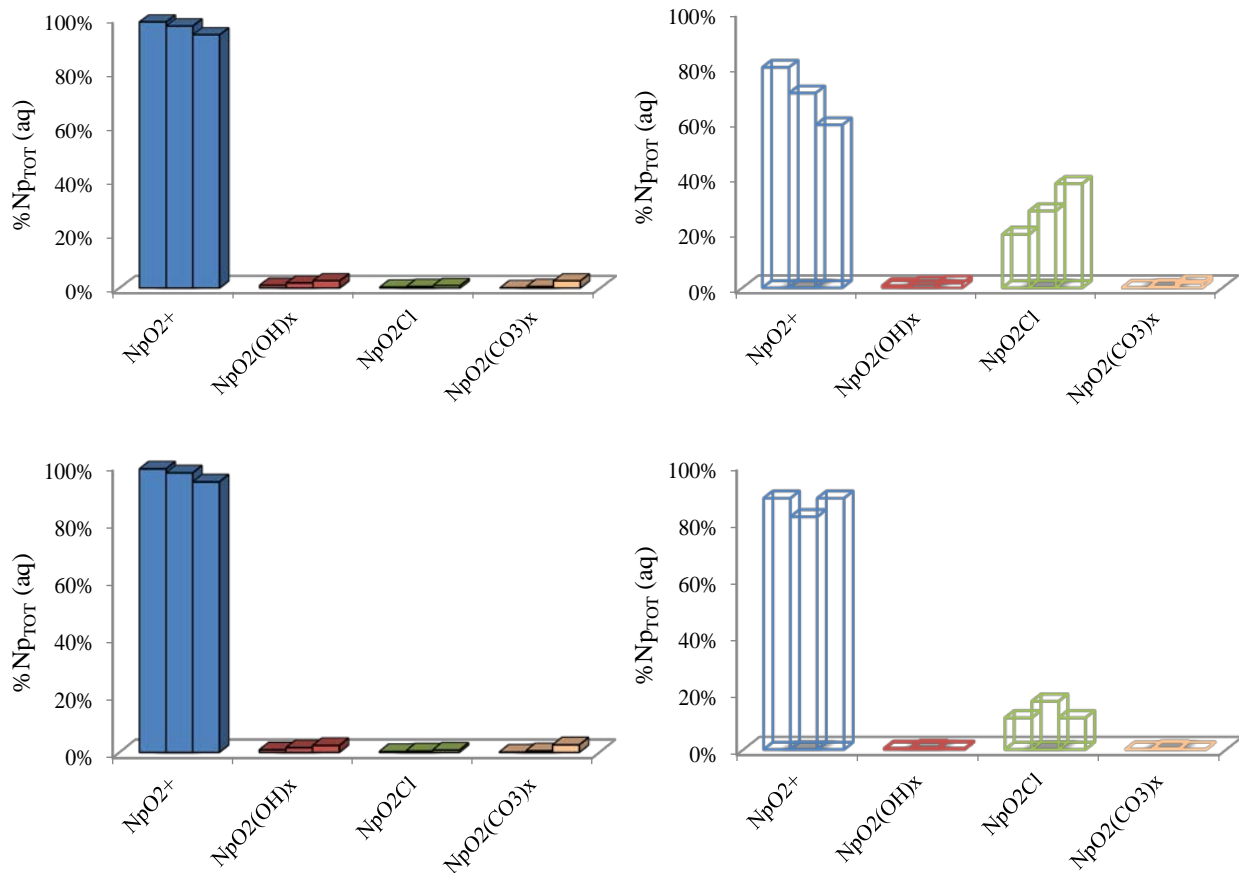


Figure 3 Neptunium aqueous speciation at pH 7, presented as a percent distribution of the total neptunium present in solution for 0.01 M NaCl (plots a and c) and 1.0 M NaCl (plots b and d). In each plot, the percent distribution of a given species at 25, 50, and 80 °C is presented in ascending order from left to right. The aqueous species distribution is depicted in terms of activities (plots a and b) and concentrations (plots c and d). Model simulations were conducted in the modeling program FIT4FD, the v8r6 database from Lawrence Livermore National Lab, and hydrolysis constants from Rao et al. [1]. The results presented here are for a total neptunium concentration of 10^{-5} M. It should be noted that there was no noticeable changes in speciation when the model was run at lower total concentrations of neptunium.

Multiple working hypotheses for explaining Np sorption to hematite

Neptunium's sorption behavior for the 0.01 M and 1.0 M NaCl systems over the temperature range studied can arise for a number of reasons that are presented here as multiple working hypotheses. While different from one another, these hypotheses are not mutually exclusive, and in all likelihood, the actual physical explanation for neptunium's sorption behavior is due to a combination of these hypotheses and perhaps others as well. Hypothesis #1 is described in greater detail than the subsequent hypotheses presented in this report due to the fact that it is less speculative than the others and based primarily on the available data.

Hypothesis #1: This hypothesis is based off the assumption that the neptunium speciation data presented in Figure 3 is complete and accurate. Furthermore, it is assumed that both NpO_2^+ and NpO_2Cl^0 are the primary aqueous species that sorb to hematite, forming surface species $\equiv\text{SOHNpO}_2$ and $\equiv\text{SOHNpO}_2\text{Cl}$, respectively. With these assumptions in mind, the observed increase and decrease in Np sorption as the temperature rises from 25 to 80°C for the 0.01 M and 1.0 M NaCl systems, respectively, can be reasoned by considering the enthalpies of reaction/formation for the surface species $\equiv\text{SOHNpO}_2$ and $\equiv\text{SOHNpO}_2\text{Cl}$.

Considering Equation 1, if the formation of $\equiv\text{SOHNpO}_2$ between 25 and 50°C is an endothermic reaction, then an increase of Np sorption would be expected over that same temperature range for systems such as the 0.01 M NaCl system where only the $\equiv\text{SOHNpO}_2$ surface species is expected to be prevalent. From 50 to 80°C however, Np sorption in the 0.01 M NaCl system is observed to decrease (Figure 1), indicating that the surface complexation reaction is no longer endothermic but rather exothermic (Equation 1). To explain the rise and fall of Np sorption in the 0.01 M NaCl system as temperature rises from 25 to 50°C and from 50 to 80°C, respectively, the heat capacity at constant pressure (C_p) for the formation of $\equiv\text{SOHNpO}_2$ is considered. If the surface complexation reaction producing $\equiv\text{SOHNpO}_2$ possesses a C_p less than zero, then it is possible that the formation reaction switches from being endothermic to exothermic at some point within the temperature range of interest (cf. Figure 4a). If a case similar to the one illustrated in Figure 4 is occurring for the $\equiv\text{SOHNpO}_2$ surface species, an increase in Np sorption from 25 to 50°C and a decrease in sorption from 50 to 80°C would be anticipated for systems where $\equiv\text{SOHNpO}_2$ is the sole/dominant surface species.

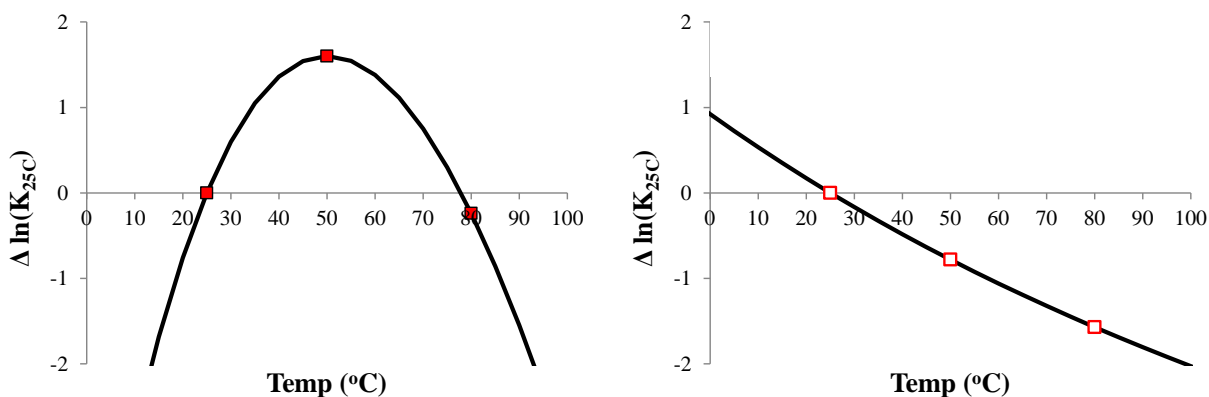


Figure 4 Example illustrating how an equilibrium constant changes with temperature due to (a) a positive standard reaction enthalpy at 25°C ($\Delta H_{25C}^\circ > 0$) and negative C_p , and (b) a negative standard reaction enthalpy at 25°C ($\Delta H_{25C}^\circ < 0$) with $C_p = 0$. The y-axis quantifies how much the natural log of the equilibrium constant changes at a given temperature from its value at 25°C (i.e., $\Delta \ln(K_{25C}) = \ln(K_{T2}) - \ln(K_{25C})$). The red boxes are used to highlight the example values of $\Delta \ln(K_{25C})$ at 25, 50, and 80°C.

Np sorption in the 1.0 M NaCl system is observed to decrease with increasing temperature from 25 to 80°C (Figure 1). Given that Np sorption in the 0.01 M NaCl system increases from 25 to 50°C, and that this rise in sorption has been attributed to the increased favorability of forming the $\equiv\text{SOHNpO}_2$ surface

species, it stands to reason that the observed drop in Np sorption over that same temperature range for the 1.0 M NaCl system must stem from a decreased favorability to form the $\equiv\text{SOHNpO}_2\text{Cl}$ surface species. This decrease in sorption with increasing temperature suggests that the surface complexation reaction forming $\equiv\text{SOHNpO}_2\text{Cl}$ is exothermic over the temperature range studied (Equation 1, Figure 4b); which in turn means that less Np will sorb as $\equiv\text{SOHNpO}_2\text{Cl}$ as temperature rises. Hence, in systems with sufficiently high concentrations of Cl^- (as in the case of the 1.0 M NaCl system), Np sorption is expected to drop as temperature increases due to the amount of Np complexed with Cl^- in solution and the decreased affinity of the NpO_2Cl^0 aqueous species for the hematite surface. It should be noted however that if the concentration of Cl^- in the system is sufficiently low enough, an increase in Np sorption from 25 to 50°C is possible due to the dominance of the NpO_2^+ aqueous species under these conditions and the increased favorability of the $\equiv\text{SOHNpO}_2$ surface species over that temperature range.

Hypothesis #2: Inner- and outer-sphere surface complexes not considered by the authors are present in the system. Spectroscopic information regarding neptunium sorption to hematite is limited and for the experimental conditions tested here, non-existent. Therefore, it is possible that the surface species considered here are not accurate or complete.

Hypothesis #3: The neptunium speciation data presented in Figure 3 is not complete and accurate. This assumption is based on the fact that studies investigating neptunium aqueous speciation are limited. Hence, the species listed in thermodynamic databases such as the v8r6 database should not be considered comprehensive nor should the equilibrium constants associated with these species be considered absolute, a fact that is highlighted by the ongoing debate between researchers concerning the correct equilibrium constants for neptunyl hydrolysis products [1–3].

Potentiometric and calorimetric acid/base titrations of hematite

Potentiometric acid/base titrations of hematite were conducted at 25 and 50°C in background electrolyte solutions of NaCl at ionic strengths of 0.01 M, 0.1 M, 0.4 M, and 1 M (Figure 5). The potentiometric titration data at 25 and 50°C reveals a two pH unit drop in the point of zero charge (PZC) for hematite from $\text{pH}_{\text{PZC}} \approx 9.3$ at 25°C to $\text{pH}_{\text{PZC}} \approx 7.3$ at 50°C. With this drop in the pH_{PZC} of hematite, increased uranium and neptunium sorption would be expected as temperature rises from 25 to 50°C due to a less positively charged surface.

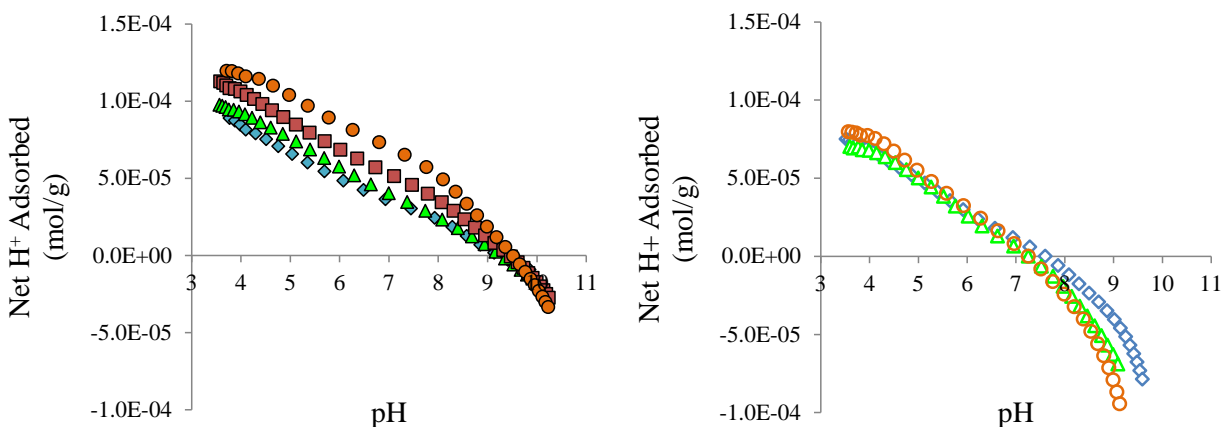


Figure 5 Potentiometric titration data for hematite at (a) 25°C and (b) 50°C. Hematite suspensions were titrated using NaCl as the background electrolyte at ionic strengths of 0.01 M (blue diamond), 0.1 M (green triangle), 0.4 M (red box), and 1 M (orange circle). Data for the 0.4 M NaCl system at 50°C and for all ionic strengths at 80°C has yet to be collected.

Isothermal micro-calorimetric acid/base titrations on hematite were conducted at 25°C in background electrolyte solutions of NaCl at the same ionic strengths as utilized in the potentiometric titrations. It should be noted that all inferences drawn from the calorimetric data at this time are tenuous given that the heat of dilution has yet to be determined for all experiments with the exception of the acid titrations for hematite in 1 M NaCl. The calorimetric data presented in Figure 6a and 6c reveals a positive increase in reaction heat with increasing ionic strength for hematite acid titrations. Since proton and electrolyte adsorption increase with increasing ionic strength and decreasing pH (Figure 5), these results suggest that surface protonation and/or chloride outer-sphere surface complexation reactions are endothermic at 25°C. The negative net reaction heat values reported in Figure 6 are believed to be due to the formation of water during the acid/base titrations since that reaction is known to be exothermic.

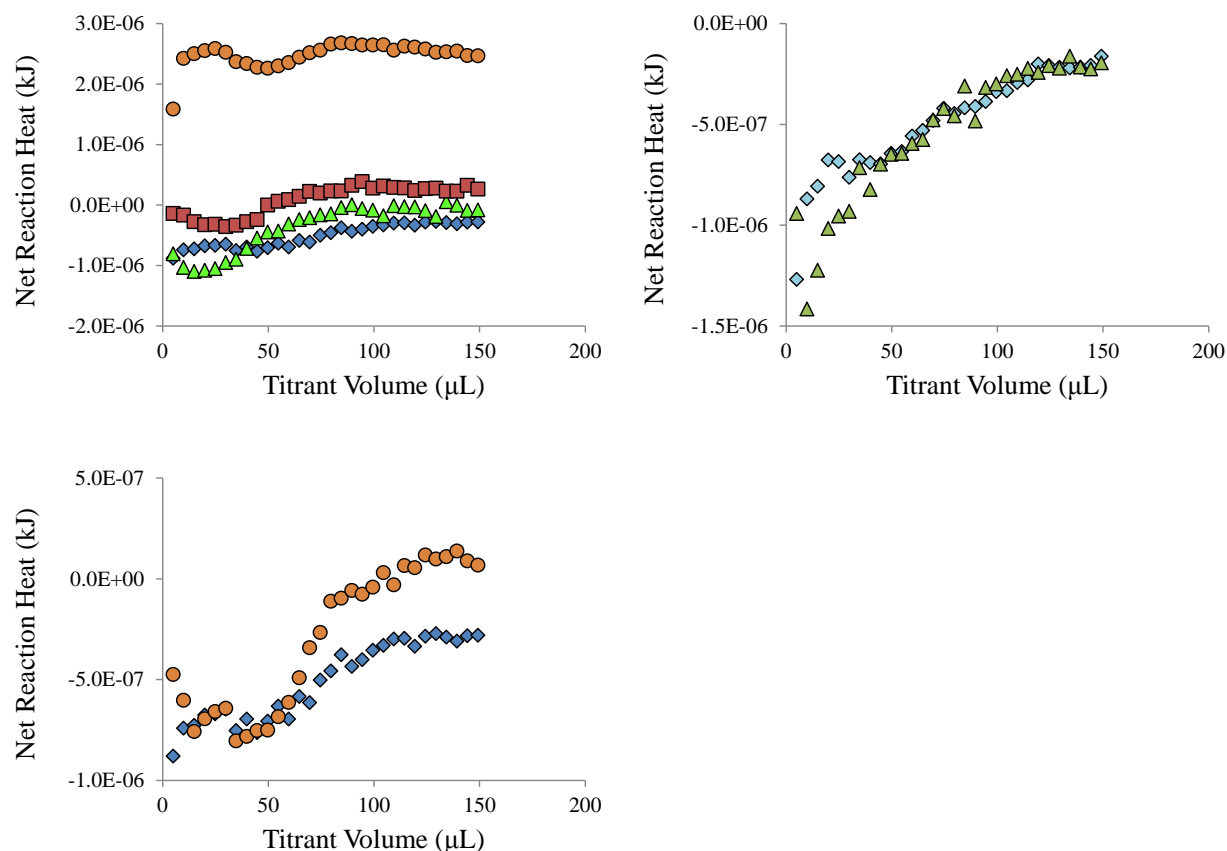


Figure 6 Hematite calorimetric titrations at 25°C using an (a and c) acid, and (b) base titrant. Hematite suspensions were titrated using NaCl as the background electrolyte at ionic strengths of 0.01 M (blue diamond), 0.1 M (green triangle), 0.4 M (red box), and 1 M (orange circle). Plots a and b have not been corrected for the heat of dilution. The 1 M NaCl data (orange circle) in plot c has been corrected for dilution heat however the 0.01 M NaCl data (blue diamond) in the same plot has not been corrected. All data points represent the average net heat of reaction from multiple experimental runs.

Future Work

Potentiometric titrations of hematite will be conducted at 50 °C and 80 °C. Additional isothermal micro-calorimetric titrations are currently being performed to complete the 25 °C data set for the four hematite suspensions studied. Subsequently, micro-calorimetric titrations will be conducted at 50 and 80°C for the same hematite suspensions. This calorimetric data, in conjunction with the potentiometric titration data, will yield a comprehensive data set allowing for the development of an accurate and robust surface complexation model capable of describing hematite's acid/base surface chemistry over a wide range of experimental conditions. Once the surface complexation model has been fit to the potentiometric and calorimetric data, it will then be used to fit the uranium and neptunium sorption data collected in this

study. The developed model can then be tested on different data sets to assess the applicability of the model in other systems. In addition, micro-calorimetric titrations looking at uranium and neptunium sorption to hematite in 0.01 M and 1 M NaCl solutions at 25, 50, and 80°C are planned. The resulting data from these calorimetric titrations will be used to determine the enthalpies of formation for hematite-actinide surface complexes and compared with the values predicted from the surface complexation model.

References

- [1] L. Rao, T.G. Srinivasan, A.Y. Garnov, P. Zanonato, P. Di Bernardo, A. Bismondo, Hydrolysis of neptunium(V) at variable temperatures (10–85°C), *Geochim. Cosmochim. Acta.* 68 (2004) 4821–4830. doi:10.1016/j.gca.2004.06.007.
- [2] L. Rao, T.G. Srinivasan, A.Y. Garnov, P. Zanonato, P.D. Bernardo, A. Bismondo, Response to the comment by V. Neck on “Hydrolysis of neptunium(V) at variable temperatures (10–85°C)”, *Geochimica et Cosmochimica Acta* 68, 4821–4830, *Geochim. Cosmochim. Acta.* 70 (2006) 4556–4562. doi:10.1016/j.gca.2006.07.002.
- [3] V. Neck, Comment on “Hydrolysis of neptunium(V) at variable temperatures (10–85 °C)” by L. Rao, T.G. Srinivasan, A.Yu. Garnov, P. Zanonato, P. Di Bernardo, and A. Bismondo, *Geochim. Cosmochim. Acta.* 70 (2006) 4551–4555. doi:10.1016/j.gca.2006.02.031.

A Comparison of the Thermodynamics of Np(V), Th(IV), and Pu(IV) Sorption onto Hematite

Shanna L. Estes and Brian A. Powell**

Environmental Engineering and Earth Sciences, Clemson University, 342 Computer Court,
Anderson, SC 29625, United States

*Corresponding author. Tel.: +1 864 656 1004; E-mail address: sestes@g.clemson.edu;
bpowell@clemson.edu

DOE NEUP Project: Quantification of cation sorption to engineered barrier materials under extreme conditions (Project #11-3180)

Report in fulfillment of Milestone: M2NU-11-SC-CU_-0204-029: Examination of actinide sorption to hematite under variable temperatures

ABSTRACT

Using multi-temperature batch sorption experiments and surface complexation modeling, we have studied the thermodynamics of Np(V), Th(IV), and Pu(IV) sorption onto hematite (α -Fe₂O₃). Np(V) experiments (0.5 g L⁻¹ α -Fe₂O₃, I = 0.01 M NaCl, Np(V)_T = (2.09 ± 0.03) × 10⁻⁸ M) were conducted over the pH range 3 to 8 at 15, 25, 35, and 50 °C, and Th(IV) and Pu(IV) sorption experiments (0.58 g L⁻¹ α -Fe₂O₃, I = 0.01 M NaCl, Th(IV)/Pu(IV)_T < 4 × 10⁻⁸ M) were conducted over the pH range 1.5 to 5.5 at 15, 25, 35, 50, and 65 °C. Surface complexation modeling with the diffuse layer model (DLM) indicated that Np(V) and Th(IV) sorption onto hematite at all temperatures was best described with monodentate unhydrolyzed

surface complexes, while Pu(IV) sorption onto hematite at 25 °C was best described as $\text{Pu}(\text{OH})_x^{4-x}$ sorbed in a monodentate fashion. Neither Np(V) nor Th(IV) sorption increased with increasing temperature, suggesting that both sorption reactions were temperature independent. Additionally, calculated sorption enthalpies and entropies suggest that Np(V) and Th(IV) sorption onto hematite occurs via predominantly outer-sphere and both outer- and inner-sphere surface complexation, respectively. Pu sorption onto hematite increased slightly with increasing temperature, suggesting that inner-sphere complexation may dominate the Pu(IV) sorption mechanism. Attempts to fit the Pu(IV) sorption behavior with the surface complexation model derived from Th(IV) were unsuccessful.

1. INTRODUCTION

Decades of nuclear weapons production and testing have resulted in significant Pu contamination of soils, sediments, and groundwater at many U.S. Department of Energy (DOE) sites (Riley and Zachara, 1992). Although this contamination is primarily localized at these DOE sites, several researchers have reported long-distance Pu transport (Kersting et al., 1999; Santschi et al., 2002; Novikov et al., 2006), which represents a significant risk to future populations because of the radiological health hazards associated with Pu exposure.

Pu chemistry at the solid-water interface is perhaps one of the most important processes controlling Pu transport in the environment, and therefore, it is important to investigate this chemistry under environmentally relevant conditions. However, the influence of temperature on Pu sorption reactions has not been widely studied, and to our knowledge, only Lu et al. (2003) have examined the effect of temperature on Pu sorption onto various minerals. This is unfortunate, because in addition to providing necessary data for empirically modeling actinide

sorption behavior under the elevated temperature conditions expected in a geologic repository (Anon, 2002), investigating these reactions over a range of temperatures can also yield important information regarding reaction mechanisms. For example, we previously demonstrated that Eu(III) (Estes et al., 2013) and U(VI) sorption onto hematite are endothermic, entropically driven reactions, which suggests that both Eu(III) and U(VI) form inner-sphere complexes with the hematite surface and that some dehydration of these elements occurs. Yet, because Pu is extremely sensitive to changes in redox conditions, and because Pu can routinely exist in aqueous solutions as mixtures of Pu(III), Pu(IV), Pu(V), and Pu(VI) (Clark et al., 2011), the interpretation of experimental data can be difficult. For this reason, researchers commonly use Np(V) and Th(IV) as redox stable chemical analogs of Pu(V) and Pu(IV), respectively. To this end, the objectives of this work were to examine the influence of temperature on Np(V), Th(IV), and Pu(IV) sorption onto hematite, and to compare the Np(V), Th(IV), and Pu(IV) data and surface complexation models in an effort to identify the mechanisms responsible for the sorption of these actinides onto hematite.

2. MATERIALS AND METHODS

2.1 Reagents

Hematite (α -Fe₂O₃) synthesis and characterization are described by (Estes et al., 2013).

La(NO₃)₃·6H₂O (99.9% Alfa Aesar), KMnO₄ (99.5%, Mallinckrodt), NaCl (99%, BDH), NaNO₂ (101.5%, Mallinckrodt), H₂SO₄ (95.0 – 98.0%, EM Science), HF (47-51%, Fisher), HCl (37%, BDH Aristar Plus), HNO₃ (67 – 70%, BDH Aristar Plus), bis-(ethylhexyl)-phosphoric acid (HDEHP, 95%, Aldrich), 4-benzyol-3-methyl-1-phenyl-2-pyrazolin-5-one (PMBP, TCI), cyclohexane (>99%, Alfa Aesar), and standardized HCl (0.01, 0.1 N, Metrohm) and NaOH

(0.01, 0.1 N, Metrohm) were used as received. Perkin Elmer Optiphase HiSafe 3 cocktail was used for all liquid scintillation counting (LSC). For Pu oxidation state analyses, PMBP (0.025 M) and HDEHP (0.5 M) solutions were prepared in cyclohexane and equilibrated with 1 M HCl for a minimum of 30 minutes, and a lanthanum stock solution containing 0.01 M LaNO₃, 0.8 M HNO₃, 0.25 M H₂SO₄, and 0.001 M KMnO₄ was prepared in ultrapure H₂O – these solutions were stored in amber glass bottles sealed with PTFE septa and screw caps. Neptunium calibration standards (in 2% HNO₃) and working solution #1 (WS1, 4.2×10^{-6} M Np(V) in 2% HNO₃) were prepared from a ²³⁷Np NIST standard reference solution (SRM 4341). Thorium calibration standards (in 2% HNO₃) and working solution #2 (WS2, 6.45×10^{-5} M Th(IV) in 1 M HCl) were prepared by diluting a Th plasma standard (1,000 µg L⁻¹ in 2% HNO₃, High Purity Standards). Working solution #3 (WS3, 1.51×10^{-6} M Pu(IV) in 1 M HCl) was prepared from a ²³⁸Pu source solution (Eckert & Ziegler, source #1556-59) by evaporating an aliquot of the source solution to dryness and reconstituting in 1 M HCl three times, with a few crystals of NaNO₂ added to the final solution to oxidize or reduce any Pu(III) or Pu(V/VI), respectively. Solvent extraction and LaF₃ coprecipitation (see Sec. 2.3) confirmed that the oxidation state distribution in WS3 was >98% Pu(IV). All experiments were prepared in ultrapure H₂O (resistivity > 18 MΩ cm, Millipore SuperQ).

2.2 Multi-Temperature Batch Sorption

Batch experiments were conducted in either 50 mL polypropylene (PP) centrifuge tubes (Np(V)) or 125 mL screw top polycarbonate (PC) Erlenmeyer flasks (Th(IV) and Pu(IV)). For the Np(V) experiments, 4 mL of a 5 g L⁻¹ hematite suspension and 4 mL of 0.1 M NaCl were added to each PP tube and diluted to a total volume of 40 mL with ultrapure H₂O. Following this step, an aliquot of WS1 was added to each tube, and the pH of each suspension was adjusted using HCl

or NaOH. For the Th(IV) and Pu(IV) experiments, hematite was added to each PC flask as the dry solid, and then suspended in 0.01 M NaCl. To hydrate the hematite, these suspensions were initially mixed for ~48 hours, before adding an aliquot of both WS2 and WS3 to each flask. Immediately after the working solution additions, the pH of each suspension was adjusted using HCl or NaOH. Although both Th(IV) and Pu(IV) were present in these suspensions, 100% sorption of both Th(IV) and Pu(IV) at the highest concentrations studied would represent < 0.05% surface coverage. Therefore, no competition between the two actinides are expected in these experiments. The final Np(V) suspensions contained 0.5 g L⁻¹ hematite, $(2.09 \pm 0.03) \times 10^{-8}$ M Np(V), and 0.01 M NaCl, with pH ranging from 3 to ~8. The final Th(IV)/Pu(IV) suspensions (prepared in duplicate) contained 0.58 g L⁻¹ hematite, $(2.11 \pm 0.02) \times 10^{-8}$ M or $(4.23 \pm 0.05) \times 10^{-8}$ M Th(IV), $(3.88 \pm 0.01) \times 10^{-10}$ M or $(2.00 \pm 0.01) \times 10^{-9}$ M Pu(IV), and 0.01 M NaCl in a total volume of ~60 mL, with pH ranging from ~1.5 to 5.5. No attempts to exclude atmospheric CO₂ were made. Additionally, no pH adjustments were made in either the Np(V) or Th(IV)/Pu(IV) experiments after the initial preparation of the batch systems.

Immediately following preparation of the batch systems, all flasks or tubes were initially placed within a temperature controlled orbital shaker (VWR) at 15 °C – PP tubes were placed horizontally in secondary containment. After 3 days of mixing, the pH of each suspension was measured using a combination pH electrode with automatic temperature compensation (Thermo 9157BNMD), and the suspensions were sampled by removing a 1.5 mL homogenous aliquot from each. Sample aliquots were centrifuged at 22,065g for 30 min to sediment particles larger than ~60 nm. For Np(V) and Th(IV) analyses, 1 mL or 0.5 mL of the supernatant was diluted with 9 mL of 2% HNO₃ and analyzed for total Np or Th by inductively-coupled plasma mass spectrometry (ICP-MS, Thermo X Series 2). For Pu(IV) analyses, 0.5 mL of the supernatant was

mixed with 4 mL of Optiphase HiSafe 3 cocktail in a 6 mL polyethylene (PE) scintillation vial and analyzed using liquid scintillation counting (30 minute count time, Perkin Elmer Tri-Carb 2910). After 5 – 7 additional days of mixing, the suspensions were sampled a second time to verify sorption equilibrium of Np(V) or Th(IV). During this second sampling event, an additional 300 μ L of the supernatant from select samples spanning the pH range of the Th(IV)/Pu(IV) batch experiment was collected for Pu oxidation state analysis, as described in Sec. 2.3. After the second sampling event, the reaction temperature was increased, and the entire sampling procedure was repeated to give Np(V) sorption data at 15, 25, 35, and 50 $^{\circ}$ C, and Th(IV) and Pu(IV) sorption data at 15, 25, 35, 50, and 65 $^{\circ}$ C.

2.3 Plutonium Oxidation State Analysis

The oxidation state of aqueous Pu was determined using a solvent extraction method adapted from Neu et al. (1994) and LaF₃ coprecipitation (Kobashi et al., 1988). For solvent extractions, an aliquot of the Pu containing sample was diluted to 1 mL with H₂O and 5 M HCl in a 1.5 mL PP centrifuge tube to give an aqueous phase with pH = 0. Following this step, 0.5 mL of either the PMBP or HDEHP cyclohexane solutions was added to each PP tube. The tubes were then immediately capped and mixed on a vortex mixer (VWR) for three minutes, and then centrifuged for 1.5 minutes at 4,600g (VWR Galaxy 5D) to quickly separate the phases. A 0.4 mL aliquot of both the organic and aqueous phases was then carefully removed and mixed with 4 mL of liquid scintillation cocktail and analyzed as above. For LaF₃ coprecipitation, an aliquot of each Pu containing sample (diluted with H₂O if necessary to give 0.5 mL total sample volume) was mixed with 1 mL of the lanthanum stock solution and 10 μ L of concentrated HF in a 1.5 mL PP centrifuge tube. The tubes were mixed and centrifuged as described for the solvent extractions, and then 0.4 mL of the aqueous phase was analyzed using LSC as described above. To limit Pu

oxidation state changes as much as possible, all extraction or coprecipitation procedures were generally completed (to the point of LSC analysis) within 5 – 7 minutes of initial sample collection. For these conditions, PMBP and HDEHP extract Pu(IV) and Pu(IV)/Pu(VI), respectively, from the aqueous phase, and both Pu(III) and Pu(IV) are coprecipitated with LaF₃, allowing quantification of the oxidation state distribution of Pu in our initial solutions or batch systems.

2.4 Surface Complexation Modeling

To describe Np(V), Th(IV), and Pu(IV) sorption onto hematite, surface complexation models (SCMs) were developed by fitting the batch sorption data at each temperature as a function of pH using a modified version of FITEQL 4.0 (Herbelin and Westall, 1999). FITEQL modifications are described by Estes et al. (2013). For each SCM, the electrical double layer (EDL) was defined using a single-site diffuse layer model (DLM) (Dzombak and Morel, 1990), which was selected for comparison with earlier work and because it has few adjustable parameters. For the Th(IV) and Pu(IV) SCMs, data from experiments at both initial actinide concentrations were combined and fit simultaneously. A 5% relative error was assigned to all experimental data during SCM optimization. Activity corrections were performed in FITEQL with the Davies model, after adjusting the Davies A parameter to each experimental temperature (Langmuir, 1997). Except where noted, the FITEQL goodness of fit parameter, the ratio of the weighted sum of squares to the degrees of freedom (WSOS/DF), was used to identify the best SCM for each data set. Calculated equilibrium constants are referenced to the 1.0 M standard state and are reported $\pm 1\sigma$. To ease comparison with future modeling efforts, equilibrium constants are also reported referenced to the site-occupancy standard state, as suggested by Sverjensky (2003).

3. RESULTS

3.1 Np(V) and Th(IV) Sorption onto Hematite

3.1.1 *Effect of Temperature*

Np(V) and Th(IV) sorption onto hematite increased sharply with increasing pH at all studied temperatures, and as expected based on the greater effective charge of Th(IV) (Choppin and Rao, 1984) and thus greater electrostatic attraction to the hematite surface, the Th(IV) sorption edge occurred at a lower pH than the Np(V) sorption edge (Fig. 1). Compared with the Th(IV) data, the Np(V) sorption data contained significant scatter (Fig. 1). Because we do not expect any Np redox chemistry (i.e., reduction of Np(V) to Np(IV)) under our experimental conditions (Teterin et al., 2006), this data scatter suggests a relatively weak interaction between Np(V) and the hematite surface.

Increasing the reaction temperature from 15 to 50 °C did not significantly affect Np(V) sorption onto hematite (Fig. 1). For the Th(IV) experiments, the sorption edge shifted to lower pH as the reaction temperature increased from 15 to 65 °C, regardless of initial Th(IV) concentration (Fig. 1). However, because K_w varies with temperature, the observed shift in the Th(IV) sorption edge is misleading, and does not necessarily indicate increased sorption. Re-plotting the Th(IV) sorption data as a function of “pH – $\frac{1}{2}pK_w$ ” (Fig. A1), reveals that Th(IV) sorption does not change with increasing temperature. Therefore, it appears that the Np(V) and Th(IV) sorption reactions are temperature independent, at least for our experimental conditions, which is contradictory to the sorption behavior reported for other metals (Rodda et al., 1996; Angove et al., 1998), lanthanides (Ridley et al., 2005; Bauer et al., 2005; Tertre et al., 2006; Ridley et al., 2012; Estes et al., 2013), and actinides (Lu et al., 2003; Almazan-Torres et al., 2008).

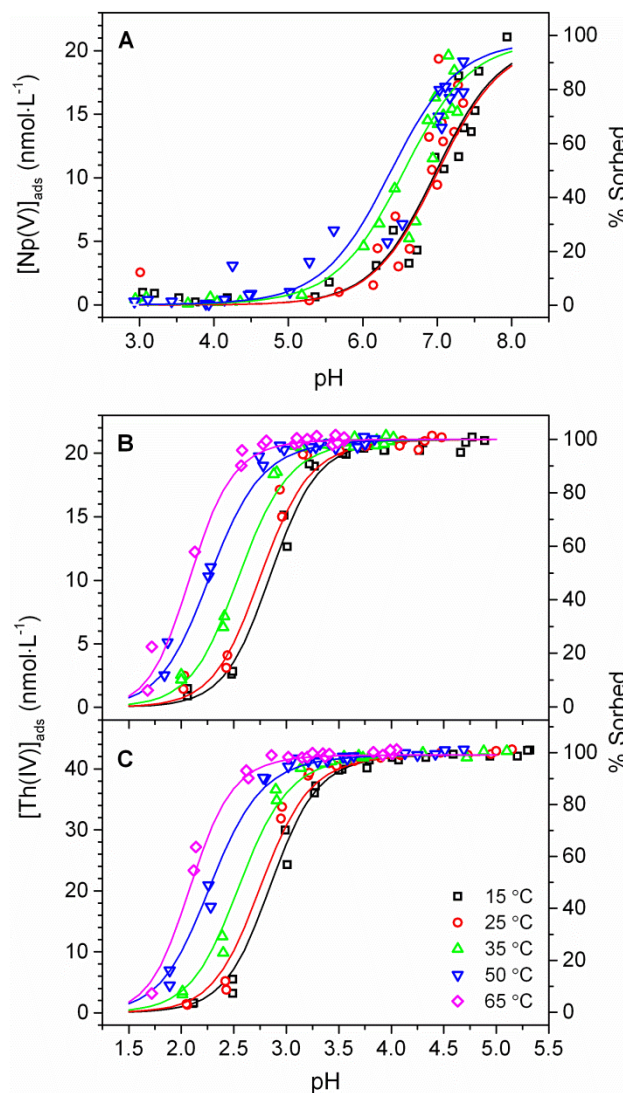


Figure 9. Np(V) and Th(IV) sorption onto hematite as a function of pH and temperature for a $[\text{Np(V)}]_{\text{TOT}}$ of $(2.09 \pm 0.03) \times 10^{-8}$ M (A) and $[\text{Th(IV)}]_{\text{TOT}}$ of $(2.11 \pm 0.02) \times 10^{-8}$ M (B) and $(4.23 \pm 0.05) \times 10^{-8}$ M (C). Solid lines are the corresponding surface complexation models (single-site DLM), which represent the following Np(V) and Th(IV) surface complexes: $\equiv\text{FeONpO}_2^0$ at 15 and 25 °C; $\equiv\text{FeOHNpO}_2^+$ at 35 and 50 °C; $\equiv\text{FeOHTh}^{4+}$ at 15, 25, 35, and 50 °C; and $\equiv\text{FeOTh}^{3+}$ at 65 °C. The WSOS/DF values, in order of increasing temperature, were: 20.32, 6.33, 11.84, and 17.91 for the Np(V) SCMs; and 3.70, 6.02, 1.15, 1.23, and 1.48 for the Th(IV) SCMs.

3.1.2 Surface Complexation Model Development

As illustrated in Fig. 2, the aqueous speciation of Np(V) is dominated by NpO_2^+ across the experimental pH range. The formation of NpO_2OH^0 was included in the final SCM, but concentrations of this species were generally insignificant in our batch systems. Although the formation of $\text{NpO}_2\text{CO}_3^-$ is significant above pH ~ 7.5 (Fig. 2), including aqueous or surface neptunyl-carbonate complexes in the SCM did not improve our fit results. Additionally, Kohler et al. (1999) previously demonstrated that the presence of atmospheric CO_2 did not affect Np(V) sorption onto hematite at pH < 8 . Therefore, all carbonate species were excluded from the final Np(V) SCM. Similarly, all carbonate species were excluded from the final Th(IV) SCM based on the expected aqueous Th(IV) speciation (Fig. 2), which indicates that Th(IV)-carbonate complexes were not present at significant concentrations in the pH range of the Th(IV) batch experiments (~ 1.5 to 5.5). However, unlike Np(V), the Th(IV) aqueous speciation includes several Th(IV) hydrolysis products and ThCl^{3+} (Fig. 2). Therefore, formation reactions for ThOH^{3+} , $\text{Th}(\text{OH})_2^{2+}$, $\text{Th}(\text{OH})_4^0$, and ThCl^{3+} were included in the SCM. All aqueous reactions and associated formation constants used in the final Np(V) and Th(IV) SCMs are listed in Table 1. Unless otherwise noted, the formation constants at each temperature were calculated using available reaction enthalpies (Table 1) and the van't Hoff equation. All pertinent hematite parameters, which were determined by Estes et al. (2013), are given in Table 2.

For both the Np(V)- and Th(IV)-hematite systems, many different surface reactions were considered during optimization of the SCM. At 15 and 25 °C, the Np(V) sorption data were best fit (i.e., lowest WSOS/DF) using a monodentate de-protonated surface complex, $\equiv\text{FeONpO}_2^0$; while at 35 and 50 °C, the data were best fit using a monodentate protonated surface complex, $\equiv\text{FeOHNpO}_2^+$ (Fig. 1). In contrast, the Th(IV) sorption data were best fit at 15, 25, 35, and 50

°C using a monodentate protonated surface complex, $\equiv\text{FeOHTh}^{4+}$ (Fig. 1). However, at 65 °C, a bidentate de-protonated surface complex, $(\equiv\text{FeO})_2\text{Th}^{2+}$, fit the Th(IV) sorption data slightly better than a monodentate de-protonated surface complex, $\equiv\text{FeOTh}^{3+}$ (WSOS/DF = 1.35 vs. 1.48, respectively). It is not clear which surface complex best represents the Th(IV) sorption onto hematite at 65 °C. However, because the relative error in the calculated log K for $(\equiv\text{FeO})_2\text{Th}^{2+}$ (log $K = 12.38 \pm 0.04$) was ~30% greater than the relative error in the calculated log K for $\equiv\text{FeOTh}^{3+}$ (log $K = 13.62 \pm 0.03$), we chose to model the Th(IV) sorption data at 65 °C with the monodentate surface complex. All surface complexation reactions and equilibrium constants chosen for the final Np(V) and Th(IV) SCMs at each temperature are listed in Table 2.

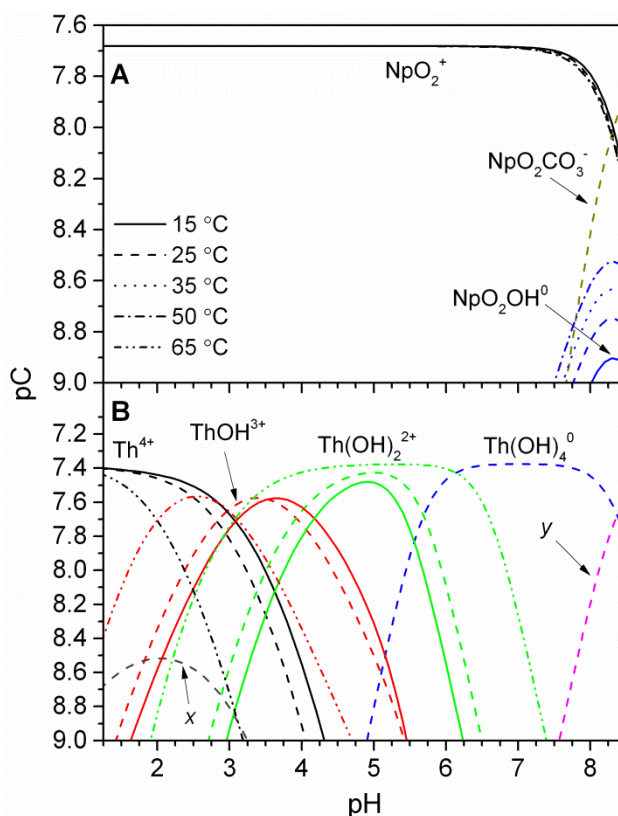


Figure 10. Aqueous speciation of Np(V) (A) and Th(IV) (B) as a function of pH and temperature in the presence of atmospheric CO_2 ($P_{\text{CO}_2} = 10^{-3.4}$ atm). Modeled using Visual

MINTEQA, with equilibrium constants given by Guillaumont et al. (2003); Rao et al. (2004); and Rand et al. (2007). The arrows *x* and *y* (B) indicate the Th(IV) species ThCl^{3+} and $\text{Th}(\text{OH})_2(\text{CO}_3)_2^{2-}$, respectively. The modeling conditions ($[\text{Np(V)}]_{\text{TOT}} = 2.09 \times 10^{-8} \text{ M}$ or $[\text{Th(IV)}]_{\text{TOT}} = 4.23 \times 10^{-8} \text{ M}$, $I = 0.01 \text{ M NaCl}$) were equivalent to the batch sorption experiments. The enthalpies for $\text{NpO}_2\text{CO}_3^-$, $\text{Th}(\text{OH})_4^0$, ThCl^{3+} , and $\text{Th}(\text{OH})_2(\text{CO}_3)_2^{2-}$ are not defined; therefore, only models at 25 °C are shown. For simplicity, only 15, 25, and 65 °C models, which illustrate the speciation range expected for our experimental conditions, are shown for other Th(IV) species.

Table 4. Aqueous reactions, equilibrium constants, and reaction enthalpies used to model Np(V) and Th(IV) sorption onto hematite at 15 – 65 °C.

<i>i</i>	reaction	<i>T</i> °C	log <i>K</i> ^{<i>a</i>}
1	K_w° $\text{H}_2\text{O} \leftrightarrow \text{H}^+ + \text{OH}^-$ $\Delta_r H_1 = 55.8 \text{ kJ mol}^{-1} \text{ }^c$	15 25 35 50 65	−14.34 ^{<i>b</i>} −13.99 ^{<i>b</i>} −13.68 ^{<i>b</i>} −13.26 ^{<i>b</i>} −12.91 ^{<i>b</i>}
4	$\beta_{1,1}^*$ (Np(V)) $\text{NpO}_2^+ + \text{H}_2\text{O} \leftrightarrow \text{NpO}_2\text{OH} + \text{H}^+$	15 25 35 50 65	−9.17 ^{<i>c</i>} −8.98 ^{<i>d</i>} −8.85 ^{<i>c</i>} −8.74 ^{<i>c</i>} —
5	$\beta_{1,1}^*$ (Th(IV)) $\text{Th}^{4+} + \text{H}_2\text{O} \leftrightarrow \text{ThOH}^{3+} + \text{H}^+$ $\Delta_r H_5 = 44.2 \text{ kJ mol}^{-1} \text{ }^i$	15 25 35 50 65	−2.77 ^{<i>e</i>} −2.50 ^{<i>f</i>} −2.25 ^{<i>e</i>} −1.90 ^{<i>e</i>} −1.58 ^{<i>e</i>}
6	$\beta_{2,1}^*$ (Th(IV)) $\text{Th}^{4+} + 2\text{H}_2\text{O} \leftrightarrow \text{Th}(\text{OH})_2^{2+} + 2\text{H}^+$ $\Delta_r H_6 = 85.7 \text{ kJ mol}^{-1} \text{ }^h$	15 25 35 50	−6.72 ^{<i>e</i>} −6.20 ^{<i>f</i>} −5.71 ^{<i>e</i>} −5.04 ^{<i>e</i>}

		80	-4.42 ^e
7	[*] $\beta_{4,1}$ (Th(IV)) $\text{Th}^{4+} + 4\text{H}_2\text{O} \leftrightarrow \text{Th}(\text{OH})_4^0 + 4\text{H}^+$	15	-17.40 ^g
		25	-17.40 ^f
		35	-17.40 ^g
		50	-17.40 ^g
		80	-17.40 ^g
8	$K_{\text{ThCl}3+}$ $\text{Th}^{4+} + \text{Cl}^- \leftrightarrow \text{ThCl}^{3+}$	15	1.70 ^g
		25	1.70 ^f
		35	1.70 ^g
		50	1.70 ^g
		80	1.70 ^g

^a All equilibrium constants are for $I = 0$ M.

^b Calculated from the standard density of water (Haynes, 2013) according to Bandura and Lvov (2006).

^c $\log K$ for neptunyl hydrolysis at 15, 35, and 50 °C was calculated from an exponential fit of $\log \beta_1^{\circ}$ (Rao et al., 2004) as a function of temperature.

^d Rao et al., 2004

^e $\log K$ values for aqueous Th(IV) reactions at 15, 35, 50, and 65 °C were calculated with the van't Hoff equation using the $\log K$ values at 25 °C and the reaction enthalpies listed in this table.

^f Rand et al., 2007

^g The reaction enthalpies for ^{*} $\beta_{4,1}$ (Th(IV)) and $K_{\text{ThCl}3+}$ are unknown. Therefore the same $\log \beta_{4,1}^{\circ}$ and $\log K_{\text{ThCl}3+}$ were used for each experimental temperature.

Table 5. Hematite characteristics, surface reactions, and associated equilibrium constants used in the final Np(V) and Th(IV) SCMs at 15 – 65 °C.

<i>i</i>	parameter / reaction	<i>T</i> °C	value / $\log K$	$\log K^{\ddagger}$
	pzc		7.36 ^a	
	A_s , BET surface area ($\text{m}^2 \text{g}^{-1}$)		30.7 ^a	
	N_s , site density (10^{18} sites m^{-2})		4.28 ^a	
	N_s^{\dagger} , molar site density (10^{-6} mol m^{-2})		7.11	
	C_s , solid phase concentration (g L^{-1}) [Np(V) experiments]		0.51	

C_s , solid phase concentration (g L ⁻¹) [Th(IV) and Pu(IV) experiments]		0.58		
2	K_+	15	6.39 ^b	6.51 ^{a,c}
	$\equiv\text{FeOH} + \text{H}^+ \leftrightarrow \equiv\text{FeOH}_2^+$	25	6.19 ^b	6.31 ^{a,c}
	$\Delta_r H_2 = -32.2 \text{ kJ mol}^{-1} \text{ }^a$	35	6.01 ^b	6.13 ^{a,c}
		50	5.75 ^b	5.87 ^{a,c}
		65	5.52 ^d	5.64 ^c
3	K_-	15	-8.30 ^b	-8.18 ^{a,c}
	$\equiv\text{FeOH} \leftrightarrow \equiv\text{FeO}^- + \text{H}^+$	25	-8.11 ^b	-7.99 ^{a,c}
	$\Delta_r H_3 = 32.2 \text{ kJ mol}^{-1} \text{ }^a$	35	-7.92 ^b	-7.80 ^{a,c}
		50	-7.67 ^b	-7.55 ^{a,c}
		65	-7.44 ^d	-7.32 ^c
9	K_{SC1}	15	-2.93 ± 0.02 ^e	-2.81 ^c
	$\equiv\text{FeOH} + \text{NpO}_2^+ \leftrightarrow \equiv\text{FeONpO}_2 + \text{H}^+$	25	-2.95 ± 0.02 ^e	-2.83 ^c
		35	—	—
		50	—	—
		65	—	—
10	K_{SC2}	15	—	—
	$\equiv\text{FeOH} + \text{NpO}_2^+ \leftrightarrow \equiv\text{FeOHNpO}_2^+$	25	—	—
		35	4.46 ± 0.03 ^e	4.58 ^c
		50	4.38 ± 0.02 ^e	4.50 ^c
		65	—	—
11	K_{SC3}	15	19.20 ± 0.02 ^e	19.32 ^c
	$\equiv\text{FeOH} + \text{Th}^{4+} \leftrightarrow \equiv\text{FeOHTh}^{4+}$	25	19.03 ± 0.02 ^e	19.15 ^c
		35	19.12 ± 0.02 ^e	19.24 ^c
		50	19.21 ± 0.02 ^e	19.33 ^c
		65	—	—
12	K_{SC4}	15	—	—
	$\equiv\text{FeOH} + \text{Th}^{4+} \leftrightarrow \equiv\text{FeOTh}^{3+} + \text{H}^+$	25	—	—
		35	—	—
		50	—	—
		65	13.62 ± 0.03 ^e	13.74 ^c

^a Estes et al. (2013)

^b Calculated by Estes et al. (2013) using a single-site diffuse layer model (DLM); *I* = 0.01 M NaCl; referenced to the 1.0 M standard state.

^c Referenced to the site occupancy standard state Sverjensky (2003), and calculated with the equation: $\log K^\ddagger = \log K + \log \frac{N_s A_s}{N^\ddagger A^\ddagger}$, where N^\ddagger and A^\ddagger are the theoretical site density (10×10^{18} sites m⁻²) and surface area (10 m² g⁻¹) suggested by Sverjensky (2003).

^d $\log K_+$ and $\log K_-$ at 65 °C were calculated using the van't Hoff equation, the $\log K_+$ and $\log K_-$ values at 25 °C, and the protonation ($\Delta_r H_2$) and de-protonation ($\Delta_r H_3$) enthalpies listed in this table.

^e Calculated in this work using a single-site DLM and referenced to the 1.0 M standard state; $I = 0.01$ M NaCl.

3.1.3 Sorption Thermodynamics

Because the best fit SCMs indicated a change in Np(V) surface speciation with increasing temperature, resulting in $\log K$ values at only two temperatures for each surface complex, it was not possible to use the van't Hoff relationship to calculate the Np(V) sorption enthalpy.

However, changes in the $\log K$ values at each temperature (Table 2) for the formation of $\equiv\text{FeONpO}_2^0$ and $\equiv\text{FeOHNPo}_2^+$ are insignificant, suggesting that the enthalpies for both reactions ($\Delta_r H_9$ and $\Delta_r H_{10}$, respectively) are ≈ 0 kJ mol⁻¹. Sufficient data were available to approximate the enthalpy of Th(IV) sorption onto hematite using a van't Hoff plot (Fig. 3). However, the linear regression yielded a slope which was not significantly different than zero (ANOVA, $P = 0.05$), suggesting that the reaction enthalpy for the formation of $\equiv\text{FeOHTh}^{4+}$ ($\Delta_r H_{11}$) is also ≈ 0 kJ mol⁻¹. These sorption enthalpies are consistent with the absence of any temperature dependent changes in the Np(V) and Th(IV) sorption edges noted earlier (Sec. 3.1.1).

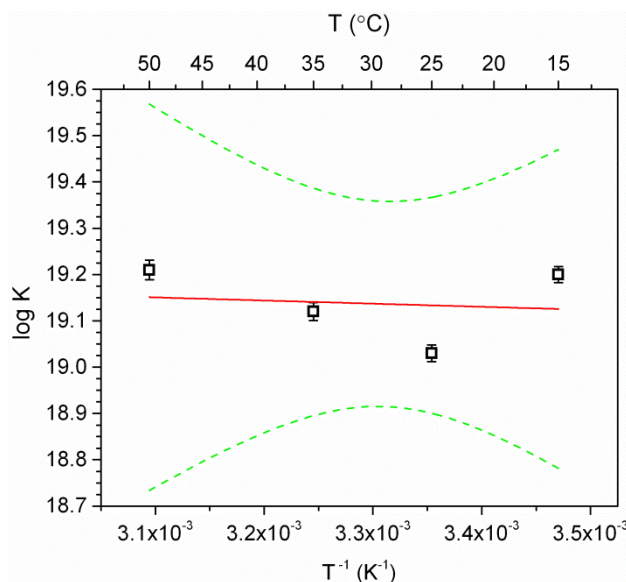


Figure 11. van't Hoff plot using $\log K$ values for the surface complex $\equiv\text{FeOHTh}^{4+}$. The solid line is the linear fit which is not significantly different than zero (at the 0.05 level), and the dashed lines are the 95% confidence intervals.

3.2 Pu(IV) Sorption onto Hematite

3.2.1 Effect of Temperature

Pu(IV) sorption onto hematite as a function of pH and temperature is shown in Fig. 4. This figure illustrates that: (1) sorption equilibrium was not reached at the first sampling event, as represented by significant differences between closed and open symbols, particularly at the higher pH values; (2) the Pu(IV) sorption edges are more shallow (i.e., sorption from 0 to 100% occurs over a wider pH range) than those observed for either Np(V) or Th(IV) (Fig. 1); and (3) there is significant scatter in the sorption data compared with the Th(IV) sorption data (Fig. 1). This anomalous sorption behavior was likely due to changes in the oxidation state of aqueous phase Pu across the studied pH range and at each reaction temperature (Fig. 5).

As pH increases, some Pu(IV) oxidation, likely to Pu(V), is evident at 15 to 50 °C (Fig. 5). This observation is consistent with the expected thermodynamic stabilities of Pu(III, IV, V, VI) under the experimental conditions (e.g, Kersting, 2013). Interestingly, at 65 °C, the aqueous phase Pu speciation in our batch experiments appears to reverse, such that oxidized Pu species become dominant at lower pH values compared to Pu(III/IV) (Fig. 5) Possible reasons for this oxidation state reversal are unknown and warrant further investigation.

If we assume that sorption equilibrium was reached at the second sampling event, and plot this data as a function of “ $\text{pH} - \frac{1}{2}\text{p}K_w$ ” (Fig. A2), Pu sorption onto hematite appears to increase with increasing temperature, which is consistent with previous observations by Lu et al. (2003). However, because we do not have direct evidence that sorption equilibrium was achieved, and because there are known changes in the Pu oxidation state, it is not clear if this increased sorption is actually due to one or more endothermic sorption reactions.

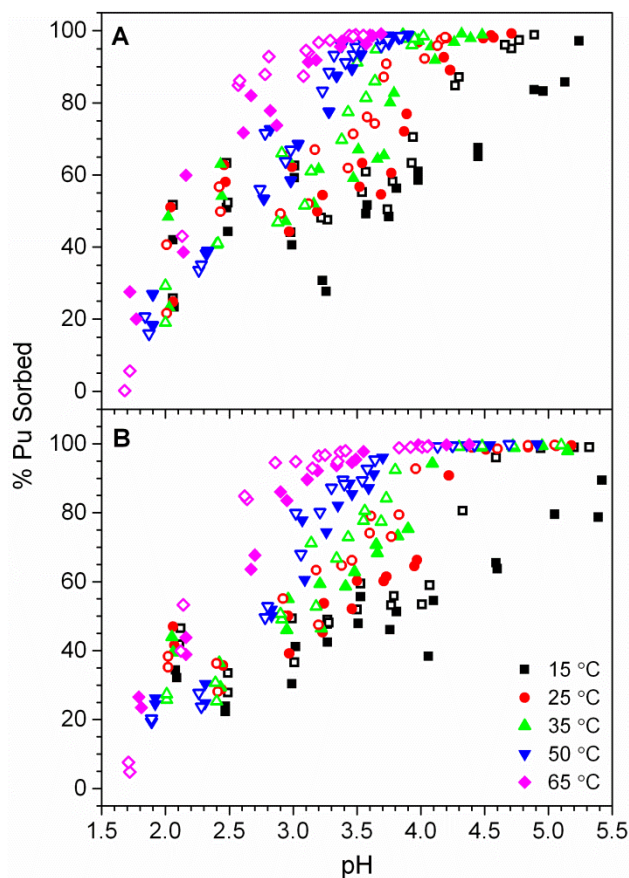


Figure 12. Pu(IV) sorption onto hematite as a function of pH and temperature for batch systems with $[\text{Pu(IV)}]_{\text{TOT}}$ of $(3.88 \pm 0.01) \times 10^{-10} \text{ M}$ (A) and $(2.00 \pm 0.01) \times 10^{-9} \text{ M}$ (B). Errors, calculated from counting statistics, are $\pm 1\sigma$. Closed and open symbols represent data from the first and second sampling events, respectively.

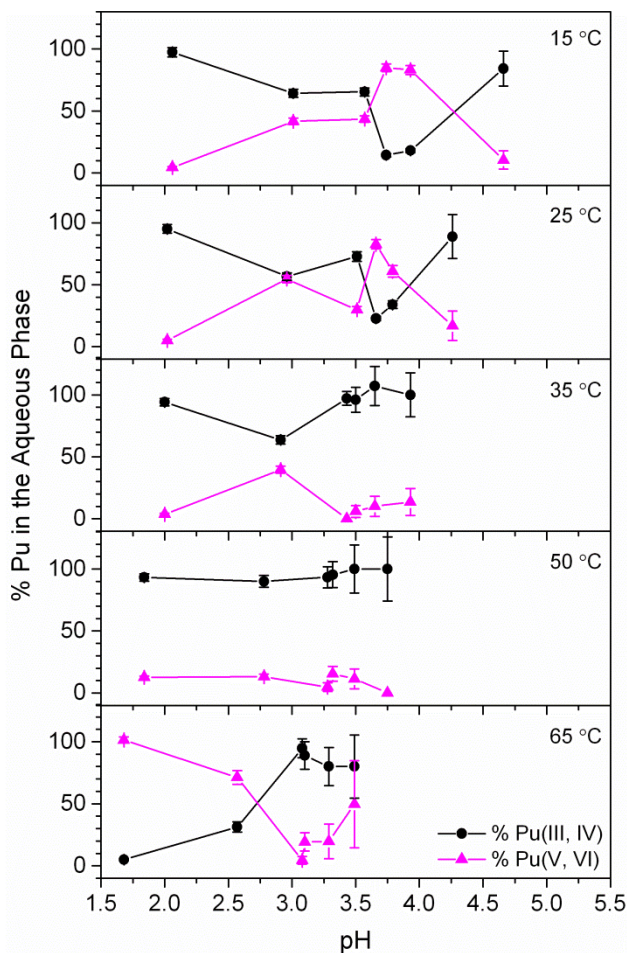


Figure 13. Pu oxidation state distribution in the aqueous phase as a function of pH and temperature for the batch systems with initial $\text{Pu(IV)}_{\text{TOT}}$ concentrations of $(3.88 \pm 0.01) \times 10^{-10}$ M. Errors, calculated from counting statistics, are $\pm 1\sigma$. Similar oxidation state distributions were measured for batch systems with higher initial Pu(IV) concentrations (Fig. A3). Pu(III,IV) concentrations are from solvent extraction with PMBP in cyclohexane, and agree well with results from LaF_3 coprecipitation. Pu(V/VI) concentrations are from coprecipitation with LaF_3 .

3.2.2 Surface Complexation Model Development at 25 °C

Using data from the second sampling event, we developed a SCM to describe the observed Pu sorption onto hematite. However, because Pu(IV) hydrolysis constants are only available at 25

°C, we were only able to fit the sorption data at that temperature. We explored several combinations of surface reactions during SCM optimization, using the Th(IV) best fit monodentate protonated surface complex as a guide. Carbonate speciation was excluded from the SCMs because Pu-carbonate species are not expected in significant concentrations in the studied pH range (e.g., Kersting, 2013). For model development, we assumed that Pu was present as 100% Pu(IV) and that neither Pu oxidation nor reduction occurred. As several researchers have observed Pu(V) reduction to Pu(IV) in the presence of various pure and mixed mineral phases (e.g., Sanchez et al., 1985; Keeney-Kennicutt and Morse, 1985; Powell et al., 2005; Hixon et al., 2013), and have suggested that Pu(IV) may be the thermodynamically favorable surface species, our assumption, that only Pu(IV) was present, may be reasonable for describing Pu surface reactions only. As clearly demonstrated in Fig. 5, a similar assumption cannot be made regarding the aqueous Pu speciation. The 25 °C data were best fit using a combination of three surface complexes, $\equiv\text{FeOHPu}(\text{OH})_2^{2+}$, $\equiv\text{FeOHPu}(\text{OH})_3^+$, and $\equiv\text{FeOHPu}(\text{OH})_4^0$ (Fig. 6). The relative importance of each surface complex is illustrated in Fig. 6, and the calculated equilibrium constants are given in Table 3.

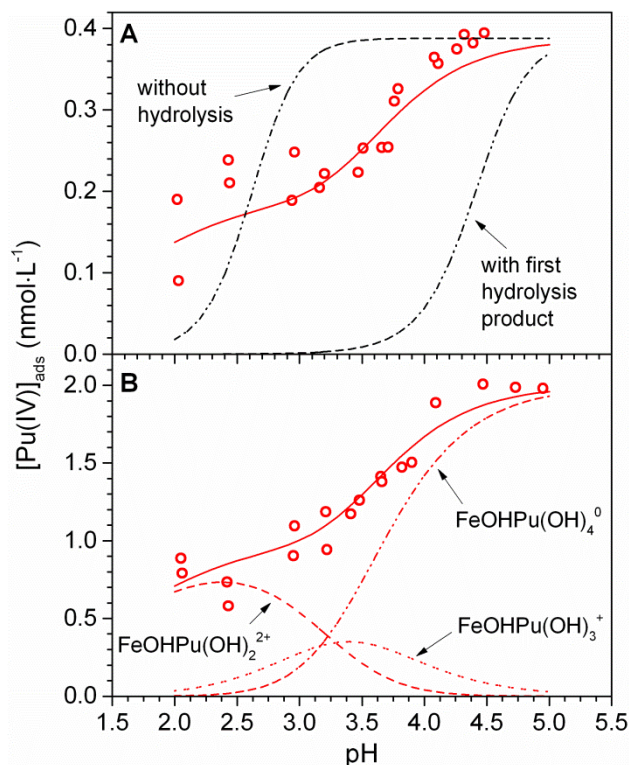


Figure 14. Pu sorption onto hematite as a function of pH at 25 °C for batch systems with $[\text{Pu(IV)}]_{\text{TOT}}$ of $(3.88 \pm 0.01) \times 10^{-10}$ M (A) and $(2.00 \pm 0.01) \times 10^{-9}$ M (B). Data is from the second sampling event only. Pu was assumed to be present as only Pu(IV), and neither reduction nor oxidation of Pu was allowed. Solid lines are the total SCM (i.e., sum of $\equiv\text{FeOHPu(OH)}_2^{2+}$, $\equiv\text{FeOHPu(OH)}_3^+$, and $\equiv\text{FeOHPu(OH)}_4^0$), which gave a WSOS/DF value of 4.99. The red dashed lines (B) represent the distribution of surface complexes across the experimental pH range. A similar distribution was observed for the batch systems with lower initial Pu(IV) concentrations. The black dashed lines (A) represent the Pu(IV) sorption that is *predicted* when the best fit Th(IV) surface complexation reaction (i.e., $\equiv\text{FeOHTh}^{4+}$, $\log K = 19.03$) is used to model the Pu sorption data in the absence and presence of Pu(IV) hydrolysis.

Table 6. Aqueous reactions, surface complexation reactions, and associated equilibrium constants used in the 25 °C Pu(IV) SCM.

<i>i</i>	reaction	log <i>K</i>	log <i>K</i> [‡] ^{<i>a</i>}
13	[*] β _{1,1} (Pu(IV)) Pu ⁴⁺ + H ₂ O ↔ PuOH ³⁺ + H ⁺	0.6 ^{<i>b</i>}	
14	[*] β _{2,1} (Pu(IV)) Pu ⁴⁺ + 2H ₂ O ↔ Pu(OH) ₂ ²⁺ + 2H ⁺	0.6 ^{<i>b</i>}	
15	[*] β _{3,1} (Pu(IV)) Pu ⁴⁺ + 3H ₂ O ↔ Pu(OH) ₃ ⁺ + 3H ⁺	−2.3 ^{<i>b</i>}	
16	[*] β _{4,1} (Pu(IV)) Pu ⁴⁺ + 4H ₂ O ↔ Pu(OH) ₄ ⁰ + 4H ⁺	−8.5 ^{<i>b</i>}	
17	<i>K</i> _{SC5} ≡FeOH + Pu ⁴⁺ + 2H ₂ O ↔ ≡FeOHPu(OH) ₂ ²⁺ + 2H ⁺	4.95 ± 0.03 ^{<i>c</i>}	5.07
18	<i>K</i> _{SC6} ≡FeOH + Pu ⁴⁺ + 3H ₂ O ↔ ≡FeOHPu(OH) ₃ ⁺ + 3H ⁺	1.61 ± 0.14 ^{<i>c</i>}	1.73
19	<i>K</i> _{SC7} ≡FeOH + Pu ⁴⁺ + 4H ₂ O ↔ ≡FeOHPu(OH) ₄ ⁰ + 4H ⁺	−1.60 ± 0.07 ^{<i>c</i>}	−1.48

^{*a*} Referenced to the site occupancy standard state (Sverjensky, 2003), and calculated with the equation: $\log K^{\ddagger} = \log K + \log \frac{N_s A_s}{N^{\ddagger} A^{\ddagger}}$, where N^{\ddagger} and A^{\ddagger} are the theoretical site density (10×10^{18} sites m^{−2}) and surface area (10 m² g^{−1}) suggested by Sverjensky (2003).

^{*b*} From Guillaumont et al. (2003) for *I* = 0 M.

^{*c*} Calculated in this work using a single-site DLM and referenced to the 1.0 M standard state; *I* = 0.01 M NaCl.

3.2.3 Ability to Predict Pu(IV) Sorption at 25 °C from Th(IV) Data

As mentioned previously, it is possible that in the presence of hematite, Pu(IV) is the dominant surface species. Therefore, we also attempted to predict the Pu sorption behavior using only the best-fit SCM for Th(IV). When Pu(IV) hydrolysis products were excluded from the simulation (i.e., only Pu^{4+} was allowed), Pu sorption is over-predicted (Fig. 6). When both the free Pu^{4+} cation and the first Pu(IV) hydrolysis product, PuOH^{3+} , are allowed, Pu sorption is under-predicted, suggesting that Pu(IV) hydrolysis is more thermodynamically favored than a $\equiv\text{FeOHPu}^{4+}$ surface complex with a log K value equal to that for $\equiv\text{FeOHTh}^{4+}$. This is not surprising when considering the large difference in Pu(IV) and Th(IV) hydrolysis formation constants (Tables 1 and 3).

4. DISCUSSION

4.1 Comparison with Previous Studies

4.1.1 Np(V) Surface Complexation

Kohler et al. (1999) investigated Np(V) sorption onto hematite over a wide range of ionic strengths, pH, Np(V) concentrations, and CO_2 partial pressures. Similar to our data, the Np(V) sorption edge was observed at pH ~ 7 . Using the triple layer model (TLM) (Davis et al., 1978), which allows differentiation between inner- and outer-sphere surface species, Kohler et al. suggested that the inner-sphere surface complex, $\equiv\text{FeONpO}_2$, was dominant below pH 8 in the presence or absence of atmospheric CO_2 . Additionally, at higher Np(V) sorption densities, they noted that a second inner-sphere surface complex, $\equiv\text{FeOHNpO}_2^+$, was needed to accurately model their sorption data. The necessary inclusion of a second surface species only at higher loadings suggests Np(V) association with a second, less favorable, binding site. Similar to this finding, the best-fit SCM determined here suggested a speciation change at elevated

temperatures. Because the acid/base properties of hematite are temperature dependent, it is not clear if the speciation change calculated with our SCM is simply the result of charge compensation within the double layer, or if another phenomenon is responsible. However, we cannot exclude the possibility that Np(V) could favor alternative binding sites at elevated temperatures. Although, this would presumably also result in increased Np(V) sorption with increasing temperature, which was not observed (Fig. A1).

Wang et al. (2001) also used the DLM to describe Np(V) sorption onto ferrihydrite from sorption data previously published by Girvin et al. (1991). Although the Wang et al. (2001) model with ferrihydrite is not directly comparable to our model with hematite, we note that a similar surface complex, $\equiv\text{FeONpO}_2$, best described the Girvin et al. (1991) data. Additionally, even though the original ferrihydrite study was conducted at $I = 0.1 \text{ M NaNO}_3$, the $\log K$ (-2.72) calculated by Wang et al. (2001) is in good agreement with our value at 25 °C (Table 2). Wang et al. (2001) also modeled Np(V) sorption onto hematite, using data previously published by Nakayama and Sakamoto (1991). The modeling results from Wang et al. (2001) suggested that two surface complexes best described the Nakayama and Sakamoto data, $\equiv\text{FeOHNpO}_2^+$ and $(\equiv\text{FeO})_2\text{NpO}_2^-$. Attempts to fit our Np(V) sorption data using these two surface complexes gave poorer fits (i.e., larger WSOS/DF values) compared with our chosen SCM (Table 2) or no convergence of the optimization procedure (depending on temperature). However, a greater ratio of $[\text{Np(V)}]_{\text{TOT}}/[\equiv\text{FeOH}]_{\text{TOT}}$ in the Nakayama and Sakamoto (1991) study (0.35) compared with our study (0.0002) may have contributed to the different modeling results.

Our surface complexation modeling results are in fairly good agreement with the model proposed by Kohler et al. (1999) and the ferrihydrite model proposed by Wang et al. (2001). However, these models, including our own, suggest that Np(V) forms a monodentate complex

with the hematite surface. This is contradictory to the results from several spectroscopic studies. For example, Arai et al. (2007) investigated the interaction between Np(V) and hematite using extended X-ray absorption fine structure (EXAFS) spectroscopy and suggested that both outer-sphere and bidentate inner-sphere surface complexes are present in sorption samples at pH ~7 to 9. Using attenuated total reflectance fourier transform infrared spectroscopy (ATR FT-IR), Müller et al. (2009) suggested that Np(V) forms bidentate complexes on the surfaces of TiO₂, SiO₂, and ZnO₂ based on the large observed shift (~30 cm⁻¹) in the antisymmetric vibrational mode of the neptunyl ion. From ATR FT-IR and EXAFS studies, Gückel et al. (2013) also suggested the presence of bidentate inner-sphere complexes on the surface of gibbsite (Al(OH)₃). However, in each of these studies, higher pH, higher Np(V) surface loadings, and generally higher ionic strengths were used compared with this study.

4.1.2 Th(IV) Surface Complexation

Cromières et al. (1998) used the DLM to describe Th(IV) sorption onto hematite colloids over the pH range 2 to 10. Their results suggested that several surface complexes, which included $\equiv\text{FeOHTh}^{4+}$, $\equiv\text{FeOTh}(\text{OH})_2^+$, $\equiv\text{FeOTh}(\text{OH})_4^-$, were needed to model the sorption data over the full pH range. However, $\equiv\text{FeOHTh}^{4+}$ was the most important species at pH values similar to those studied here. Their calculated log *K* value for $\equiv\text{FeOHTh}^{4+}$ (18.7) is in good agreement with our log *K* value (19.03). Using the TLM, Murphy et al. (1999) also suggested that Th(IV) sorption onto hematite was best described using the inner-sphere surface complex, $\equiv\text{FeOHTh}^{4+}$. However, Rojo et al. (2009) suggested that Th(IV) sorption onto ferrihydrite and magnetite (Fe₃O₄) could be described equally well using either a bidentate surface complex, $(\equiv\text{FeO})_2\text{Th}^{2+}$, or a monodentate hydrolyzed surface species, $\equiv\text{FeOThOH}^{2+}$. Jakobsson (1999) modeled Th(IV) sorption onto TiO₂ over a wide range of Th(IV) concentrations using several different EDL

models. Although monodentate Th(IV) surface complexes described most of the lower concentration data adequately, Jakobsson suggested that the proton stoichiometry associated with Th(IV) sorption onto TiO₂ was sensitive to the surface site density. For example, when higher site densities were specified in FITEQL, a surface reaction with zero net proton release gave the best fit to the data. As the site density was decreased (equivalent to increasing Th(IV) surface loading), surface reactions with an increasing number of released protons were predicted. This finding is somewhat reverse to that of Kohler et al. (1999), where fewer protons were released at higher Np(V) sorption densities. However, it is clear from both of these studies that the sorbate concentration may significantly affect the reaction stoichiometry predicted with SCMs.

In contrast to our modeling results, EXAFS studies of Th(IV) sorption onto SiO₂ (Östhols et al., 1997), magnetite (Seco et al., 2009), and ferrihydrite (Seco et al., 2009) indicate that Th(IV) may form bidentate inner-sphere complexes on these surfaces. Similar to the case for Np(V), there are significant discrepancies between the Th(IV) surface complexes indicated by SCMs and spectroscopic studies, making it difficult to determine if the Th(IV) (or Np(V)) surface complexes we propose here are representative of the surface coordination.

4.1.3 Plutonium Sorption onto Hematite

Although it is not clear if sorption equilibrium was achieved in the Pu(IV) experiment, we were able to accurately fit the second sampling event sorption edge data using a combination of three hydrolyzed Pu(IV) surface complexes (Sec. 3.2.3). A similar approach was taken by Sanchez et al. (1985), who demonstrated increasingly better fits to their sorption data as hydrolyzed Pu(IV) surface complexes were incrementally added to the SCM. Recently, Herr (2013) re-modeled the Pu(IV) sorption data from Sanchez et al. (1985), and suggested that the data was best described

with the surface complexes $\equiv\text{FeOPuOH}^{2+}$ and $\equiv\text{FeOPu}(\text{OH})_3$. Not surprisingly, the results by Herr (2013) agree well with the expected aqueous Pu(IV) speciation over the studied pH range (Table 3).

As shown in Sec. 3.2.1, when Pu(IV) was reacted with hematite over the pH range ~1.5 to 5.5, some oxidation and potentially some reduction of Pu(IV) occurred. We proposed that these oxidation state changes were the cause of the significant data scatter and shallow sorption edges observed for Pu sorption at each temperature. However, similar behavior has not been observed when Pu(IV) was reacted with goethite (Sanchez et al., 1985) or hematite (Romanchuk et al., 2011). As mentioned previously, this Pu oxidation appears to be the result of the thermodynamic favorability of Pu(V) in the aqueous phase. In many cases, researchers have added Pu(IV) to water free of complexing agents and found that the aqueous phase is dominated by Pu(V) at equilibrium 149,150. Thus, in these studies, the longer equilibration periods used relative to previous work may allow for greater concentrations of aqueous Pu(V) to form. Previous studies examining Pu(V) reduction to Pu(IV) on hematite and goethite found that Pu remaining in the aqueous phase was always dominated by Pu(V). However, oxidation of Pu(IV) to Pu(V) is considered kinetically hindered because of the necessary formation of the trans-dioxo moiety of the plutonyl structure (Clark et al., 2011). Considering that Pu(IV) sorption should be comparatively fast (Romanchuk et al., 2011), it is surprising that Pu oxidation appears to have had such a large effect on the sorption of Pu(IV). We therefore propose that the low pH in our systems facilitates a relatively weak Pu-surface interaction allowing for greater mobility of the Pu(IV) ion on the surface, and thus greater potential for re-oxidation to and subsequent desorption of Pu(V). Therefore, this observation of Pu(IV) oxidation to Pu(V) may be due to the additional time allowed for the equilibration of our samples. To support this, the fraction of Pus

orbed in samples at the lowest pH values generally decreased between the first and the second sampling events (Fig. 4). Therefore, Pu may have sorbed to the hematite surface initially as Pu(IV), but then desorbed after ~1.5 weeks as Pu(V). Clearly, this behavior warrants further research. However, such an investigation is currently outside the scope of this work.

4.1.4 Using Th(IV) to Describe Pu(IV) Sorption onto Hematite

Because Pu is extremely redox sensitive, and because of the hazards imposed by and the regulatory limits of working with Pu, it is very appealing to use stable oxidation state analogs to study plutonium chemistry. However, comparisons between analog sorption behavior and Pu sorption behavior are few. Banik et al. (2009) observed relatively little difference between Pu(IV) and Th(IV) uptake on kaolinite in relation to the percent sorption of each actinide. However, the Pu(IV) concentration in their experiment was 10^4 times greater than the Th(IV) concentration, suggesting that Th(IV) behavior actually is not comparable with Pu(IV). Similarly, we observed poor agreement with the Pu sorption predicted when a Th(IV) SCM was employed. These results are not surprising, considering that several researchers have already suggested that Th(IV) is not an adequate analog for Pu(IV) (Choppin, 1999; Wilson, 2011) due to the larger ionic radius of Th(IV) compared with Pu(IV) (1.048 vs. 0.962 Å) (Shannon, 1976), which makes Th(IV) significantly “softer” than Pu(IV).

4.3 Thermodynamic Interpretation

As mentioned previously, our primary objective in this paper is to relate the thermodynamics of Np(V), Th(IV), and Pu(IV) sorption onto hematite with sorption mechanisms and changes in actinide hydration. We have previously demonstrated a correlation between the enthalpy and entropy of Eu(III) and U(VI) sorption onto hematite and the extent of Eu(III) or U(VI)

dehydration upon sorption. We would like to do the same here; however, the spectroscopic data for adsorbed Np(V) and Th(IV) are not consistent with our SCMs or the SCMs developed from other similar batch sorption experiments (see Sec. 4.1). These inconsistencies may be due to differences in experimental conditions between studies. For example, we previously noted that nearly all Np(V) spectroscopic studies were performed at ionic strengths greater than the ionic strength used for our experiments. Lützenkirchen (1997) suggested that high ionic strengths may effectively shield highly charged surface species, perhaps leading to greater surface stability or different sorption mechanisms. Therefore, we will use a different approach toward understanding the thermodynamics and mechanisms of Np(V), Th(IV), and Pu(IV) sorption onto hematite.

If we consider that the formation of inner-sphere surface complexes will perturb the hydration sphere of the actinide in question, we can perhaps infer some binding mechanisms from the calculated thermodynamic parameters listed in Table 5. Because actinide dehydration is both an entropically favorable and endothermic reaction, we would expect inner-sphere surface complexation to result in positive entropy and enthalpy changes, as we previously observed for Eu(III) and U(VI). Only considering the 25 °C surface complexation reaction for Np(V) sorption onto hematite, we in fact calculate a negative entropy change (Table 5). Combined with the apparent sorption enthalpy of $\sim 0 \text{ kJ mol}^{-1}$, the thermodynamics suggest that there may be a greater contribution from outer-sphere Np(V) surface species than inner-sphere Np(V) surface species in our batch sorption data. This is despite our ability to model the Np(V) sorption data with the DLM, which assumes all surface species are inner-sphere complexes, and despite the spectroscopic literature which indicate mostly inner-sphere Np(V) surface complexation (albeit under very different experimental conditions). Furthermore, the presence of a significant

contribution of outer-sphere species may also explain the significant amount of scatter observed in the Np(V) sorption data (Fig. 1). For Th(IV) sorption onto hematite, the story is similar, however, the rather large entropy value (Table 5) suggests that some dehydration occurs upon sorption. However, because the calculation of sorption entropies are quite dependent on the SCM employed (Estes et al., 2013), and because the hydration entropies of the different actinides vary significantly, one cannot assume from the entropy value that only inner-sphere complexation occurs for Th(IV). If only inner-sphere complexation were present, a larger positive enthalpy should also be determined. Therefore, we propose that Th(IV) sorption onto hematite should also be described with a combination of outer-sphere and inner-sphere surface complexes. Considering the strong sorption of Th(IV) at low pH values where there is a large net positive surface charge, formation of outer sphere surface complexes is a reasonable conceptual model.

Because we could not develop SCMs for Pu(IV) sorption onto hematite at all temperatures, we were unable to extrapolate any thermodynamic parameters using the van't Hoff analysis. However, plots of K_d values as a function of inverse temperature (see Fig. A4) indicate that sorption increased with increasing temperature (i.e., the reaction is endothermic), as previously indicated based on Fig. A3 which illustrates Pu(IV) sorption as a function of " $\text{pH} - \frac{1}{2}\text{p}K_w$." These findings suggest that Pu(IV) sorption onto hematite occurs predominantly via an inner-sphere mechanism, although outer-sphere complexation cannot be excluded. The observed differences between Th(IV) and Pu(IV) data are likely due to the stronger affinity of Pu(IV) for both hydrolysis and sorption to metal oxide minerals. Thus, the stronger interactions are likely a greater indication of the formation of inner-sphere surface complexes.

Table 5. Calculated Thermodynamic Parameters for Np(V), Th(IV), and Pu(IV) Sorption onto Hematite.^a

<i>i</i>	reaction	$\Delta_r G_i^b$ (kJ mol ⁻¹)	$\Delta_r H_i$ (kJ mol ⁻¹)	$\Delta_r S_i^c$ (J mol ⁻¹ K ⁻¹)
9	K_{SC1} $\equiv\text{FeOH} + \text{NpO}_2^+ \leftrightarrow \equiv\text{FeONpO}_2 + \text{H}^+$	+16.8	~0	-56.4
11	K_{SC3} $\equiv\text{FeOH} + \text{Th}^{4+} \leftrightarrow \equiv\text{FeOHTh}^{4+}$	-108	~0	+364
17	K_{SC5} $\equiv\text{FeOH} + \text{Pu}^{4+} + 2\text{H}_2\text{O} \leftrightarrow \equiv\text{FeOHPu}(\text{OH})_2^{2+} + 2\text{H}^+$	-28.2	—	—
18	K_{SC6} $\equiv\text{FeOH} + \text{Pu}^{4+} + 3\text{H}_2\text{O} \leftrightarrow \equiv\text{FeOHPu}(\text{OH})_3^+ + 3\text{H}^+$	-9.2	—	—
19	K_{SC7} $\equiv\text{FeOH} + \text{Pu}^{4+} + 4\text{H}_2\text{O} \leftrightarrow \equiv\text{FeOHPu}(\text{OH})_4^0 + 4\text{H}^+$	+9.1	—	—

^a All values are for 25 °C and *I* = 0.01 M NaCl.

^b Calculated from: $\Delta_r G_i = -RT \cdot \ln K$, where *T* is 298.15 K.

^c Calculated from: $\Delta_r G_i = \Delta_r H_i - T\Delta_r S_i$, where *T* is 298.15 K.

5. CONCLUSIONS

Additional research is clearly needed to understand Np(V), Th(IV), and Pu(IV) sorption onto hematite over a wider range of experimental conditions, particularly with respect to surface speciation at both low and high actinide concentrations. However, under the conditions studied, the data and analyses given above support the following conclusions:

(1) Np(V) and Th(IV) sorption onto hematite are temperature independent;

- (2) Np(V) and Th(IV) sorption onto hematite may occur via both outer- and inner-sphere complexation mechanisms, with outer-sphere complex formation dominating Np(V) sorption;
- (3) Assuming sorption equilibrium was achieved, Pu sorption onto hematite increases with increasing temperature, indicating the formation of inner-sphere surface complexes;
- (4) Pu(IV) sorption onto hematite cannot be predicted using Th(IV) sorption data.

ACKNOWLEDGEMENTS

This research was supported by the U.S. Department of Energy Office of Biological and Environmental Research through the Nuclear Energy University Partnership Program (project number 11-3180) and the Subsurface Biogeochemical Research Program (project number DE-SC0004883).

APPENDIX A. SUPPLEMENTARY DATA

Th(IV) sorption as a function of “ $\text{pH} - \frac{1}{2}\text{pK}_w$ ” and temperature (Fig. A1); Pu(IV) sorption as a function of “ $\text{pH} - \frac{1}{2}\text{pK}_w$ ” and temperature (Fig. A2); aqueous phase Pu oxidation state distribution for batch systems with $\text{Pu}_T = (2.00 \pm 0.01) \times 10^{-9} \text{ M}$ (Fig. A3); and Pu distribution coefficients (K_d) at several pH values as a function of inverse temperature (Fig. A2).

Supplementary data associated with this article can be found, in the online version, at DOI.

REFERENCES

- Almazan-Torres M. G., Drot R., Mercier-Bion F., Catalette H., Den Auwer C. and Simoni E. (2008) Surface complexation modeling of uranium(VI) sorbed onto zirconium oxophosphate versus temperature: Thermodynamic and structural approaches. *J. Colloid Interface Sci.* **323**, 42–51.

- Angove M. J., Johnson B. B. and Wells J. D. (1998) The Influence of Temperature on the Adsorption of Cadmium(II) and Cobalt(II) on Kaolinite. *J. Colloid Interface Sci.* **204**, 93–103.
- Anon (2002) *Yucca Mountain Science and Engineering Report, Rev. 1.*, U.S. Department of Energy, Office of Civilian Radioactive Waste Management, North Las Vegas, NV.
- Arai Y., Moran P. B., Honeyman B. D. and Davis J. A. (2007) In Situ Spectroscopic Evidence for Neptunium(V)-Carbonate Inner-Sphere and Outer-Sphere Ternary Surface Complexes on Hematite Surfaces. *Environ. Sci. Technol.* **41**, 3940–3944.
- Bandura A. V. and Lvov S. N. (2006) The Ionization Constant of Water over Wide Ranges of Temperature and Density. *J. Phys. Chem. Ref. Data* **35**, 15–30.
- Banik N. L., Buda R. A., Bürger S., Kratz J. V. and Trautmann N. (2009) Sorption of tetravalent plutonium and humic substances onto kaolinite. *Radiochim. Acta* **95**, 569–575.
- Bauer A., Rabung T., Claret F., Schäfer T., Buckau G. and Fanghänel T. (2005) Influence of temperature on sorption of europium onto smectite: The role of organic contaminants. *Appl. Clay Sci.* **30**, 1–10.
- Choppin G. R. (1999) Utility of Oxidation State Analogs in the Study of Plutonium Behavior. *Radiochim. Acta* **85**, 89–95.
- Choppin G. R. and Rao L. F. (1984) Complexation of Pentavalent and Hexavalent Actinides by Fluoride. *Radiochim. Acta* **37**, 143–146.
- Clark D. L., Hecker S. S., Jarvinen G. D. and Neu M. P. (2011) Plutonium. In *The Chemistry of the Actinide and Transactinide Elements* (eds. L. R. Morss, N. M. Edelstein, and J. Fuger). Springer, Dordrecht, The Netherlands. pp. 813–1264. Available at: http://link.springer.com/chapter/10.1007/978-94-007-0211-0_7 [Accessed October 29, 2014].
- Cromières L., Moulin V., Fourest B., Guillaumont R. and Giffaut E. (1998) Sorption of Thorium onto Hematite Colloids. *Radiochim. Acta* **82**, 249–256.
- Davis J. A., James R. O. and Leckie J. O. (1978) Surface Ionization and Complexation at the Oxide/Water Interface. I. Computation of Electrical Double-Layer Properties in Simple Electrolytes. *J. Colloid Interface Sci.* **63**, 480–499.
- Dzombak D. and Morel F. M. M. (1990) *Surface complexation modeling: Hydrous ferric oxide.*, Wiley, New York, NY.
- Estes S. L., Arai Y., Becker U., Fernando S., Yuan K., Ewing R. C., Zhang J., Shibata T. and Powell B. A. (2013) A self-consistent model describing the thermodynamics of Eu(III) adsorption onto hematite. *Geochim. Cosmochim. Acta* **122**, 430–447.

- Girvin D. C., Ames L., Schwab A. P. and McGarrah J. E. (1991) Neptunium Adsorption on Synthetic Amorphous Iron Oxyhydroxide. *J. Colloid Interface Sci.* **141**, 67–78.
- Gückel K., Rossberg A., Müller K., Brendler V., Bernhard G. and Foerstendorf H. (2013) Spectroscopic Identification of Binary and Ternary Surface Complexes of Np(V) on Gibbsite. *Environ. Sci. Technol.* **47**, 14418–14425.
- Guillaumont R., Fanghanel T., Neck V., Fuger J., Palmer D. A., Grenthe I. and Rand M. H. (2003) *Update on the chemical thermodynamics of uranium, neptunium, plutonium, americium and technetium*. eds. F. J. Mompean, M. Illemassène, C. Domenech-Orti, and K. BEN SAID, Elsevier, New York, NY.
- Haynes W. M. ed. (2013) Standard Density of Water. In *CRC Handbook of Chemistry and Physics* CRC Press/Taylor and Francis, Boca Raton, FL. pp. 6–7 – 6–8.
- Herbelin A. and Westall J. C. (1999) *FITEQL. A computer program for the determination of chemical equilibrium constants from experimental data.*, Department of Chemistry, Oregon State University, Corvallis, OR, USA.
- Herr S. M. (2013) Describing Plutonium Contamination Issues in Hanford Soils: Development of a Thermodynamic Surface Complexation Model. Master of Science Thesis, Clemson University.
- Hixon A. E., Arai Y. and Powell B. A. (2013) Examination of the effect of alpha radiolysis on plutonium(V) sorption to quartz using multiple plutonium isotopes. *J. Colloid Interface Sci.* **403**, 105–112.
- Jakobsson A.-M. (1999) Measurement and Modeling of Th Sorption onto TiO₂. *J. Colloid Interface Sci.* **220**, 367–373.
- Keeney-Kennicutt W. L. and Morse J. W. (1985) The redox chemistry of Pu(V)O₂⁺ interaction with common mineral surfaces in dilute solutions and seawater. *Geochim. Cosmochim. Acta* **49**, 2577–2588.
- Kersting A. B. (2013) Plutonium Transport in the Environment. *Inorg. Chem.* **52**, 3533–3546.
- Kersting A. B., Efurud D. W., Finnegan D. L., Rokop D. J., Smith D. K. and Thompson J. L. (1999) Migration of plutonium in ground water at the Nevada Test Site. *Nature* **397**, 56–59.
- Kobashi A., Choppin G. and Morse J. (1988) A study of techniques for separating plutonium in different oxidation states. *Radiochim. Acta* **43**, 211–215.
- Kohler M., Honeyman B. D. and Leckie J. O. (1999) Neptunium(V) sorption on hematite (α -Fe₂O₃) in aqueous suspension: The effect of CO₂. *Radiochim. Acta* **85**, 33–48.
- Langmuir D. (1997) *Aqueous Environmental Geochemistry.*, Prentice Hall, Upper Saddle River, NJ.

- Lu N., Reimus P. W., Parker G. R., Conca J. L. and Triay I. R. (2003) Sorption kinetics and impact of temperature, ionic strength and colloid concentration on the adsorption of plutonium-239 by inorganic colloids. *Radiochim. Acta* **91**, 713–720.
- Lützenkirchen J. (1997) Ionic Strength Effects on Cation Sorption to Oxides: Macroscopic Observations and Their Significance in Microscopic Interpretation. *J. Colloid Interface Sci.* **195**, 149–155.
- Müller K., Foerstendorf H., Brendler V. and Bernhard G. (2009) Sorption of Np(V) onto TiO₂, SiO₂, and ZnO: An in Situ ATR FT-IR Spectroscopic Study. *Environ. Sci. Technol.* **43**, 7665–7670.
- Murphy R. J., Lenhart J. J. and Honeyman B. D. (1999) The sorption of thorium (IV) and uranium (VI) to hematite in the presence of natural organic matter. *Colloids Surf. Physicochem. Eng. Asp.* **157**, 47–62.
- Nakayama S. and Sakamoto Y. (1991) Sorption of Neptunium on Naturally-Occurring Iron-Containing Minerals. *Radiochim. Acta* **52/53**, 153–157.
- Neu M. P., Hoffman D. C., Roberts K. E., Nitsche H. and Silva R. J. (1994) Comparison of Chemical Extractions and Laser Photoacoustic Spectroscopy for the Determination of Plutonium Species in Near-Neutral Carbonate Solutions. *Radiochim. Acta* **66/67**, 251–258.
- Novikov A. P., Kalmykov S. N., Utsunomiya S., Ewing R. C., Horreard F., Merkulov A., Clark S. B., Tkachev V. V. and Myasoedov B. F. (2006) Colloid Transport of Plutonium in the Far-Field of the Mayak Production Association, Russia. *Science* **314**, 638–641.
- Östhols E., Manceau A., Farges F. and Charlet L. (1997) Adsorption of Thorium on Amorphous Silica: An EXAFS Study. *J. Colloid Interface Sci.* **194**, 10–21.
- Powell B. A., Fjeld R. A., Kaplan D. I., Coates J. T. and Serkiz S. M. (2005) Pu(V)O₂⁺ Adsorption and Reduction by Synthetic Hematite and Goethite. *Environ. Sci. Technol.* **39**, 2107–2114.
- Rand M., Fuger J., Grenthe I., Neck V. and Rai D. (2007) *Chemical Thermodynamics of Thorium*. eds. F. J. Mompean, J. Perrone, and M. Illemassène, OECD Nuclear Energy Agency, Issy-les-Moulineaux, France.
- Rao L., Srinivasan T. G., Garnov A. Y., Zanonato P., Di Bernardo P. and Bismondo A. (2004) Hydrolysis of neptunium(V) at variable temperatures (10–85°C). *Geochim. Cosmochim. Acta* **68**, 4821–4830.
- Ridley M. K., Hiemstra T., Machesky M. L., Wesolowski D. J. and van Riemsdijk W. H. (2012) Surface speciation of yttrium and neodymium sorbed on rutile: Interpretations using the charge distribution model. *Geochim. Cosmochim. Acta* **95**, 227–240.
- Ridley M. K., Machesky M. L., Wesolowski D. J. and Palmer D. A. (2005) Surface complexation of neodymium at the rutile-water interface: A potentiometric and modeling study in NaCl media to 250°C. *Geochim. Cosmochim. Acta* **69**, 63–81.

- Riley R. G. and Zachara J. M. (1992) *Chemical contaminants on DOE lands and selection of contaminant mixtures for subsurface science research.*, Pacific Northwest Laboratory, Richland, WA.
- Rodda D. P., Johnson B. B. and Wells J. D. (1996) Modeling the Effect of Temperature on Adsorption of Lead(II) and Zinc(II) onto Goethite at Constant pH. *J. Colloid Interface Sci.* **184**, 365–377.
- Rojo I., Seco F., Rovira M., Giménez J., Cervantes G., Martí V. and de Pablo J. (2009) Thorium sorption onto magnetite and ferrihydrite in acidic conditions. *J. Nucl. Mater.* **385**, 474–478.
- Romanchuk A. Y., Kalmykov S. N. and Aliev R. A. (2011) Plutonium sorption onto hematite colloids at femto- and nanomolar concentrations. *Radiochim. Acta* **99**, 137–144.
- Sanchez A. L., Murray J. W. and Sibley T. H. (1985) The adsorption of plutonium IV and V on goethite. *Geochim. Cosmochim. Acta* **49**, 2297–2307.
- Santschi P. H., Roberts K. A. and Guo L. (2002) Organic Nature of Colloidal Actinides Transported in Surface Water Environments. *Environ. Sci. Technol.* **36**, 3711–3719.
- Schmidt M., Lee S. S., Wilson R. E., Soderholm L. and Fenter P. (2012) Sorption of tetravalent thorium on muscovite. *Geochim. Cosmochim. Acta* **88**, 66–76.
- Seco F., Hennig C., Pablo J. de, Rovira M., Rojo I., Martí V., Giménez J., Duro L., Grivé M. and Bruno J. (2009) Sorption of Th(IV) onto Iron Corrosion Products: EXAFS Study. *Environ. Sci. Technol.* **43**, 2825–2830.
- Shannon R. D. (1976) Revised effective ionic radii and systematic studies of interatomic distances in halides and chalcogenides. *Acta Crystallogr.* **A32**, 751–767.
- Sverjensky D. A. (2003) Standard states for the activities of mineral surface sites and species. *Geochim. Cosmochim. Acta* **67**, 17–28.
- Tertre E., Berger G., Simoni E., Castet S., Giffaut E., Loubet M. and Catalette H. (2006) Europium retention onto clay minerals from 25 to 150 °C: Experimental measurements, spectroscopic features and sorption modelling. *Geochim. Cosmochim. Acta* **70**, 4563–4578.
- Teterin A. Y., Maslakov K. I., Teterin Y. A., Kalmykov S. N., Ivanov K. E., Vukcevic L., Khasanova A. B. and Shcherbina N. S. (2006) Interaction of neptunyl with goethite (α -FeOOH), maghemite (γ -Fe₂O₃), and hematite (α -Fe₂O₃) in water as probed by X-ray photoelectron spectroscopy. *Russ. J. Inorg. Chem.* **51**, 1937–1944.
- Wang P., Anderko A. and Turner D. R. (2001) Thermodynamic Modeling of the Adsorption of Radionuclides on Selected Minerals. I: Cations. *Ind. Eng. Chem. Res.* **40**, 4428–4443.
- Wang Z. and Giammar D. E. (2013) Mass Action Expressions for Bidentate Adsorption in Surface Complexation Modeling: Theory and Practice. *Environ. Sci. Technol.* **47**, 3982–3996.

Wilson R. E. (2011) Structural Periodicity in Plutonium(IV) Sulfates. *Inorg. Chem.* **50**, 5663–5670.

**APPENDIX C: REPORT FOR MILESTONE: M3NU-11-SC-CU__-0204-026: X-RAY
ABSORPTION SPECTROSCOPIC CHARACTERIZATION OF ACTINIDE SPECIATION AT
HEMATITE:WATER AND MONTMORILLONITE:WATER INTERFACES**

XAS Studies of Actinide Sorption to Hematite and Montmorillonite

Daniel Olive, Deborah Wang, Ken Gregorich, Heino Nitsche
Department of Chemistry, University of California-Berkeley

Brian A. Powell
Environmental Engineering and Earth Sciences, Clemson University

DOE NEUP Project: Quantification of cation sorption to engineered barrier materials under extreme conditions (Project #11-3180)

Report in fulfillment of Milestone: M3NU-11-SC-CU__-0204-026: X-ray absorption spectroscopic characterization of actinide speciation at hematite:water and montmorillonite:water interfaces

I. Introduction

The fate and transport of neptunium in the environment is an important issue for nuclear waste management and remediation efforts. Reliable performance assessments depend on accurate geochemical models, which in turn depends on reliable input parameters. Np(V), found in oxidizing conditions, is expected to be the largest contribution for the spread of Np, as compared to the more reduced forms, i.e. Np(III)/Np(IV), and so here we have focused on the measurements of Np in that oxidation state. Hematite is expected to play an important role both as an engineered barrier as iron corrosion product from waste drums, as well as constituting a large portion of the mineral content in many soils. Clay materials, such as montmorillonite, will likewise be used for repository backfill, also account for a large fraction of many soils. Batch sorption experiments are useful for determining the relationship between variables such as pH, ionic strength, and temperature on the sorption behavior of cations to mineral surfaces, however, discovering the underlying physical mechanism responsible for those changes can be difficult. X-ray absorption spectroscopy (XAS) experiments have the ability to determine oxidation state and local geometry, and have the benefits of being element specific, and not requiring long-range order. Here we combine batch sorption studies and XAS experiments to study the properties of Np(V) sorbed onto hematite and montmorillonite surfaces.

II. Methods

For the montmorillonite XAS experiments, a stock solution of ^{237}Np was prepared using an ion-exchange column (BioRad AG 1-X4, 50-100 mesh) and verified to be Np(V) based on optical absorption spectroscopy. Background ionic strength, μ , was adjusted with sodium perchlorate. A high ionic strength sample, with $\mu = 0.9 \pm 0.1 \text{ M}$, and a low ionic strength sample, with $\mu = 0.008 \pm 0.002 \text{ M}$, were prepared by adding 25 mg of montmorillonite and 2 ml of sodium perchlorate solution in an acid-washed polypropylene tube. Portions of the stock were added to samples to result in 2.54 mM Np(V) , and the pH adjusted to 8.0 ± 0.2 .

Preparations were carried out in a similar fashion for the hematite EXAFS samples. For the initial run of room temperature experiments four samples were prepared, with ionic strengths of $\mu = 0.001 \pm 0.002 \text{ M}$, $\mu = 0.01 \pm 0.02 \text{ M}$, $\mu = 0.1 \pm 0.1 \text{ M}$, and $\mu = 1.0 \pm 0.1 \text{ M}$, by adding 50 mg of hematite and 4 mL of sodium perchlorate solution in an acid-washed polypropylene tube. Portions of the stock were added to samples to result in 4.11 mM Np(V) , and the pH adjusted to $\text{pH} = 6.0 \pm 0.2$. After commissioning the high-temperature rocker another set of hematite samples was prepared, in room temperature/75 °C pairs, in NaClO_4 with $\mu = 0.01 \pm 0.02 \text{ M}$ and $\mu = 1.0 \pm 0.1 \text{ M}$, and in NaCl with $\mu = 1.0 \pm 0.1 \text{ M}$. A final set of hematite samples was prepared with ionic strengths of $\mu = 0.01 \pm 0.02 \text{ M}$, $\mu = 1.0 \pm 0.1 \text{ M}$ with seven day contact times, compared to four days for the first high-temperature samples.

X-ray absorption spectroscopy experiments were performed at beamline 11-2 at the Stanford Synchrotron Radiation Lightsource (SSRL) at SLAC (Stanford, CA). The storage ring was operated in top-up, maintaining a current of 495—500 mA of 3.0 GeV electrons. A wiggler is used to produce polychromatic X-rays, and wavelength was selected using a Si(220) double crystal monochromator. Higher harmonics were removed by applying a 30% detuning to the second crystal. The energy was calibrated to the Zr K-edge, 17997.6 eV [1], of a Zr foil run in transmission geometry with incident and transmitted X-ray flux monitored by ionization chambers using 100% N_2 fill gas. The Np samples were measured in fluorescence geometry using a 100-element Ge detector (Canberra). Samples were triply contained in nesting aluminum holders with Kapton windows and indium wire seals, and were placed in a liquid helium cryostat (Janus). All of the samples were run at approximately 30 K to mitigate the risk of beam induced chemical changes during the experiment.

EXAFS data was analyzed according to the standard EXAFS analysis procedures [2], [3] data reduction including alignment, summation, calibration, and error correction was done using Athena [4] and SixPack [5]. Spectral fitting to determine structural parameters was performed using Artemis [4] with theoretical EXAFS paths created with FEFF6 [6–9]. Uncertainties of the fitting parameters were determined by inversion of the covariance matrix [10] unless otherwise indicated.

III. Results and Discussion

A. Hematite

The normalized absorption edge spectra for the four hematite samples are shown in figure 1. Also plotted is the absorption edge of a NpO_2 sample, which is used as a Np(IV) standard. The absorption edge energies of the Np(V) samples, as determined by the peak of the first derivative

of the normalized absorption spectrum, are shifted higher than the Np(IV) spectrum by 0.8-1.4 eV, which is consistent with a higher oxidation state. The peak positions, as measured by the white line maximum are also shifted slightly higher, between 0.2 and 0.7 eV, compared to the Np(IV) standard. These parameters are listed in table 1. Also of note is the presence of the neptunyl shoulder in the samples, characteristic of the presence of short axial Np-O bonds found in oxidized Np.

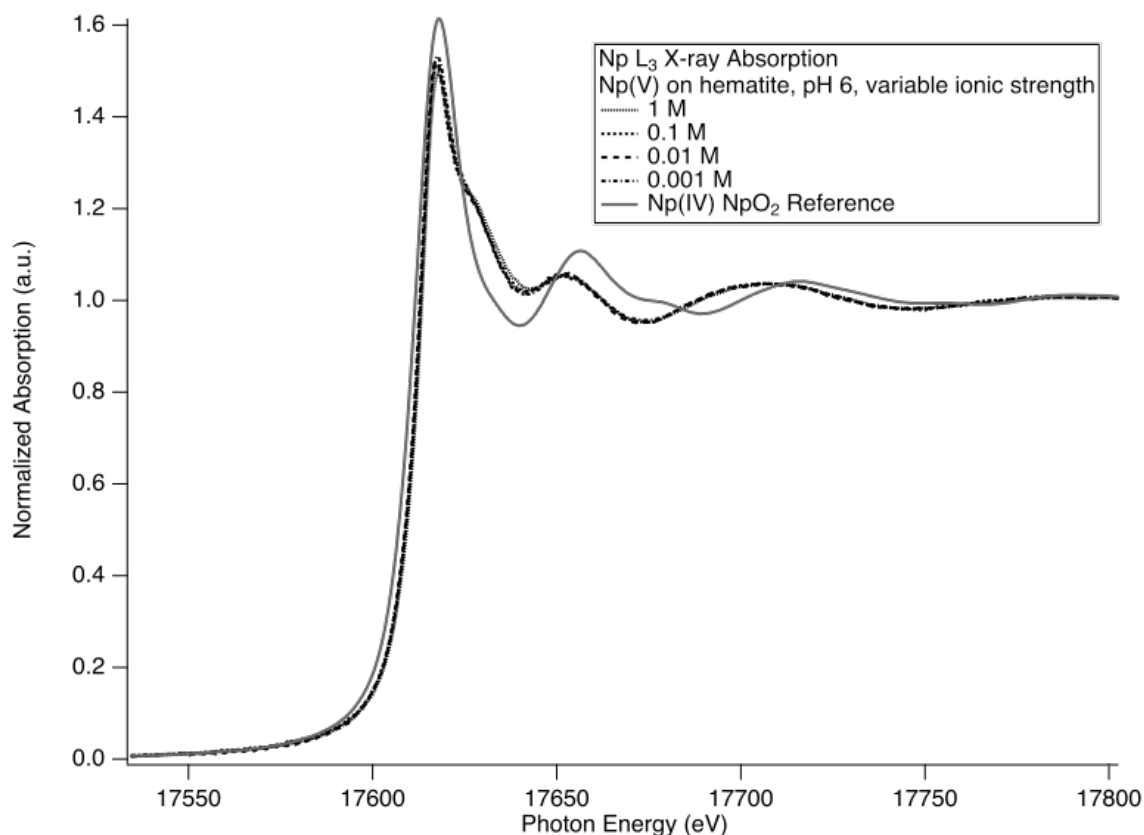


Figure 1. XANES spectra of the Np(V) sorbed to hematite at pH 6 at different ionic strengths. All four samples show remarkably similar spectra in the XANES region, and include a characteristic neptunyl shoulder found around 17625 eV. A Np(IV) reference spectrum of NpO₂ is also shown as a comparison.

Table 1. XANES parameters for Np(V) sorbed to hematite, figure 1, at pH 6 at different ionic strengths. The edge position as determined using the first derivative and location of the white line maximum are indicated.

Sample	Edge Energy, eV	Peak Position, eV
1 M	17613.8 ± 0.5	17617.8 ± 0.5
0.1 M	17613.3 ± 0.5	17617.3 ± 0.5
0.01 M	17613.2 ± 0.5	17617.3 ± 0.5

0.001 M	17613.8 ± 0.5	17617.6 ± 0.5
NpO ₂	17612.4 ± 0.5	17618.0 ± 0.5

The extracted EXAFS are shown for the four samples in figure 2. Some of the samples were sensitive to monochromator glitches higher in k-space, but otherwise overlap quite well. Fourier transforming the EXAFS, figure 3, the axial and radial oxygen scattering shells are visible at 1.5 and 2.0 (not corrected for phase shift) Å in the plot. Little structure at higher R values is evident, suggesting there is no evidence for bulk-like precipitates which would exhibit Np-Np scattering at higher R values, or other neighbors at regular distances common to the Np in the sample. This is consistent with an outer sphere sorption mechanism.

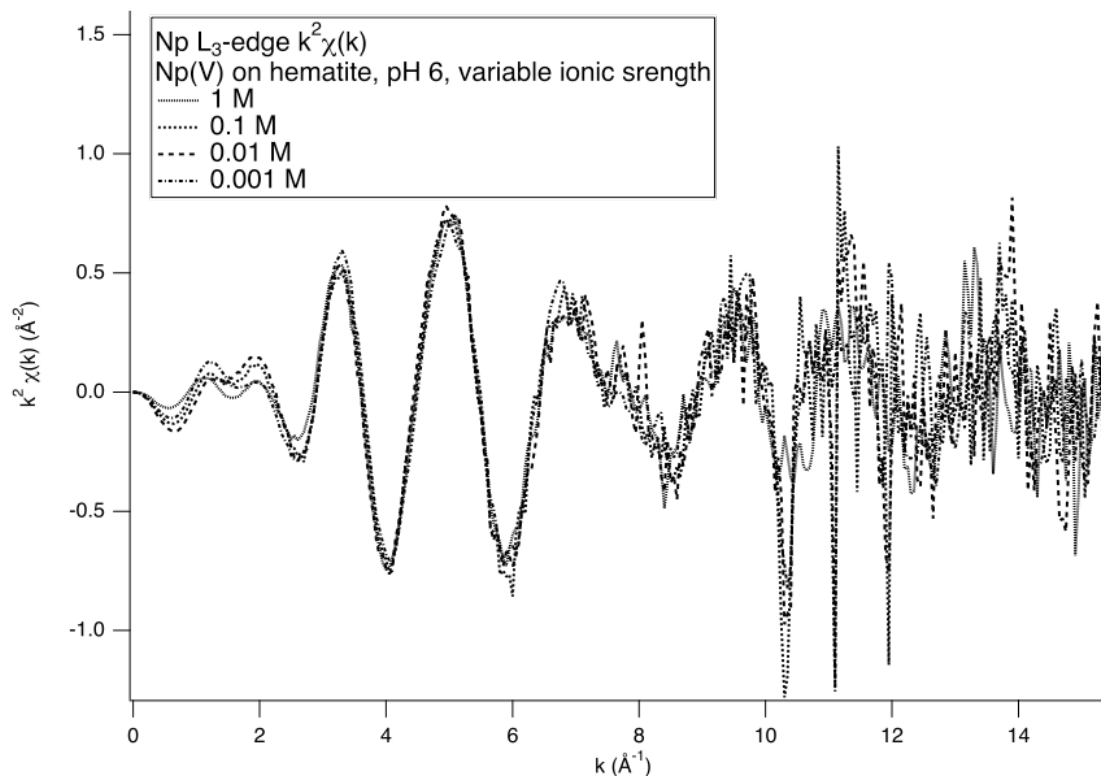


Figure 2. EXAFS spectra of the Np(V) sorbed to hematite at pH 6 at different ionic strengths. The three lowest ionic strength samples show glitches between $k = 10$ and $k = 12 \text{ Å}^{-1}$, but otherwise the spectra are similar.

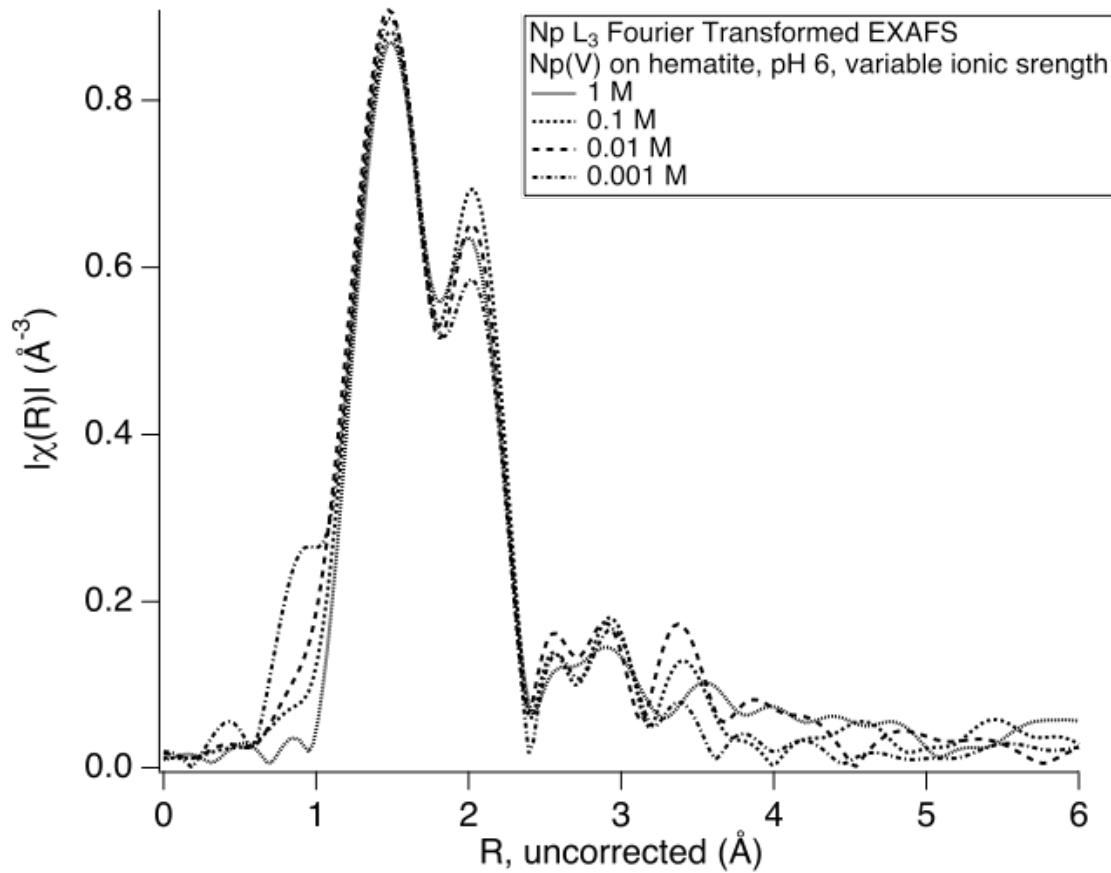


Figure 3. Fourier transform of the EXAFS spectra of the Np(V) sorbed to hematite at pH 6 at different ionic strengths. Strong scattering contributions can be seen from the axial and radial oxygen atoms.

Fitting of the EXAFS equation [3], [11],

$$\chi(k) = \sum_i \frac{N_i S_0^2 F_i(k)}{k R_i^2} \sin(2k R_i + \phi_i(k)) e^{(-2\sigma_i^2 k^2)} e^{\frac{-2R_i}{\lambda(k)}} \quad (1)$$

to the measured $\chi(k)$ involved performing a non-linear least-squares fit summing over each scattering path used, i , in order to find the best values for the amplitude of each path, N_i , scattering half-path length, R_i , energy shift, ΔE_0 , and mean squared displacement, σ_i^2 , also known as the EXAFS Debye-Waller factor. The values for the effective scattering amplitude, $F_i(k)$, effective scattering phase shift, $\phi_i(k)$, and mean free path, $\lambda(k)$, were taken from the FEFF6 calculations.

Fitting of the EXAFS data was performed using the structure for Np_2O_5 [12] as the basis for setting up the geometry of the two axial and five radial oxygen single scattering paths. Two

oxygen single scattering paths at a distance of 1.86 Å and 5 oxygen single scattering paths at a distance of 2.41 Å were used as the initial model. In the fitting model the number of axial oxygen atoms was set to two, as those bonds in Np(V) are not easily changed. To allow for the possibility that slight changes in the radial oxygen peaks seen in figure 3 are real and not within experimental variation, those amplitudes were allowed to float in the fitting process. Since the amplitude and EXAFS Debye-Waller factors are highly correlated, all four data sets were refined simultaneously in ARTEMIS using the same σ^2 , ΔR , E_0 values, while the radial oxygen amplitudes were allowed to float. Fitting results are summarized in table 2.

Table 2. Fitting results for the simultaneous fit of the four Np(V) hematite data sets, uncertainties determined by inversion of the covariance matrix.

Fitting Variable	Value
Energy shift (E_0), eV	-1.9 ± 1.1
Axial oxygen distance, Å	1.86 ± 0.00
Axial oxygen σ^2 , Å ²	0.0009 ± 0.0005
Radial oxygen distance, Å	2.42 ± 0.01
Radial oxygen σ^2 , Å ²	0.0093 ± 0.0021
1 M radial oxygen amplitude	6.0 ± 0.9
0.1 M radial oxygen amplitude	5.6 ± 1.0
0.01 M radial oxygen amplitude	5.5 ± 1.0
0.001 M radial oxygen amplitude	5.8 ± 0.9

As a confirmation that the differences in the spectra are within experimental noise, a Monte-Carlo technique [13] was used to estimate how uncertainties in the measured EXAFS signal change the Fourier transform. An estimate of noise in the summed k-space spectra was established, and multiple spectra were generated based on the averaged spectra but with representative noise added in. A sample of generated spectra plotted along with the scan average is shown in figure 3. A script was used to repeatedly generate four experimental spectra with noise added, perform the IFEFFIT fitting, and save the results. The mean and standard deviation of each of the fitting parameters was then determined. The results from the Monte-Carlo analysis were, within uncertainty, in agreement with the traditional IFEFFIT results.

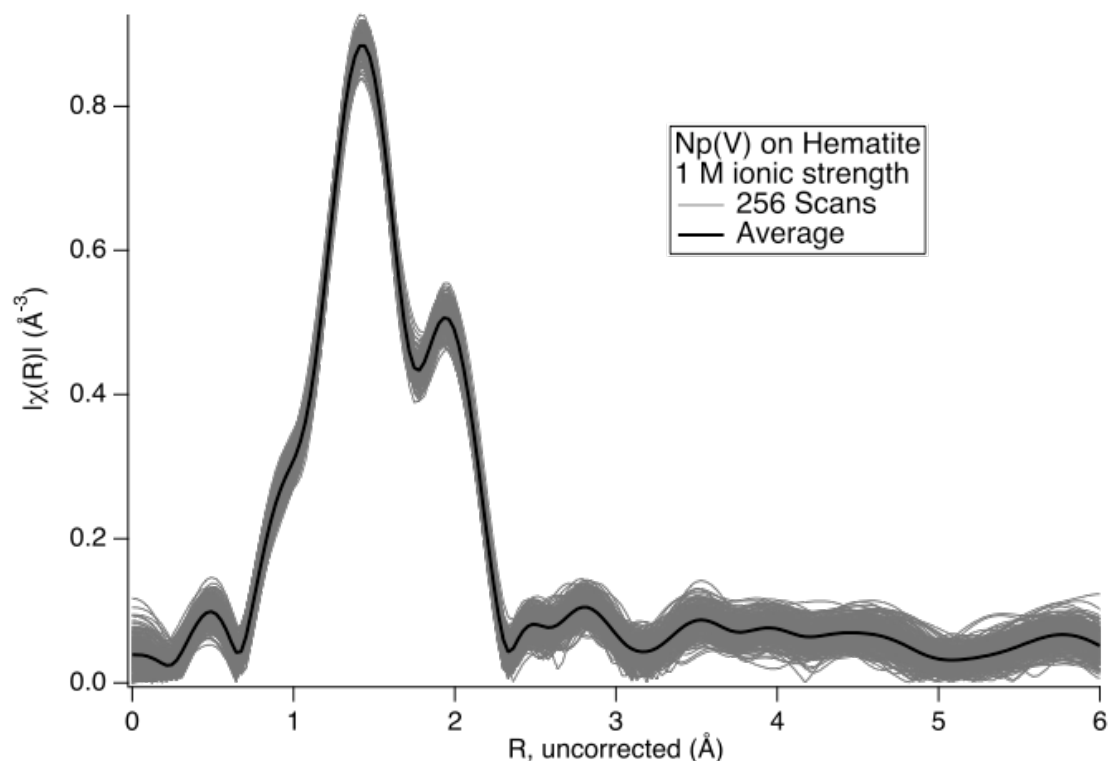


Figure 4. The 1 M background ionic strength Np(V) on hematite data shown with 256 overlaid spectra generated by the Monte-Carlo error analysis technique.

After commissioning the high-temperature incubating rocker another set of batch sorption experiments was prepared. Room temperature and 75 °C pairs of high and low ionic strength NaClO₄, as well as high ionic strength NaCl matrices were studied. All of the samples showed sorption as Np(V), without reduction or precipitation. The absorption spectra of all six samples were quite similar, figure 5, as were the Fourier-transformed EXAFS, figure 6, suggesting little difference in sorption mechanism between complexing and non-complexing media at room and high temperatures.

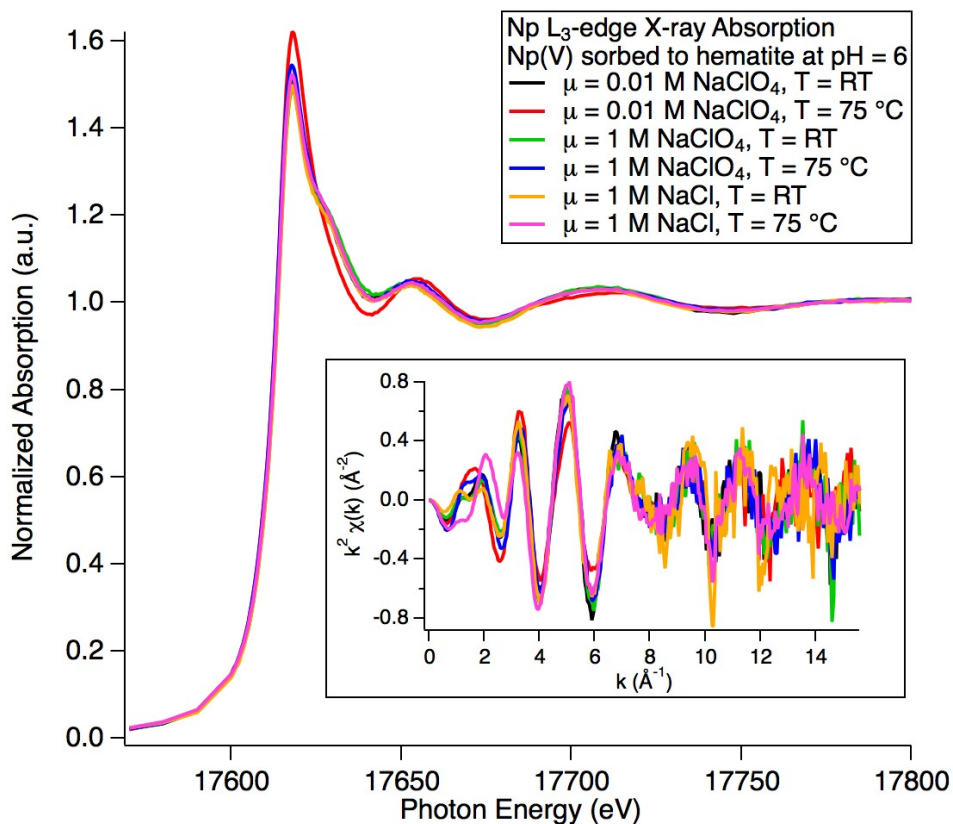


Figure 5. XANES spectra of the Np(V) sorbed to hematite at pH 6 at different ionic strengths at room and elevated temperatures. The samples show similar spectra in the XANES region, and include a characteristic neptunyl shoulder. EXAFS oscillations (inset) are shown in momentum space.

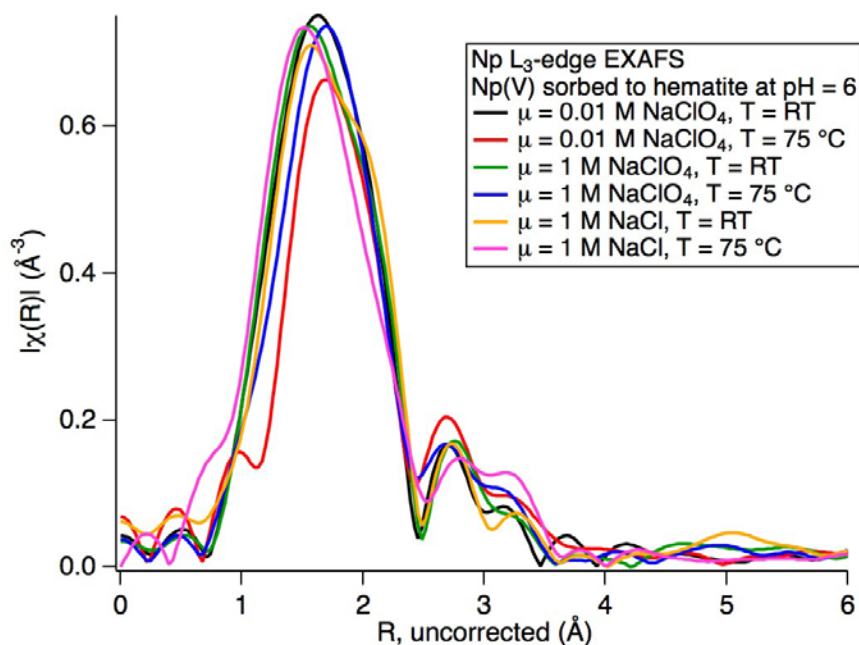


Figure 6. Fourier-transformed EXAFS from the initial set of high temperature comparison experiments. All samples showed similar coordination environment independent of sorption conditions.

Although similar, the low ionic strength high temperature NaClO_4 sample exhibited the greatest variation compared to the other samples. Another batch of sorption samples was prepared with longer contact time, seven days instead of four, and higher quality data was taken using the $\phi = 90^\circ$ monochromator crystal set to avoid crystal glitches (instead of the $\phi = 0^\circ$) and with increased data acquisition time to improve the signal to noise ratio. Although technical problems precluded satisfactory measurement on the low ionic strength/low temperature NaClO_4 sample, high quality data was collected on the remaining three combinations, figure 7. Fitting results, table 3, show no statistically different results between the high and low temperature sorption samples, suggesting no change in the apparent outer-sphere sorption mechanism at work in the room temperature samples.

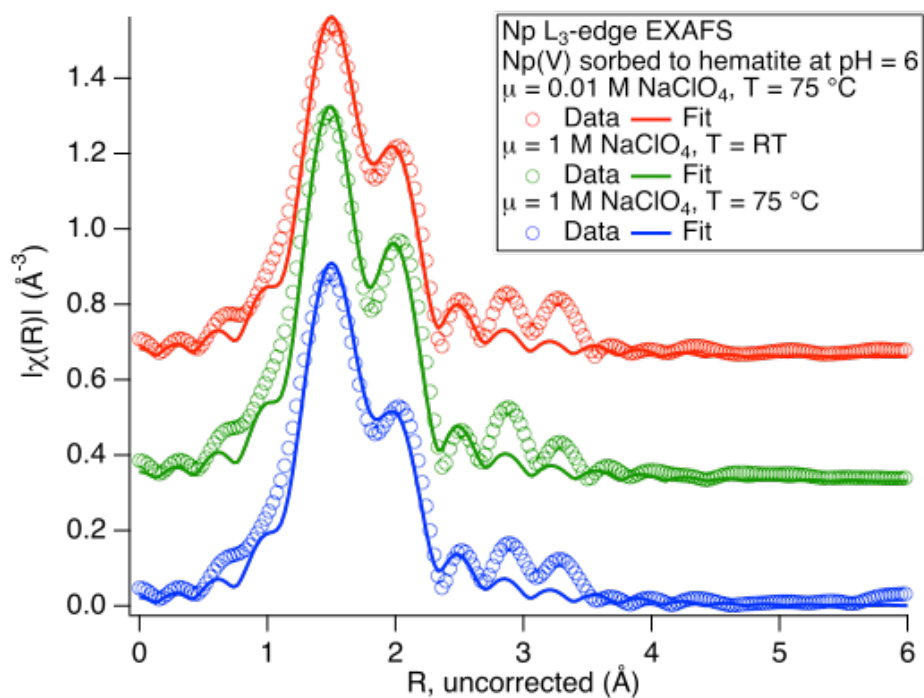


Figure 7. Fourier-transformed EXAFS of the room and high temperature sorption experiments, repeated with higher quality. The data and best-fit models of the inner oxygen shells are shown for each set, offset for clarity.

Table 3. Fitting results for the Np(V) hematite data sets shown in Fig. 7, uncertainties determined by inversion of the covariance matrix. There were 12 independent points, and 7 variables in each fit.

Parameter	$\mu = 0.01 \text{ M}$, $T = 75 \text{ }^{\circ}\text{C}$	$\mu = 0.01 \text{ M}$, $T = \text{RT}$	$\mu = 0.01 \text{ M}$, $T = 75 \text{ }^{\circ}\text{C}$
Energy shift (E_0), eV	8.3 ± 1.9	9.4 ± 2.2	8.5 ± 2.2
Axial oxygen amplitude	1.9 ± 0.3	2.0 ± 0.3	2.0 ± 0.3
Axial oxygen distance, Å	1.88 ± 0.01	1.88 ± 0.01	1.88 ± 0.01
Axial oxygen σ^2 , Å ²	0.0004 ± 0.0015	0.0002 ± 0.0010	0.0008 ± 0.0018
Radial oxygen amplitude	5.0 ± 0.9	4.7 ± 1.0	5.3 ± 1.2
Radial oxygen distance, Å	2.45 ± 0.02	2.47 ± 0.02	2.45 ± 0.03
Radial oxygen σ^2 , Å ²	0.0078 ± 0.0029	0.0066 ± 0.0034	0.0098 ± 0.0040
Goodness-of-fit, R-factor	0.011	0.015	0.014

B. Montmorillonite

The normalized absorption edge spectra for the two montmorillonite samples are shown in figure 8, and XANES parameters are listed in table 4. Also plotted is the absorption edge of the NpO₂ sample, which is used as a Np(IV) standard. The absorption edge energies of the Np(V) samples, are shifted higher than the Np(IV) spectrum by 0.7 eV, which is consistent with a higher oxidation state. The peak positions, as measured by the white line maximum are slightly lower, between 1.4 and 1.8 eV, compared to the Np(IV) standard, and between 0.7 and 1.6 eV compared to the hematite samples. Although not a large difference, it could be indicative of a slightly different bonding environment. However, the presence of the neptunyl shoulder in the samples, characteristic of the presence of short axial Np-O bonds found in oxidized Np, would preclude reduction of the Np.

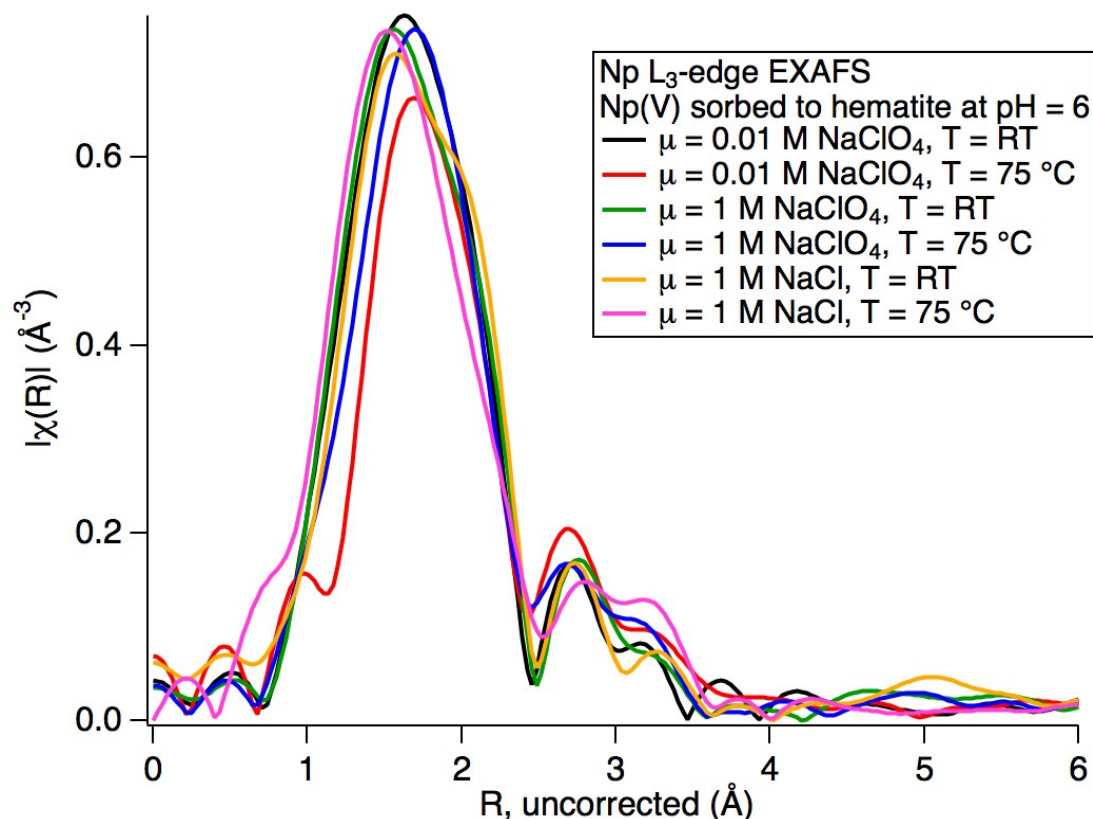


Figure 8. XANES spectra of the Np(V) sorbed to montmorillonite at pH 8 at high and low ionic strengths. Both samples show remarkably similar spectra in the XANES region, and include a characteristic neptunyl shoulder found around 17625 eV. A Np(IV) reference spectrum of NpO₂ is also shown as a comparison.

Table 4. XANES parameters for Np(V) sorbed to montmorillonite, figure 8, at pH 8 at different ionic strengths. The edge position as determined using the first derivative and location of the white line maximum are indicated.

Sample	Edge Energy, eV	Peak Position, eV
0.8M	17613.1 ± 0.5	17616.2 ± 0.5
0.009 M	17613.1 ± 0.5	17616.6 ± 0.5
NpO ₂	17612.4 ± 0.5	17618.0 ± 0.5

The extracted EXAFS are shown for the two montmorillonite samples in figure 9, along with that of the Np(IV) standard. The spectra of the two samples overlap well over the entire k-space region, and are distinct from the NpO₂ standard. Fourier transforming the EXAFS, figure 10, the

axial and radial oxygen scattering shells are visible at 1.5 and 2.0 (not corrected for phase shift) Å in the plot, just as in the hematite samples. There is some additional structure, the largest peak at 4.2 (uncorrected) Å, and little else at higher R values.

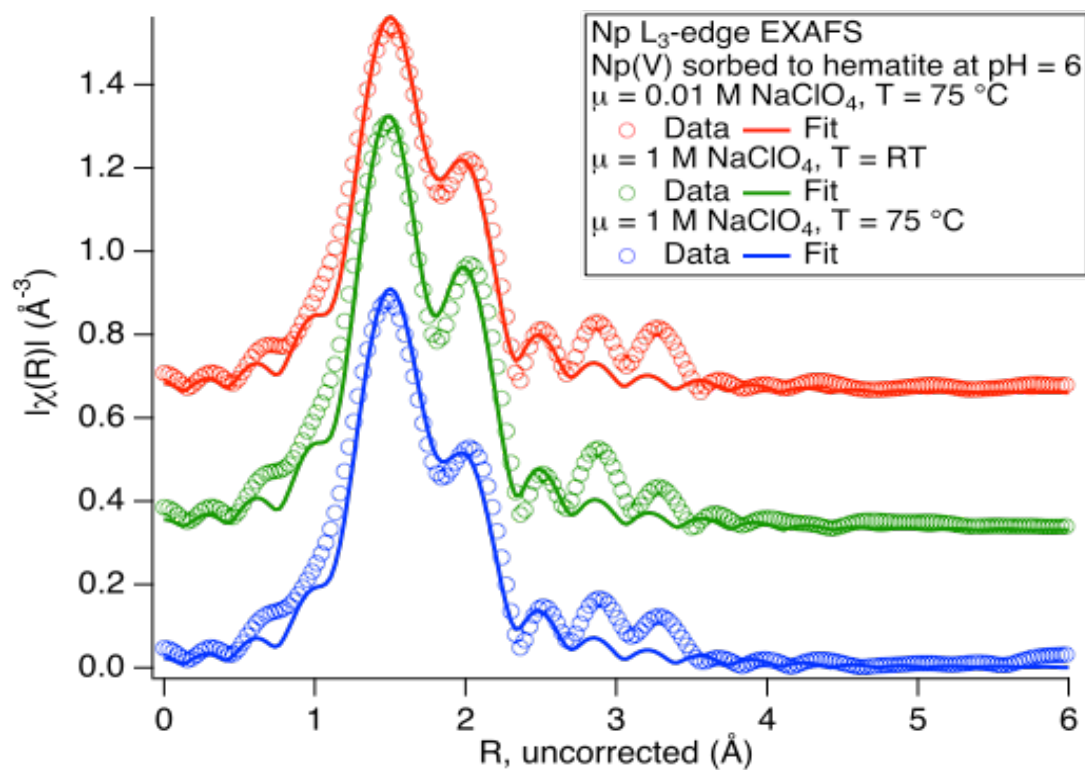


Figure 9. EXAFS spectra of the Np(V) sorbed to montmorillonite at pH 8 at high and low ionic strengths, as well as the EXAFS from the NpO₂ reference.

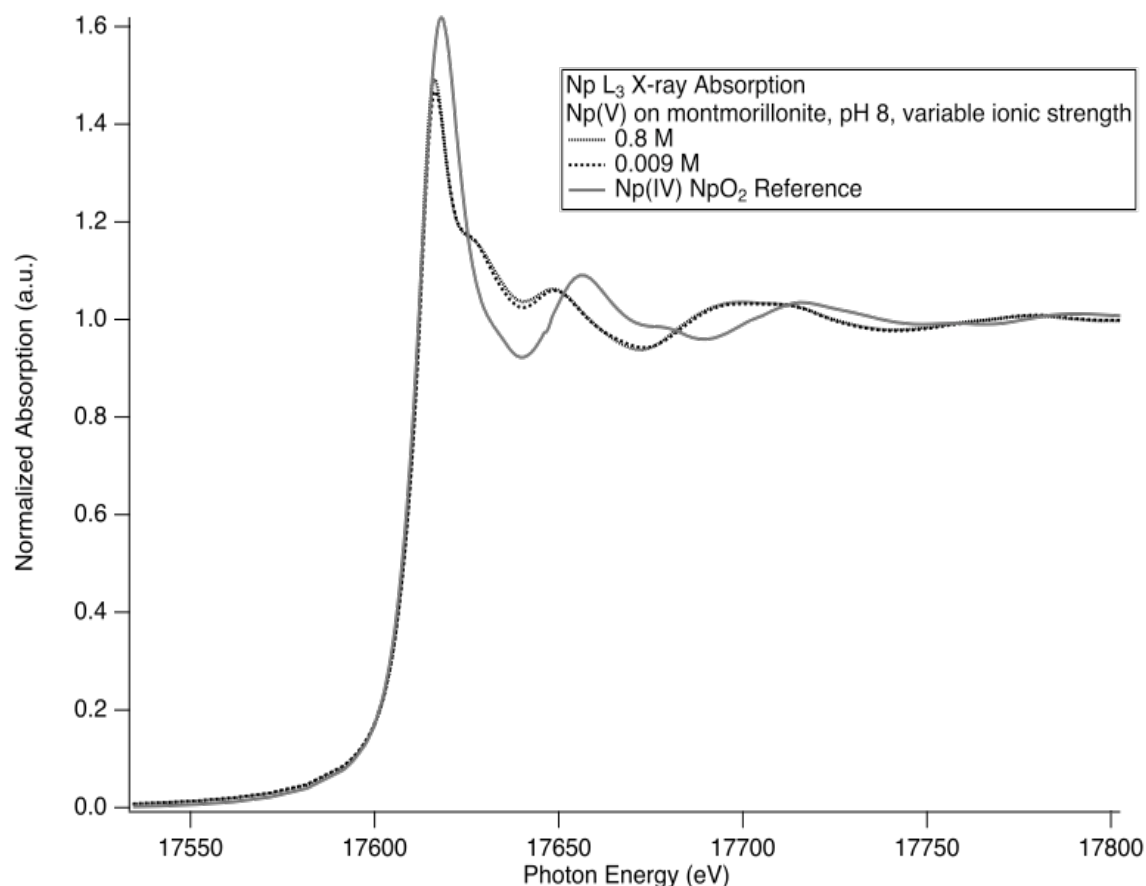


Figure 10. Fourier transform of the EXAFS spectra of the Np(V) sorbed to montmorillonite at pH 8 at high and low ionic strengths. Strong scattering contributions can be seen from the axial and radial oxygen atoms. The Fourier transform is also shown for the NpO_2 reference, which shows scattering characteristic of a single oxygen coordination sphere, and Np-Np scattering at $R = 3.76 \text{ \AA}$.

Comparing the Np(V) samples to the Np(IV) reference in figure 10, there is no evidence of Np-Np scattering at $3.75 \text{ uncorrected \AA}$, which we might expect if there had been any precipitation of NpO_2 . To check for the possibility that the feature at 4.2 \AA is a result of a Np_2O_5 precipitate, additional fitting paths from the model were tested, including Np-Np single scattering at $R = 3.62 \text{ \AA}$ and at $R = 4.2 \text{ \AA}$ corresponding to higher coordination shells. However, the fitting would not converge on physical values. Several other single scattering paths were tested including oxygen, magnesium, aluminum, silicon, and iron. In no case could a single scattering path be made to fit that feature. It is possible that more than one scattering atom type or geometry could be contributing to that peak, however, without additional information over-parameterization might lead to a meaningless fit. It should be noted that the feature has the same amplitude in both samples, thus it does not appear to change as a function of background ionic strength. Proceeding in the same manner as the hematite samples, an example fit of the low ionic strength montmorillonite data using the first two oxygen paths is shown in figure 11. The best fit values of the fitting parameters for both samples are shown in table 5.

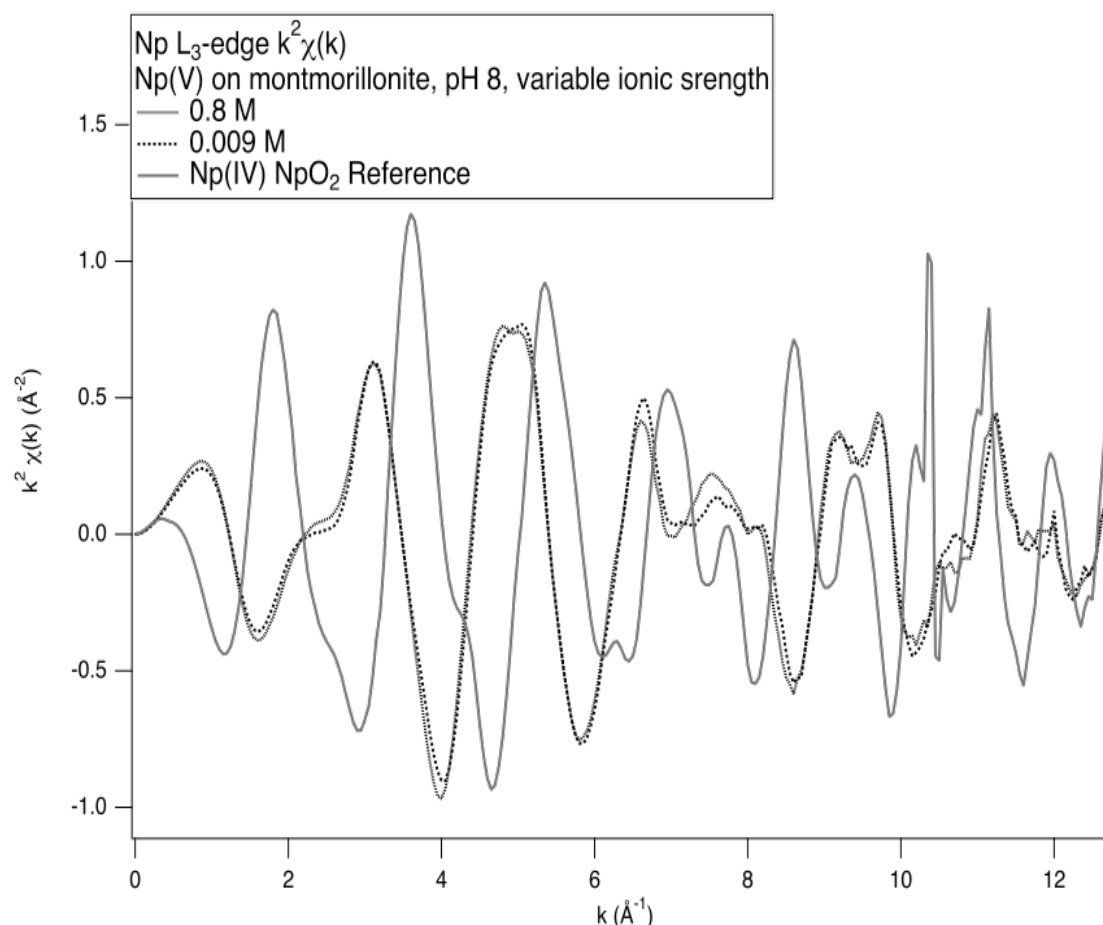


Figure 11. The magnitude and imaginary components of the EXAFS fitting of the Np(V) sorbed to montmorillonite at pH 8 at low ionic strength. The data and fit are shown, along with the axial and radial oxygen single scattering paths that make up the fit.

Table 5. Fitting results for the two Np(V) montmorillonite data sets, uncertainties determined by inversion of the covariance matrix. There were 14.27 independent points, and 7 variables in each fit.

Parameter	0.8 M data	0.009 M data
Energy shift (E_0), eV	8.1 ± 1.3	8.3 ± 1.7
Axial oxygen amplitude	2.1 ± 0.3	2.1 ± 0.2
Axial oxygen distance, Å	1.86 ± 0.01	1.87 ± 0.01
Axial oxygen σ^2 , Å ²	0.0004 ± 0.0012	0.0006 ± 0.0011
Radial oxygen amplitude	4.4 ± 0.7	4.4 ± 0.6
Radial oxygen distance, Å	2.51 ± 0.01	2.50 ± 0.01
Radial oxygen σ^2 , Å ²	0.0019 ± 0.0017	0.0016 ± 0.0014
Goodness-of-fit, R-factor	0.0285	0.0259

IV. Conclusions

X-ray absorption spectroscopy studies on Np(V) sorbed onto hematite and montmorillonite showed essentially no variation with ionic strength, temperature, or NaClO₄ vs NaCl media, suggesting outer-sphere complexation. In all cases the Np remained in the (+V) oxidation state. The Np-hematite samples showed little scattering beyond the first oxygen shells indicating the absence of neptunium oxide precipitation or regular structure much beyond the first surrounding oxygen atoms. Although the Np-montmorillonite samples did show some evidence of scattering beyond the first oxygen atoms, that feature could not be fit using only a single scattering path. However, we were able to exclude precipitation of either NpO₂ or Np₂O₅ as the cause of the feature.

Acknowledgements

Use of the Stanford Synchrotron Radiation Lightsource, SLAC National Accelerator Laboratory, is supported by the U.S. Department of Energy, Office of Science, Office of Basic Energy Sciences under Contract No. DE-AC02-76SF00515. The SSRL Structural Molecular Biology Program is supported by the DOE Office of Biological and Environmental Research, and by the National Institutes of Health, National Institute of General Medical Sciences (including P41GM103393). The contents of this publication are solely the responsibility of the authors and do not necessarily represent the official views of NIGMS or NIH.

- [1] J. A. Bearden and A. F. Burr, "Reevaluation of X-ray atomic energy levels," *Reviews of Modern Physics*, vol. 39, no. 1, p. 125, 1967.
- [2] J. J. Rehr and R. C. Albers, "Theoretical approaches to x-ray absorption fine structure," *Reviews of modern physics*, vol. 72, no. 3, pp. 621–654, 2000.
- [3] D. C. Koningsberger and R. Prins, Eds., *X-ray absorption: principles, applications, techniques of EXAFS, SEXAFS and XANES*. John Wiley and Sons Inc., New York, NY, 1988.
- [4] B. Ravel and M. Newville, "ATHENA, ARTEMIS, HEPHAESTUS: data analysis for X-ray absorption spectroscopy using IFEFFIT," *Journal of Synchrotron Radiation*, vol. 12, no. 4, pp. 537–541, 2005.
- [5] S. M. Webb, "SIXPACK: a graphical user interface for XAS analysis using IFEFFIT," *Physica Scripta*, vol. 115, pp. 1011–1014, 2005.
- [6] J. de Leon, J. J. Rehr, S. I. Zabinsky, and R. C. Albers, "Ab initio curved-wave x-ray-absorption fine structure," *Physical Review B*, vol. 44, no. 9, pp. 4146–4156, 1991.
- [7] J. J. Rehr and R. C. Albers, "Scattering-matrix formulation of curved-wave multiple-scattering theory: Application to x-ray-absorption fine structure," *Physical Review B*, vol. 41, no. 12, pp. 8139–8149, 1990.
- [8] J. J. Rehr, J. de Leon, S. I. Zabinsky, and R. C. Albers, "Theoretical X-ray absorption fine structure standards," *Journal of the American Chemical Society*, vol. 113, no. 14, pp. 5135–5140, 1991.

- [9] J. J. Rehr, R. C. Albers, and S. I. Zabinsky, "High-Order Multiple-Scattering Calculations of X-Ray-Absorption Fine Structure," *Physical Review Letters*, vol. 69, no. 23, pp. 3397–3400, 1992.
- [10] M. Newville, "EXAFS analysis using FEFF and FEFFIT," *Journal of synchrotron radiation*, vol. 8, no. 2, pp. 96–100, 2001.
- [11] G. Bunker, *Introduction to XAFS: A Practical Guide to X-Ray Absorption Fine Structure Spectroscopy*. Cambridge University Press Cambridge, UK, 2010.
- [12] T. Z. Forbes, P. C. Burns, S. Skanthakumar, and L. Soderholm, "Synthesis, structure, and magnetism of Np_2O_5 ," *Journal of the American Chemical Society*, vol. 129, no. 10, pp. 2760–2761, 2007.
- [13] P. J. Ellis and H. C. Freeman, "XFIT-an Interactive EXAFS Analysis Program," *Journal of Synchrotron Radiation*, vol. 2, no. 4, pp. 190–195, 1995.

APPENDIX D: MILESTONE: M2NU-11-SC-CU__0204-028: EXAMINATION OF ACTINIDE SORPTION TO MONTMORILLONITE AT VARIABLE TEMPERATURES AND VARIABLE IONIC STRENGTHS.

Reports contained within this appendix.

- Powell, B. A., Baldwin, J., Black, E. M., DeMille, R., Waterhouse, T., “Examination of actinide sorption to montmorillonite as a function of temperature and ionic strength.
- Olive, D. T., Wang, D. L., Baldwin, J., Black, E. M., DeMille, R., Waterhouse, T., Powell, B. A. “Examination of neptunium sorption to montmorillonite as a function of temperature and ionic strength”

Examination of actinide sorption to montmorillonite as a function of temperature and ionic strength

Brian A. Powell, Jonathan Baldwin, Erin M. Black, Richard DeMille, and Tyler Waterhouse

Environmental Engineering and Earth Sciences, Clemson University

DOE NEUP Project: Quantification of cation sorption to engineered barrier materials under extreme conditions (Project #11-3180)

Report in fulfillment of Milestone: M2NU-11-SC-CU__-0204-028: Examination of actinide sorption to montmorillonite at variable temperatures and variable ionic strengths.

I. Introduction

Understanding sorption of actinide elements to clay minerals is a necessary component of a nuclear waste repository performance assessment. Interactions of actinide elements with clay minerals has been studied extensively under standard conditions but little data exist at elevated temperatures. For example, thermodynamic constants for U(VI) hydrolysis are provided in Appendix A and show that increasing temperature has a profound influence on U(VI) speciation. In most cases hydrolysis of uranium is an entropically driven reaction [1]. This work centers on a similar hypothesis that strong sorption of actinide ions to metal oxide minerals is due to positive entropies which are mechanistically driven by displacement of hydrating waters from the actinides¹ and mineral surfaces upon sorption. Furthermore, few experiments have been performed examining the influence of ionic strength. In this work, sorption of Eu(III), Th(IV), Np(V), U(VI) to SWy-2 montmorillonite is examined as a function of pH in 0.01 M NaCl and 1.0 M NaCl. Experiments were conducted at 25 °C, 50 °C, and 80 °C to examine the influence of temperature.

II. Methods

Sorption of Eu(III), Th(IV), Np(V), and U(VI) to montmorillonite was examined in batch sorption experiments as a function of temperature and ionic strength. Samples were prepared following a matrix of temperature (25 °C, 50 °C, and 80 °C) and ionic strength (0.01 M NaCl and 1.0 M NaCl). All

¹In this work the generic term “actinides” is used for convenience despite studies with the lanthanide Eu(III). Eu(III) is used as an oxidation state analog of Am(III) and Cm(III).

experiments were run with a constant montmorillonite concentration of 1 g/L using SWy-2 montmorillonite from the Clay Minerals Society. Sorption experiments were conducted by preparing clay mineral suspensions in either 1.0 M or 0.01 M NaCl at the desired pH values in polypropylene vials. All additions of the montmorillonite stock or NaCl electrolyte were determined gravimetrically. Each vial was then spiked with $^{151/153}\text{Eu(III)}$, $^{232}\text{Th(IV)}$, or $^{238}\text{U(VI)}$ at 10 ppb ($\mu\text{g/L}$) or $^{237}\text{Np(V)}$ at 1 ppb ($\mu\text{g/L}$). The Eu(III), Th(IV), and U(VI) working solutions used for the spike were obtained as NIST traceable standards in 2% HNO_3 from High Purity Standards (Charleston, SC). The same standards were used to prepare calibration standards for Inductively Coupled Plasma Mass Spectrometric (ICP-MS) analysis. The $^{237}\text{Np(V)}$ working solution was prepared by dilution of 5 mL of a $1\mu\text{Ci/mL}$ ^{237}Np stock in 4M HNO_3 obtained from Eckert and Zeigler Isotope Products (Valencia, CA) into water to produce a 1 mM $^{237}\text{Np(V)}$ working solution. The pentavalent state of Np(V) was verified spectrophotometrically. This solution was further diluted in ultrapure water ($>18.2\text{ M}\Omega\cdot\text{cm}$) to prepare a 1000 $\mu\text{g/L}$ working solution. In all cases the volume of the working solution addition was 100 μL or less and determined gravimetrically. Thus, the addition of the working solution did not change the ionic strength and the concentration can be exactly determined using the known concentration of the stock solution and the total mass of the sample.

The spiked suspensions were mixed in a shaking incubator at 25 °C (VWR Shaking Incubator) for 7 days. Then a 1.3 mL aliquot of the suspension was transferred to a 2mL polypropylene centrifuge vial and centrifuged 20 minutes at 8000 rpm. This centrifugation time was estimated to remove particles greater than 100 nm from solution assuming spherical particles as calculated using Stokes law. A 1.0 mL aliquot of the supernatant was transferred to a 15mL polypropylene tube and diluted with 9 mL 2% HNO_3 (Aristar plus, VWR) for subsequent ICPMS analysis. The pH of the primary suspension was measured using a temperature compensated Thermo Ross electrode calibrated with pH 4.0, 7.0, and 10.0 buffer solutions. If needed, the pH of the suspensions was adjusted with small amounts of 0.01 or 0.10 M HCl or NaOH. After this sampling protocol was completed, the samples were returned to the incubating shaker for an additional 7 days. After the additional days of mixing, the suspensions were sampled a second time, and equilibrium was assumed if there were no significant differences between measured Eu(III), Th(IV), Np(V), or U(VI) concentrations for the two sampling events. If equilibrium was not achieved, the suspensions were mixed for an additional 2 – 4 days, and then sampled again. Once equilibrium was achieved (within three sampling events for all temperatures), the reaction temperature was increased to 50 °C and the sampling protocol was continued as described above. After equilibrium was reached at 50 °C, the samples were transferred to a VWR shaking water bath held at 80 °C for equilibration. Again the sampling protocol described above with multiple sampling events to ensure equilibrium had been reached

was followed. All ICPMS samples were analyzed on a Thermo X Series II quadrupole ICPMS using ^{242}Pu as an internal reference standard.

III. Results and Discussion

General Considerations

As shown in Figures 1 and 2, sorption of Eu(III), Th(IV), Np(V), and U(VI) to montmorillonite increased with the trend:

$$\text{Th(IV)} > \text{Eu(III)} \sim \text{U(VI)} > \text{Np(V)}.$$

These trends are consistent with the frequently observed relationship between sorption and complexation strength with effective charge of the ions [2, 3]. The effective charges of Th(IV), U(VI), Eu(III), and Np(V) are 4+, 3.2+, 3+, and 2.2+, respectively [2-6].

shown in the sorption edge plots in Figure 1. Generally, sorption of Eu(III), Th(IV), Np(V), and U(VI) increased with increasing temperature. This is consistent with the overarching hypothesis that sorption increases with temperature due to displacement of solvating waters of the cations and the mineral surfaces. This removal of ordered water from the cation to bulk disordered water results in an entropically favorable reaction. There are notable exceptions to this behavior which are discussed in detail below.

Uranium sorption to montmorillonite

Sorption of uranium to montmorillonite (Figures 1 and 2) exhibits the expected trends of uranium sorption to metal oxide phases in which sorption increases with increasing pH up until a pH of approximately 6. Within this pH range of 3 to 6 uranium is predominantly the oxyanion UO_2^{2+} and exhibits increasing sorption as the surface charge of the montmorillonite edge sites transitions from a net positive to a net negative surface charge. Above pH 6, U(VI) speciation is dominated by $\text{UO}_2(\text{CO}_3)_x^{2-2x}$ species which exhibit weak sorption and thus a decrease in the fraction sorbed shown in Figures 1 and 2. This is again consistent with previous observations of U(VI) sorption to metal oxides under atmospheric conditions [7-14].

To allow a more direct comparison of the data, the uranium sorption data are re-plotted in Figure 3 and divided by temperature. The influence of ionic strength is minimal in the low pH region where surface complexation of UO_2^{2+} , UO_2OH^+ , $\text{UO}_2\text{CO}_3(\text{aq})$ are the dominant reactions. Since these weakly charged species are not as significantly influenced by the high ionic strength of the 1.0 M NaCl solution, there is little change in the sorption data. These similarity in these data up to approximately pH 6 also indicate that competition with Na^+ for sorption sites is not occurring and formation of $\text{UO}_2\text{Cl}_x^{2-x}$ species does not significantly influence sorption. In the high pH region where sorption decreases due to formation of $\text{UO}_2(\text{CO}_3)_x^{2-2x}$ species there are notable differences between the 0.01 M NaCl and 1.0 M NaCl datasets

at 25 °C. Detailed speciation modeling of the high ionic strength systems is required. However, the data indicate that the high ionic strength suppresses formation of $\text{UO}_2(\text{CO}_3)_x^{2-2x}$ species and causes greater sorption relative to the 0.01 M NaCl system. This difference in the datasets does not appear in the 50 °C and 80 °C systems. It is hypothesized that the high temperature reduces the fugacity of $\text{CO}_2(\text{g})$ in the system and suppresses formation of $\text{UO}_2(\text{CO}_3)_x^{2-2x}$ species in both ionic strength systems. Again, detailed modeling is required to verify this hypothesis.

Neptunium sorption to montmorillonite

The sorption of Np(V) to montmorillonite is the weakest of all the cations studies in this work. Sorption of Np(V) is relatively weak at low pH values and only increases significantly above pH 7. This behavior is extremely similar to that of Zavarin et al., [15] who also examined sorption of Np(V) to SWy-2 montmorillonite. For comparison, the data at 25 °C collected in this work is plotted with the data from Zavarin et al., [15] in Appendix A (Figure A2). Sorption of Np(V) increases with increasing temperature in the 0.01 M NaCl solution. In the low pH systems, Np(V) sorption increases from below 5% to approximately 20% at 50 °C and 30 % at 80 °C. The difference in sorption between the 25 °C and 50 °C data are much greater than the difference in sorption between the 50 °C and 80 °C datasets. The underlying cause of this behavior is unclear at this time and speciation modeling may be required to deconvolute the mechanisms. However, thermodynamic data for Np(V)-chloride complexes are unavailable to perform these calculations. A literature search is underway to determine if an approximation method can be used for these complexation constants.

Increasing the ionic strength from 0.01 M to 1.0 M resulted in a decrease in Np(V) sorption to montmorillonite. This is expected based on competition with Na^+ for sorption sites. Based on the comparison with Pu(IV)/Pu(V) data presented by Zavarin et al., [15] and previous studies examining Np(V) sorption to montmorillonite [15-17], it appears Np(V) undergoes little ion exchange with montmorillonite and that the dominant sorption process is surface complexation. Surface complexation likely occurs at the terminal edges of the clays consisting of octahedral aluminol sites and tetrahedral silanol sites [16, 18, 19]. There is significant scatter in the data from the 1.0 M NaCl, 80 °C system but overall sorption of Np(V) appears to increase slightly with temperature, consistent with the overarching hypothesis of this work. As discussed above, speciation models capable of distinguishing between the Np(V)-chloride and Np(V)-hydroxide complexes are necessary to fully evaluate these data. Preliminary indications are that the surface speciation is similar for both ionic strength systems. Extended X-ray Absorption Spectroscopy (EXAFS) was used to examine the sorbed Np species. The data (Figure 5) indicate there is little difference between the sorbed Np(V)-montmorillonite complexes in 0.009 M and

0.8 M NaCl. A more detailed analysis of these data is underway and provided in a report to DOE NEUP accompanying this report.

Eu(III) sorption to montmorillonite

Ionic strength and temperature both significantly influence sorption of Eu(III) to montmorillonite. In 0.01 M NaCl and 25 °C, sorption of Eu(III) is strong and generally above 90% across the pH range 3 to 9. Similar behavior is observed at 50 °C and this is presumed to be due to the increased sorption energy of Eu(III) to at elevated temperatures, consistent with the hypothesis of this work. This has previously been observed by Estes et al., [20] examining Eu(III) sorption to hematite at variable temperatures in 0.01 M NaCl. However, it is noteworthy that sorption of Eu(III) to montmorillonite appears to be significantly stronger than hematite. Sorption was markedly decreased at low pH values when the temperature is raised to 80 °C. It was initially assumed that leaching of native Eu from montmorillonite at the higher temperature was responsible for this behavior. Measurements of Eu(III), Th(IV), and U(VI) leaching from montmorillonite in 0.01 M NaCl and 1.0 M NaCl and all three temperatures examined are shown in Figures 6-8. Measureable concentrations of each cation are leached. However, the amount leached is not sufficient to account for the aqueous phase concentrations measured in Figure 1.

Based on the observations discussed above, it is hypothesized that Eu(III) sorption at low pH primarily occurs via ion exchange. Therefore, the elevated temperatures may weaken the ion exchange reaction or alter the properties of water (i.e. dielectric constant) within the exchange layer sufficiently to reduce Eu(III) sorption. Further evidence of this comes from comparison with the sorption data in 1.0 M NaCl. Sorption of Eu(III) at low pH values decreases significantly at 25 °C in 1M NaCl. There is a further decrease when the temperature is raised to 50 °C and 80 °C. The shape of the sorption edge curve also changes at 80 °C and more closely resembles that of cation sorption via surface complexation. The increased sorption via surface complexation at elevated temperatures would be consistent with the shift of the surface complexation sorption edge to lower pH values. Thus a combination of ion exchange and surface complexation reactions appears to be a plausible explanation for the observed sorption data. Development of a ion exchange/surface complexation model describing these data is underway.

Th(IV) sorption to montmorillonite

Th(IV) strongly sorbs to montmorillonite at almost all pH values, ionic strengths and temperatures considered in this work. In 0.01 M NaCl, there is greater sorption of Th(IV) at lower pH values than at higher pH values. This is unexpected behavior for cation sorption to a metal oxide mineral based on electrostatic attraction of a cation with the mineral surface as the surface develops and increasingly negative charge with increasing pH. However, similar behavior in a Pu(IV) system has been

previously observed [19]. Formation of tetravalent actinide hydroxycarbonate species is a possible explanation [21, 22]. However, a detailed sorption/speciation modeling study was unable to produce a reliable model describing the influence of these hydroxycarbonate complexes on sorption [19]. The primary issue is the underlying uncertainty in the stoichiometry and stability constants of the tetravalent actinide hydroxycarbonate species [21, 22]. Another possible explanation of the observed sorption results is that formation of tetravalent actinide nanocolloids is reducing sorption at high pH. Formation of hydrolysis products would be favored at high pH and the concentration of Th(IV) results in a saturated solution with respect to ThO₂ at circumneutral pH values. Therefore, formation of ThO₂ nanocolloids is possible. Sorption of Th(IV) in 1.0 M NaCl is over 95% at all pH values and temperatures examined. Therefore, if nanocolloids are involved in the observed sorption behavior, they do not appear to be stable in 1.0 M NaCl. This behavior is consistent with the expected collapse of the double layer in higher ionic strength solutions which would facilitate aggregation/sorption of the nanocolloids.

Sorption of Th increases with increasing temperature in the 0.01 M NaCl suspensions. This is consistent with the other actinides discussed in this work and consistent with the overarching hypothesis discussed above. However, based on the discussion above, it is unclear if these data represent sorption of a monomeric species or of a ThO₂ nanocolloid. In 1.0 M NaCl there is complete sorption of Th at virtually all pH values and temperatures. Thus, the influence of temperature on Th sorption in 1.0 M NaCl cannot be ascertained from Figures 1 and 2. The Th(IV) sorption data has been re-plotted in Figure 9 with log K_d values on the y-axis calculated as:

$$K_d = \frac{[Th]_{solid}}{[Th]_{aqueous}} \quad (1)$$

Comparison of the K_d values indicates there is relatively little change in Th sorption between 25 °C and 50 °C in 1.0 M NaCl. However, there is a significant change in K_d with the temperature increase to 80 °C. It is noteworthy that the aqueous concentrations of Th were close to the detection limits for the ICPMS. Thus K_d values in Figure 9 for the 80 °C system were calculated from aqueous concentrations with a high level of uncertainty. These data may be more appropriately represented listing a K_d value of > 10⁶ L/kg.

IV. Conclusions

The data presented in this report indicate that sorption of actinides to montmorillonite increased with increasing temperature and decreases with increasing ionic strength. The overarching hypothesis that strong sorption of actinide ions to metal oxide minerals is due to positive entropies which are mechanistically driven by displacement of hydrating waters from the actinides and mineral surfaces upon sorption may be true. Further examination of the systems is required to explicitly verify this hypothesis. Surface complexation models and/or ion exchange models are being developed are currently being

developed for these data. However, most sorption models developed will be limited to 25 °C data due to the lack of reliable aqueous complexation constants and surface protonation/deprotonation constants at temperatures other than 25 °C.

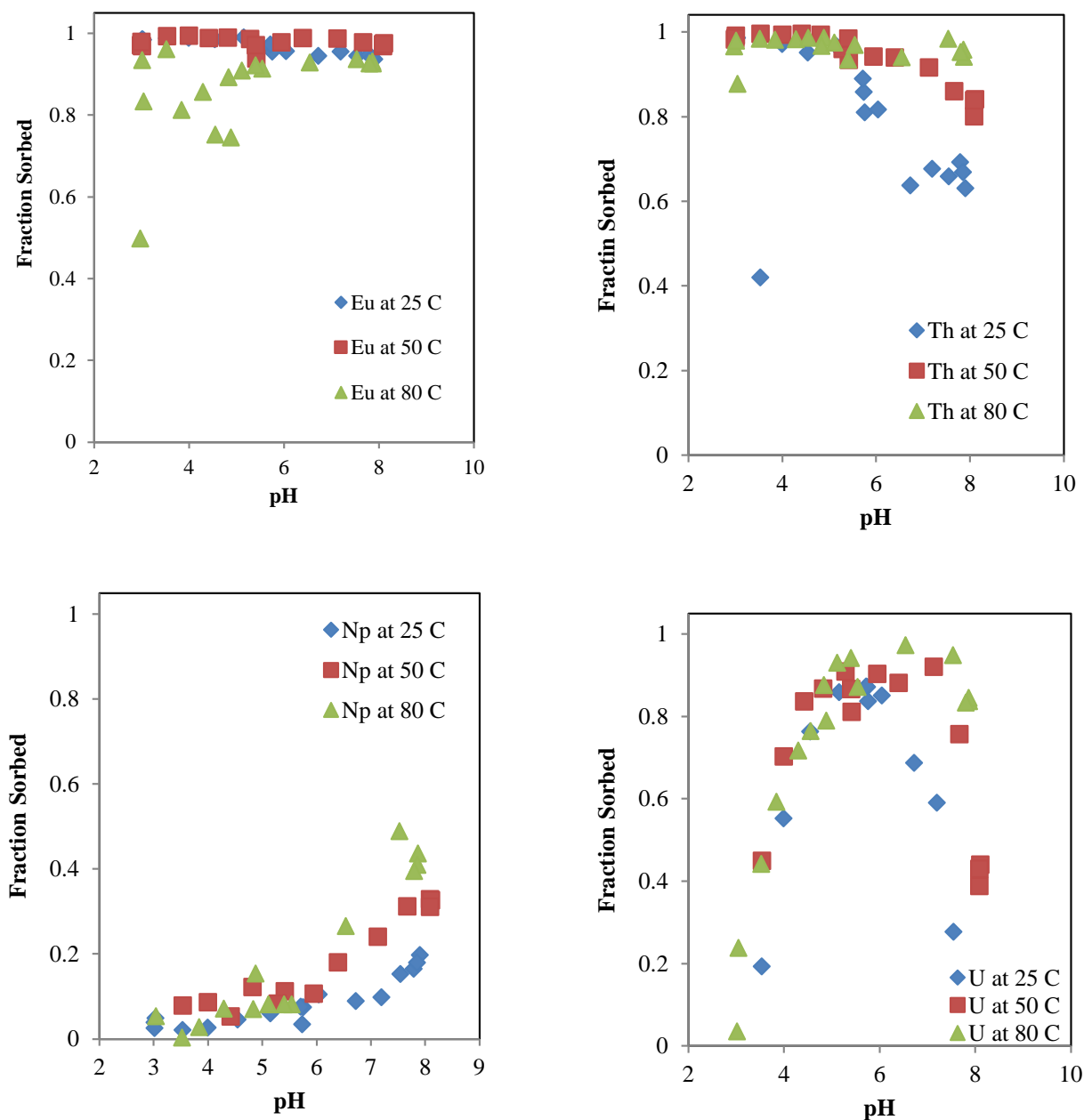


Figure 1: Sorption of Eu(III), Th(IV), Np(V), and U(VI) to montmorillonite as a function of pH and temperature in 0.01 M NaCl

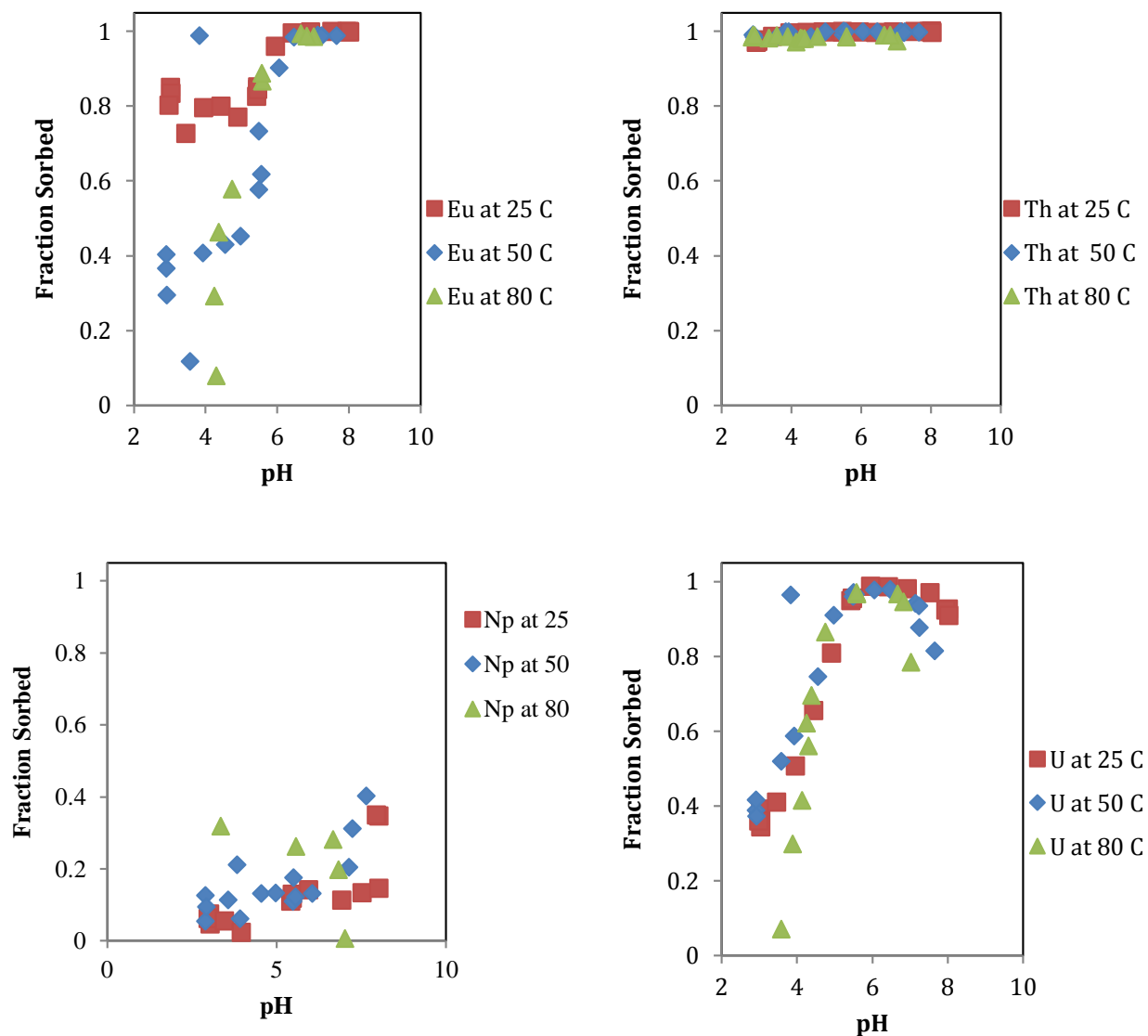


Figure 2: Sorption of Eu(III), Th(IV), Np(V), and U(VI) to montmorillonite as a function of pH and temperature in 1.0 M NaCl

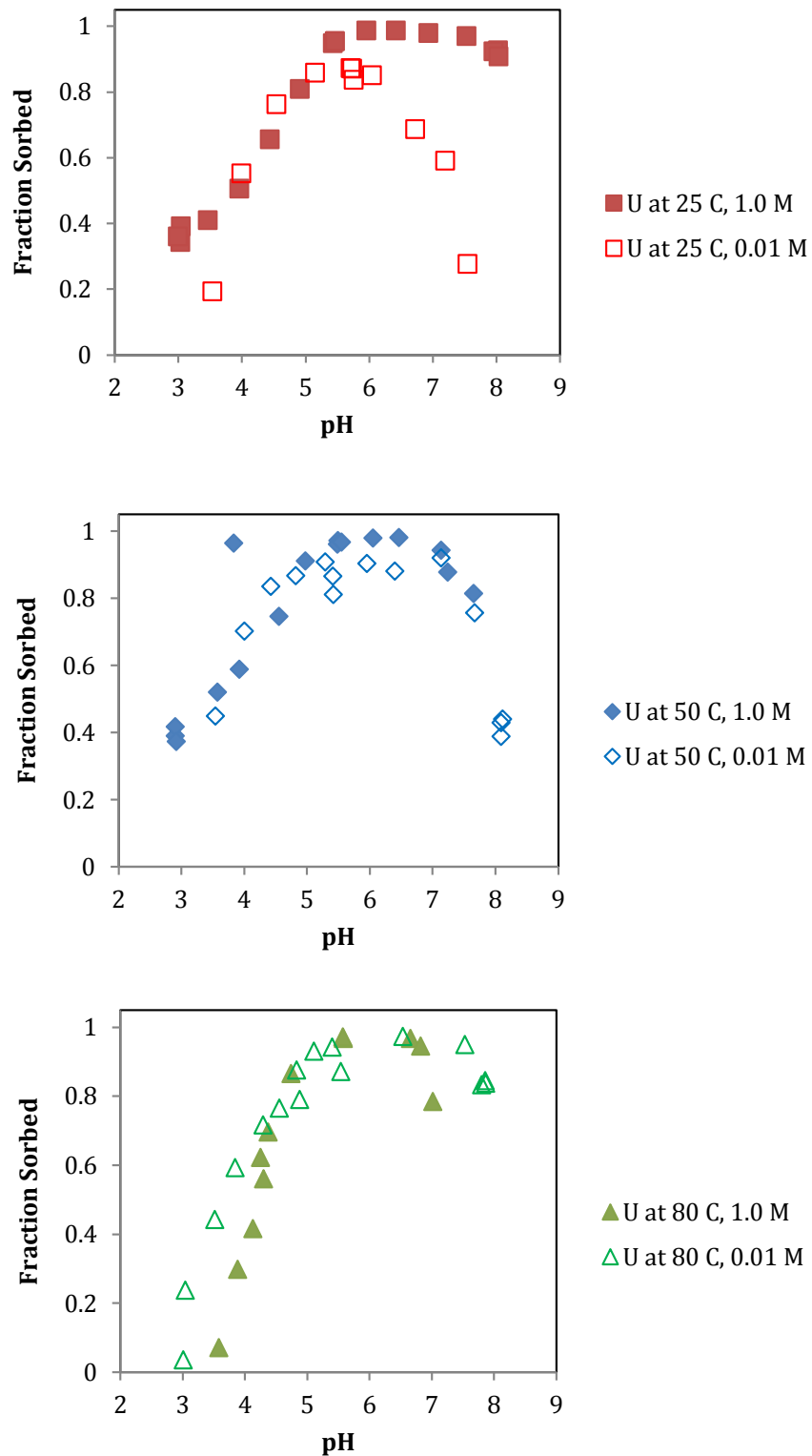


Figure 3: Comparison of U(VI) sorption to montmorillonite under variable temperature and variable ionic strength conditions.

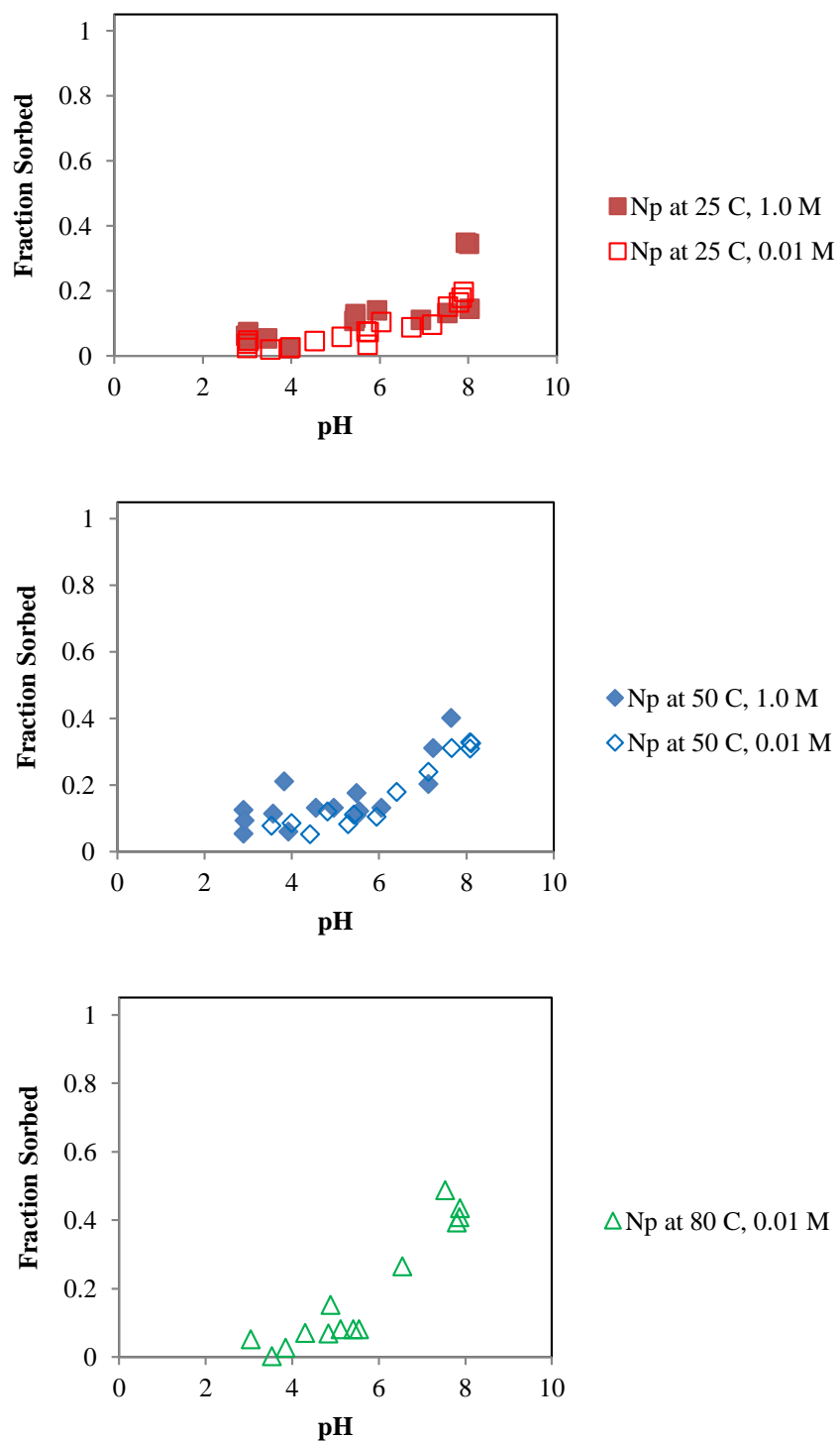


Figure 4: Comparison of Np(V) sorption to montmorillonite under variable temperature and variable ionic strength conditions.

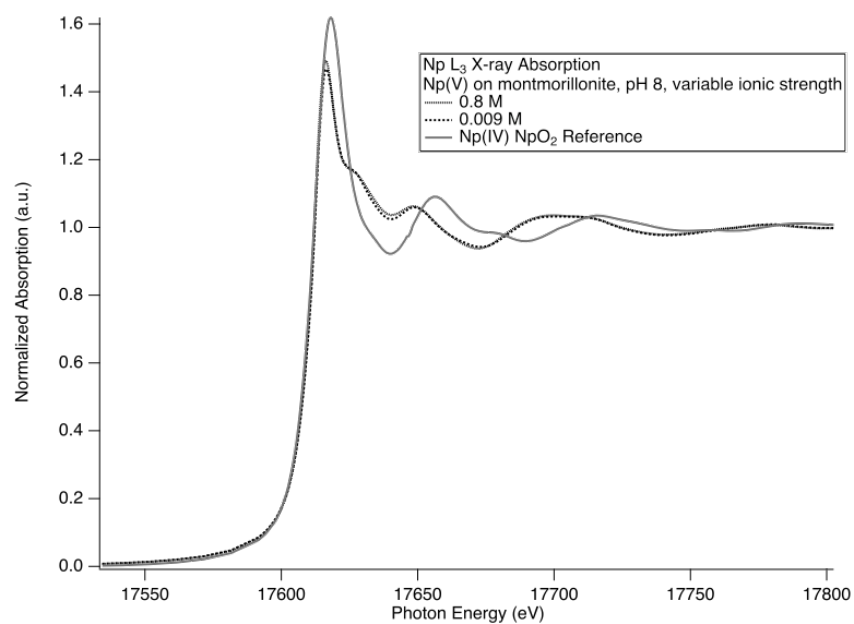


Figure 5. XANES spectra of the Np(V) sorbed to montmorillonite at pH 8 at high and low ionic strengths. Both samples show remarkably similar spectra in the XANES region, and include a characteristic neptunyl shoulder found around 17625 eV. A Np(IV) reference spectrum of NpO₂ is also shown as a comparison.

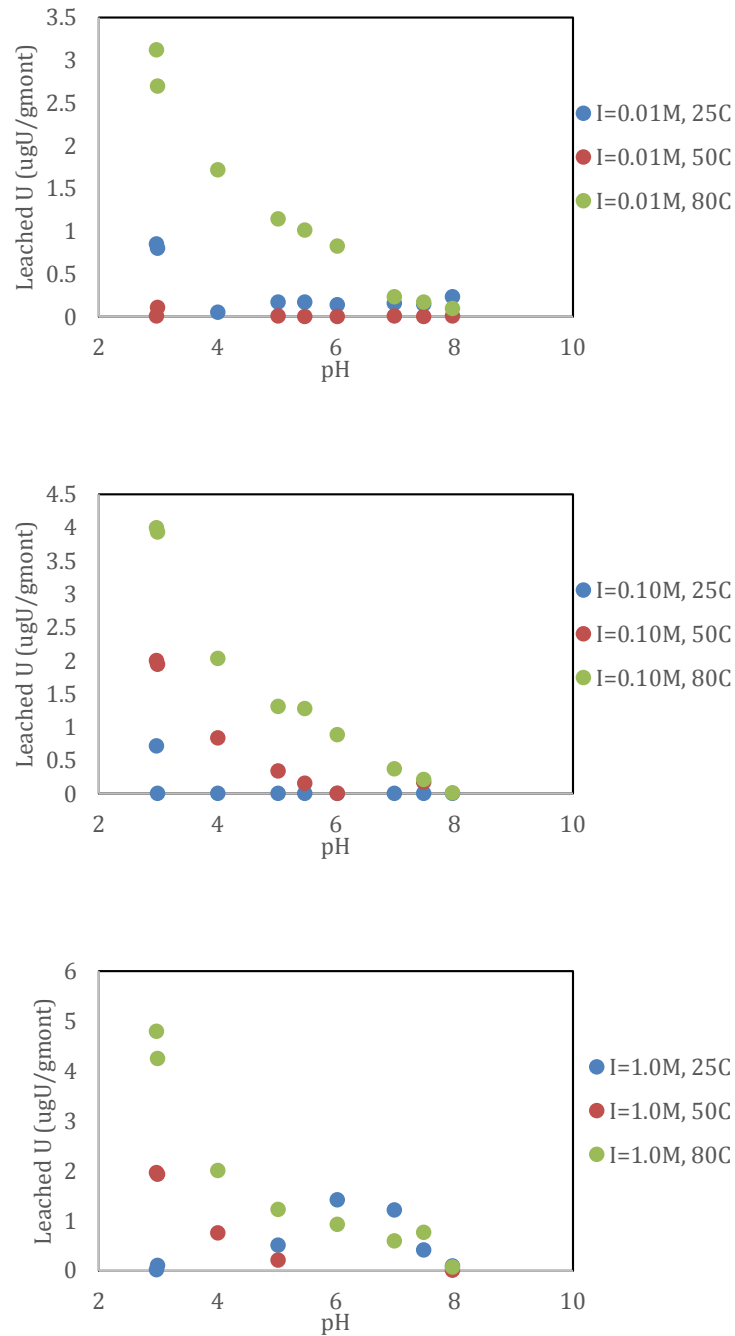


Figure 6. Aqueous concentrations of U leached from montmorillonite as a function of pH, temperature and ionic strength. The aqueous concentrations are a results of the leaching of native U from the montmorillonite.

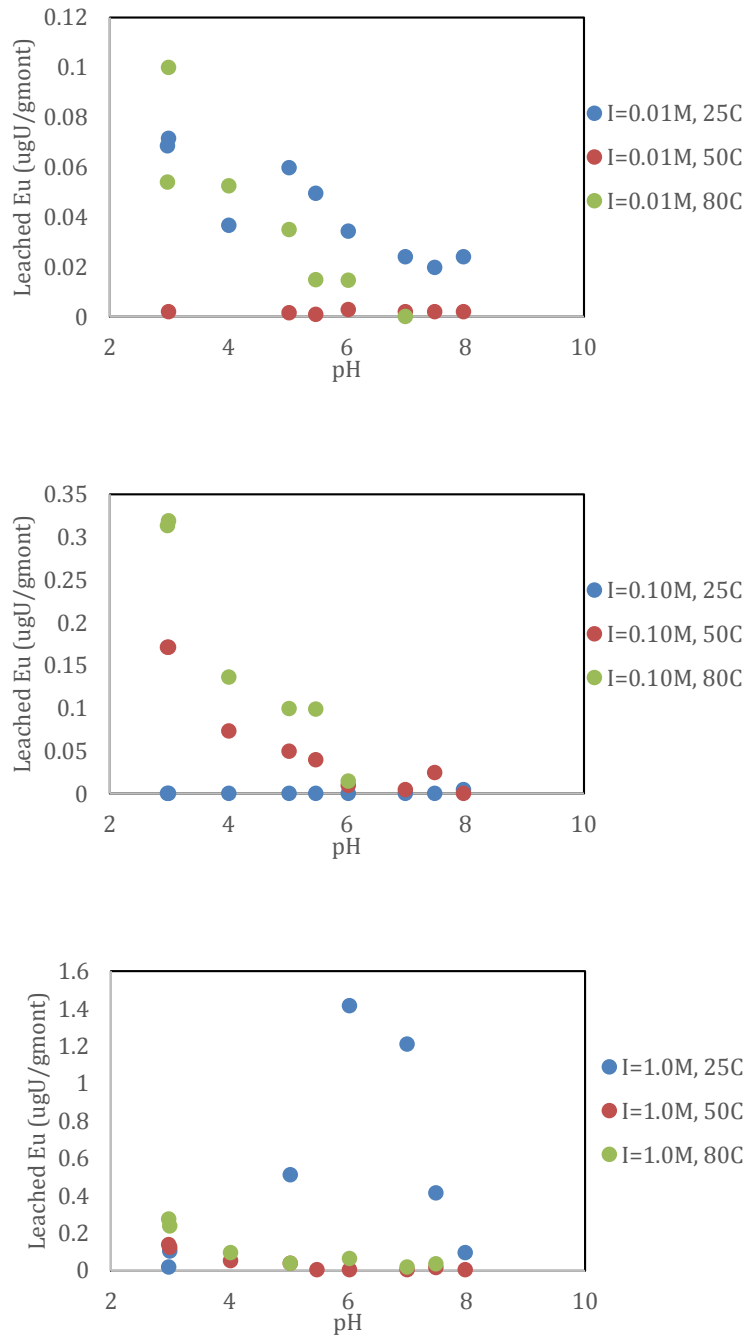


Figure 7. Aqueous concentrations of Eu leached from montmorillonite as a function of pH, temperature and ionic strength. The aqueous concentrations are a results of the leaching of native Eu from the montmorillonite.

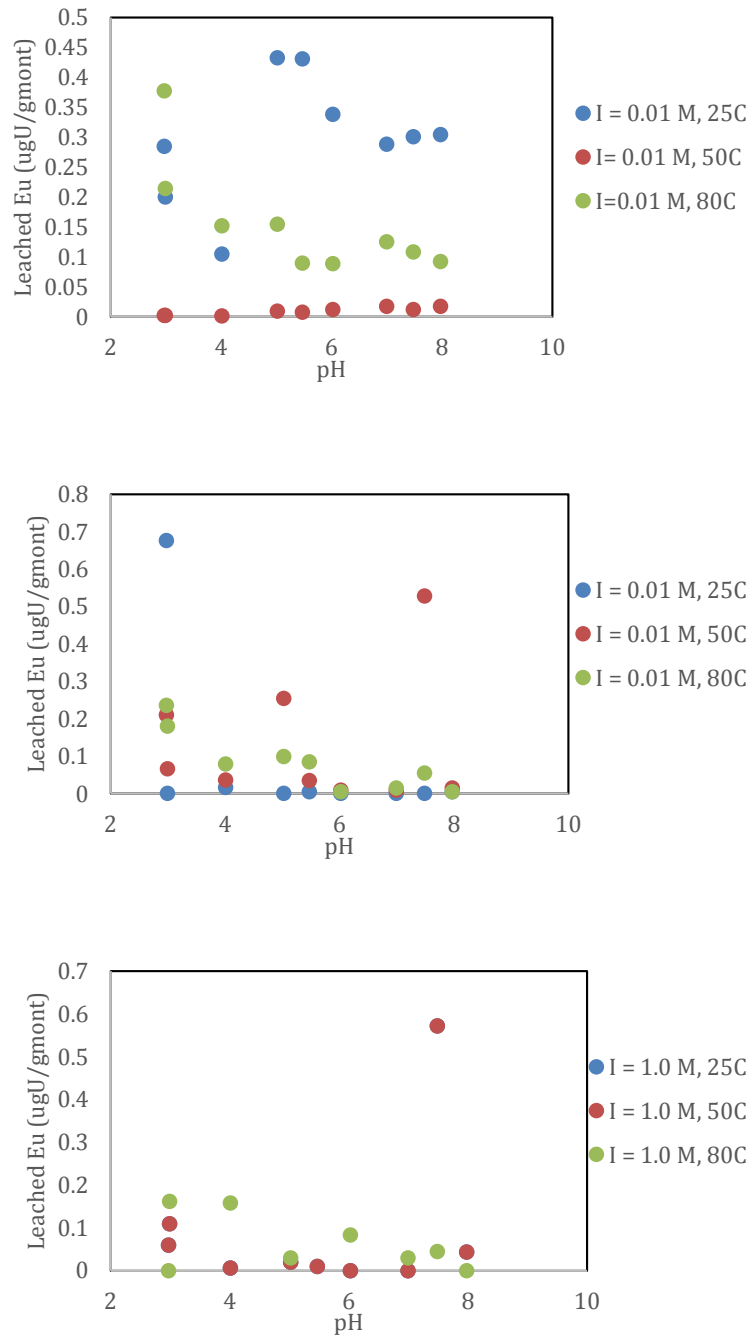


Figure 8. Aqueous concentrations of Th leached from montmorillonite as a function of pH, temperature and ionic strength. The aqueous concentrations are a results of the leaching of native Th from the montmorillonite.

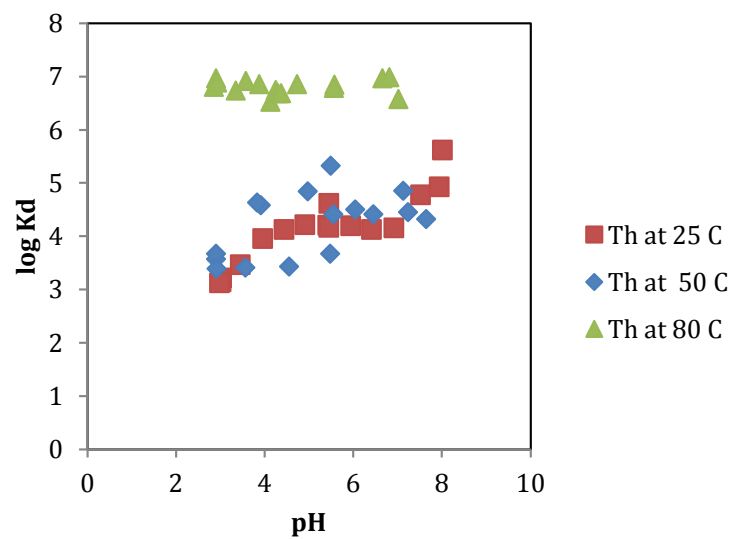


Figure 9: Sorption of Th(IV) to montmorillonite versus temperature in a 1.0 M NaCl suspension.

References

1. Zanonato, P., et al., *Hydrolysis of uranium(VI) at variable temperatures (10-85 degrees C)*. Journal of the American Chemical Society, 2004. **126**(17): p. 5515-5522.
2. Silva, R.J. and H. Nitsche, *Actinide environmental chemistry*. Radiochimica Acta, 1995. **70-1**: p. 377-396.
3. Kim, J.I., *Chemical Behavior of Transuraniuc Elements in Natural Aquatic Systems*, in *Handbook on the Physics and Chemistry of the Actinides*, A.J. Freeman and C. Keller, Editors. 1986, Elsevier Science Publishers B. V.
4. Choppin, G.R., *Actinide speciation in the environment*. Journal of Radioanalytical and Nuclear Chemistry, 2007. **273**(3): p. 695-703.
5. Choppin, G.R., *Solution Chemistry of the Actinides*. Radiochimica Acta, 1983. **32**(1-3): p. 43-53.
6. Choppin, G.R. and L.F. Rao, *Complexation of Pentavalent and Hexavalent Actinides by Fluoride*. Radiochimica Acta, 1984. **37**(3): p. 143-146.
7. Arai, Y., et al., *Uranyl adsorption and surface speciation at the imogolite-water interface: Self-consistent spectroscopic and surface complexation models*. Geochimica Et Cosmochimica Acta, 2006. **70**(10): p. 2492-2509.
8. Bargar, J.R., et al., *Characterization of U(VI)-carbonato ternary complexes on hematite: EXAFS and electrophoretic mobility measurements*. Geochimica Et Cosmochimica Acta, 2000. **64**(16): p. 2737-2749.
9. Catalano, J.G., et al., *Spectroscopic and diffraction study of uranium speciation in contaminated vadose zone sediments from the Hanford site, Washington state*. Environmental Science & Technology, 2004. **38**(10): p. 2822-2828.
10. Dong, W.M. and S.C. Brooks, *Formation of aqueous $MgUO_2(CO_3)_3(2-)$ complex and uranium anion exchange mechanism onto an exchange resin*. Environmental Science & Technology, 2008. **42**(6): p. 1979-1983.
11. Fein, J.B. and B.A. Powell, *Uranium adsorption: Speciation at mineral-water and bacterial cell-water interfaces*, in *Uranium: Cradle to Grave*, P.C. Burns and G.E. Sigmon, Editors. 2013, Mineralogical Association of Canada: Winnipeg, Manitoba.
12. Garcia-Rosales, G., et al., *Interaction between U(VI) and $SrTiO_3$ surfaces versus temperature*. Journal of Colloid and Interface Science, 2009. **333**(1): p. 104-113.
13. Lee, S.Y., M.H. Baik, and J.W. Choi, *Biogenic Formation and Growth of Uraninite (UO_2)*. Environmental Science & Technology, 2010. **44**(22): p. 8409-8414.
14. Lenhart, J.J. and B.D. Honeyman, *Uranium(VI) sorption to hematite in the presence of humic acid*. Geochimica Et Cosmochimica Acta, 1999. **63**(19-20): p. 2891-2901.
15. Zavarin, M., et al., *$Np(V)$ and $Pu(V)$ Ion Exchange and Surface-Mediated Reduction Mechanisms on Montmorillonite*. Environmental Science & Technology, 2012. **46**(5): p. 2692-2698.
16. Turner, D.R., R.T. Pabalan, and F.P. Bertetti, *Neptunium(V) sorption on montmorillonite: An experimental and surface complexation modeling study*. Clays and Clay Minerals, 1998. **46**(3): p. 256-269.
17. Benedicto, A., et al., *Effect of major cation water composition on the ion exchange of $Np(V)$ on montmorillonite: NpO_2^{+} - Na^{+} - K^{+} - Ca^{2+} - Mg^{2+} selectivity coefficients*. Applied Geochemistry, 2014. **47**: p. 177-185.

18. McKinley, J.P., et al., *The influence of uranyl hydrolysis and multiple site-binding reactions on adsorption of U(VI) to montmorillonite*. Clays and Clay Minerals, 1995. **43**(5): p. 586-598.
19. Powell, B.A., et al., *Development of a Composite Non-Electrostatic Surface Complexation Model Describing Plutonium Sorption to Aluminosilicates*. 2008, Lawrence Livermore National Laboratory: Livermore, California.
20. Estes, S.L., et al., *A self-consistent model describing the thermodynamics of Eu(III) adsorption onto hematite*. Geochimica Et Cosmochimica Acta, 2013. **122**: p. 430-447.
21. Clark, D.L., D.E. Hobart, and M.P. Neu, *Actinide Carbonate Complexes and Their Importance in Actinide Environmental Chemistry*. Chemical Reviews, 1995. **95**(1): p. 25-48.
22. Zavarin, M., et al., *Eu(III), Sm(III), Np(V), Pu(V), and Pu(IV) sorption to calcite*. Radiochimica Acta, 2005. **93**(2): p. 93-102.

Appendix A

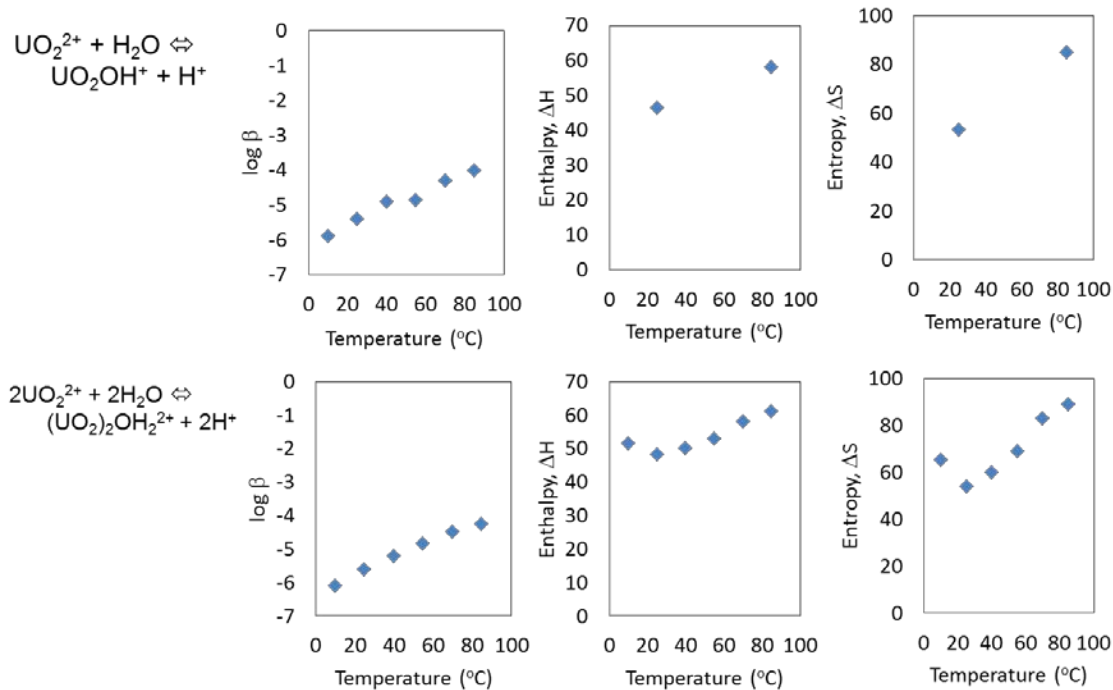


Figure A1: log stability constants, entropy, and enthalpy of the formation of UO_2OH^+ and $(\text{UO}_2)_2(\text{OH})_2^{2+}$. Data are from Zanonato et al., [1]. The data show that both 1:1 and 2:2 uranium hydrolysis species become more favorable with increasing temperature. In both cases, the endothermic hydrolysis enthalpy is overcome by a strongly positive entropy value.

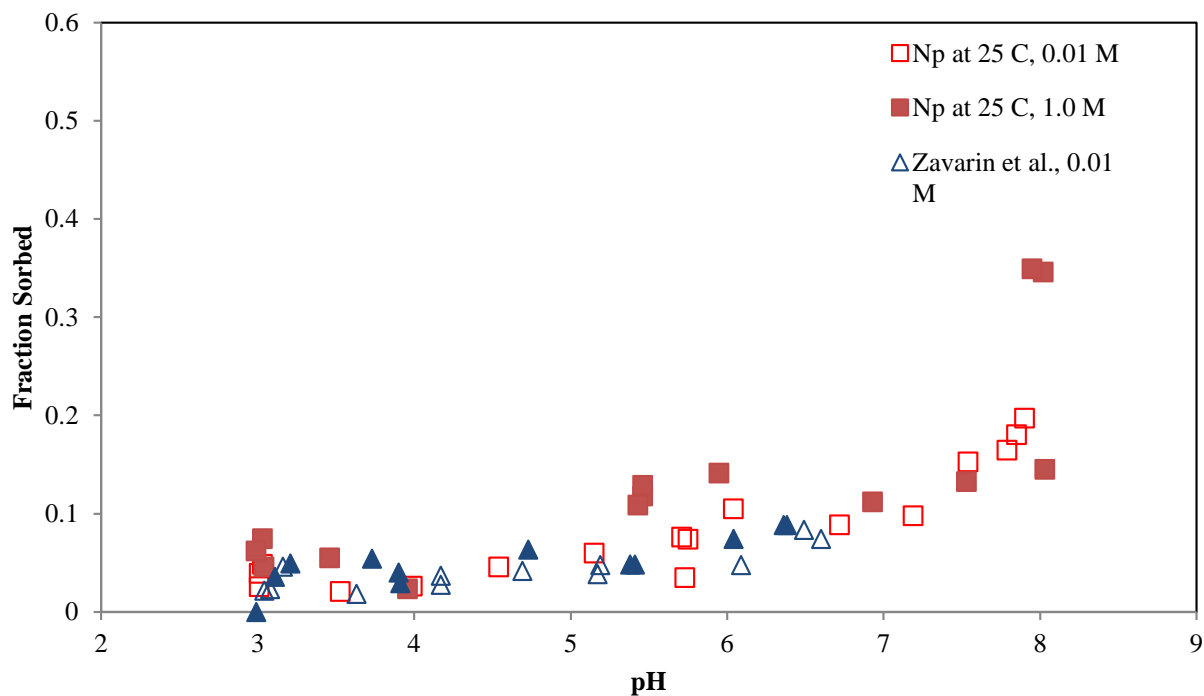


Figure A2: Comparison of Np(V) sorption to montmorillonite measured in this work and reported by Zavarin et al., [15]. Numbers in the figure legend refer to the concentration of NaCl in the system. Experiments in this work were performed in a controlled 25 °C atmosphere and those by Zavarin et al., [15] were performed under ambient laboratory conditions (~20 °C). As shown in Figure 1 above, there is a significant influence of temperature on Np(V) sorption. Thus it is possible the slightly higher sorption observed in this work is due to the difference in temperature between the two studies.

Examination of neptunium sorption to montmorillonite as a function of temperature and ionic strength

Daniel T. Olive^{a,b}, Deborah L. Wang^{a,b}, Jonathan Baldwin^c, Erin M. Black^c, Richard DeMille^c, Tyler Waterhouse^c, and Brian A. Powell^{c*}

^aDepartment of Chemistry, University of California, Berkeley, Berkeley, CA 94720, USA

^bNuclear Science Division, Lawrence Berkeley National Laboratory, Berkeley, CA 94720, USA

^cEnvironmental Engineering and Earth Sciences, Clemson University, Clemson, SC 29634, USA

I. Introduction

Background

The presence of actinides in the environment, from production and testing of nuclear weapons, purposely emplaced nuclear waste, and accidental release, necessitates the understanding of actinide interactions in various environmental matrices. Examples of such locations include the Savannah River Site where 1400 Ci of ²³⁹Np was released into streams and seepage basins¹, the Hanford Site where 55 Ci of ²³⁷Np was intentionally disposed to the near-surface environment², and the Nevada Test Site where 49 Ci of ²³⁷Np was deposited in the subsurface as a result of underground nuclear tests^{3,4}. The fate and transport of Np in the environment is an important issue for nuclear waste management and remediation efforts.

Understanding sorption of actinide elements to clay materials is necessary for maintaining environmental quality and assessment of nuclear waste repository performance. Because clay constitutes a large fraction of many rocks, soils, and sediments, radionuclide sorption onto clays play a role in radionuclide migration in many geochemical systems. Moreover, clay materials are expected to play an important role as an engineered barrier material, as most geologic disposal plans for spent nuclear fuel (SNF) propose bentonite as backfill material, placed between the waste containers and the surrounding rock.

The primary component of bentonite is montmorillonite, resulting in the terms “bentonite” and “montmorillonite” being used interchangeably. Montmorillonite, a member of the smectite group, is a dioctahedral 2:1 aluminosilicate clay mineral. The montmorillonite layers consist of 2 infinite tetrahedral sheets of [SiO₄] sandwiching an octahedral aluminum oxide/hydroxide sheet. Oxygen atoms on the siloxane surface are less reactive, being fully saturated. 2/3 of the octahedral sites between the sheets are occupied by Al³⁺ ions. Isomorphic ion substitutions of Mg²⁺ and Fe²⁺ for Al³⁺ occur in the octahedral sheet; consequentially, montmorillonite has a permanent negative cation exchange capacity (CEC). Montmorillonite has its layer charge resulting only from octahedral substitutions. It is to these sites that cations can coordinate via pH-independent ion-exchange processes.

Previous Studies

Interactions of aqueous Np with clay materials under various experimental conditions has been studied previously.^{6–12} Turner *et al.*¹³ conducted batch sorption experiments of Np to montmorillonite to determine the effects of pH and CO₂. They observed sorption is strongly influenced by pH and P_{CO2}. In the absence of CO₂, Np sorption steadily increases with pH over the pH range studied (pH 3–10), consistent with the increasing stability of the Np-hydroxy

complexes. In the presence of CO₂, sorption peaks at pH ~8.5 and decreases at higher or lower pH values due to the stability of the aqueous Np-carbonate complexes. Turner *et al.* estimated K_d values for Np on SAz-1 montmorillonite at 0.1 M NaNO₃ to range from ~10 mL/g for pH < 6 to ~1000 mL/g for pH ~ 10.5 in the closed system, and a maximum K_d ~100 mL/g in the open system. In a parallel study by Bertetti *et al.*¹⁰, changes in ionic strength were found to have little influence on Np sorption to SAz-1 montmorillonite. Sabodina *et al.*¹¹ also studied the effect of ionic strength. Sorption experiments of Np(V) were performed on bentonite in anaerobic conditions at 0.01 M and 0.1 M NaClO₄. The influence of ionic strength was pronounced only at low pH values, for which they attributed the sorption mechanism at acidic pH to be ion exchange. At high ionic strength, they propose the ion exchange mechanism is suppressed and Np is sorbed by surface complexation instead. Finally, Zavarin *et al.*¹² investigated the effects of ionic strength. They observed that sorption was relatively weak and showed an ionic strength dependence. The reported K_d values between pH 3-5 was 24 mL/g in 0.01 M NaCl and <6 mL/g in 1.0 M NaCl. The majority of the previous work, including the above cited studies, however, was collected at standard conditions. Elevated temperatures and high ionic strength are the conditions expected in nuclear waste repositories. It is expected that during the hundreds and thousands of years of storage time, the infrastructure of these repositories will be subjected to radiative heating as well as variations in humidity. Relatively little data exist examining the effect of elevated temperature and ionic strength on Np sorption behavior to montmorillonite.

Having a high ionic strength environment should decrease actinide sorption due to competition for a finite number of sorption and/or exchange sites. The background cation occupies the majority of available fixed charge sites under high ionic strength conditions, resulting in Np(V) undergoing little ion exchange and Np sorption being minimized.

On the opposite side, it is hypothesized that actinide sorption will increase as temperature increases, due to entropy-driven displacement of solvating water molecules. For example, thermodynamic data for U(VI) (Supplemental Information, Figure S1) show that increasing temperature has a profound influence on U(VI) speciation. In most cases, hydrolysis of uranium is an entropically driven reaction.¹⁴ This work centers on the hypothesis that strong sorption of Np ions to clay minerals is due to positive entropies, which are mechanistically driven by displacement of hydrating waters from the actinides and mineral surfaces upon sorption. Thus, it is essential to determine the effects that high temperature and ionic strength will have on Np sorption.

It is crucial to evaluate Np(V) sorption behavior with regards to Np(V) aqueous speciation. Neptunium is predominantly the oxycation NpO₂⁺ species in acid to neutral pH environments. The axial oxygen bonds lowers the effective charge of Np(V) to approximately +2.2.^{15,16} This lowered effective charge limits hydrolysis, aqueous complexation, and the affinity of Np(V) for solid phases. For example, NpO₂⁺ remains as the free oxycation up to pH 7. Under atmospheric CO₂ conditions, Np hydrolysis and Np carbonate species form at neutral to alkaline pH values. The stability of the Np hydroxy species, NpO₂OH⁰, reaches a maximum near pH 8.5, and negatively-charged Np carbonate complexes, NpO₂CO₃⁻, NpO₂(CO₃)₂³⁻, and NpO₂(CO₃)₃⁵⁻, dominate with further increasing pH.

Batch sorption experiments are useful in determining the relationship between variables such as pH, ionic strength, and temperature on the sorption behavior of cations to mineral surfaces. However, discovering the underlying physical mechanism responsible for those changes can be difficult. The *in situ* method of choice to probe these interactions is with X-ray absorption spectroscopy (XAS). XAS measurements have the ability to determine oxidation

state and local geometry, have the benefit of being element specific, and do not require long-range order. Extended X-ray absorption fine structure (EXAFS) spectroscopy will provide information about the coordination environment of the sorbed Np atom and help distinguish between inner-sphere and outer-sphere complexes.

In this work, we combine batch sorption experiments and XAS measurements to investigate Np(V) sorption behavior on SWy-2 montmorillonite at repository conditions of elevated temperature and ionic strength. Np-montmorillonite sorption studies were conducted as a function of pH (pH 3-8), temperature (25 °C, 50 °C, and 80 °C), and ionic strength (μ = 0.01 M NaCl and 1.0 M NaCl). To complement the information garnered from sorption studies, XAS studies were conducted as a function of ionic strength (μ = 0.008 NaCl and 0.9 NaCl).

II. Materials and Methods

Montmorillonite preparation

The montmorillonite used in this study (SWy-2) was obtained from the Source Clay Minerals Repository of the Clay Minerals Society. The SWy-2 is a Na-smectite from Crook County, Wyoming. The reported CEC for SWy-2 montmorillonite is 0.764 meq/g and its external surface area, calculated from a N₂-BET isotherm, is 32 m²/g (Source Clays Repository).

Neptunium stock solutions

On the basis of Np redox potentials, Np(IV) and Np(V) are the oxidation states likely to be present in environmental conditions. Np(IV) will form under anoxic conditions; under mildly oxic environmental conditions, Np(V) is the expected dominant oxidation state. Thus, this work focuses on Np in the pentavalent state.

For the batch sorption experiments, a ²³⁷Np(V) working solution was prepared by dilution of 5 mL of a 1 μ Ci/mL ²³⁷Np stock in 4 M HNO₃ (Eckert and Zeigler Isotope Products (Valencia, CA)) into water to produce a 1 mM ²³⁷Np(V) working solution. The solution was verified spectrophotometrically to be the pentavalent state of Np. This solution was further diluted in ultrapure water (18.2 M Ω -cm resistivity) to prepare a 4.22 μ M Np working solution.

For the XAS experiments, a stock solution of ²³⁷Np in 8 M HNO₃ was purified using anion exchange resin (BioRad AG 1-X4, 50-100 mesh) to remove any transuranic impurities. The isotopic purity of the Np solution was confirmed using alpha spectrometry and the pentavalent oxidation state was confirmed using optical absorption spectroscopy. The solution matrix was converted to 1 M HClO₄ and final Np concentration of the stock solution was determined by liquid scintillation counting (Wallac 1414 LSC and Ecolume cocktail).

Neptunium batch sorption experiments

Batch Np(V) sorption experiments to montmorillonite was examined by preparing clay mineral suspensions as a function of temperature and ionic strength. In the following description, we use the nominal terms “low ionic strength” to refer to experiments of μ = 0.01 M and “high ionic strength” for experiments of μ = 1 M. Samples were prepared following a matrix

of temperature (25 °C, 50 °C, and 80 °C) and ionic strength (0.01 M NaCl and 1.0 M NaCl) across the pH range of 3 to 8. All batch sorption experiments were performed under air with a constant montmorillonite concentration of 1 g/L in polypropylene vials. Select samples were performed in triplicate. All additions of the montmorillonite stock or NaCl electrolyte were determined gravimetrically. Each vial was then spiked with $^{237}\text{Np(V)}$ for a final concentration of 4.22 nM. The experiments were conducted at low Np solution concentrations to avoid complicating effects from Np precipitation. In all cases, the volume of the Np spike was 100 μL or less and determined gravimetrically. Thus, the addition of the working solution did not alter the ionic strength significantly, and the concentration can be determined using the known concentration of the stock solution and the total mass of the sample.

The spiked samples were mixed in a shaking incubator at 25 °C (VWR Shaking Incubator) for 7 days. Then a 1.3 mL aliquot of the suspension was transferred to a 2 mL polypropylene centrifuge vial and centrifuged for 20 minutes at 8000 rpm to remove particles greater than 100 nm from solution, assuming spherical particles as calculated using Stokes law. A 1.0 mL aliquot of the supernatant was transferred to a 15 mL polypropylene tube and diluted with 9 mL 2% HNO_3 (Aristar Plus, VWR) for subsequent Inductively Coupled Plasma Mass Spectrometric (ICP-MS) analysis. The pH of the primary suspension was measured using a temperature-compensated Thermo Ross electrode calibrated with standard pH buffers. If needed, sample pH was adjusted with small amounts of HCl or NaOH. Upon completion of this sampling protocol, the samples were returned to the shaking incubator for an additional 7 days. The suspensions were then sampled a second time, and equilibrium was assumed if there were no significant differences between measured Np(V) concentrations for the two sampling events. If equilibrium was not achieved, the suspensions were mixed for an additional 2 – 4 days, then sampled again. Once equilibrium was achieved (within 3 sampling events for all temperatures), the reaction temperature was increased to 50 °C and the sampling protocol continued as described above. After equilibrium was reached at 50 °C, the samples were transferred to a VWR shaking water bath held at 80 °C. Again the sampling protocol described above with multiple sampling events to ensure equilibrium had been reached was followed. To determine the amount of Np sorbed on montmorillonite after reaching sorption equilibrium, Np concentrations in solution were measured by ICP-MS (Thermo X Series II quadrupole, with ^{242}Pu as an internal reference standard).

Neptunium XAS experiments

The physical mechanism of Np(V) sorption on montmorillonite was examined with XAS as a function of ionic strength. In the following description, we use the nominal terms “low ionic strength” to refer to samples of $\mu = 0.008 \text{ M NaCl}$ and “high ionic strength” for samples of $\mu = 0.9 \text{ M NaCl}$. XAS samples were at NaCl concentrations of 0.008 M and 0.9 M and prepared open to air with 1.5 g/L montmorillonite in acid-washed polypropylene vials. Samples were spiked with $^{237}\text{Np(V)}$ for a final Np concentration of 2.54 mM and the pH quickly adjusted to 8.0 with small volumes of HClO_4 or NaOH. A relatively high Np concentration, compared to batch sorption experiments, is required to acquire high-quality XAS data. Solution pH was measured with a VWR pH meter (Model 8025) equipped with a Ross combination pH electrode (Orion 8103 Ross) calibrated with standard pH buffers. Measurement of pH over the course of the experiment indicated pH drift was less than 0.2 pH units. Samples were mixed end-over-end on a rocker for 7 days at room temperature. The montmorillonite samples were then loaded as wet

pastes into Kapton tubes and triply contained in nesting aluminum sample holders with Kapton windows and indium wire seals in the packaging method described by Hu *et al.*¹⁷

Neptunium L_{III}- edge XAS spectra were collected at the Stanford Synchrotron Radiation Lightsource (SSRL) on wiggler beamline 11-2. X-ray wavelength was selected using a Si(220) double crystal monochromator. Higher harmonics were removed by applying a 30% detuning to the second crystal. Energy calibration was performed by setting the first inflection point at the K-edge absorption spectrum of a Zr foil run in transmission mode to 17997.6 eV.¹⁸ All samples were run at approximately 30 K using a specially engineered liquid helium cryostat (Janis) to mitigate the risk of beam-induced chemical changes during the experiment. Data were collected in fluorescence mode using a 100-element Ge detector with a sample orientation of 45° to the incident beam.

EXAFS data were analyzed according to the standard EXAFS analysis procedures,^{19,20} data reduction including alignment, summation, calibration, and error correction were done using Athena²¹ and SixPack²². Spectral fitting to determine structural parameters was performed using Artemis²¹ with theoretical EXAFS paths created with FEFF6^{23–26}. Uncertainties of the fitting parameters were determined by inversion of the covariance matrix.²⁷

III. Results and Discussion

Neptunium batch sorption

The sorption of Np(V) to montmorillonite was studied as a function of pH, ionic strength, and temperature. The resulting sorption profiles shown in Figure 1 indicate that Np(V) sorption to montmorillonite is dependent on solution pH, ionic strength, and temperature. To allow a more direct comparison of the data, the sorption data are re-plotted in Figure 2 and separated by temperature. Np(V) sorption at 25 °C in both low and high ionic strength systems is relatively weak (Figure 2A). The low sorption is expected, given the effective charge ion of +2.2 for Np(V). Between pH 3 and 5, no pH dependence was observed, but sorption increases with pH values above 6. This compares favorably with the study by Turner *et al.*¹³ who observed a maximum in Np(V) sorption on montmorillonite near pH 8 with decreasing values at more acidic or alkaline pH values. Zavarin *et al.*, who examined sorption of Np(V) to SWy-1 montmorillonite, also observed low sorption.¹² For comparison, the Np sorption previously reported by Zavarin *et al.* is shown alongside the data at 25 °C collected in this work in the Supplemental Information, Figure S2. The sorption profiles are extremely similar.

Ion exchange sites in montmorillonite consist of negative surface charges that arise from isomorphic substitutions of Mg²⁺ and Fe²⁺ cations for Al³⁺ in the clay structure.¹³ Because ion exchange sites are not affected by pH, ion-exchange is pH independent. The NpO₂⁺ species competes with the background electrolyte cation Na⁺ for sorption sites below pH 5. With low sorption that is independent of pH, we attribute ion-exchange as the likely sorption mechanism in the pH range below pH 5 for Np sorption on montmorillonite. Np sorption increases with pH, suggesting the likely sorption mechanism for Np sorption on montmorillonite above pH 6 is dominated by surface complexation.

The impact of ionic strength on Np(V) sorption to montmorillonite varies with temperature (Figure 2). The influence of ionic strength at 25 °C is minimal (Figure 2A), but increasing the ionic strength from 0.01 M to 1.0 M resulted in a significant decrease of Np(V) sorption to montmorillonite at 50 °C and 80 °C (Figures 2B and 2C). This is expected based on

competition with Na^+ for ion exchange sites. Under high ionic strength conditions, the Na^+ cation occupies the majority of available ion exchange sites, Np(V) undergoes little ion exchange, and the sorption of Np is minimized. The dominant sorption process is then surface complexation. Surface complexation likely occurs at the terminal edges of the clays consisting of octahedral aluminol sites and tetrahedral silanol sites.^{13,28,29}

For a given ionic strength, the effect of temperature on Np(V) sorption to montmorillonite generally increases with increasing temperature. In particular, sorption of Np(V) significantly increases with increasing temperature for low ionic strength (Figure 1A). At low pH values, Np(V) sorption increases from below 5% to approximately 20% at 50 °C and to 30 % at 80 °C. The difference in sorption between the 25 °C and 50 °C data are much greater than the difference in sorption between the 50 °C and 80 °C datasets. This trend is consistent with the overarching hypothesis that sorption increases with temperature due to displacement of solvating waters of the cations and the mineral surfaces.¹³ This removal of ordered water from the cation to bulk disordered water results in an entropically favorable reaction. There is significant scatter in the data of the high ionic strength-80 °C system, but overall sorption of Np(V) appears to increase slightly with temperature for high ionic strength (Figure 1B), consistent with the overarching hypothesis of this work. While sorption observed in this work is slightly higher than what Zavarin *et al.* observed (Figure S2), experiments in this work were performed with temperature held at 25 °C atmosphere and those by Zavarin *et al.* under ambient laboratory conditions (~20 °C). As discussed above, there is a influence of temperature on Np(V) sorption, and the slight difference in sorption could be attributed to the difference in temperature between the two studies.

Neptunium XAS

Because batch sorption provides an overall view, additional information concerning the coordination sphere of the Np(V) ion to the montmorillonite surface was obtained. XAS was used to examine the sorbed Np species to SWy-2 montmorillonite for both low and high ionic strength systems. The data indicate the surface speciation is similar for both ionic strength systems, as there is little difference between the sorbed Np(V) -montmorillonite complexes in $\mu = 0.008 \text{ M}$ and $\mu = 0.9 \text{ M}$. The normalized absorption edge spectra for the two montmorillonite samples are shown in Figure 3, and XANES parameters are listed in Table 1. Also plotted is the absorption edge of the NpO_2 sample, as determined by the peak of the first derivative of the normalized absorption spectrum, which was used as a Np(IV) standard. The absorption edge energies of the samples are shifted higher than the Np(IV) spectrum by 0.7 eV, which is consistent with the higher oxidation state of Np(V) . Both samples show a primary absorption peak at 17.63 keV with a shoulder at 17.62 keV. These two features are indicative of the NpO_2^+ moiety, with the primary absorption peak associated with the $2p_{3/2} \rightarrow 6d$ transition and the shoulder associated with multiple scattering resonances from the linear neptunyl $[\text{O}=\text{Np}=\text{O}]^+$ structure.³⁰ The peak positions, as measured by the white line maximum are slightly lower, between 1.4 and 1.8 eV, compared to the Np(IV) standard. Although not a large difference, it could be indicative of a slightly different bonding environment. However, the presence of the neptunyl shoulder in the samples, characteristic of the presence of short axial Np-O bonds found in oxidized Np , would preclude Np reduction.

Neptunium L_{III}-edge EXAFS spectra of the two montmorillonite samples and the Np(IV) standard are shown in Figure 4. The spectra of the two samples overlap well over the entire k-space region, and are distinct from the NpO₂ standard. The corresponding Fourier transforms of the EXAFS, representative of the configuration of atoms surrounding the Np atom, are shown in Figure 5. The Fourier transforms are not corrected for EXAFS phase shifts, Δ , causing peaks to appear at shorter distances ($R+\Delta$) relative to the real near-neighbor distances (R). The axial and radial oxygen scattering shells are visible at 1.5 and 2.0 Å (not corrected for phase shift) in the plot and there is some additional structure, the largest peak at 4.2 Å (uncorrected). Little structure at higher R values is evident, suggesting there is no evidence for bulk-like precipitates which would exhibit Np-Np scattering at higher R values, or other neighbors at regular distances common to the Np in the sample. This is consistent with an outer sphere sorption mechanism.

Fitting of the EXAFS equation^{20,31}

$$\chi(k) = \sum_i \frac{N_i S_0^2 F_i(k)}{k R_i^2} \sin(2kR_i + \phi_i(k)) e^{(-2\sigma_i^2 k^2)} e^{\frac{-2R_i}{\lambda(k)}}$$

to the measured $\chi(k)$ involved performing a non-linear least-squares fit summing over each scattering path used, i , in order to find the best values for the amplitude of each path, N_i , scattering half-path length, R_i , energy shift, ΔE_0 , and mean squared displacement, σ_i^2 , also known as the EXAFS Debye-Waller factor. The values for the effective scattering amplitude, $F_i(k)$, effective scattering phase shift, $\phi_i(k)$, and mean free path, $\lambda(k)$, were taken from the FEFF6 calculations.

Fitting of the EXAFS data was performed using the structure for Np₂O₅³² as the basis for configuring up the geometry of the two axial and five radial oxygen single scattering paths. Two oxygen single scattering paths at a distance of 1.86 Å and five oxygen single scattering paths at a distance of 2.41 Å were used as the initial model. In the fitting model, the number of axial oxygen atoms was set to two, as those bonds in Np(V) are not easily changed. To allow for the possibility that slight changes in the radial oxygen peaks seen in Figure 5 are real and not within experimental variation, those amplitudes were allowed to float in the fitting process. Because the amplitude and EXAFS Debye-Waller factors are highly correlated, both data sets were refined simultaneously in ARTEMIS using the same σ^2 , ΔR , E_0 values, while the radial oxygen amplitudes were allowed to float. Fitting results are summarized in table 2.

Comparing the Np-montmorillonite samples to the Np(IV) reference in Figure 5, there is no evidence of Np-Np scattering at 3.75 Å (uncorrected), which we might expect if there had been any precipitation of NpO₂. To check for the possibility that the feature is a result of a Np₂O₅ precipitate, additional fitting paths from the model were tested, including Np-Np single scattering at $R = 3.62$ Å and at $R = 4.2$ Å corresponding to higher coordination shells. However, the fitting would not converge on physical values. Several other single scattering paths were tested including oxygen, magnesium, aluminum, silicon, and iron. In no case could a single scattering path be made to fit that feature. It is possible that more than one scattering atom type or geometry could be contributing to that peak, however, without additional information over-parameterization might lead to a meaningless fit. It should be noted that the feature has the same amplitude in both samples, thus it does not appear to change as a function of background ionic strength. This is further evidence for the outer-sphere coordination of Np(V) to montmorillonite. An example fit of the low ionic strength montmorillonite data using the first two oxygen paths is

shown in Figure 6. The best fit values of the fitting parameters for both samples are shown in Table 2.

IV. Conclusions

The data presented in this study indicate that sorption of Np(V) to montmorillonite increases with increasing temperature and decreases with increasing ionic strength. The overarching hypothesis that strong sorption of actinide ions to metal oxide minerals is due to positive entropies which are mechanistically driven by displacement of hydrating waters from the actinides and mineral surfaces upon sorption may be true. While the sorption behavior changes as a function of ionic strength, XAS measurements showed essentially no variation in surface speciation between low and high ionic strength samples. This suggests Np sorption to montmorillonite is that of outer-sphere coordination. No redox chemistry of Np was observed for either low or high ionic strength samples, as Np was measured in the +5 oxidation state. Although the Np-montmorillonite samples did show some evidence of scattering beyond the first oxygen atoms, that feature could not be fit using only a single scattering path. However, we were able to exclude precipitation of either NpO_2 or Np_2O_5 as the cause of the feature.

Acknowledgements

Use of the Stanford Synchrotron Radiation Lightsource, SLAC National Accelerator Laboratory, is supported by the U.S. Department of Energy, Office of Science, Office of Basic Energy Sciences under Contract No. DE-AC02-76SF00515. The SSRL Structural Molecular Biology Program is supported by the DOE Office of Biological and Environmental Research, and by the National Institutes of Health, National Institute of General Medical Sciences (including P41GM103393). The contents of this publication are solely the responsibility of the authors and do not necessarily represent the official views of NIGMS or NIH.

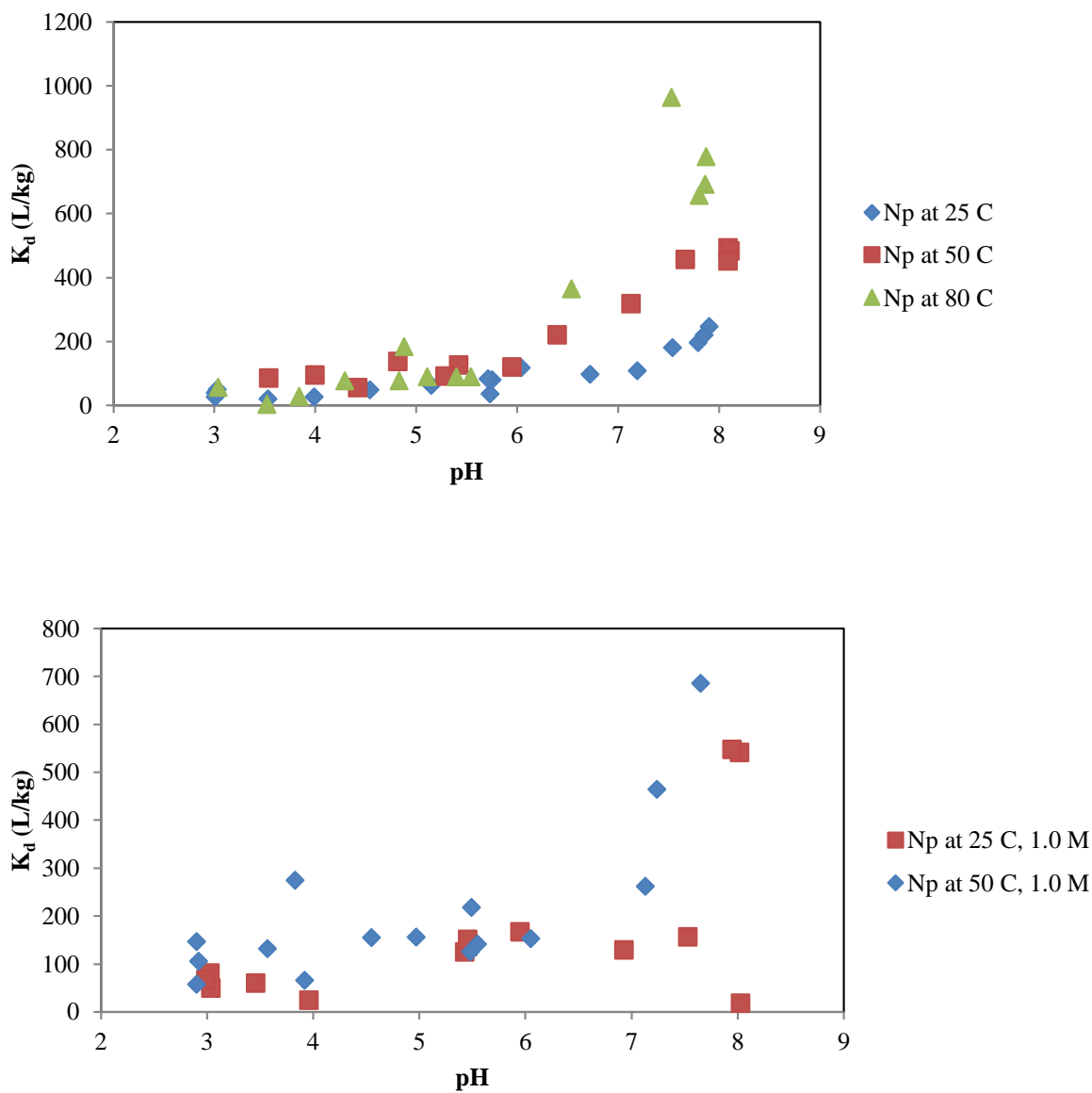


Figure 1: Np(V) sorption to montmorillonite as a function of pH and temperature in (A) 0.01 M NaCl and (B) 1.0 M NaCl.

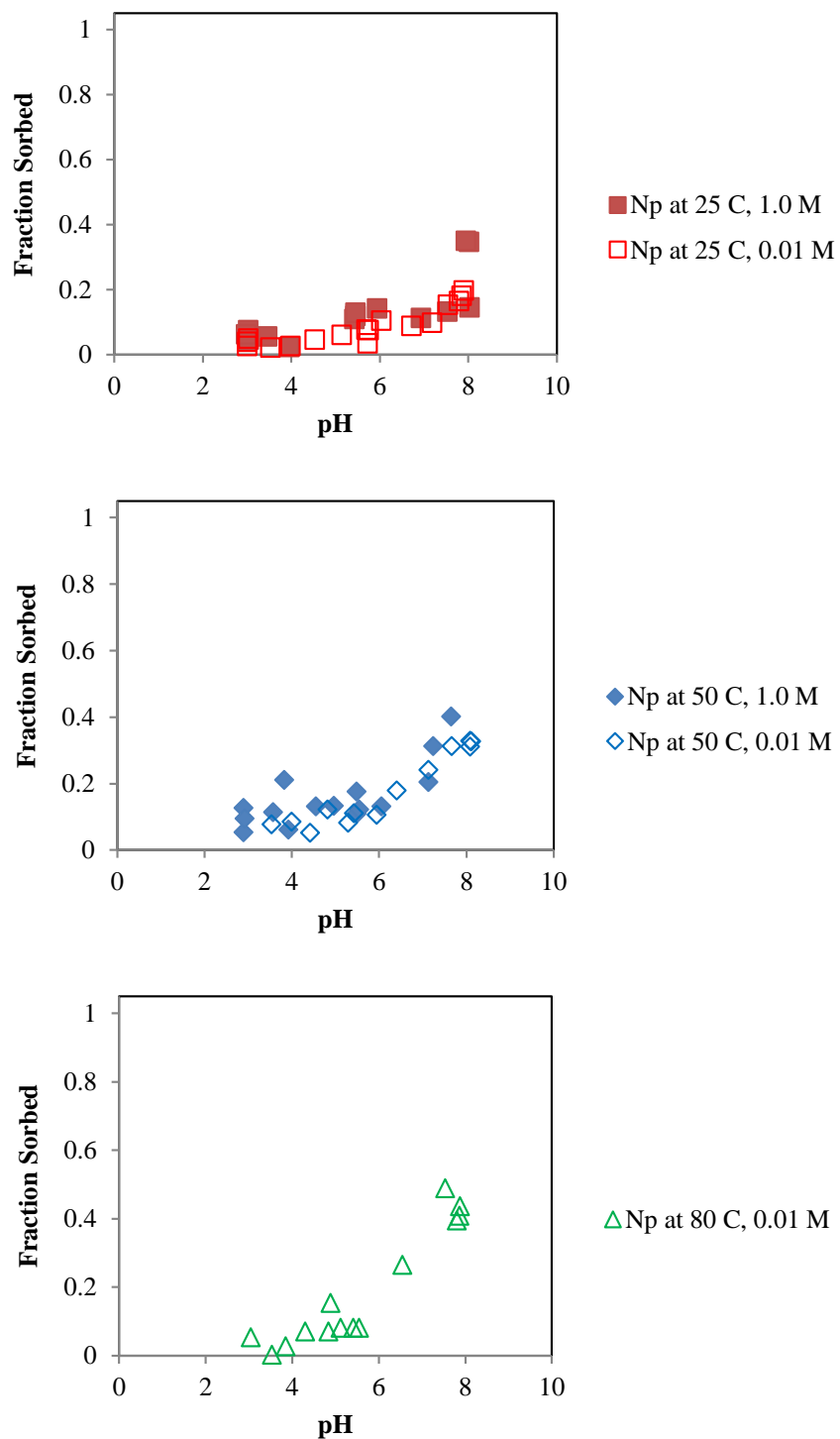


Figure 2: Comparison of Np(V) sorption to montmorillonite in low and high ionic strength conditions at (A) 25 °C, (B) 50 °C, and (C) 80 °C.

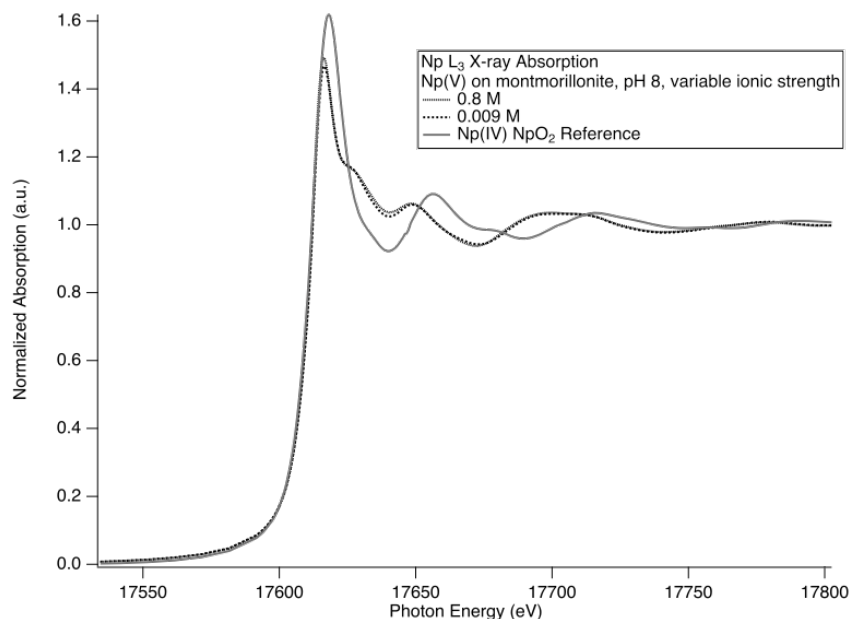


Figure 3: XANES spectra of the Np(V) sorbed to montmorillonite at pH 8 at high and low ionic strengths. Both samples show remarkably similar spectra in the XANES region, and include a characteristic neptunyl shoulder found around 17625 eV. A Np(IV) reference spectrum of NpO₂ is also shown as a comparison.

Table 1: XANES parameters for Np(V) sorbed to montmorillonite (Figure 3) at pH 8 at different ionic strengths. The edge position was determined using the first derivative and locations of the white line maximum are indicated.

Sample	Edge Energy (eV)	Peak Position (eV)
$\mu = 0.009$ M	17613.1 ± 0.5	17616.6 ± 0.5
$\mu = 0.8$ M	17613.1 ± 0.5	17616.2 ± 0.5
NpO ₂ reference	17612.4 ± 0.5	17618.0 ± 0.5

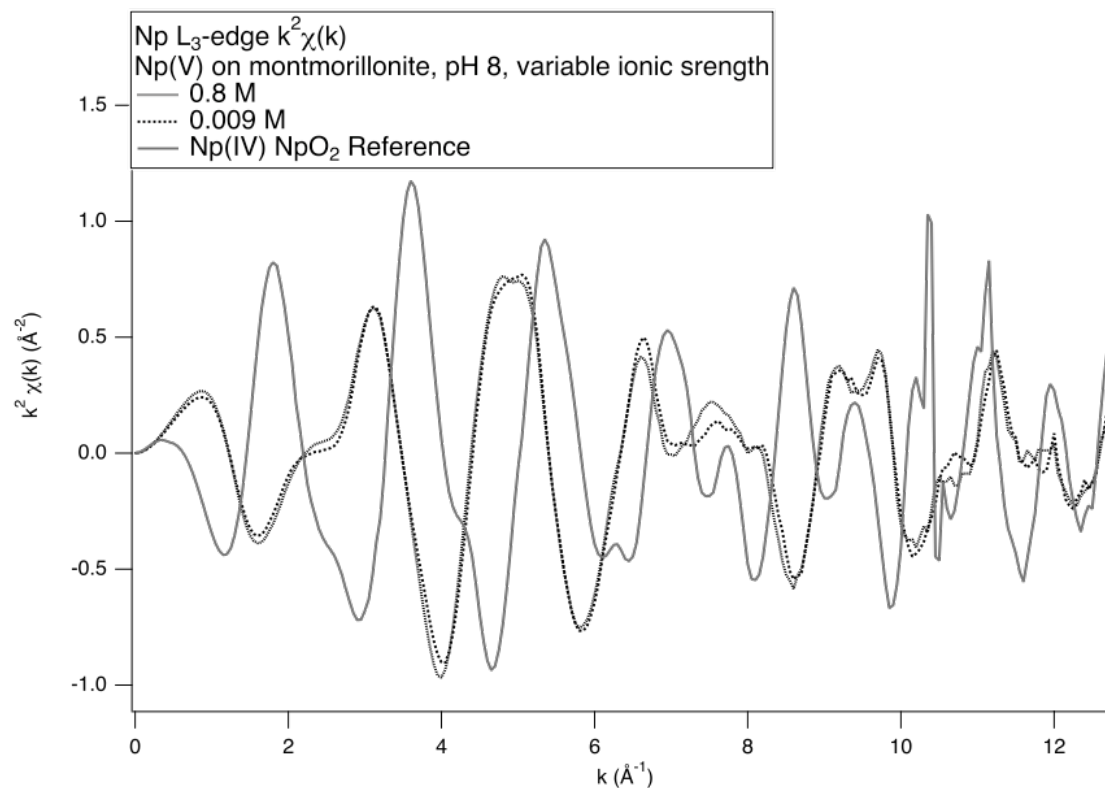


Figure 4: EXAFS spectra of the Np(V) sorbed to montmorillonite at pH 8 at high and low ionic strengths, as well as the EXAFS from the NpO_2 reference.

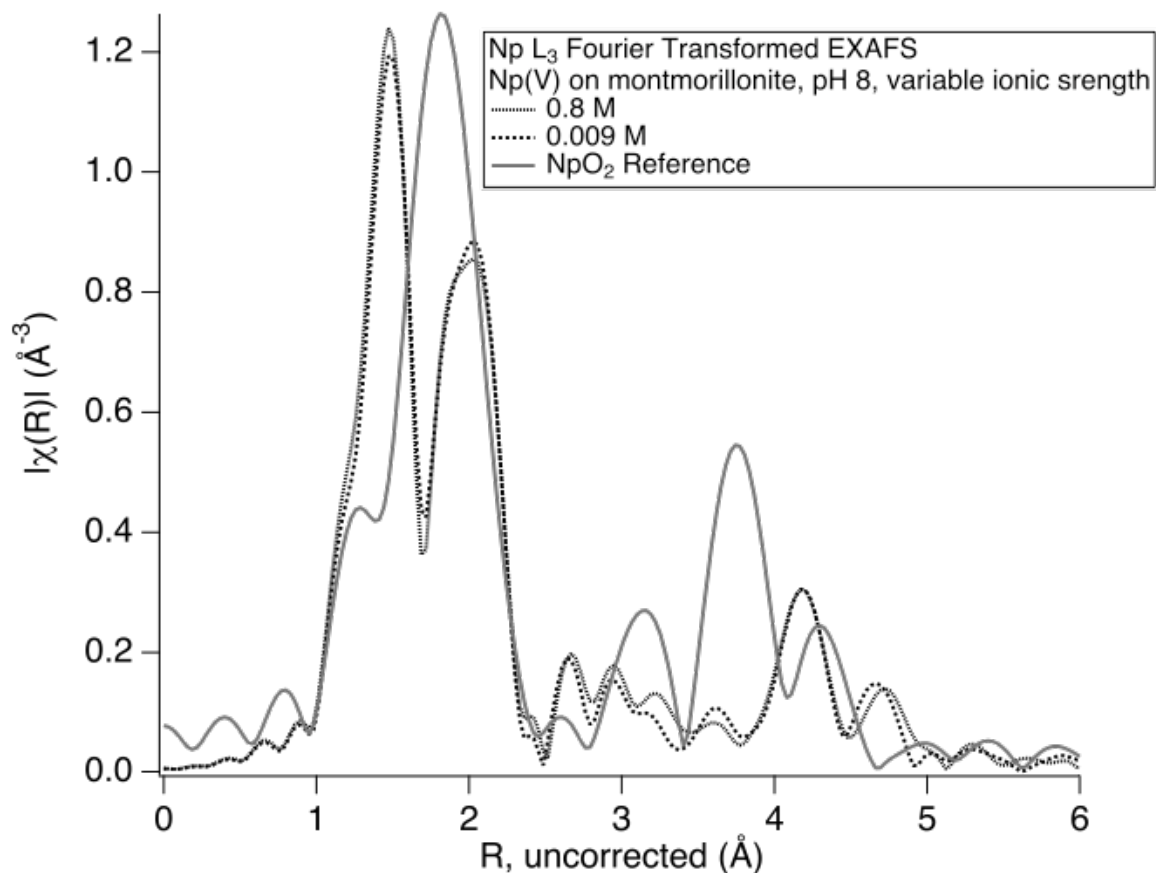


Figure 5: Fourier transform of the EXAFS spectra of the Np(V) sorbed to montmorillonite at pH 8 at high and low ionic strengths. Strong scattering contributions can be seen from the axial and radial oxygen atoms. The Fourier transform is also shown for the NpO₂ reference, which shows scattering characteristic of a single oxygen coordination sphere, and Np-Np scattering at $R = 3.76 \text{ \AA}$.

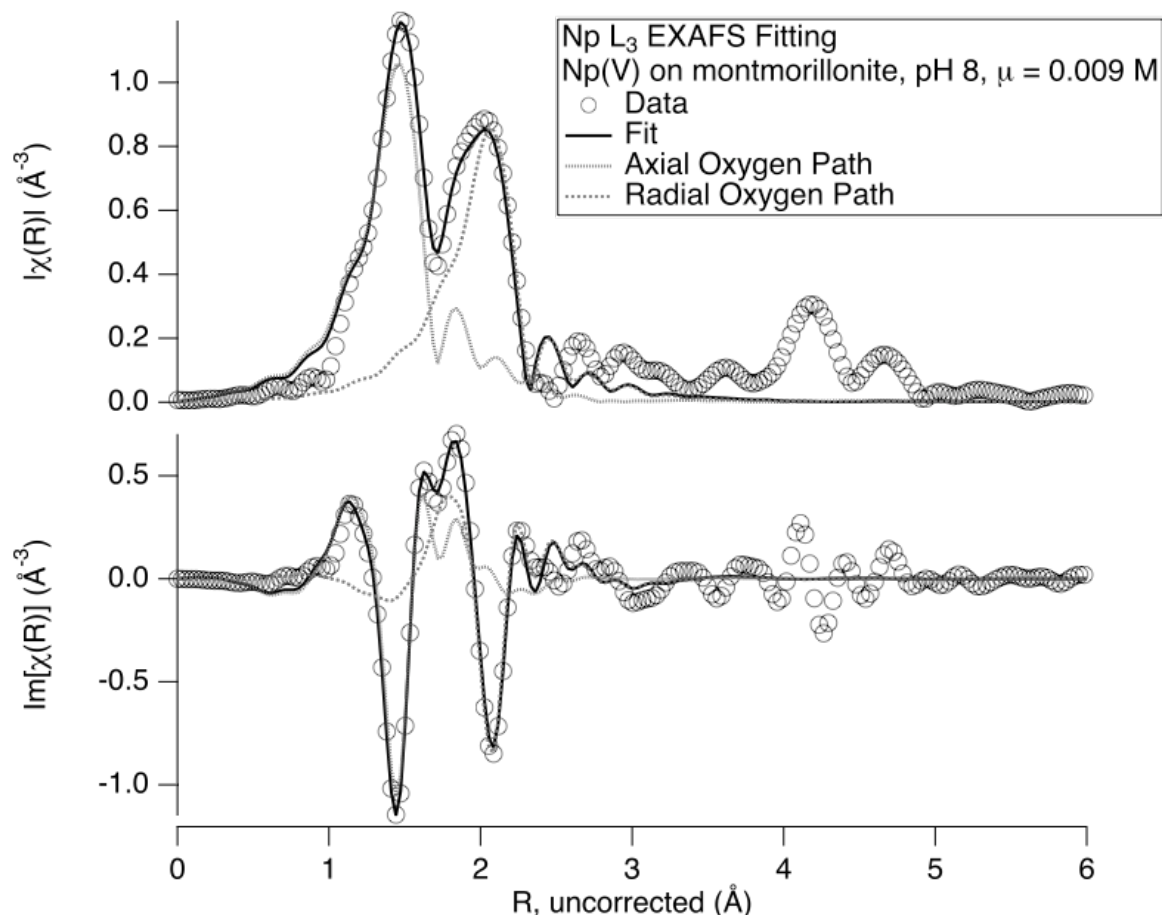


Figure 6: The magnitude and imaginary components of the EXAFS fitting of the Np(V) sorbed to montmorillonite at pH 8 at low ionic strength of 0.009 M. The data and fit are shown, along with the axial and radial oxygen single scattering paths that make up the fit.

Table 2: Fitting results for the two Np(V) montmorillonite data sets, uncertainties determined by inversion of the covariance matrix. There were 14.27 independent points, and 7 variables in each fit.

Parameter	0.8 M data	0.009 M data
Energy shift (E_0), eV	8.1 ± 1.3	8.3 ± 1.7
Axial oxygen amplitude	2.1 ± 0.3	2.1 ± 0.2
Axial oxygen distance, Å	1.86 ± 0.01	1.87 ± 0.01
Axial oxygen σ^2 , Å ²	0.0004 ± 0.0012	0.0006 ± 0.0011
Radial oxygen amplitude	4.4 ± 0.7	4.4 ± 0.6
Radial oxygen distance, Å	2.51 ± 0.01	2.50 ± 0.01
Radial oxygen σ^2 , Å ²	0.0019 ± 0.0017	0.0016 ± 0.0014
Goodness-of-fit, R-factor	0.0285	0.0259

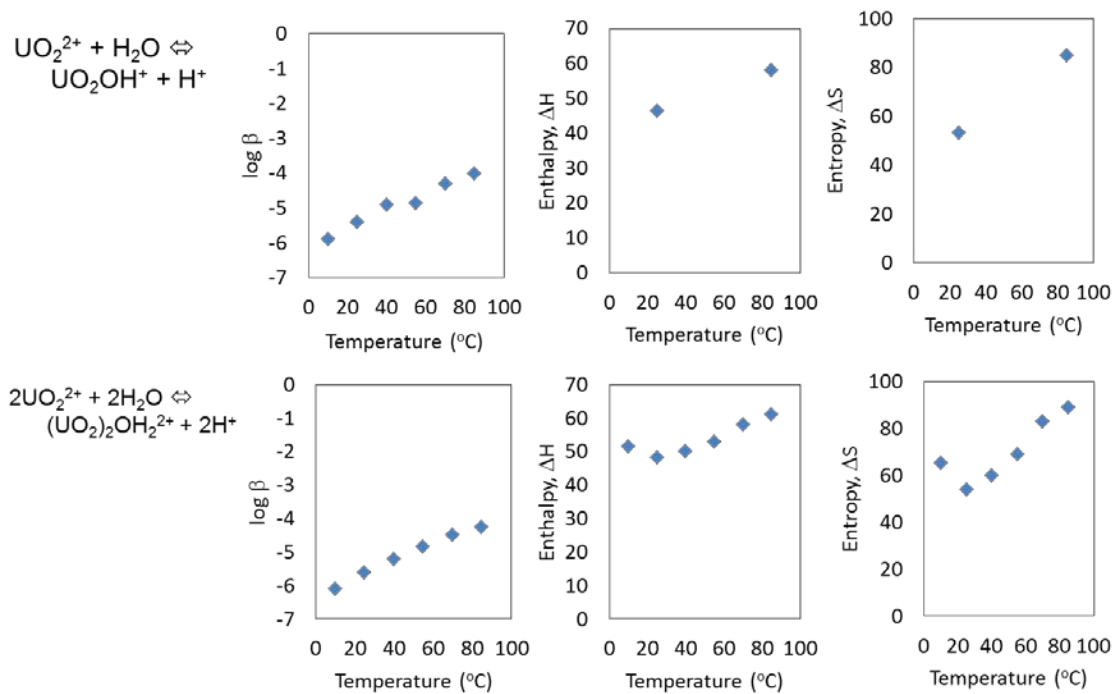


Figure S1: Log stability constants, entropy, and enthalpy of the formation of UO_2OH^+ and $(\text{UO}_2)_2(\text{OH})_2^{2+}$. Data are from Zanonato *et al.*¹⁴ The data show that both 1:1 and 2:2 uranium hydrolysis species become more favorable with increasing temperature. In both cases, the endothermic hydrolysis enthalpy is overcome by a strongly positive entropy value.

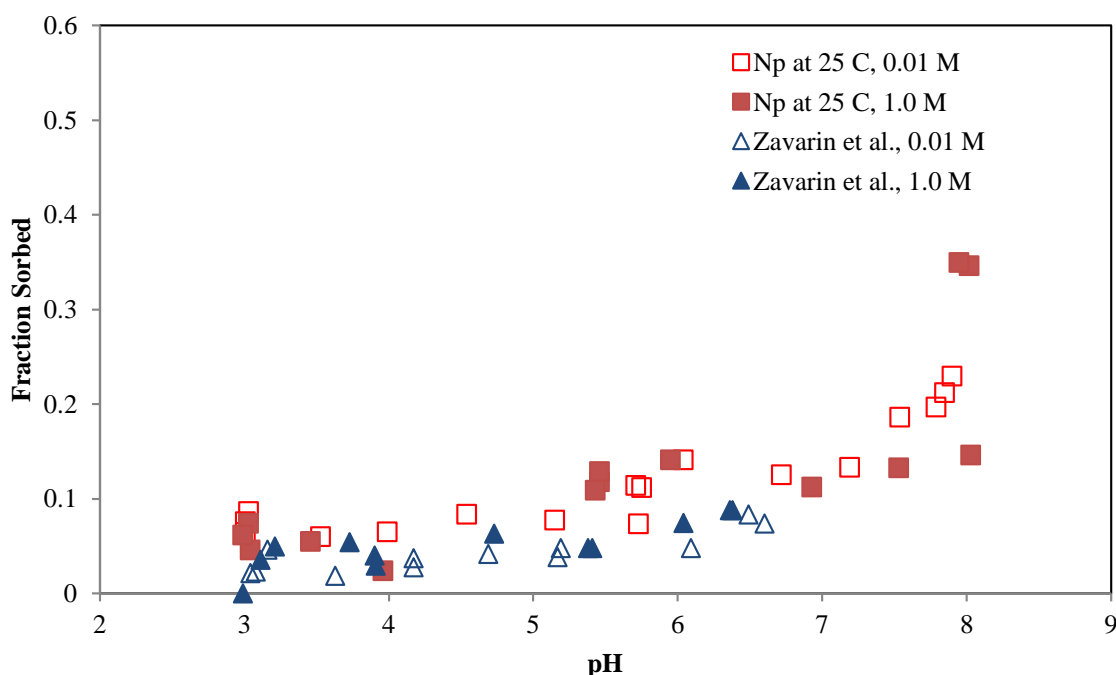


Figure S2: Comparison of Np(V) sorption to montmorillonite measured in this work and reported by Zavarin *et al.*¹² Numbers in the figure legend refer to the concentration of NaCl in the system. Experiments in this work were performed in a controlled 25°C atmosphere and those by Zavarin *et al.*¹² were performed under ambient laboratory conditions (~20 °C). As shown in Figure 1 above, there is a significant influence of temperature on Np(V) sorption. Thus it is possible the slightly higher sorption observed in this work is due to the difference in temperature between the two studies.

References

- (1) Carlton, W. H. Assessment of Neptunium, Americium, and Curium in the Savannah River Site Environment (U). **1997**, *WSRC-TR-97*.
- (2) Cantrell, K. J. Transuranic Contamination in Sediment and Groundwater at the U.S. DOE Hanford Site. **2009**, *PNNL-18640* (August).
- (3) Bowen, S. M.; Finnegan, D. L.; Thompson, J. L.; Miller, C. M.; Baca, P. L.; Olivas, L. F.; Geoffrion, C. G.; Smith, D. K.; Goishi, W.; Esser, B. K.; et al. Nevada Test Site Radionuclide Inventory, 1951-1992. **2001**, *LA-13859-M* (September).
- (4) Smith, D. K.; Finnegan, D. L.; Bowen, S. M. An Inventory of Long-Lived Radionuclides Residual from Underground Nuclear Testing at the Nevada Test Site, 1951-1992. *J. Environ. Radioact.* **2003**, 67 (1), 35–51.
- (5) Hennig, C.; Reich, T.; Dähn, R.; Scheidegger, a. M. Structure of Uranium Sorption Complexes at Montmorillonite Edge Sites. *Radiochim. Acta* **2002**, 90 (9-11), 653–657.
- (6) Beall, G. W.; Allard, B. Sorption of Actinides from Aqueous Solutions Under Environmental Conditions. In *Adsorption From Aqueous Solutions*; Springer US: New York, NY, 1981; pp 193–212.

- (7) Allard, B.; Olofsson, U.; Torstenfelt, B. Environmental Actinide Chemistry. *Inorganica Chim. Acta* **1984**, *94*, 205–221.
- (8) Torstenfelt, B.; Rundberg, R. S.; Mitchell, A. J. Actinide Sorption on Granites and Minerals as a Function of pH and Colloids/Pseudocolloids. *Radiochim. Acta* **1988**, *44-45*, 111–117.
- (9) Triay, I. R.; Robinson, B. A.; Lopez, R. M.; Mitchell, A. J.; Overly, C. M. Neptunium Retardation with Tuffs and Groundwaters from Yucca Mountain. In *1993 International High-level Radioactive Waste Management Conference*; 1993.
- (10) Bertetti, F. P.; Pabalan, R. T.; Almendarez, M. G. Studies of Neptunium(V) Sorption on Quartz, Clinoptilolite, Montmorillonite, and α -Alumina. In *Adsorption of Metals by Geomedia*; Jenne, E. A., Ed.; Academic Press, 1998; pp 131–148.
- (11) Sabodina, M. N.; Kalmykov, S. N.; Sapozhnikov, Y. a.; Zakharova, E. V. Neptunium, Plutonium and ^{137}Cs Sorption by Bentonite Clays and Their Speciation in Pore Waters. *J. Radioanal. Nucl. Chem.* **2006**, *270* (2), 349–355.
- (12) Zavarin, M.; Powell, B. A.; Bourbin, M.; Zhao, P.; Kersting, A. B. Np(V) and Pu(V) Ion Exchange and Surface-Mediated Reduction Mechanisms on Montmorillonite. *Environ. Sci. Technol.* **2012**, *46* (5), 2692–2698.
- (13) Turner, D. R. Neptunium(V) Sorption on Montmorillonite: An Experimental and Surface Complexation Modeling Study. *Clays Clay Miner.* **1998**, *46* (3), 256–269.
- (14) Zanonato, P.; Di Bernardo, P.; Bismondo, A.; Liu, G.; Chen, X.; Rao, L. Hydrolysis of Uranium(VI) at Variable Temperatures (10–85°C). *J. Am. Chem. Soc.* **2004**, *126* (17), 5515–5522.
- (15) Silva, R. J.; Nitsche, H. Actinide Environmental Chemistry. *Radiochim. Acta* **1995**, *70-71* (Supplement), 377–396.
- (16) Choppin, G. R. Actinide Speciation in the Environment. *J. Radioanal. Nucl. Chem.* **2007**, *273* (3), 695–703.
- (17) Hu, Y.-J.; Kestrel Schwaiger, L.; Booth, C. H.; Kukkadapu, R. K.; Cristiano, E.; Kaplan, D.; Nitsche, H. Molecular Interactions of plutonium(VI) with Synthetic Manganese-Substituted Goethite. *Radiochim. Acta* **2010**, *98* (9-11), 655–663.
- (18) Bearden, J. A.; Burr, A. F. Reevaluation of X-Ray Atomic Energy Levels. *Rev. Mod. Phys.* **1967**, *39* (1), 125–142.
- (19) Rehr, J. J.; Albers, R. C. Theoretical Approaches to X-Ray Absorption Fine Structure. *Rev. Mod. Phys.* **2000**, *72* (3), 621–654.
- (20) *X-Ray Absorption: Principles, Applications, Techniques of EXAFS, SEXAFS and XANES*; Koningsberger, D. C., Prins, R., Eds.; John Wiley and Sons: New York, NY, 1988.
- (21) Ravel, B.; Newville, M. ATHENA, ARTEMIS, HEPHAESTUS: Data Analysis for X-Ray Absorption Spectroscopy Using IFEFFIT. *J. Synchrotron Radiat.* **2005**, *12* (4), 537–541.
- (22) Webb, S. M. SIXPack a Graphical User Interface for XAS Analysis Using IFEFFIT. *Phys. Scr.* **2005**, *115*, 1011–1014.
- (23) De Leon, J.; Rehr, J. J.; Zabinsky, S. I.; Albers, R. C. Ab Initio Curved-Wave X-Ray-Absorption Fine Structure. *Phys. Rev. B* **1991**, *44* (9), 4146–4156.
- (24) Rehr, J. J.; Albers, R. C. Scattering-Matrix Formulation of Curved-Wave Multiple-Scattering Theory: Application to X-Ray-Absorption Fine Structure. *Phys. Rev. B* **1990**, *41* (12), 8139–8149.
- (25) Rehr, J. J.; de Leon, J.; Zabinsky, S. I.; Albers, R. C. Theoretical X-Ray Absorption Fine Structure Standards. *J. Am. Chem. Soc.* **1991**, *113* (14), 5135–5140.

- (26) Rehr, J. J.; Albers, R. C.; Zabinsky, S. I. High-Order Multiple-Scattering Calculations of X-Ray-Absorption Fine Structure. *Phys. Rev. Lett.* **1992**, *69* (23), 3397–3400.
- (27) Newville, M. EXAFS Analysis Using FEFF and FEFFIT. *J. Synchrotron Radiat.* **2001**, *8* (2), 96–100.
- (28) McKinley, J. P.; Zachara, J. M.; Smith, S. C.; Turner, G. D. The Influence of Uranyl Hydrolysis and Multiple Site-Binding Reactions on Adsorption of U(VI) to Montmorillonite. *Clays Clay Miner.* **1995**, *43* (5), 586–598.
- (29) Powell, B. A.; Kersting, A.; Zavarin, M.; Zhao, P. Development of a Composite Non-Electrostatic Surface Complexation Model Describing Plutonium Sorption to Aluminosilicates. **2011**, *LLNL-TR-40*.
- (30) Denecke, M. A.; Dardenne, K.; Marquardt, C. M. Np(IV)/Np(V) Valence Determinations from Np L3 Edge XANES/EXAFS. *Talanta* **2005**, *65* (4), 1008–1014.
- (31) Bunker, G. *Introduction to XAFS: A Practical Guide to X-Ray Absorption Fine Structure Spectroscopy*; Cambridge University Press Cambridge: UK, 2010.
- (32) Forbes, T. Z.; Burns, P. C.; Skanthakumar, S.; Soderholm, L. Synthesis , Structure , and Magnetism of Np₂O₅. *J. Am. Chem. Soc.* **2007**, *129* (10), 2760–2761.

APPENDIX E: REPORT FOR MILESTONE: M3NU-11-SC-CU__-0204-0210: CALORIMETRIC TITRATIONS OF ACTINIDE SORPTION TO MONTMORILLONITE

Reporting Status: The following report was uploaded to PICSNE which describes work done up to the end of this project on September 30, 2015. Because of the difficulties encountered modeling the hematite ITC data, we did not have sufficient time to perform detailed experiments with montmorillonite. So this is an abbreviated study examining surface reactivity of montmorillonite and Eu(III) sorption at 25 °C and ionic strengths of 0.01 M, 0.10M and 1.0 M using NaCl. The results are considered a preliminary study and are not suitable for publication. A great lesson in subtraction of dilution heats was learned. When performing the titrations, the 0.01 M NaOH titrant solution must be adjusted to the appropriate ionic strength. Otherwise, dilution heats from the changing ionic strength cause a swamping signal and masks the true data.

Examination of Eu(III) sorption to montmorillonite using isothermal titration calorimetry

Yu Xie and Brian A. Powell
Environmental Engineering and Earth Sciences, Clemson University

DOE NEUP Project: Quantification of cation sorption to engineered barrier materials under extreme conditions (Project #11-3180)

Report in fulfillment of Milestone: Milestone: M3NU-11-SC-CU__-0204-0210: Calorimetric titrations of actinide sorption to montmorillonite

Method

Isothermal Titration Calorimetry

Three sets of ITC titrations were conducted by incrementally titrating 0.01 M NaOH into 10 g/L montmorillonite suspensions (initially adjusted to pH ~3.5) with ionic strength of 0.01 M, 0.1 M, and 1 M respectively using NaCl. Three sets of Eu ITC titrations were also conducted by incrementally titrating a 5mM EuCl₃ solution (I = 0.01 M adjusted using NaCl) into 10 g/L montmorillonite suspension with ionic strength of 0.01 M, 0.1 M and 1 M respectively. Both the EuCl₃ titrant and montmorillonite suspension were adjusted at a constant pH 5. During each titration, 16 additions of 13 μ L were added to 0.8 ml of montmorillonite suspension with a 30 minute delay between additions. The pH of the montmorillonite suspension was monitored before titration and after titration. The concentration of initial Eu and aqueous Eu at the end of each titration was monitored using inductively coupled plasma mass spectrometry (ICP-MS). To examine the influence of dilution heats, background ITC titrations were also conducted by incrementally titrating 0.01 M NaCl to 0.1 M NaCl and 1 M NaCl solutions without montmorillonite present.

Results

Acid-base titrations of montmorillonite suspensions

A 10 g/L montmorillonite suspension in 0.01 M NaCl was titrated with 0.01 M NaOH. A small volume of HCl was initially added to lower the pH to 3.8. The exact experimental parameters are provided in table 1 and the thermogram is shown in Figure 1.

Table 7: ITC base titration to montmorillonite experiment set up

Weight measurement (g)	Sample	Reference	Ionic Strength (M)
Ampoule Weight	11.3737	11.3367	
Montmorillonite	0.0074	0.0083	
NaCl (0.01 M)	0.5128	0.5274	
HCl (0.01 M)	0.3012	0.3020	
pH (pre-ITC titration)	3.42	4.28	0.01
pH (after-ITC titration)	8.94	4.92	0.01

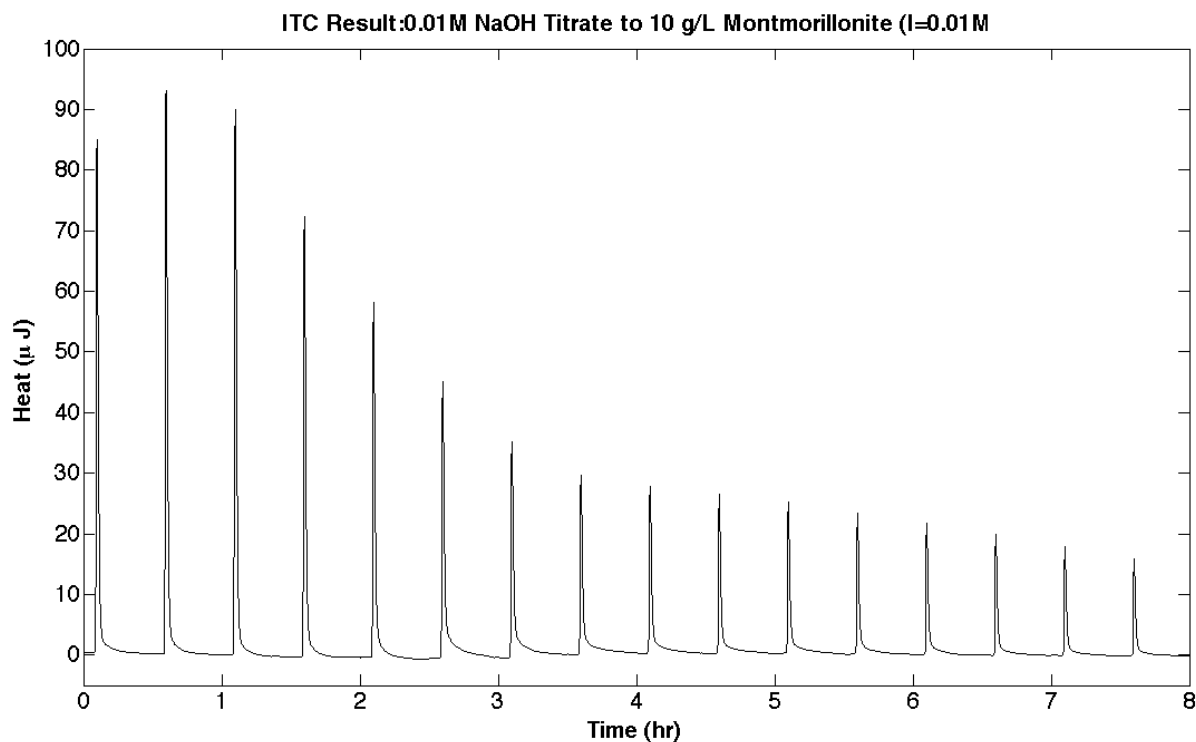


Figure 1: Heat flow of 0.01 M NaOH titrated to 10 g/L Montmorillonite (I = 0.01 M)

A 10 g/L montmorillonite suspension in 0.1 M NaCl was titrated with 0.01 M NaOH. A small volume of HCl was initially added to lower the pH but after equilibration, the initial pH was 8. The exact experimental parameters are provided in table 2 and the thermogram is shown in figure 2.

Table 8: ITC base titration to montmorillonite experiment set up

Weight measurement (g)	Sample	Reference	Ionic Strength (M)
Ampoule Weight	11.3733	11.3370	
Montmorillonite	0.0084	0.0080	
NaCl (0.1 M)	0.6578	0.6656	
HCl (0.01 M)	0.1610	0.1611	
pH (pre-ITC titration)	3.61	3.87	0.082
pH (after-ITC titration)	9.91	8.25	0.068

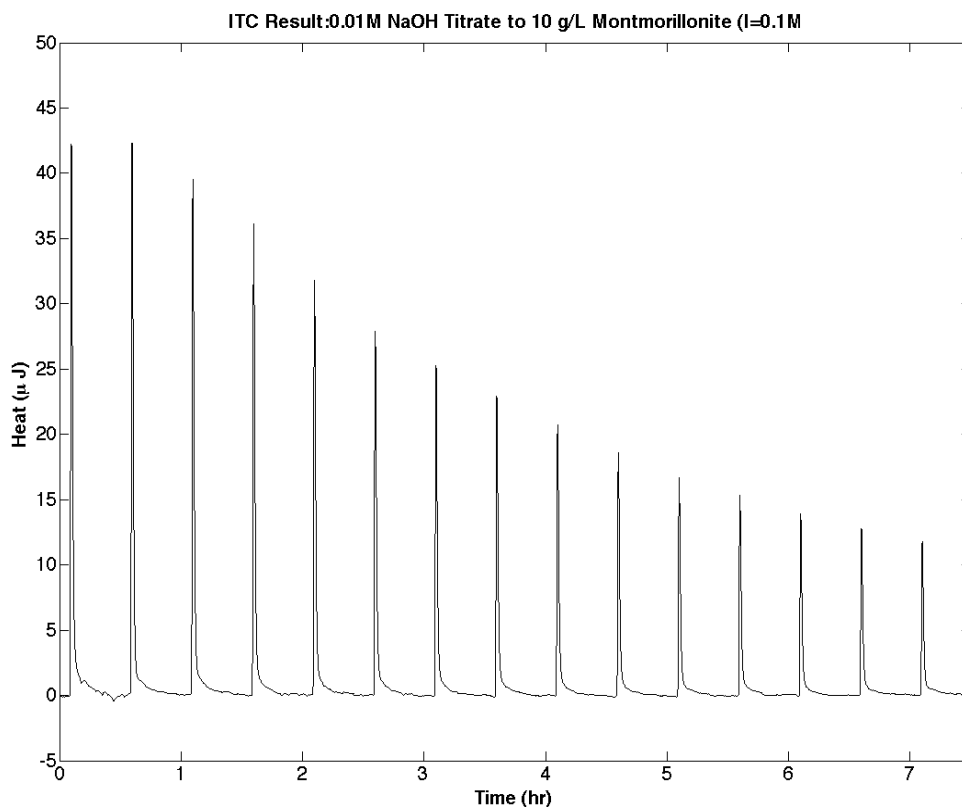


Figure 2: Heat flow of 0.01 M NaOH titrated to 10 g/L Montmorillonite (I = 0.1 M)

A 10 g/L montmorillonite suspension in 1.0 M NaCl was titrated with 0.01 M NaOH. A small volume of HCl was initially added to lower the pH but after equilibration, the initial pH was 8. The exact experimental parameters are provided in table 3 and the thermogram is shown in figure 3. The thermogram indicates an endothermic reaction is occurring. It was initially suspected this was due to ion exchange effects. However, background titrations adding 0.01 M NaCl to 1.0 M NaCl indicate that the dilution heats are quite significant and responsible for these endothermic peaks.

Table 9: ITC base titration to montmorillonite experiment set up

Weight measurement (g)	Sample	Reference	Ionic Strength (M)
Ampoule Weight	11.3083	11.3083	
Montmorillonite	0.0079	0.0084	
NaCl (1 M)	0.6240	0.6297	
HCl (0.01 M)	0.2014	0.2010	
pH (pre-ITC titration)	3.46	3.24	0.76
pH (after-ITC titration)	9.67	7.61	0.62

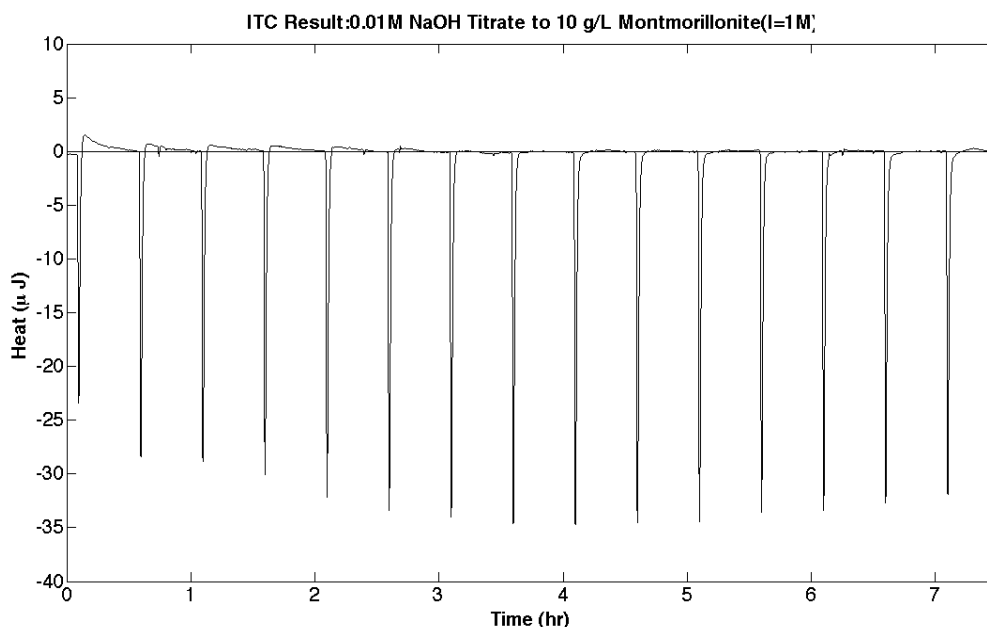


Figure 3: Heat flow of 0.01 M NaOH titrated to 10 g/L Montmorillonite (I = 1 M)

ITC Measurements: EuCl_3 titration to montmorillonite at pH 5

Determination of the aqueous Eu concentrations in the final solution after titrations indicated that 95%, 80%, and 20% sorption occurred at ionic strengths of 0.01 M, 0.10 M, and 1.0 M NaCl, respectively. Thus, the competition with Na^+ for sorption sites significantly reduced Eu(III) sorption as expected based on previous batch sorption studies. This effect combined with the relatively high background due to dilution of the high ionic strength NaCl systems caused significant problems when analyzing the data. The thermograms from these titrations are shown in figures 4-6. While the expected endothermic heat release is observed, the data are compromised by the dilution heat of the changing ionic strength over the course of the titration. Thus correction of the data is required.

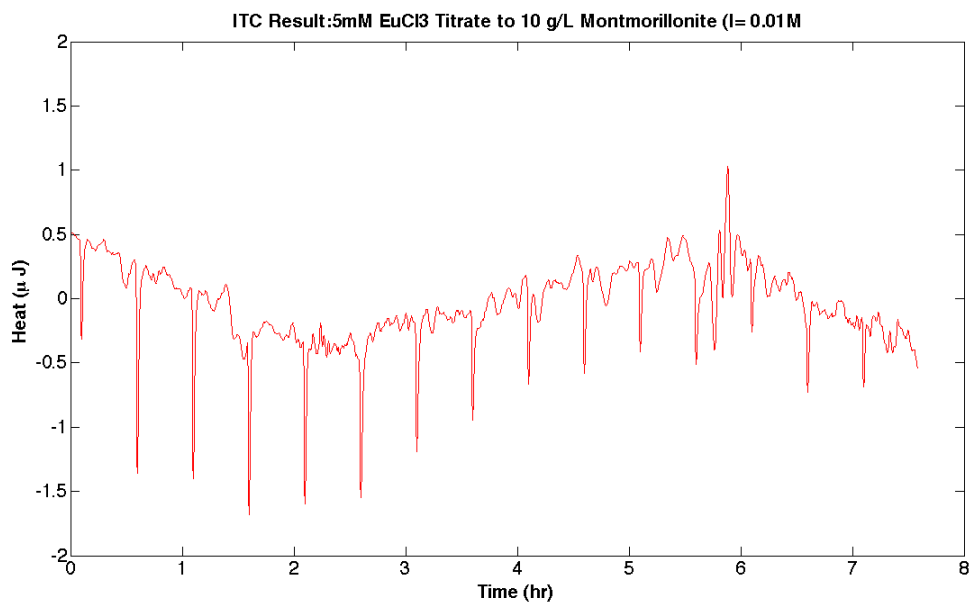


Figure 4: Heat flow of 5 mM of EuCl₃ titrated to 10 g/L Montmorillonite (I = 0.01 M, pH ~5)

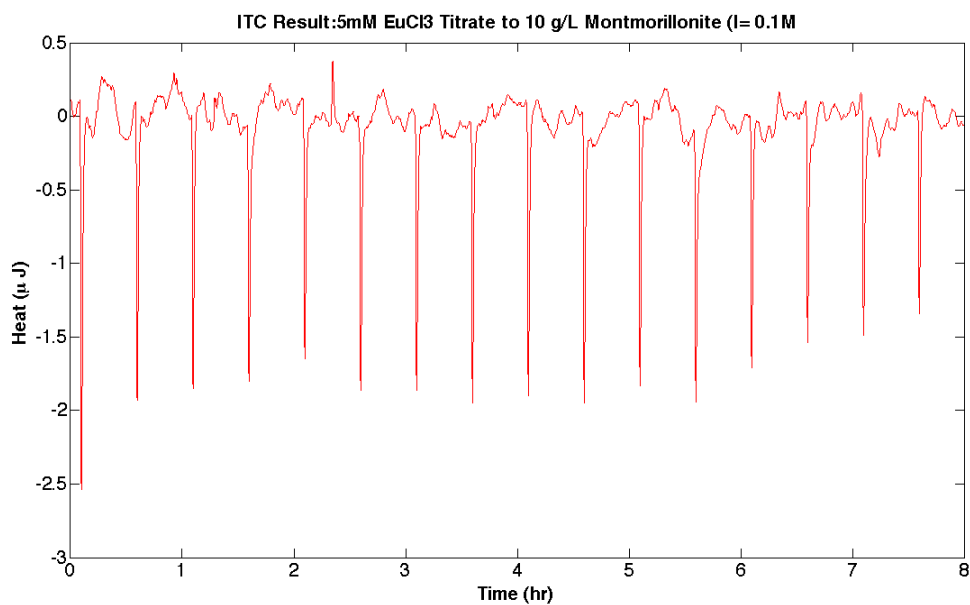


Figure 5: Heat flow of 5 mM of EuCl₃ (I = 0.01M) to 10 g/L montmorillonite (I = 0.1M; pH ~5)

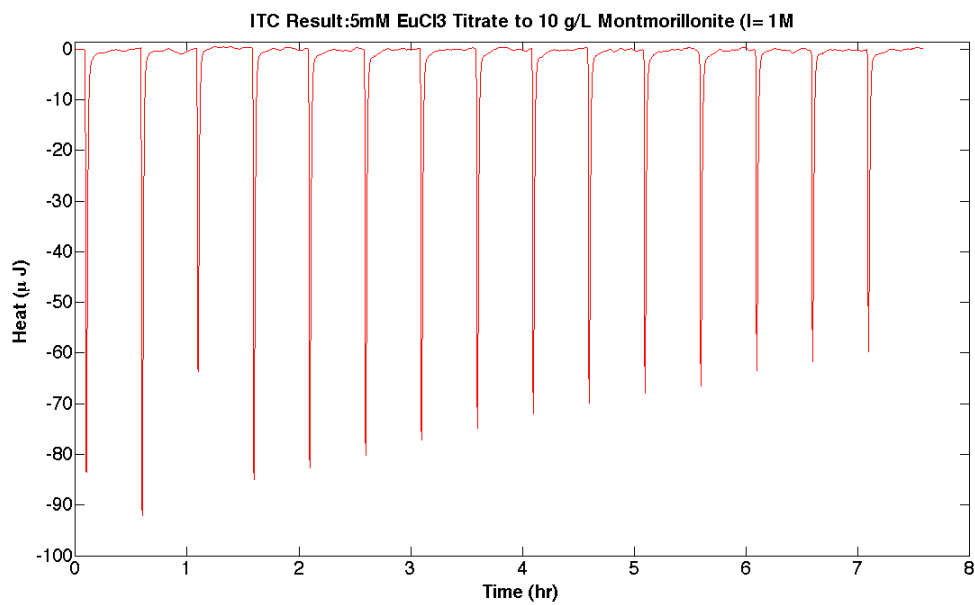


Figure 6: Heat flow of 5 mM of EuCl₃ (I = 0.01M) to 10 g/L montmorillonite (I = 1M; pH ~5)

Background titrations of variable ionic strength solutions at a constant pH.

To examine the influence of dilution heats, a 0.01 M NaCl solution was titrated into both 0.10 M NaCl and 1.0 M NaCl. The thermograms for these titrations are shown in figures 7 and 8 and the results indicate that titrating high ionic strength, the dilution heat dominates the signal.

Therefore, some of the endothermic peaks observed in the titrations discussed above are due to these dilution heats and not necessary due to the protonation/deprotonation, ion exchange, and Eu(III) sorption reactions. Thus future titrations must adjust the ionic strength to a consistent level to avoid this high background during ITC experiments.

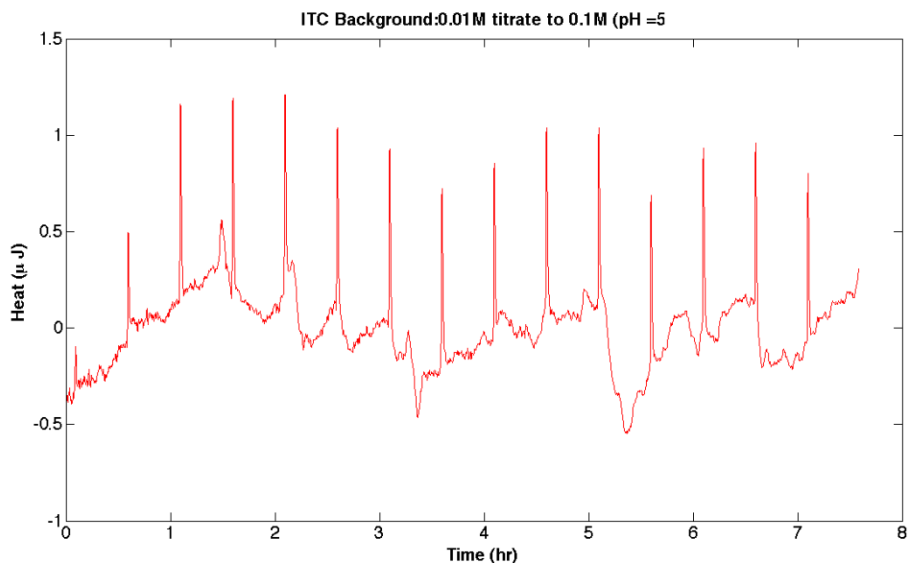


Figure 7: Heat flow of 0.01 M NaCl titration to 0.1 M NaCl. (pH ~ 5)

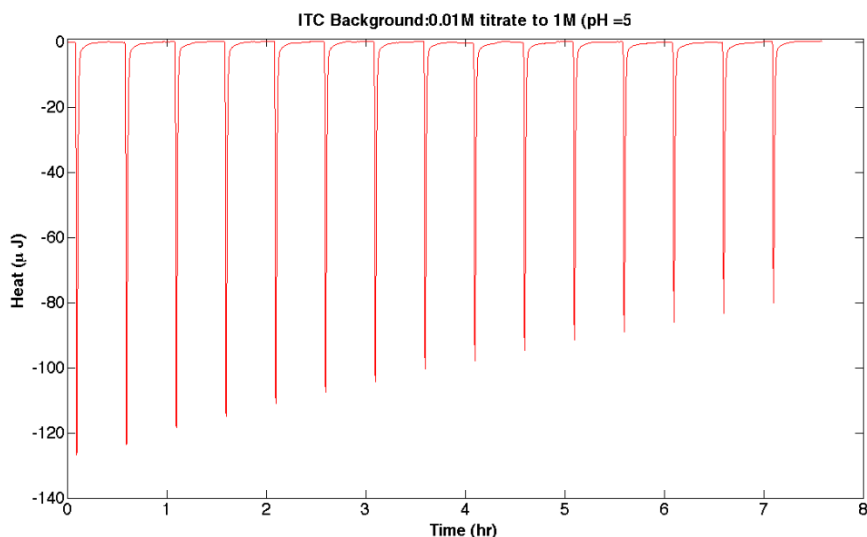


Figure 8: Heat flow of 0.01 M NaCl titration to 1 M NaCl (pH ~ 5).

APPENDIX F: REPORT FOR MILESTONE: M3NU-11-SC-CU__-0204-0211: EVALUATION OF BENTONITE PERFORMANCE UNDER REPOSITORY CONDITIONS

Reporting Status:

The following report was uploaded to PICSNE showing the data collected up to the end of this project on September 30, 2015. The studies are continuing and additional data will be included in an eventual peer reviewed publication based on this study. In particular, we will complete the experiments at 50 °C and attempt experiments at 80 °C. Additionally, we will segment the clay plugs from all experiments and measure the Np concentration as a function of distance from the inlet of the cell. A more rigorous quantitative model than what is presented below will be applied to the data which will also include evaluation of the solid phase Np concentration measurements.

Evaluation of Bentonite Engineered Barrier Performance Under Repository Conditions: Diffusion of Np(V) through Montmorillonite

Rachel Pope, Mark Schlautman, and Brian. A Powell

Environmental Engineering and Earth Sciences, Clemson University

DOE NEUP Project: Quantification of cation sorption to engineered barrier materials under extreme conditions (Project #11-3180)

Report in fulfillment of Milestone: M3NU-11-SC-CU__-0204-0211: Evaluation of bentonite performance under repository conditions

Introduction

The purpose of this research is to examine the diffusion of $^{237}\text{Np(V)}$ through montmorillonite clay under elevated temperatures. Np(V) is a byproduct in high level nuclear waste that causes concern if mobile in the environment. Heat and water can contribute to corrosion of stainless steel canisters that house nuclear waste and potentially lead to leaching of radioisotopes overtime. To mitigate this, a barrier consisting of highly compacted clay provides secondary containment. The hydraulic conductivity of this system is low because the dry bulk density of the clay is so high that the only pathway for radionuclides to move through the environment is via molecular diffusion. Thus, diffusion cells were constructed that contain the compacted clay, and the diffusion of $^{237}\text{Np(V)}$ and ^3H through montmorillonite was studied. Experiments were conducted at elevated temperatures with various dry bulk densities to simulate the conditions of the engineered barrier surround the stainless steel canisters. Samples were analyzed with liquid scintillation counting (LSC) and inductively-coupled plasma-mass spectroscopy (ICP-MS).

Materials and Methods

Diffusion cells were constructed based off the designs proposed in S. Brockman's analysis of *Migration of Caesium in Bentonite (2006)*¹. All parts of the cell were composed of 316L stainless steel. The top of the cell was formed into a t-shape with an inlet and an outlet for threaded tubing connectors. The fittings that connected the tubing to the diffusion cells were Swagelok male connectors (Part number -100-1-1). Furthermore, the top had holes for bolts and washers which extend to the bottom of the cell and can be adjusted to alter the pressure inside the sample chamber. Sintered stainless steel 316L filters with a pore diameter of 20 μm were used (MOTT industrial division, Farmington, USA) to provide a uniform, saturated front at the inlet and outlet of the cell. O-rings (AS568-210 Viton 75) were used to maintain a seal inside the sample chamber. A load cell connected to a digital display from Omega Engineering was attached to the bottom of each diffusion cell to monitor the pressure inside the sample chamber. Diagrams of the diffusion cell setup and flow paths are shown in Figures 1-3.

Solutions were run through an 8-channel Ismatec peristaltic pump using peristaltic tubing with an inner diameter of 0.5 mm (Fisherbrand, Cat No. 14-190-502). Tubing running into and out of the diffusion cells was semi-rigid PEEK tubing with an inner diameter of 0.5 mm (Agilent Technologies, Part No. 0890-1761). Connectors were used to connect the soft peristaltic pump tubing to the semi-rigid PEEK tubing (Idex, P-794).

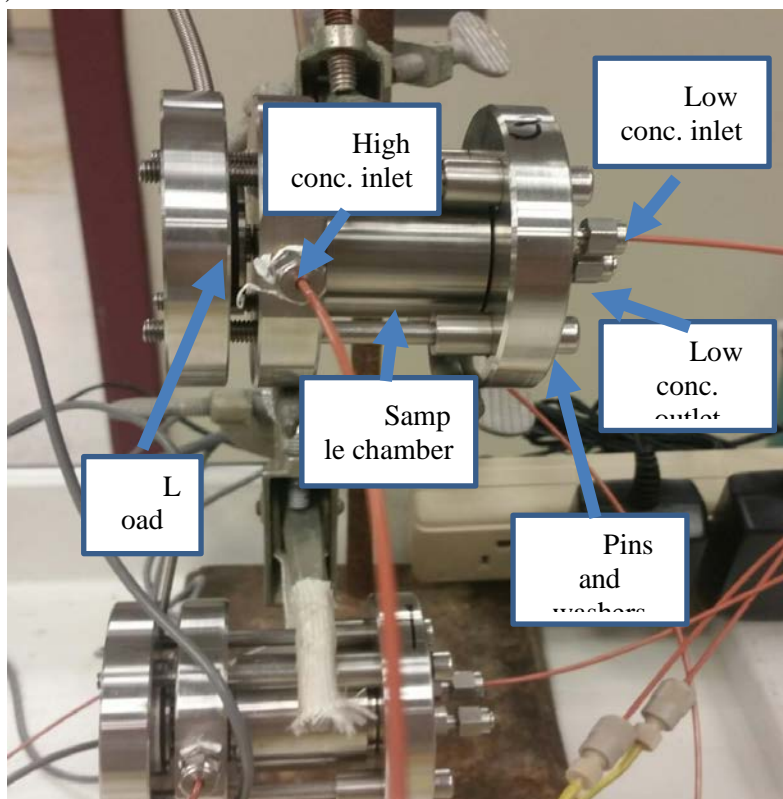


Figure 1. Labeled diffusion cell

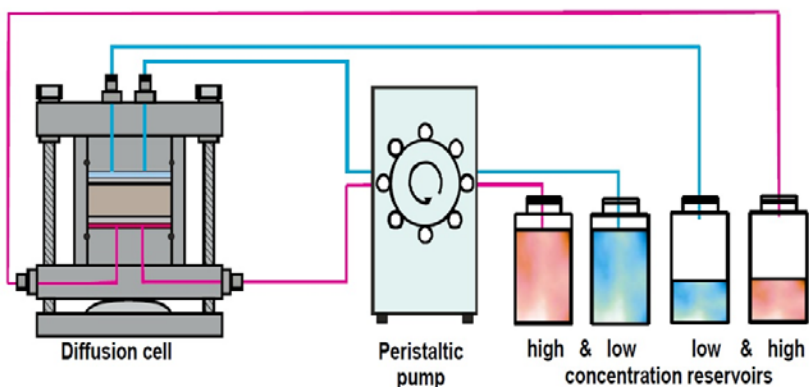


Figure 2. Schematic representation of experimental setup.¹

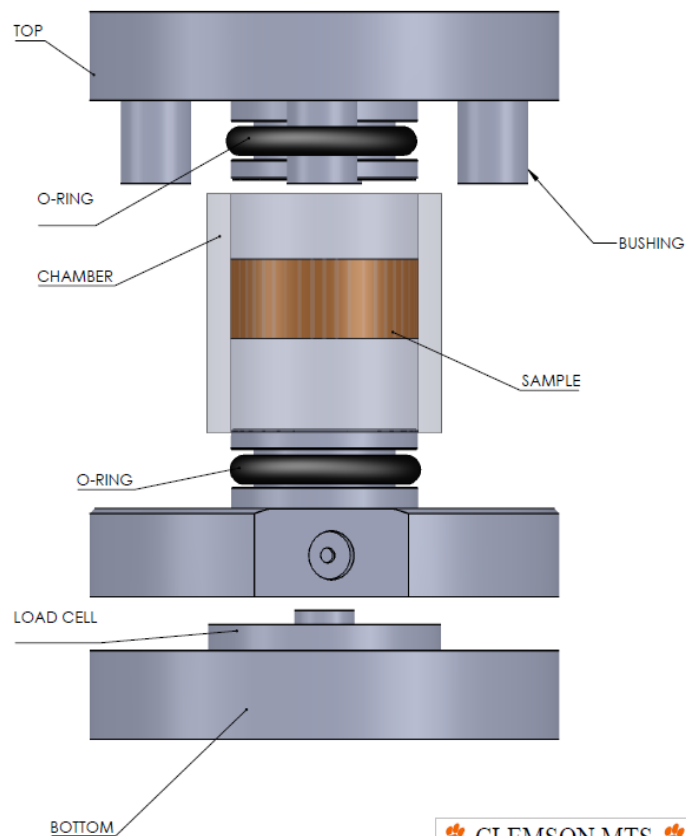


Figure 3. Deconstructed representation of diffusion cell.

Diffusion of radioisotopes

Diffusion experiments through montmorillonite clay were performed using ^3H and $^{237}\text{Np(V)}$ over a range of dry bulk densities (1.15 to 1.6 g cm^{-3}) and elevated temperatures (25°C and 50°C). Because the cells were loaded with dry clay, the cells were initially saturated with 0.1 M NaCl adjusted to $\text{pH } 6$. This process took approximately four weeks to complete. The diffusion cells were oriented vertically for the saturation process. Since the inside of each cell could not physically be observed, the pressure inside the sample chamber was monitored until a steady pressure was reached. This steady state of pressure and the observation of outflow water indicated that the saturation process was complete and the diffusion of the radioisotopes could begin. The pressure was also recorded every time a sample was taken to ensure the porosity stayed relatively consistent (Figure 4). To maintain similar porosities at 25°C and 50°C , the tension bolts were adjusted to maintain similar pressures at each bulk density examined.

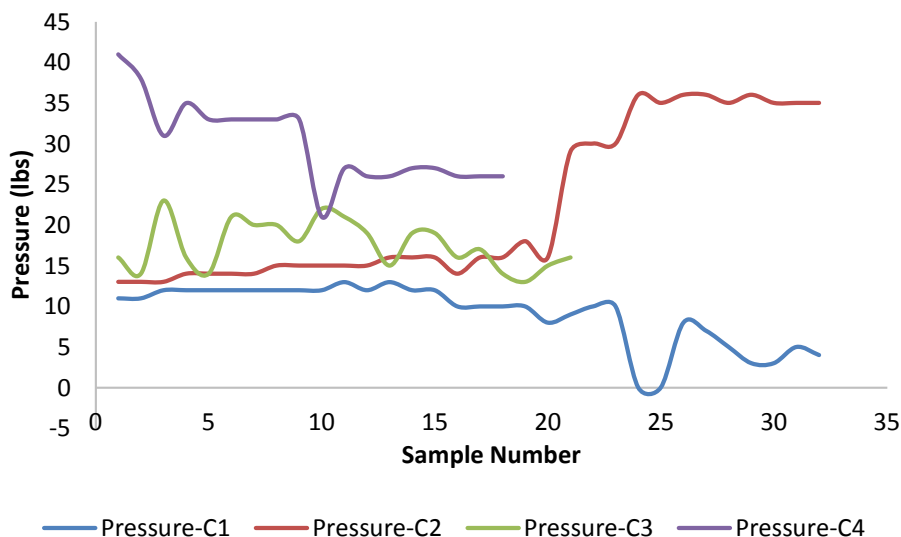


Figure 4. Pressure at each sampling event for each cell.

A high concentration reservoir initially contained 1000 ppb $^{237}\text{Np(V)}$ (approximately 2.63×10^6 Bq ^{237}Np) and 166 Bq/mL ^3H in 100 mL of synthetic pore water. A separate solution was prepared for each diffusion cell. Furthermore, four solutions of low concentration reservoir were made consisting of 20 mL of 0.01 M NaCl at pH 6; no radioisotopes were initially in these low concentration reservoirs. The diffusion cells were oriented horizontally as to avoid any advective flow that could contribute to the final results, allowing for the observation of pure molecular diffusion. Once the high and low concentration solutions were made, each was connected to a cell on one side and circulated through the stainless steel filters on each end of the cell using the peristaltic pump. The high concentration side flowed through the tubing into the cell and back out again on the same side while the low concentration side flowed through the tubing into the cell and back out again on the opposite side. A flow rate of 50 $\mu\text{L}/\text{min}$ was established based on previous experimentation performed by Brockman.¹

After saturation of the diffusion cell and assembly of the low and high concentration reservoirs, sampling of the low concentration reservoir began. Sampling events of the low concentration reservoir occurred approximately every 24 to 48 hours, and the date, time, temperature, and pressure inside the cell were recorded. Two mL were sampled from each low concentration reservoir and stored for analysis. After approximately every five sampling events, the low concentration reservoir solution was replaced with a new bottle containing 20 mL of 0.01 M NaCl at pH 6. This was necessary to ensure the concentration of the radioisotopes in the low reservoir did not exceed ~1% of the concentration in the high reservoir. If the concentrations became too similar, then the concentration gradient would not be significant enough to allow for effective diffusion. The high concentration reservoirs were also sampled once every one to two weeks to ensure that the concentrations of the radioisotopes remained consistent. The diffusion process continued until neptunium breakthrough occurred on the low concentration reservoir side for at least one diffusion cell.

Tritium is a non-sorbing tracer that allows for the diffusion process to be monitored accurately because of its low detection limits. The tritium was added as $^3\text{H}_2\text{O}$ and thus behaves as stable water. Thus,

observation of ^3H in the low concentration reservoir indicates the diffusion cells are working properly. Furthermore, the accumulated activity of tritium is important in data analysis to obtain constants for neptunium diffusion. The tritium samples were analyzed using liquid scintillation counting (LSC) using a 1:5 sample:scintillation cocktail ratio. This diffusion process can be mathematically described using Fick's first and second laws of diffusion. Fick's second law describes the diffusion with a changing concentration gradient. Fick's first law can be applied to the tritium LSC data:

$$J = D_e \cdot \frac{\partial C}{\partial x} \quad [1]$$

where J is diffusive flux [$\text{Bq} \cdot \text{m}^{-2} \cdot \text{s}^{-1}$]
 D_e is the effective diffusion coefficient [$\text{m}^2 \cdot \text{s}^{-1}$]
 C is concentration [$\text{mol} \cdot \text{L}^{-1}$]
 x is distance [m]

D_e can be found by extrapolating constants from accumulated activity in the system which provides a linear relationship

$$A_{cum} = a \cdot t + b \quad [2]$$

where A_{cum} is the linearly accumulated activity [Bq]
 t is time [s]

This linear equation can be rearranged using the following equations to find the effective diffusion coefficient and the dimensionless rock capacity factor.

$$a = \frac{S \cdot C_0 \cdot D_e}{L} \quad [3]$$

where S is the cross section area of the sample [m^2]
 C_0 is the initial concentration [Bq/L]
 L is the sample thickness [m]

$$-b = \frac{S \cdot L \cdot C_0 \cdot \alpha}{6} \quad [4]$$

where α is the rock capacity factor

The effective diffusion coefficient describes the diffusion of a non-sorbing tracer such as tritium through a layer. This constant can be used to find the apparent diffusion coefficient of neptunium through the system using the relationship:

$$D_a = \frac{D_e}{\alpha} \quad [5]$$

where D_a is the apparent diffusion coefficient [$\text{m}^2 \cdot \text{s}^{-1}$]

The tritium data can also be used to calculate the distribution coefficient of neptunium onto montmorillonite.

$$\alpha = \varepsilon + \rho \cdot K_D \quad [6]$$

where ϵ is the effective porosity
 ρ is the dry bulk density of the clay [$\text{g}\cdot\text{cm}^{-3}$]

Because tritium is a non-sorbing tracer, it can be assumed that $K_D=0$ ($\alpha=\epsilon$), so the rock capacity factor determined from the tritium data can be incorporated into equation 6 as the rock capacity factor for the ^{237}Np data. Then equation 6 can be rearranged as follows:

$$K_D = \frac{\alpha - \epsilon}{\rho} \quad [7]$$

where K_D is the equilibrium distribution coefficient [$\text{cm}^3\cdot\text{g}^{-1}$]

Epsilon becomes the rock capacity factor found from the tritium diffusion because. Then the accumulated activity for neptunium can be plotted, and the y-intercept can aid in calculating the K_D based on the equation above.

The actinide of interest in this particular study is $^{237}\text{Np(V)}$. Neptunium is a major byproduct in nuclear waste with a half-life of 2.14 million years. Because ^{237}Np is in a pentavalent oxidation state, it has a low affinity for sorption onto surfaces at environmentally relevant pH values, thus making this actinide highly mobile. The stainless steel canisters that house the nuclear waste have a compacted layer of bentonite surrounding them. One of the major components of bentonite is montmorillonite clay which has a high swelling and ion exchange capacity. In milestone M2NU-11-SC-CU__-0204-028: Examination of actinide sorption to montmorillonite at variable temperatures and variable ionic strengths of this project, sorption of Np(V) to montmorillonite as a function of ionic strength and temperature was monitored. In all cases, sorption of Np(V) has been shown to increase with an increase in temperature. Due to this increase in Np partitioning onto the clay surface, less of the radioisotope will diffuse through the compacted clay. Thus, at elevated temperatures, it is theorized that the diffusion rates of Np(V) will decrease. Because tritium is used in this study as a non-sorbing tracer, this radioisotope will diffuse through the compacted clay at a much higher rate than Np(V) , especially at the higher temperatures. For the analysis of neptunium samples, 0.5 mL of each sample taken were diluted in 2% HNO_3 and analyzed with inductively coupled plasma-mass spectrometry (ICP-MS). Standards for ICP-MS analysis were made using NIST Standard Reference Material 4341 and ranged from 0.01 to 100 ppb neptunium.

Once the diffusion experiments were complete at room temperature, an oven was used to regulate the temperature for the 50°C experiments (Figure 5).



Figure 5. Diffusion Experiment Setup at 50°C.

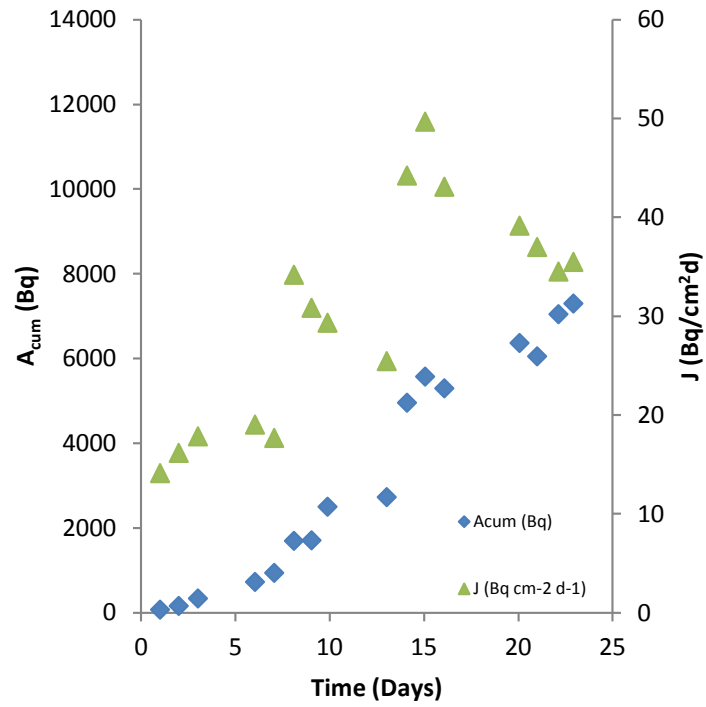
Results and Discussion

Tritium diffusion through montmorillonite at 25°C

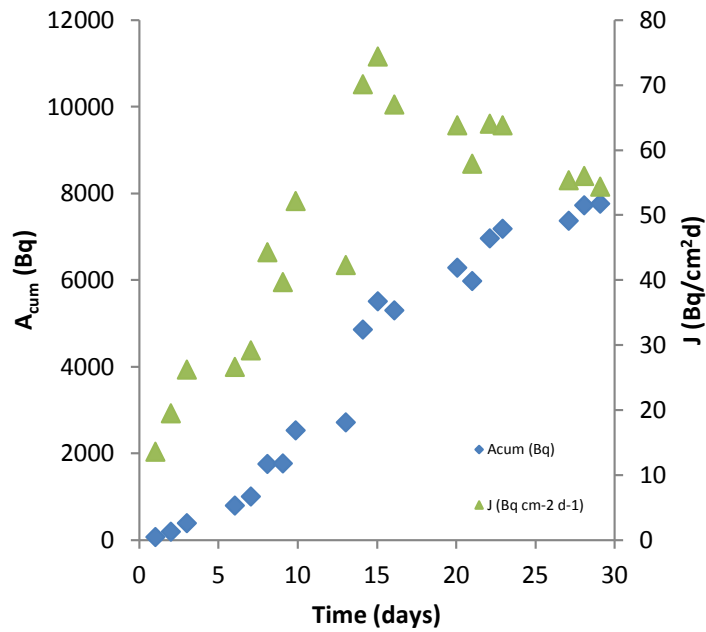
The accumulated activity of tritium (Bq) and diffusive flux (Bq/cm²d) were plotted against time, allowing for linear extrapolation of diffusion constants for each dry bulk density. The data that provided the best linear regression fit between approximately one and 20 days were used. Results for the derived constants are presented in table 1. The initial concentration used for each high concentration reservoir came from the same stock solution made, so all four high concentration solutions have the same high concentration values. The calculated effective diffusion coefficients are in agreement with previous literature values. For 1.15 g/cm³, Trepte² found diffusion coefficients of 1.04×10^{-10} m²/s and 7.36×10^{-11} m²/s which are on the same order of magnitude for the results of 1.15 and 1.30 g/cm³ dry bulk density in this work. The accumulated activity and flux data versus days are shown below in Figure 6 and a comparison of the effective diffusion coefficient as a function of bulk density is shown in Figure 7. While agreement with literature values is promising, these fits to the data are considered preliminary and we are continuing to evaluate these data.

A comparison of the accumulated ³H activity in the low concentration reservoir for each bulk density is shown in Figure 8. It is clear that the amount of ³H diffusing through the cell decreases with increasing bulk density. This is consistent with a decrease in the pore volume, and thus available ³H, with increasing bulk density.

1.15 g/cm³ Dry Bulk Density



1.3 g/cm³ Dry Bulk Density



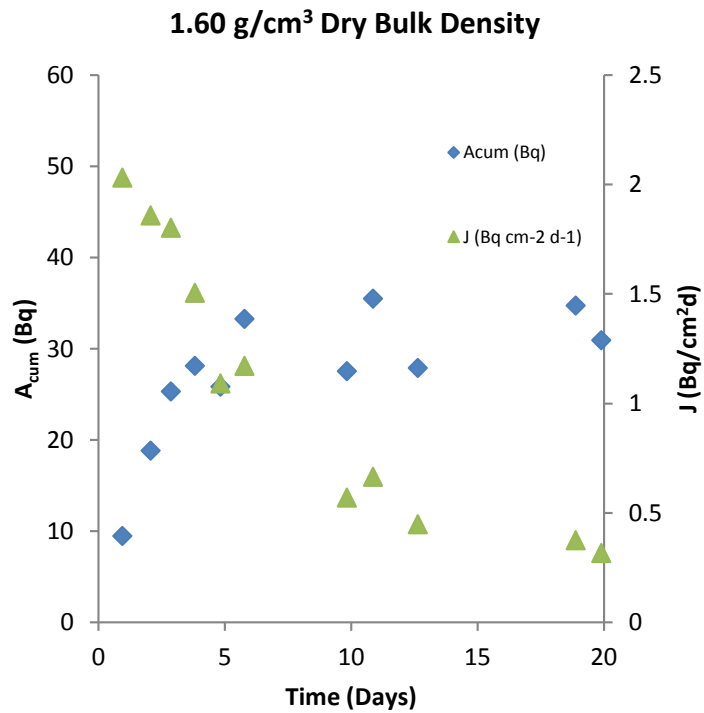
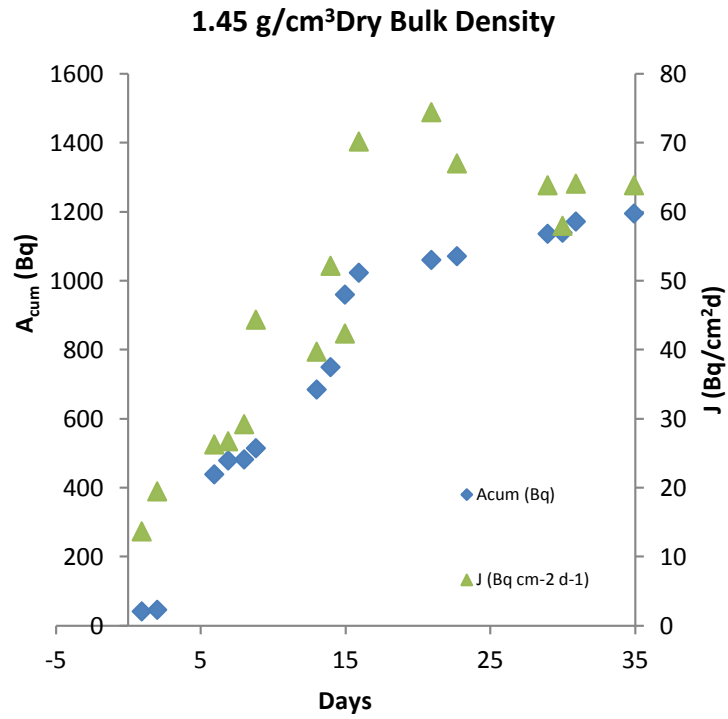


Figure 6. Diffused activity and diffusive flux versus time.

Table 1. The diffusion coefficients and effective porosities for tritium at 25°C.

Bulk Density	C_o (Bq/m³)	De (m²/s)
1.15	1.86E+08	2.03E-10
1.3	1.86E+08	9.48E-11
1.45	1.86E+08	4.02E-11
1.6	1.86E+08	2.63E-12

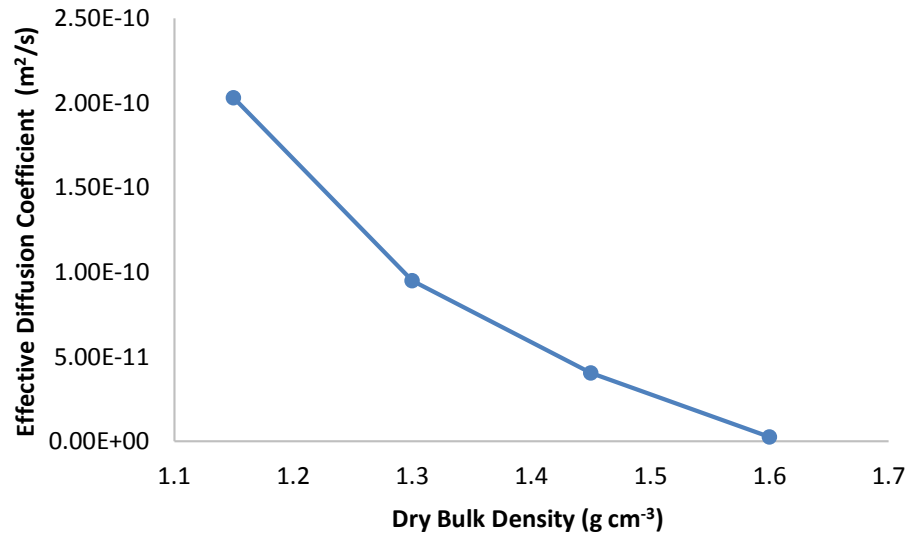


Figure 7. Effective diffusion coefficients of tritium versus dry bulk density.

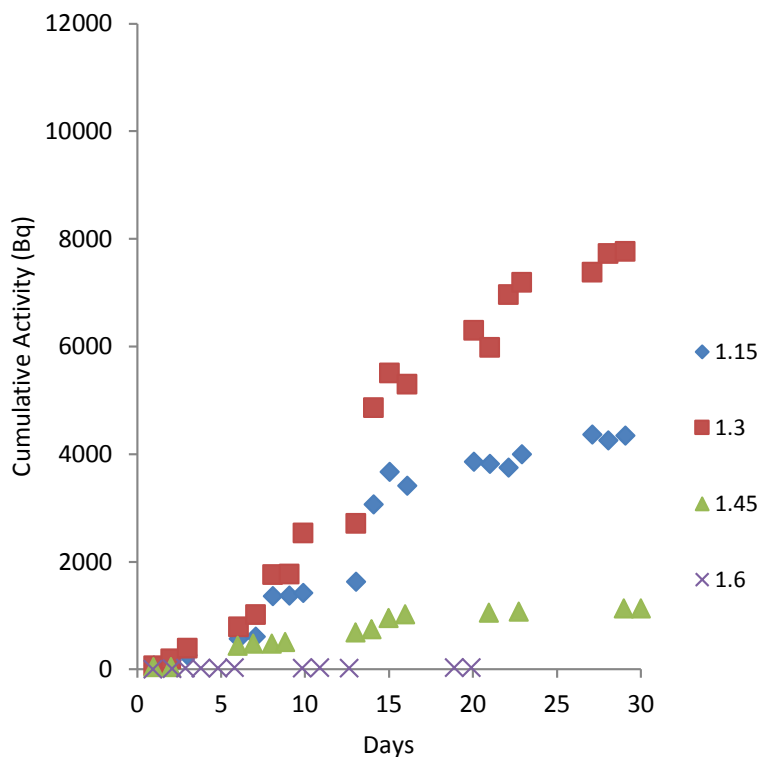


Figure 8. Comparison of linear accumulated activity versus days.

Neptunium diffusion through montmorillonite at 25°C

Diffusion of Np(V) through the compacted montmorillonite was analyzed via ICP-MS. While the tritium data was easily monitored and collected, the neptunium did not produce data as quickly. Due to sorption processes and the limited mobility of Np(V), only cells that contained 1.15 and 1.30 g/cm³ saw Np(V) breakthrough. The accumulated activity is shown below in Figure 9. From the tritium data, effective porosities were determined based on previously presented equations. However, these data are still being fully analyzed and will be included in an eventual peer reviewed report describing these data. Until the 3H breakthrough curves are properly fit, reported values for Np(V) are tenuous at best.

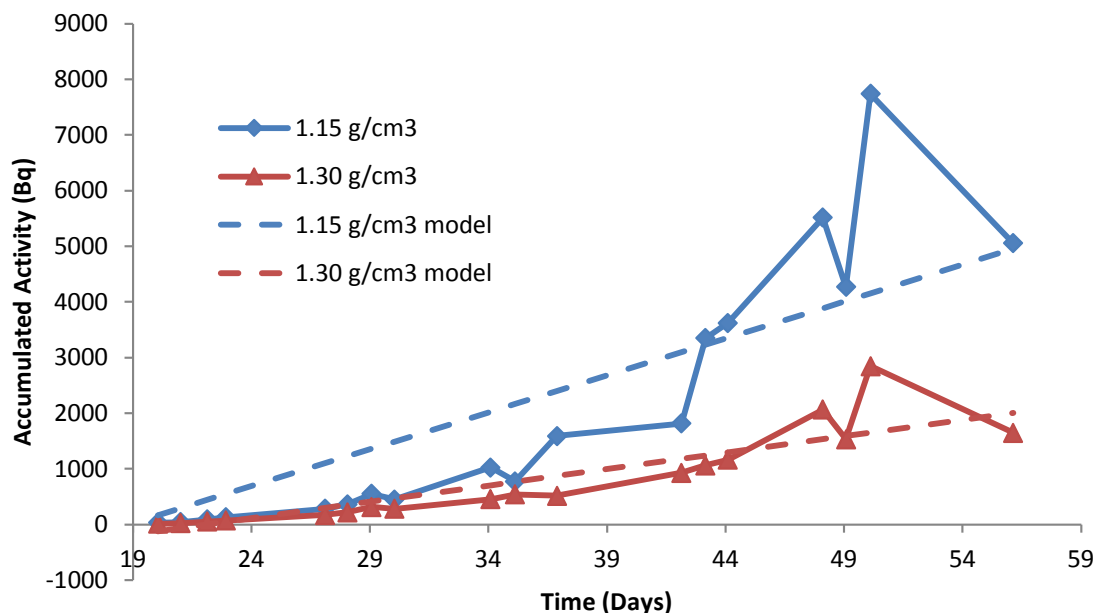


Figure 9. Linear accumulated activity of Np(V) through compacted montmorillonite clay at 25°C.

Tritium diffusion through montmorillonite at 50°C

Diffusion of ^3H and ^{237}Np was also monitored at 50 °C and evaluated using the same methodology described above. The breakthrough of ^3H for each cell is shown in Figure 10 and the effective diffusion coefficients were derived from the plotted accumulated activity are shown in table 3. Each cell has slightly different initial concentrations because they were made individually as opposed to one stock solution used from the reservoirs from 25°C. These data show that the diffusion was slower at 50 °C when compared with 25 °C (Figure 11).

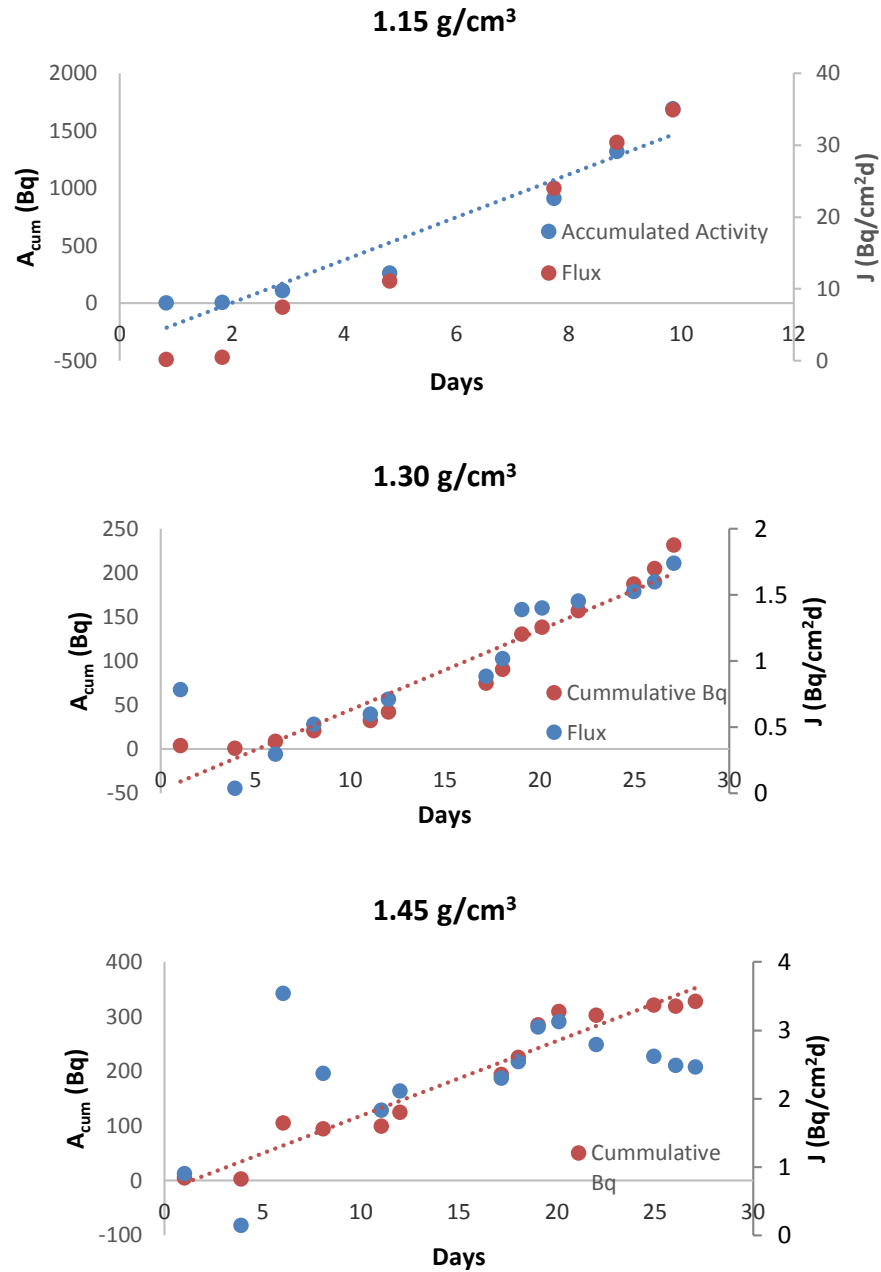


Figure 6. Diffusive flux and accumulated activity for 50 °C. Data for the cell with a bulk density of 1.6 g cm⁻³ are not shown because no breakthrough of ³H occurred.

Table 3. Effective diffusion coefficients for tritium at 50 °C.

Bulk Density	C ₀ (Bq/m ³)	D _e (m ² /s)
1.15	1.40E+10	2.27E-14
1.3	1.37E+10	9.45E-16
1.45	1.37E+10	1.59E-15

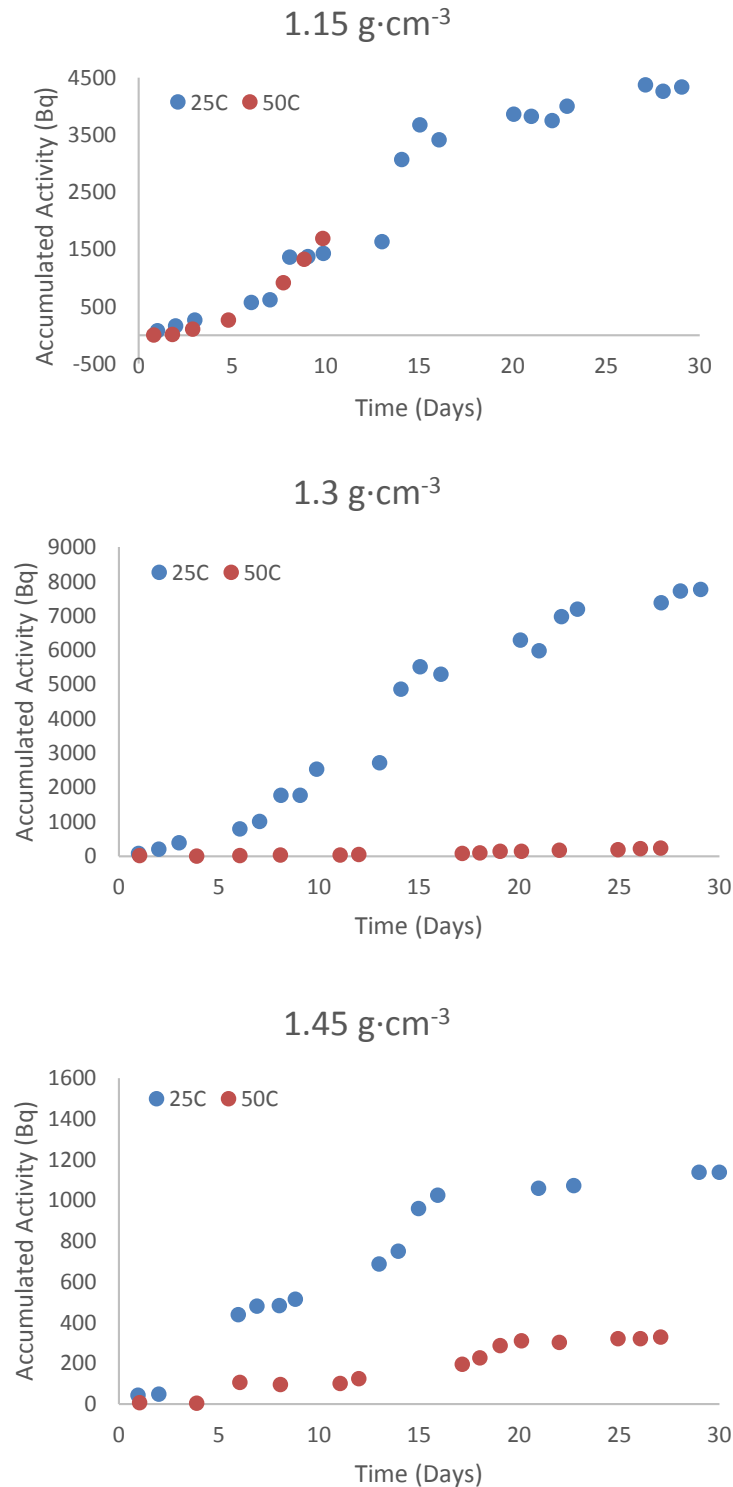


Figure 11: Comparison of ³H diffusion through montmorillonite at 25 °C and 50 °C.

From collected data of the tritium samples at 50°C, breakthrough at the highest dry bulk density 1.6 g/cm³ has not occurred as seen in figure 6 while tritium breakthrough was observed in the other three cells. Comparing the effective diffusion coefficients of tritium for 25 and 50°C, the diffusion rates of tritium at

higher temperatures are orders of magnitude slower than at room temperature (Figure 7). This observation is consistent with the expected decrease in diffusion rate with increasing temperature. To date, no breakthrough of Np(V) has occurred. This is consistent with the expected stronger sorption of Np to montmorillonite with increasing temperature.

Conclusions and Future Work

The objective of this study was to understand the effect of temperature on diffusion of $^{237}\text{Np(V)}$. The data indicate that Np(V) diffusion through montmorillonite decreases with increasing temperature. This is consistent with the decreased diffusion of ^3H observed at 50 °C as well as the increased sorption of Np(V) expected at elevated temperatures. While this project has formally ended, these experiments will be continued to monitor long term diffusion of Np. Additionally, the clay plugs in each diffusion cell will be extruded and the Np concentration as a function of distance from the inlet will be monitored.

As part of our future plans for this work, we will examine diffusion at 80 °C for comparison with the batch sorption data also collected as part of this project. Additionally we plan to examine the influence of ionic strength at a constant bulk density at all three temperatures (25 °C, 50 °C, and 80 °C).

References

1. Brockmann, S. (2006). *Migration of Caesium in Bentonite: Influence of the Pore Water Composition*. Practical Report, Helmholtz-Zentrum Dresden-Rossendorf, Dresden.
2. Trepte, P. (n.d.). *Diffusion of Tritiated Water (HTO) through compacted Bentonite samples: Effect of sample thickness*. Practical Report, Helmholtz-Zentrum Dresden-Rossendorf, Dresden.